UNIVERSITAT POLITÈCNICA DE CATALUNYA
BARCELONATECH

UPC

Institut de Tècniques Energètiques

Neutron capture cross section measurement of the heaviest s-process branching ^{204}Tl and of ^{203}Tl at CERN n_TOF

Doctoral thesis by
Adrià Casanovas Hoste

Supervisors:
César Domingo Pardo
Francisco Calviño Tavares

Doctoral Programme in Nuclear and Ionizing Radiation Engineering

Als meus pares,
a l'Andrea.

Abstract

Neutron capture cross sections are fundamental in the study of the slow neutron capture process of nucleosynthesis, also known as the s-process, which produces half of the observed solar system abundances of elements heavier than iron.

Some nuclei along the nucleosynthesis chain are unstable, and there the capture process competes with the decay process, creating a split in the nucleosynthesis path. The nuclear properties of some of these radionuclides change with the conditions of the stellar environment, a fact that influences the local abundance pattern. ^{204}Tl is a very interesting branching point, because it is shielded from any contribution from other nucleosynthesis processes. The result is that both ^{204}Tl and its stable daughter isotope ^{204}Pb are only produced by the s-process. Hence, by competing with the beta decay, the capture cross section of ^{204}Tl crucially determines the final abundance of ^{204}Pb. A faithful prediction of the solar abundances of *s-only* isotopes, like ^{204}Pb, is one of the key accuracy tests for modern stellar nucleosynthesis calculations.

However, until the present work, due to the challenges of performing a capture measurement on ^{204}Tl, there was no experimental data of its cross section. Thus, large uncertainties existed in its capture cross section, which hampered a more accurate and precise knowledge of the predicted s-process production of ^{204}Pb.

By affecting the abundance of ^{204}Pb, the cross section of ^{204}Tl(n, γ) also influences the ratio of abundances ^{205}Pb/^{204}Pb. ^{205}Pb is also produced only by the s-process, and it is radioactive, with a long half-life of 17.2 My. Therefore, the ratio of abundances of ^{205}Pb/^{204}Pb has the potential to be used as a chronometer of the s-process.

In the year 2013, a sample enriched up to a few percent in ^{204}Tl was produced by neutron irradiation of a ^{203}Tl seed sample at the high thermal neutron flux nuclear reactor of the ILL, in Grenoble (France). Two years later, the ^{204}Tl enriched sample was employed to measure, for the first time, the capture cross section of ^{204}Tl at the n_TOF time-of-flight facility at CERN. The measurement was possible thanks to the unique

features of this facility, in particular, its high instant neutron flux and low background levels. The measurement was performed employing the well-established total energy detection technique (TED), which offers a lower neutron sensitivity, and lower amounts of background, compared to the total absorption method. The TED method, however, requires the use of the Pulse Height Weighting Technique. Its application to this particular experiment was studied in detail, in order to keep its associated systematic uncertainty under control.

The main challenges for the ^{204}Tl measurement were the very high background due to the activity of the sample, the very low amount of material, and the limited knowledge of the geometry of the sample. Such difficulties required the adoption of specific solutions during the measurement and the posterior data analysis. Related to this, several sources of systematic error were evaluated by means of Monte Carlo simulations.

The complications with the ^{204}Tl sample geometry required to apply an in-sample normalization procedure. For this purpose, an ancillary capture measurement on a ^{203}Tl sample was also performed in the same experimental campaign. As a stable nuclide, most of the sources of systematic error could be kept under control. This allowed for an accurate R-matrix analysis of the most relevant capture levels in the resolved resonance region of ^{203}Tl, including the first ever measurement under 3 keV of neutron energy. As a result, the present work has contributed, as well, to improve the ^{203}Tl stellar capture cross section in the 8 to 25 keV neutron energy range.

With the improved ^{203}Tl(n, γ) cross section, an R-matrix analysis of several ^{204}Tl resonances was made possible. These results were employed to experimentally constrain the ^{204}Tl stellar cross section at low energies, and setting additional limits to the stellar cross section at s-process temperatures predicted by nuclear data evaluations.

Keywords: Neutron capture, cross section, resonance level, neutron source, time-of-flight, s-process, nucleosynthesis, branching point, radionuclide, gamma ray detector

Acknowledgements
Agraïments

After 5 years of work, the list of people and institutions who have been important, in some way or another, in the realization of this work is, fortunately, considerably long.

The first place in this long list is, of course, for my mentors Paco and César. I am deeply grateful to both. To Paco, for giving me the opportunity to start this amazing journey into the world of neutron experiments in the ANT group of the UPC. And to César, for guiding me through the long analysis steps with his always serene and resolutive approach, no matter how difficult some of them would appear at first glance. I am deeply grateful to both for they always encouraging and supportive disposition, and for their admirable attitude towards science and work in general: passionate and committed, but at the same time, patient, serene and always in a good mood.

I am also really thankful to my lab colleague Ariel Tarifeño. In the first place, for helping me with the day-to-day issues, from coding to bureaucracy, and for keeping always alive our beloved antsim simulations computer, even during the most strict lockdown in the middle of the covid-19 crisis. And most importantly, I would like to thank him for his decisive participation in the ^{204}Tl experiment with his experienced experimental "eye", which taught me many valuable things that cannot be read in books or papers.

This thesis has also been possible thanks to support from several other institutions. I would like to acknowledge the concession of the Argos scholarship by the Nuclear Engineering Section (SEN) of the UPC, which supported one and a half year of thesis work, and the additional support from INTE, in the form of travel

and thesis finalization scholarships.

During the Ph.D. years, I had the privilege to meet lots of new people during experiments, meetings and conferences. In the first place, I would like to express my gratitude towards the whole n_TOF "crew". I think what makes n_TOF an "outstanding" collaboration, apart from its scientific productivity, is the personal, almost familiar, relationship that has established between members over the years. It would take too much to thank every member of the Collaboration, young or senior, that helped me in some way for this work. Still I would like to mention some names. In the first place, Carlos Guerrero, who was in charge in-situ for the ^{204}Tl(n, γ) experiment at n_TOF, and to whom I am very grateful for basically tutoring me in my first weeks around at n_TOF, when everything was new and challenging for me. Another person to whom I owe much is Jorge. I have shared with him the master courses and every step as an n_TOF Ph.D. student. I would like to thank him for every discussion concerning the data analysis we had, and for having the patience to bear with my constant flow of annoying questions as a newbie ROOT user and as a beginner at n_TOF.

Still related to n_TOF, I would like mention as well some more people with whom I shared many working hours, but also many enjoyable moments during coffe times, lunches, and some well-deserved afterwork beers. Some of these people are Federica, Massimo, Javi, Marta, Thanos, Mario, Aris, Michi, Victor Alcayne, Victor Babiano, Alice, Simone, Mirko, Sarah and many others. Thank you all for making my stays at n_TOF so much rewarding on more personal side as well. Last but not least, I also would like to thank the n_TOF Collaboration for supporting part of my research stays at CERN.

La mayor parte del tiempo de la tesis, sin embargo, lo he pasado en el INTE, con muy breves –e intensas– estancias en el IFIC de València. En cuanto al IFIC, querría agradecer al Grupo de Espectroscopía Gamma por recibirme siempre como a uno más, y en particular a José Luís Taín, por valiosas discusiones sobre algunos asuntos de este trabajo, y a Álvaro Tolosa, con quien he compartido algunos de los "dramas" típicos del estudiante de fin de tesis.

Respecte a l'INTE, voldria agrair la sempre plena disponibilitat del personal dels laboratoris per a qualsevol necessitat material, mesura o petit test que haguéssim de fer. També agrair als òrgans de govern, als directors Yuri Koubychine i Ignasi Casanova, i a la comissió de formació i als seus successius responsables,

Mercè Ginjaume i Jordi Llorca, per les ajudes abans esmentades. En especial, voldria donar-li també les gràcies a la Maria Amor Duch, que com a cap de radioprotecció de l'INTE ha hagut de patir les meves presses d'última hora per tenir a punt els certificats imprescindibles per a treballar al CERN. Igualment, vull agrair-li la seva tasca al personal d'administració de l'ETSEIB, al qual he marejat una mica amb tant de viatge, i en particular a l'Esther Yoldi, sempre resolutiva fos quin fos el "marrón" que li portés.

Las buenas experiencias científicas en congresos y reuniones han venido acompañadas de aún mejores experiencias en lo personal. En este sentido, no querría olvidarme de los compañeros de doctorado de la comunidad nuclear hispánica, y en concreto, además de a Jorge, quisiera agradecer a Carlos Vivo, y al resto de estudiantes de doctorado de la universidad de Sevilla, por todos los buenos momentos vividos durante el máster, y luego, ya como doctorandos, en las Bienales de Física y en los CPAN. Y también durante alguna aparición mía, sin objetivo científico alguno, por Sevilla.

També vull tenir paraules d'agraïment per als amics del màster de Barcelona, l'Oriol I la Irene, amb qui vaig compartir viatges amunt i avall per la geografia ibèrica, nits eternes d'informes de pràctiques (d'acord, tu no Mari, ja ho tenies acabat) i esperes "eternes" d'autobusos, però també molta diversió i alguna caiguda tonta.

Vull donar les gracies, també, a la gent de l'INTE que m'ha acompanyat en el dia a dia durant gairebé 5 anys. Als treballadors dels laboratoris de l'INTE, que han fet que el dinar fos una hora de relaxament imprescindible entre tant número I tanta gràfica. I sobretot, vull agrair als "miniINTEs": Dani, Sara, David Mani, Luisa, María, Almu, Víctor, Susana, Anna, Daniel, David i als que han passat més fugaçment; gràcies per aquells nostres suposats "afterworks" de divendres que s'allargaven fins a les tantes, tant necessaris per buidar el cap saturat de nuclis i estrelles.

Entrant ja de ple al camp personal, cap feina és possible sense les persones més properes, que són al mateix temps suport i motivació. Començant per als amics "de siempre", als i a les que sempre hi són quan necessites veure una cara amiga. Àlex, Dodo, Edo, Riki, Rocío, Ez, Isolda... Gràcies, tant si seguiu a prop o una mica més lluny, per cada paraula d'ànim, cada estona de dissabte, cada sopar, cada tarda de cine, i cada ruta noctàmbula per Barcelona que hem passat junts.

Vull agrair-li a la meva família el seu recolzament en tots els passos de la vida: als avis, als tiets i a la Marina, i en especial als meus pares, que m'han cuidat sempre i han aguantat estoicament les meves petites frustracions diàries doctorals. A vosaltres us dec l'anhel de coneixement, el sentit crític cap a la realitat, i fins i tot la fascinació des de ben petit per la ciència i la tècnica, i en especial per les "coses nuclears I radioactives" (sí mama, ho vas encertar amb aquell llibre).

I finalment, vull donar-li les gràcies, especialment, a una persona que potser porta una mica menys de temps al meu costat, però que ha estat la que ha viscut i ha "sofert"de més a prop cada "pasín" del període menys amable de la tesi. Gràcies, Andrea, simplement per ser-hi, per la teva paciència, per les tardes, nits i caps de setmana sacrificats, per el teu suport constant i incondicional, i sobretot, per creure sempre en mi i animar-me en els moments més difícils.

Contents

List of Figures

List of Tables

Chapter 1

Introduction

1.1 Introduction: the origin of the heavy elements

The synthesis of the heavy elements, which are those heavier than iron, is one of the most important open questions in modern astrophysics. The first direct evidence that heavy elements had a stellar origin was provided by Merrill, who discovered technetium spectral lines in the light of red giant stars [1]. Only a few years later, most important aspects of the modern understanding of nucleosynthesis were already depicted by Burbidge et al. in their seminal article entitled "Synthesis of the Elements in Stars" [2] –also known as the "B^{2}FH" paper–. A similar analysis was performed, independently, by Cameron [3]. From the contemporary knowledge of solar elemental abundances, spectroscopic observations of astronomical objects and terrestrial and meteoritic isotopic abundances, these authors proposed several processes and stellar scenarios that could lead to the observed distributions. In the process, they pointed out the decisive role of nuclear physics, particularly that of neutron induced reactions, in providing a quantitative description of the isotopic patterns observed.

One of the central contributions of the B^{2}FH analysis was the clear distinction between the different processes that gave shape to the observed isotopic abundances. They proposed a slow (s) neutron capture process, involving low neutron fluxes and time scales; a rapid (r) neutron capture process, on the contrary, with high fluxes and very short time scales, and a proton capture (p) process, responsible for the production of several proton rich isotopes that could not be produced
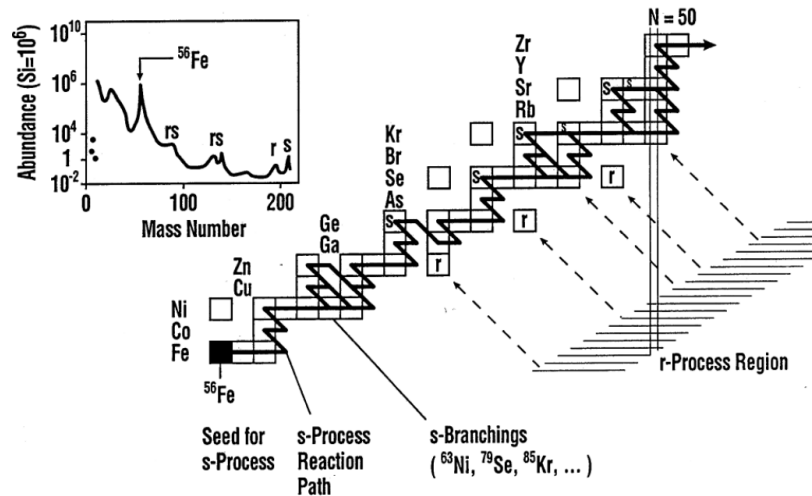
Figure 1.1: *Schematic view of the chart of nuclides, showing the path of the s-process from the seed nucleus ^{56}Fe. The "r-process region" corresponds to the very neutron rich nuclei produced during r-process, which ultimately decay, producing the r abundances. The insert graph shows the solar isotopic composition as a function of mass, with the abundance peaks of each nucleosynthesis process indicated. Figure extracted from [4].*

by the other two. Over the decades, even if much detail and complexity has been added into this picture, it remains true in its essential features.

The **s-process** is responsible of approximately half the elemental abundances from iron to bismuth. Starting from ^{56}Fe seeds, the nuclide production is characterised by successive neutron capture reactions and beta decays, following closely the valley of nuclear stability (see Figure 1.1). It takes place in very well identified evolutionary stages of red giant stars and massive stars, and its time scale is long, of several thousands years. Essentially, two inputs are needed for modelling the s-process: capture cross sections, and beta decay rates. Additionally, the main s-process contribution is produced in mostly stable conditions in terms of temperature ($\sim 10^8$ K) and neutron density ($\sim 10^7$ cm^{-3}). Therefore, in a first approximation, it can be modelled analytically for remarkable results. A detailed description of the different s-process models and components will be given in the next sections.

The **r-process** is responsible for the other half of the abundances, including all the long-lived radionuclides heavier than bismuth present in nature. Although

it also involves neutron captures and beta decays, it is characterized by very high neutron densities in excess of $10^{20}\,\mathrm{cm}^{-3}$ and temperatures in the range of 1 to 2 GK, and very short time scales, of the order of a few seconds, at most. The huge neutron fluxes lead to the build-up of extremely neutron rich nuclides, far away from stability. When the neutron irradiation ceases, these nuclides decay rapidly towards stability, producing a unique isotope signature. However, modelling the *r*-process is extremely complex. It requires nuclear data (nuclear masses, beta decay rates and many others) of a vast number of very exotic isotopes, almost impossible to access experimentally. On top of that, although the conditions required are only achieved in supernova explosions and neutron star mergers, the particular astrophysical sites are still unclear. Despite this, the recent observation of heavy element production [5], and particularly strontium [6] in the aftermath of neutron star mergers strongly suggests that this might be, indeed, one of the most probable sites. A detailed review of the *r*-process may be found in [7].

Finally, the **p-process** is the responsible of the production of 32 isotopes from Se to Hg [8], which cannot be produced by the neutron capture processes. These nuclei are between 10 and 100 times less abundant than *s* or *r* process nuclei. It is hypothesized that it also occurs in explosive events, like supernovae.

1.2   The classical *s*-process model

The first phenomenological description of the *s*-process was already given in the B^{2}FH paper. Without any detailed knowledge of the stellar models environment, it was assumed a certain source producing a neutron density n_n, with temperature T constant. In this situation, the variation of the *s*-process abundance N_s of a certain isotope of mass A can be written as

$$\frac{dN_s(A)}{dt} = \lambda_n(A-1)N_s(A-1) - (\lambda_n(A) + \lambda_\beta(A))N_s A \ . \qquad (1.2.1)$$

In this expression, we have:

- $\lambda_n = n_n \langle \sigma_A \rangle v_T$ is the neutron capture rate, with $v_T = \sqrt{2kT/m}$ the neutron thermal velocity. In stellar environments T is very high and neutrons are quickly thermalized, with their velocity spectrum being described by a Maxwell-Boltzmann distribution. The quantity $\langle \sigma_A \rangle$ is defined as the capture

cross section averaged by the energy spectrum of the neutrons,

$$\langle\sigma\rangle_A = \frac{\langle\sigma v\rangle}{v_T} = \frac{2}{\sqrt{\pi}} \frac{\int_0^\infty \sigma(E_n) \cdot E_n \cdot e^{-E_n/kT} dE_n}{\int_0^\infty E_n \cdot e^{-E_n/kT} dE_n} \ , \qquad (1.2.2)$$

and is commonly referred to as maxwellian –or stellar– averaged cross section, or "MACS".

- $\lambda_\beta = \ln(2)/t_{1/2}$ is the disintegration rate for beta decaying isotopes. Most nuclei in the s-process chain are either stable ($\lambda_\beta = 0$), or have half-lives much smaller than the average time scale of neutron capture, of $\approx 1 - 10$ y, and hence $\lambda_\beta \ll \lambda_n$.

The assumption of constant T avoids the dependency on the temperature of the cross section and the beta decay rate. We can introduce the *neutron exposure*, defined as

$$\tau = v_T \int n_n(t) dt \qquad \text{or} \qquad d\tau = v_T n_n(t) dt \ , \qquad (1.2.3)$$

which has units of neutrons/cm^2. Rewriting equation (1.2.1) in terms of τ and neglecting the beta decay,

$$\frac{dN_s(A)}{d\tau} = \langle\sigma\rangle_{A-1} N_s(A-1) - \langle\sigma\rangle_A N_s(A) \ . \qquad (1.2.4)$$

This equation implies that the system will tend to minimize the difference between $\langle\sigma\rangle_{A-1} N_s(A-1)$ and $\langle\sigma\rangle_A N_s(A)$. If the equilibrium is defined as

$$\frac{dN_s(A)}{d\tau} \approx 0 \implies \langle\sigma\rangle_{A-1} N_s(A-1) \approx \langle\sigma\rangle_A N_s(A) \qquad (1.2.5)$$

$$\implies \langle\sigma\rangle_A N_s(A) \approx const \ , \qquad (1.2.6)$$

which is called the *local equilibrium approximation*. This approximation works well in mass regions in-between neutron shell closures, as depicted in Figure 1.2, and a steady flow will be achieved. However, it is not generally satisfied near neutron shell closure nuclei, whose capture cross section is very low to reach the equilibrium. The model was later improved by Seeger et al. [10], proposing that the solar abundances were the result of a series exponential distribution of neutron exposures of a given fraction f of the iron seeds $N(56)$,

$$\rho(\tau) = \frac{f \cdot N(56)}{\tau_0} e^{-\tau/\tau_0} \ . \qquad (1.2.7)$$
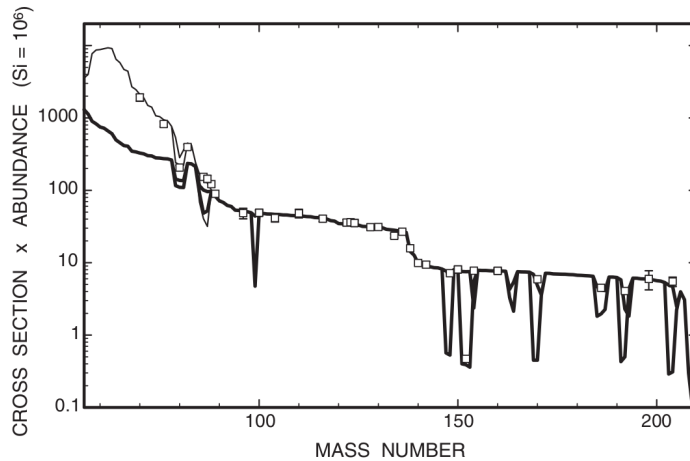
Figure 1.2: *Plot of the $\langle\sigma\rangle_A N_s$ predicted quantities by the classical model as a function of the mass number. The thick line corresponds to the main component, whereas the thin line is the same with the addition of the weak component from massive stars. Empty squares represent empirical abundances of s-only nuclides. Some important branching are also shown. Figure extracted from [4].*

Then, the product of the stellar cross section and the *s* abundance can be given in analytic form for all nuclei from iron to bismuth [11]:

$$\langle\sigma\rangle_A N_s(A) = \frac{f \cdot N(56)}{\tau_0} \prod_{i=56}^{A} \left(1 + \frac{1}{\tau_0 \langle\sigma\rangle_i}\right)^{-1}. \tag{1.2.8}$$

The factors f and τ_0 are adjusted by fitting the curve to the solar abundances of nuclei only produced by the *s*-process. Hence, the only required input in the expression are the stellar capture cross sections. In spite of the schematic nature of the classical model, it provides an excellent general reproduction of the solar abundances for $A > 90$, as can be seen in Figure 1.2. The root mean square deviation is of 3% for *s*-only nuclei far from neutron magic number [12], and not affected by branchings. The nuclide abundance distribution obtained with equation (1.2.8) is commonly referred as the *main* component of the *s*-process.

1.2.1   Shortcomings of the classical model

As it can also be seen in Figure 1.2, the classical main component fails to describe the abundances for nuclei with $A < 90$. In order to do so, it was necessary to

propose a second contribution, known as the *weak s*-process, which operates in Massive Stars ($> 8M_\odot$) [13, 14]. Furthermore, the main component also failed short to reproduce the observed abundances of the lead isotopes ^{206}Pb, ^{207}Pb and ^{208}Pb, which form the so-called third s-process peak. To solve this issue, an additional *strong* component was postulated [13]. This was characterized by a very large neutron exposure, leading to a much higher number of neutrons per seed, and consequently, to an increase of the third peak nuclide production. In addition, measurements performed during the 1990s [15–17] led to substantial improvements in the accuracy of several important cross sections, which showed that the classical model overestimated the production of several *s*-only isotopes [18].

Finally, there are nuclei in the *s*-process chain in which $\lambda_n \sim \lambda_\beta$, and thus, the assumptions of the model simply do not hold. These nuclei are known as *branching points* because the competition between the reactions causes a split in the *s*-process flow. The decay rate of some of these nuclei is much sensitive to temperature changes [19], and thus the abundance pattern of nuclei directly influenced by the branching will be dependent on the temperature. On the other hand, some branches are weakly affected by temperature, and hence they are mostly sensitive to neutron density variations of the nucleosynthetic environment. Historically, the disagreements between classical predictions and observations in the abundances near branching points were seen as an indication of a more complex *s*-process scenario, in which temperature and neutron density were not constant.

Despite this, the classical model could be locally adjusted to reproduce specific isotopic branching patters, by simply setting the temperature and neutron density as free parameters. This was used, in fact, to obtain a first estimation of the neutron density and temperature of the *s*-process environment [18].

1.3   The stellar s-process model

Stellar models are based on the detailed study of the evolution of stars to determine the stellar sites, and physical conditions, in which the *s*-process occurs. Over the last 30 years, there has been much development in stellar evolutionary codes like FRANEC [20, 21], or MESA [22], which simulate the whole lifespan of a star and provide its time-dependent thermodynamic conditions. In parallel, nucleosynthesis network calculation codes have been developed. These codes employ the

data provided by the evolutionary codes to calculate numerically the production of nuclei as the star evolves. Two methods exist for the network calculation: either coupled to the star evolution, like the one employed for the FRUITY database [23], or a post-processing approach, like NuGrid [24] and others [25]. The emergence of nucleosynthesis calculation codes permitted in-depth studies of the nuclide production in many star models, which ultimately led to the development of the *stellar s*-process model. The different classical *s*-process components required for a comprehensive description of the solar abundances are naturally obtained as contributions from different stars and stellar evolutionary phases.

An exhaustive analysis of the stellar model, and its *main* and *weak* components, is featured in the comprehensive review of the *s*-process by Käppeler et al. [4]. In this work we will concentrate on the main component, since it is responsible for the production of most isotopes for which the ^{203}Tl(n, γ) and ^{204}Tl(n, γ) cross sections are relevant.

1.3.1 AGB stars

The main *s*-process takes place in the thermally pulsating phase of the Asymptotic Giant Branch (AGB) evolutionary stage of low mass stars, typically with masses between 1.5 and 3 $M_\odot$ [26, 27]. A schematic view of the structure and evolution of a typical AGB star can be seen in Figure 1.3. In this advanced stage of their evolution, these stars are mainly composed of an inert carbon-oxygen core, a thin carbon and helium intershell, and an extended envelope mainly composed of H and He.

In its quiescent phase between thermal pulses (TP), hydrogen is fused into helium radiatively in a layer at the base of the convective envelope. Over thousands of years, helium slowly accumulates in the intershell, which is partly degenerate. In this condition temperature rises until the runaway thermonuclear fusion of He is ignited at the bottom of the shell, an event referred to as *He-flash*. The He-flash drives the formation of a convective zone in the shell, pushing the envelope outwards, and leading to a considerable increase in the luminosity of the star. After just a few hundred years, the expansion of the shell caused by the He-flash leads to a decrease of the temperature, and fusion stops. The H-rich envelope shrinks back, engulfing a sizable part of the underlying He-shell, a process called *third dredge-up*.
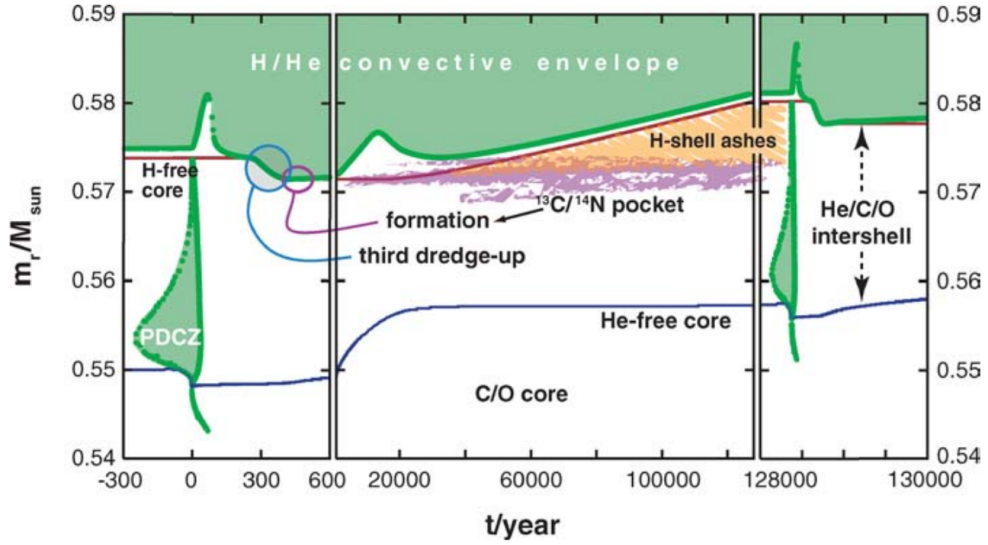
Figure 1.3: *Diagram of the structure of an AGB staras a function of time. In this type of plot, also known as Kippenhahn diagram, the y-axis represents the radius* r *of the star, in terms of fraction of the total mass contained for a given value of* r. *Figure extracted from [26].*

Due to the convective nature of the envelope, it brings newly synthesized s-process material during the interpulse phase into the star surface, and enriches the He-shell with protons. Eventually H-burning restarts at the bottom of the envelope, and the whole process restarts again. A typical AGB star experiences between 20 and 30 thermal pulse episodes. In this series of events, s-process occurs in two main stages.

^{13}C pocket

The bulk of the nuclide production occurs during the H-burning phase. The neutron source is provided by the reaction ^{13}C$(\alpha, \mathrm{n})^{16}$O, which is activated when temperatures approaches $\sim 0.9 \cdot 10^8$ K (corresponding to a thermal energy of $kT \sim 8$ keV). ^{13}C is produced in a very thin layer of the intershell, by the reaction ^{12}C$(p, \gamma)^{13}$N$(\beta^+)^{13}$C. The protons required for the ^{13}C pocket formation are injected into the shell during the third dredge-up, in a mechanism not fully understood yet (see [28], and references therein). The neutron density produced is $n_n \sim 10^7$ cm^{-3}, which lasts for some $\sim 25,000$ years, leading to a large and long neutron exposure.

He-flash

During thermal pulses, temperatures in excess of $3 \cdot 10^8$ K ($kT \sim 26$ keV) are easily reached near the bottom of the convective zone, triggering the release of neutrons by the activation of the reaction ^{22}Ne$(\alpha, \mathrm{n})^{25}$Mg. For a very short time of about 100 years, neutron densities up to 10^9 to 10^{11} cm^{-3} are produced, with the peak value depending on the star mass and metallicity. Although this second burst contributes very little to the overall neutron exposure [18], the high flux is sufficient to alter the abundance pattern around branching points.

1.4   Branching points: the case of ^{204}Tl

As explained earlier, branching points are characterized by stellar decay rates comparable to the average neutron capture rate. The strength of the branching can be described by the *branching factor* f_β,

$$f_\beta = \frac{\lambda_\beta}{\lambda_n + \lambda_\beta} \ . \tag{1.4.1}$$

The thallium isotope ^{204}Tl, decaying by β decay to ^{204}Pb with $t_{1/2} = 3.78$ y, is a branching point of the s-process. Its particularity lies in the fact that it is shielded against any r-process contribution by the stable nuclide ^{204}Hg. Additionally, ^{204}Pb is neither affected by the α-recycling beyond ^{209}Hg, nor by the radiogenic contribution from the thorium and uranium decay chains. Consequently, both ^{204}Tl and its daughter isotope are only produced by the s-process. Furthermore, thallium and lead are in termination region of the s-process path, which is represented in Figure 1.4.

This region is interesting for several reasons. ^{206,207,208}Pb form the previously mentioned third s-process peak. A considerable part of the abundances of these isotopes is now believed to be produced by low metallicity stars, which constitutes a natural explanation for the *strong* component [25, 29–31]. However, ^{204}Pb, with a much less solar abundance than the rest, is produced *only* by the main component without a relevant contribution from low metallicity stars.

Under ^{13}C-pocket conditions, the branching strength of ^{204}Tl is $f_\beta \lesssim 0.9$, leading to a significant production of ^{204}Pb. However, during the TP event, the increase of the neutron flux increases considerably the chance of capture, and $f_\beta \sim 0.5$.
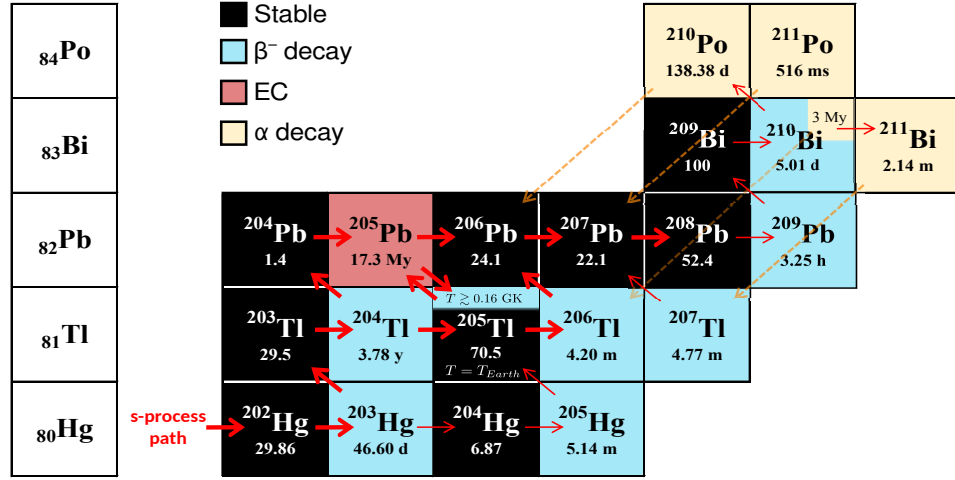
Figure 1.4: *View of the chart of nuclei at the termination zone of the s-process. Thick red arrows correspond to the main s-process flow path, whereas thin arrows to marginally activated paths.*

Therefore, the branching at ^{204}Tl crucially influences the abundance of ^{204}Pb and the ^{204}Pb/^{206}Pb abundance ratio. Current main stellar *s*-process calculations reproduce between 87% and 91% of the solar ^{204}Pb abundance [28, Appendix B3.3], but this value is affected by the uncertainty in determining the solar abundances of lead [32], and by the accuracy of the nuclear data involved. Specifically, of the stellar β^- decay rate of ^{204}Tl can only be calculated theoretically. From the experimental point of view, the capture cross section of ^{204}Pb is well known [33], and the main source of uncertainty is due to the capture cross section of ^{204}Tl.

So far, this could not be determined owing to the difficulties to produce such a sample in sufficient amount, and to the complexity of measuring such a radioactive sample. Theoretical evaluations of ^{204}Tl(n, γ) diverge considerably between them (see Figure 1.5) [34]. Thus, the present measurement should contribute to a more accurate and precise determination of the ^{204}Pb *s*-process abundance.

By affecting the ^{204}Pb abundance, the branching at ^{204}Tl has also influence on the ratio of *s*-only isotopes ^{205}Pb/^{204}Pb. The isotope ^{205}Pb is of particular interest because it is radioactive, decaying by electron capture (EC) to ^{205}Tl, with $t_{1/2} = 17.2$ My. Hence, the ^{205}Pb/^{204}Pb ratio has the potential to be used as a chronometer of the last *s*-process events that contributed to the Solar System isotopic abundances [35–37]. Such calculation, in fact, has been done already with
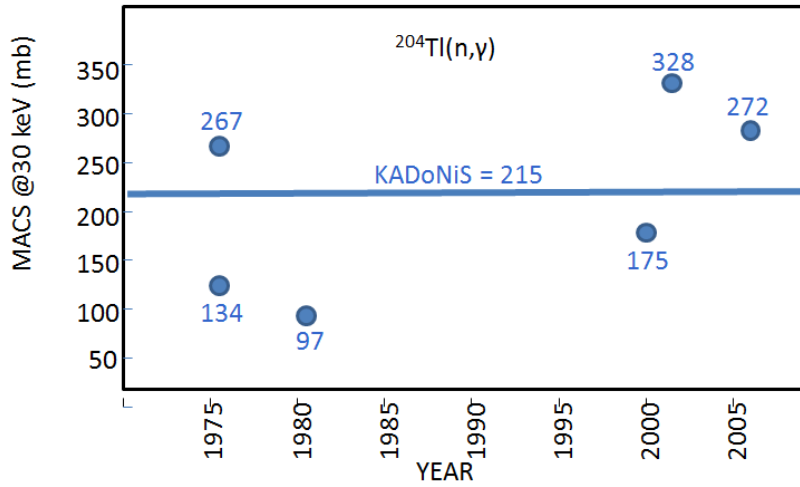
Figure 1.5: *The different theoretical evaluations of the ^{204}Tl(n,γ) MACS at kT = 30 keV, compared to the recommended value by the Kadonis database [39]. Figure from [34].*

the ratios ^{107}Pd/^{109}Pd and ^{182}Hf/^{180}Hf [38], but unlike ^{205}Pb/^{204}Pb, those ratios have an important *r*-process contribution. Thus, a similar study with ^{205}Pb/^{204}Pb would be highly interesting.

The survival of ^{205}Pb in *s*-process environments was a matter of considerable debate for decades [35, 37, 40]. Due to the interaction with the plasma and the photon bath of the stellar interior, atoms are highly ionized, and their nuclei can populate excited levels. In the case of ^{205}Pb the population of its first nuclear excited state at 2.3 keV was predicted to produce a high enhancement of its EC decay at He-shell temperatures, which would lead to its destruction before it was released in the interstellar medium. However, as Yokoi et al. pointed out, beyond $\sim 1.6 \cdot 10^8$ K the highly ionized state of the terrestrially stable ^{205}Tl could lead to a strong activation of its bound state beta decay to ^{205}Pb. At a certain temperature, such decay process could counterbalance, and even exceed, the decay rate of ^{205}Pb. In this way ^{205}Tl, which is stable at ^{13}C temperatures and thus abundantly produced, would be a potential source of ^{205}Pb.

The prediction of the ^{205}Pb survival renewed the interest in the search of its live presence in meteorites which crystallized at the time of the birth of the Solar System, thus conserving the primordial solar abundances. In recent years, this led to a successful determination of the original ^{205}Pb/^{204}Pb ratio by mass spectroscopy

in iron meteorites [41], carbonaceous condrites (CC) [42] and ordinary condrites. [43].

In order to extract a chronological s-process estimation, the measured values of initial ^{205}Pb/^{204}Pb should be compared to predictions, which rely on careful modelling of the injection of s-process material in the presolar nebula [44], and in the determination of the ^{205}Pb/^{204}Pb ratio from nucleosynthesis models. However, the latter is hampered by the lack of additional nuclear data inputs, such as the cross sections of ^{205}Tl(n, γ)and ^{205}Pb(n, γ), and the still not experimentally observed decay of ^{205}Tl. The abundance of ^{205}Pb is dominated by the balance of the decay system ^{205}Pb-^{205}Tl, and by the respective capture cross sections.

In this sense, the measurement presented in this work can be considered to be the first of a series, which also includes a new of measurement of ^{205}Tl(n, γ), successfully performed also at n_TOF in 2018 [45], and the plan to measure ^{205}Pb(n, γ) in the next experimental phase of the facility. At the same time, the crucial bound state beta decay of highly excited ^{205}Tl will be investigated at the ESR experiment at GSI [46], with the measurement planned for the near future.

All these present and future experiments should reduce considerably the mentioned nuclear data uncertainties, allowing for a more reliable prediction of the ^{205}Pb/^{204}Pb ratio from stellar models, and enabling its reliable interpretation as a chronometer for the s-process in the Solor System composition.

1.5   Cross section measurements of radioactive isotopes

The radioactive nature of branching points is what makes them relevant in s-process studies. But at the same time, this is what makes experiments with these type of isotopes so complex and challenging. The main challenges for a (n, γ) measurement on a radioactive sample are:

- **Very low mass.** Short-lived radioactive nuclides must be produced from scratch, usually from long neutron irradiations in nuclear reactors. The resulting amount available is usually on the order of a few 10^{18}–10^{19} atoms, or milligrams. In a few cases, the target nuclide is obtained by the decay of the irradiation product. This procedure allows to perform chemical purification of the interest nuclide and the seed. However, in most cases the irradiated

seed is the preceding $(A - 1, Z)$ isotope, and thus chemical separation is not possible.

- **Impurities.** In a non-purified sample, the nuclide of interest will be present in very low relative concentration compared to the seed isotope, which adds much complexity to the posterior data analysis. In this sense, it is highly convenient to measure, as well, the seed sample alone. Additionally, in the seed there will be trace impurities of elements which become activated in the irradiation process. Although most of them are very short-lived and thus disintegrate after a cool down period, some ubiquitous elements, like cobalt, have very large cross section and yield medium-lived radioisotopes like ^{60}Co, which is a strong gamma ray emitter.

- **Sample activity.** The short half-lives of the nuclides of interest imply very high activities, which usually pose practical concerns regarding handling and radiation protection. Most importantly, the radiation from the sample –and from the mentioned impurities– generates considerable amount of background signals. This issue must be carefully addressed during the measurement, and in the posterior analysis.

1.5.1 Activation measurements

For a few radionuclides the product of neutron capture is also radioactive, and hence, the reaction cross section can be measured with activation techniques. In this method, the sample is typically irradiated by a neutron source with a quasi-maxwellian spectrum (usually of 25–30 keV), and the MACS is directly measured by means of gamma ray spectroscopy techniques, with a few corrections needed to account for differences in the neutron spectrum. The activation technique avoids most of the above issues, although the cross section information is limited to a single energy range. In the case of ^{204}Tl the activation was not possible because the capture product is the stable ^{205}Tl.

1.5.2 Time-of-flight measurements

The time-of-flight method –explained in full detail in chapter 3– makes it possible to measure the energy dependent capture cross section in a broad energy window,

from thermal energies up to several hundred keV, which is the range of interest for s-process studies. In this range, the capture cross section of most nuclides shows a very pronounced resonant structure. For both ^{203}Tl and ^{204}Tl, the limited amount of material and statistics available made it only possible to analyse of this resonant region, commonly referred to as the Resolved Resonance Region (RRR). The theoretical framework necessary to extract a cross section from the RRR will be discussed in the next section.

1.6 Radiative neutron capture in the Resolved Resonance Region

A brief description of the radiative neutron capture process from the theoretical point of view will be given in the following sections. As it was just mentioned, the analysis will be centred on the RRR. By applying the results provided by the Compound Nucleus theory [47] and the R-matrix formalism [48], we will obtain an expression of the capture cross section in terms of resonance parameters, which can be readily determined experimentally.

1.6.1 Compound Nucleus theory

In most intermediate and heavy nuclei between the neutron magic numbers, the process by which a nucleus captures a neutron is successfully described by the Compound Nucleus theory. In this theory, proposed originally by Bohr in 1936 [47], the target nucleus X, of atomic number Z and mass A, forms with the incoming particle –in our case a neutron– a new Compound Nucleus, of equal Z and mass $A + 1$. This nucleus is left in a high excitation state, with the excitation energy given by

$$E^* = S_n + \frac{A}{A+1} E_n \ , \tag{1.6.1}$$

where S_n is the neutron separation energy of the nucleus $^{A+1}_{Z}$X and E_n the energy of the incoming neutron. As depicted in Figure 1.6, the Compound Nucleus is a many-body quantum system, and thus shows a series of excited levels beyond the separation energy, which are populated if the energy of the neutron matches it appropriately. Hence, a quasi-stationary or *resonant* state will form.
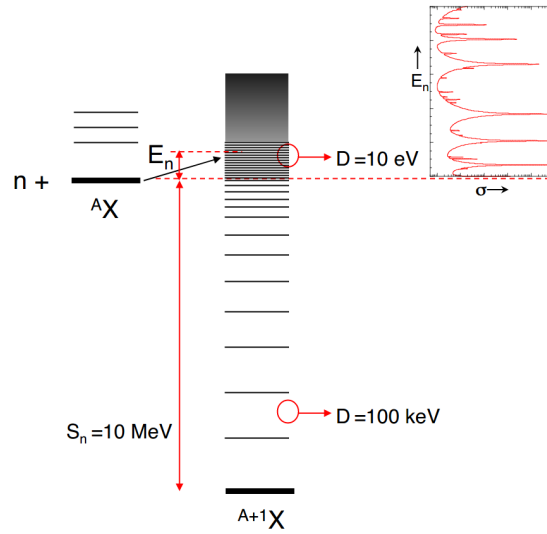
Figure 1.6: *Schematic view of the formation of the compound nucleus after the capture of a neutron by the nuclide $^A X$. The excited levels beyond the neutron separation energy correspond to resonant states of the compound nucleus, which in capture experiments are observed as cross section resonances. Extracted from [49].*

This resonance level will decay with a half-life τ, which will be determined by the quantum properties of the compound nucleus. In addition, by the uncertainty principle, τ will be related to the energy width Γ of the resonance level by $\tau \approx \hbar/\Gamma$. The state will de-excite through any of the possible exit channels. These can be the emission of radiation, the emission of a neutron with the same or different energy, the fission of the nucleus, the emission of charge particles, etc. The total resonance width will be equal to the sum of the partial widths of each process,

$$\Gamma = \Gamma_\gamma + \Gamma_n + \Gamma_f + \dots \tag{1.6.2}$$

The observed values of Γ are of the order of electronvolts, and thus the half-life of the resonance state will be $\tau \sim 10^{-15}$ s. In the case of the thallium isotopes, the only competing channel with the radiative capture in the measured RRR is the elastic channel, with all the other having much smaller widths, and hence much higher lifetimes.

The probability of excitation to a resonance level, at a given incoming energy E_n, determines the total cross section of the reaction at that energy. Similarly, the probability of de-excitation through some of the possible exit channels defines the

corresponding partial cross section.

1.6.2   Direct Capture

In light nuclei and neutron shell closure nuclei, the number of nuclear excited states is usually very low. In this situation, an important contribution to the capture cross section can come from the Direct Capture (DC) mechanism [50]. In this mechanism, the capture of the neutron leaves the newly formed nucleus in a bound state below the neutron separation energy, without the formation of a compound nucleus intermediate state. The DC component cannot be measured in the experiments described in this work, since they rely on detecting the de-excitation of the compound nucleus.

The DC process has a relevant contribution, for instance, in the stellar capture cross section of ^{208}Pb [51]. Although thallium isotopes have relatively low number of excited levels, the situation is not comparable to the few excited states of ^{209}Pb. Therefore, it is not expected a relevant contribution of DC to their capture cross section.

1.6.3   R-matrix formalism

From the mathematical point of view, the Compound Nucleus theory is accurately described by the R-Matrix formalism, introduced by Wigner and Eisenbud [52]. A detailed and comprehensive review of the theory was given by Lane and Thomas [48].

The basic idea of the theory is to split the particle-target interaction space into two regions:

- An external region, where the particles are separated enough so that the nuclear interaction is negligible. This condition is expressed as $r > a_c$, where a_c is the so-called channel radius. In the external region the Schrödinger equation can be solved to obtain the wave functions of the system. These are divided into the incoming wave function, which describes the system before the collision, and the outgoing wave function, describing the system of the reaction products.

- An internal region, where –unknown– nuclear forces predominate, the Schrödinger

equation is not solvable and the states of the system are equally unknown. The solution provided by the theory is to write the internal wave functions as a superposition of ingoing and outgoing eigenstates, that at $r = a_c$ matches the boundary conditions determined by the external wave functions. In this way, every possible combination of the ingoing wave and the outgoing waves, that is, every partial cross section, can be parametrized by the eigenstates and eigenvalues of the internal region, which correspond to the decay amplitudes and energies of the compound state.

It is convenient to employ the formalism of nuclear reaction theory to describe the state of the system before and after the collision. In this context, every entrance and exit state of the system is called a channel c, characterized by quantum numbers $c = \{\alpha, l, s, J, m\}$, where

- α is the index which identifies each entrance and exit channel in terms of the type of both interacting particles (mass, charge) and their energy state.

- l is the orbital angular momentum.

- s is the quantum number of the channel spin $\vec{s}$, defined as the vector sum of i, the spin of the incident particle, and I, the spin of the target, that is, $\vec{s} = \vec{I} + \vec{i}$. This satisfies the triangular condition $|I - i| \leq J \leq I + i$.

- J is the quantum number of total angular momentum of the channel, defined as $\vec{J} = \vec{l} + \vec{s}$, and satisfying $|l - s| \leq J \leq l + s$.

Blatt and Biedenharn solved the non-relativistic Schrödinger equation for particles of any spin, in the absence of Coulomb interaction, by applying the boundary condition of a stationary ingoing plane wave with a stationary outgoing spherical wave [53]. If the resulting partial differential cross section is integrated for all dispersion angles, and summed over all possible channel reactions, an expression is obtained for the cross section from the entrance channel c to any other exit channel c',

$$\sigma_{cc'} = \pi \lambdabar_c^2 g_c |\delta_{cc'} - U_{cc'}|^2 , \qquad (1.6.3)$$

where $U_{cc'}$ are the elements of the collision matrix $\mathbf{U}$, and $|U_{cc'}|^2$ is the probability of transition from channel c to c'. Thus, for $c \neq c'$, the cross section is proportional to the transition probability. The de Broglie wave length $\lambdabar_c = \hbar/2\pi(\mu_c \cdot v_{rel})$ is

related to the relative motion v_{rel} of the interacting particles, with μ_c the reduced mass of the system. Hence, it relates the probability to the physical cross section. The quantity g_c is the so-called *spin factor*

$$g_c = \frac{2J + 1}{(2i + 1)(2I + 1)} \ , \tag{1.6.4}$$

which represents the probability of getting the angular momentum J from the spins of the interacting pair. Considering that the sum of the transition probabilities to any channel must be $\sum_{c'} |U_{cc'}|^2 = 1$, from equation (1.6.3) an expression of the total cross section for entrance channel c can be obtained:

$$\sigma_c \equiv \sum_{c'} \sigma_{cc'} = 2\pi \lambda_c^2 g_c (1 - \mathrm{Re}\ U_{cc}) \ . \tag{1.6.5}$$

The resonant behaviour of the cross section is introduced by expressing **U** in terms of the **R** channel matrix (see [48] for details), whose elements are defined as

$$R_{cc'} = \sum_\lambda \frac{\gamma_{\lambda c} \gamma_{\lambda c'}}{E_\lambda - E} \ . \tag{1.6.6}$$

Alternatively, it can be convenient to express the collision matrix in terms of the matrix **A** [48], whose elements refer to the levels λ of the compound system, rather than to the reaction channels c.

$$U_{cc'} = e^{-i(\varphi_c + \varphi_{c'})} \left(\delta_{cc'} + i \sum_{\lambda,\mu} \Gamma_{\lambda c}^{1/2} A_{\lambda\mu} \Gamma_{\mu c'}^{1/2} \right) \ , \tag{1.6.7}$$

$$\Gamma_{\lambda c}^{1/2} \equiv \gamma_{\lambda c} \sqrt{2P_c} \ , \tag{1.6.8}$$

$$\left(\mathbf{A}^{-1} \right)_{\lambda\mu} = (E_\lambda - E)\delta_{\lambda\mu} - \sum_c \gamma_{\lambda c} L_c^0 \gamma_{\mu c} \ . \tag{1.6.9}$$

In these equations, Greek subscripts refer to compound levels, and Roman subscripts to reactions channels. E_λ are the level energies, and $\gamma_{\lambda c}$ are probability amplitudes for decay (or formation) of compound states λ via exit (or entrance) channels c. The sign of these amplitudes is practically random except near the ground state. The φ_c and the logarithmic derivates L_c are functions of the ingoing and outgoing radial wave functions at the channel radius a_c, and $P_c \equiv \mathrm{Im}\ L_c$ is the centrifugal barrier penetrability. For neutral particles, the in- and outgoing radial

wave functions are proportional to the Hankel spherical functions of the first kind [54], which satisfy the following recursive relations:

$$L_0 = ik_c a_c = iP_0 \; , \qquad L_\ell = -\ell - \frac{(k_c a_c)^2}{L_{\ell-1}} - \ell \; , \qquad (1.6.10)$$

$$\varphi_0 = k_c a_c \; , \qquad\qquad \varphi_\ell = \varphi_{\ell-1} + \arg(\ell - L_{\ell-1}) \; , \qquad (1.6.11)$$

where $k_c = 1/\lambda$. Thus, the penetrabilities P_c are functions of the kinematic parameters of the collision, namely the masses, the relative velocity and the angular momentum l, and the channel radius a_c. This is usually chosen to be slightly larger than the radius of the compound nucleus. A common adopted parametrization is $a_c = \left(1.23 A^{1/3} + 0.80\right)$ fm.

The resonance parameters E_λ and $\gamma_{\lambda c}$ depend on the unknown nuclear interaction, and thus cannot be calculated theoretically. They can, however, be adjusted to experimental values when a cross section, calculated with the R-Matrix formalism, is fit to experimental data of the reaction. This procedure will be shown in chapters 6 and 7 for the analysis of ^{203,204}Tl(n, γ).

The determination of the elements of the collisional matrix requires inverting a matrix involving $\mathbf{R}$, or equivalently inverting the matrix $\mathbf{A^{-1}}$. Both matrices have very high rank, which makes the task very complex. Therefore, in calculations which employ the R-matrix formalism, some assumptions must be taken, which are briefly described in the following section.

1.6.4 R-matrix approximations

A detailed review of the several approximations of the R-matrix relevant in the context of neutron-induced reactions can be found in [54]. For the purposes of this work, we will focus on two. In the **Single-Level Breit-Wigner (SLBW)** approximation, only one level λ is considered. Although it is known from experiments that this is not true, this approximation works well enough near single and isolated resonances, where all other levels can be in practice neglected. Thus the relation between cross section and resonance parameters can be extracted. In this situation, the element of the matrix $\mathbf{A^{-1}}$ reduces to

$$\left(\mathbf{A}^{-1}\right)_{\lambda\mu} \to E_0 - E - \sum_c L_c^0 \gamma_c^2 \equiv E_0 + \Delta - E - i\Gamma/2 \; , \qquad (1.6.12)$$

where the total width is $\Gamma = \sum_c \Gamma_c$, and $\Delta = E_r - E_0$ is the level shift between the energy of the level and the energy of the resonance. Δ is a function of E, thus making explicit the dependency of the resonance levels on the energy incoming neutron. The collision matrix for a single level is,

$$U_{cc'} = e^{-i(\varphi_c + \varphi_{c'})} \left(\delta_{cc'} + \frac{i\Gamma_c^{1/2}\Gamma_{c'}^{1/2}}{E_0 + \Delta - E - i\Gamma/2} \right). \tag{1.6.13}$$

The boundary conditions can be chosen in such a way that the energy of the resonance matches exactly the level energy, and thus $\Delta = 0$. Applying the previous matrix element to equation (1.6.5), the expression of the total cross section will be

$$\sigma_c = 4\pi\lambda_c^2 g_c \left\{ \sin^2(\varphi_c) + \frac{\cos(2\varphi_c)\Gamma_c\Gamma/4}{(E - E_0) + \Gamma^2/4} + \frac{\sin(\varphi_c)\cos(\varphi_c)\Gamma_c(E - E_0)}{(E - E_0) + \Gamma^2/4} \right\} \tag{1.6.14}$$

For incident neutrons and in the case of $\ell = 0$ ("s-wave") resonances at low neutron energies, $\varphi_0 = k_c a_c$ and $k_c a_c \ll 1$. Adopting a_c as the radius R of the compound nucleus, the previous expression reduces to

$$\sigma_c = 4\pi g_n R^2 + \pi\lambda_c^2 g_n \frac{\Gamma_n\Gamma}{(E - E_0) + \Gamma^2/4} + 4\pi\lambda_c g_n R \frac{\Gamma_n(E - E_0)}{(E - E_0) + \Gamma^2/4} \tag{1.6.15}$$

The first term is the potential scattering cross section. The second term is the symmetrical resonant contribution, and the third one is an asymmetric term arising from the interference between the potential and the resonant scattering. In the case of $\ell = 1$ or "p-wave" resonances, $\varphi_1 = k_c a_c + \arctan(k_c a_c)$ and thus the interference term vanishes. The presence of an interference "dip" for s-waves is employed in transmission measurements to identify correctly the parity of resonance, with parity given by $\pi = (-1)^\ell$. Such knowledge is very useful to constrain the fit parameters in posterior analysis.

Finally, the partial cross section from channel c to channel $c' \neq c$ will be given by

$$\sigma_{nc'} = \pi\lambda_c^2 g_c |U_{cc'}|^2 = \pi\lambda_c^2 g_c \left(\frac{\Gamma_n\Gamma_{c'}}{(E - E_0)^2 + (\Gamma/2)^2} \right), \tag{1.6.16}$$

also known as the Breit-Wigner formula [55].

Another approach to simplify the R-matrix is the **Reich-Moore approximation** [56]. It is based on the fact that there are many photon channels contributing

to the matrix elements. Their amplitudes tend to have similar magnitudes but random sign, and hence, except in the diagonal elements, their contributions cancel out. The approximation consists in neglecting all photon channel contributions to off-diagonal matrix elements. In that case, the element of the inverse matrix in equation (1.6.9) becomes

$$(\mathbf{A}^{-1})_{\lambda\mu} = (E_\lambda + \Delta_{\lambda\gamma} - E - i\Gamma_{\lambda\gamma}/2)\delta_{\lambda\mu} - \sum_{c\notin\gamma} \gamma_{\lambda c} L_c^0 \gamma_{\mu c} \tag{1.6.17}$$

which in the limit of a single level reduces to the SLBW matrix element.

Experience with experimental data has shown that this approximation is accurate enough to describe in detail all cross section resonance data [54]. The Reich-Moore approximation is the first choice of the R-matrix code SAMMY [57], which was the one employed in the analysis of resonances in this work (a mode detailed description of SAMMY will be given in section 4.12).

1.7 Experimental analysis of resonances

As it was mentioned in the previous section, the several parameters required for an accurate description of the cross section with the R-matrix theory, namely resonance energy E_r, spin and parity J^π, channel radius a_c, and resonance widths $(\Gamma, \Gamma_\gamma, \Gamma_n \dots)$ can only be obtained by adjusting them experimental data.

Let us consider a capture experiment with a nuclide for which only the elastic and the capture channels are significant, i.e. $\Gamma = \Gamma_\gamma + \Gamma_n$, which in fact is the case for virtually all species with $A \leq 210$ at low neutron energies. In this range of energies, This nuclide has an s-wave resonance, at an energy $\lesssim 10^4$ eV, similar to the one represented in the left plot in Figure 1.7. In ideal experimental conditions, the peak total cross section would be given by equation (1.6.15),

$$\sigma_0 = 4\pi \lambda_c^2 g_c \frac{\Gamma_n}{\Gamma} \ , \tag{1.7.1}$$

and the capture contribution to be measured (from equation (1.6.16))

$$\sigma_\gamma = 4\pi \lambda_c^2 g_c \left(\frac{\Gamma_n \Gamma_\gamma}{\Gamma^2}\right) = \sigma_0 \frac{\Gamma_\gamma}{\Gamma} \ . \tag{1.7.2}$$

Therefore, in such conditions one could directly extract E_r, $\sigma_0 \frac{\Gamma_\gamma}{\Gamma}$ and Γ. However, in real measurements several experimental effects contribute to broaden and change
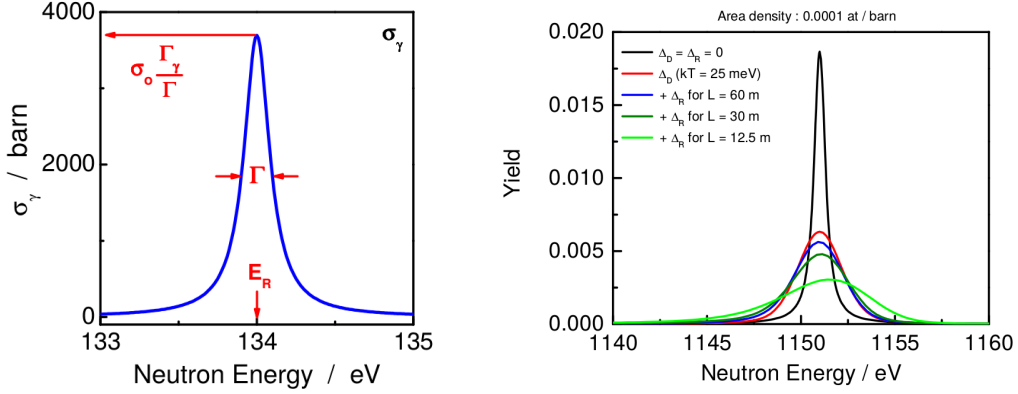
Figure 1.7: *Left: representation of an ideal generic neutron capture resonance. Right: Influence of experimental effects in the shape of the resonance due to Doppler broadening (Δ_D), and the facility neutron energy resolution (Δ_R). Both figures extracted from [58].*

the shape of the resonance, as it is illustrated in the right plot in Figure 1.7. The main effects are the neutron energy resolution of the facility and the Doppler broadening effect (more details on each will be given in sections 3.3.3 and 4.6 and in section 4.12, respectively) and, depending on the sample characteristics, *thickness effects* like multiple scattering and self-shielding. The first experimental observable one can define is the resonance area. This is obtained by integrating the capture cross section,

$$A_r = \int \sigma_\gamma(E_n) dE_n = \int g_J \pi \lambda_n^2 \frac{\Gamma_n \Gamma_\gamma}{(E_n - E_r)^2 + (\Gamma/2)^2} dE_n \qquad (1.7.3)$$

$$= 2\pi^2 \lambda_n^2 g_J \frac{\Gamma_n \Gamma_\gamma}{\Gamma} \text{ , with } K_r \equiv g_J \frac{\Gamma_n \Gamma_\gamma}{\Gamma} \qquad (1.7.4)$$

defined as the *reaction kernel*. In a transmission measurement of a thin sample, thickness effects can be neglected and $A_r \propto n g_J \Gamma_n$ [58], where n is the atomic thickness, measured in atoms/barn. In this situation, one can extract the following parameters

$$E_r, \Gamma_n, \Gamma, g \qquad \text{for } \ell = 0 \qquad (1.7.5)$$

$$E_r, g\Gamma_n \qquad \text{for } \ell \geq 1 \text{ .} \qquad (1.7.6)$$

The transmission results can be employed in a capture measurement to correct for

thickness related effects, and hence allow to obtain

$$E_r, \Gamma_\gamma \qquad \text{if } g, \Gamma_n \text{ are known,} \qquad (1.7.7)$$

$$E_r, g\Gamma_\gamma \qquad \text{if only } g\Gamma_n \text{ are known.} \qquad (1.7.8)$$

However, if transmission results are not available, the only information reliable from a capture measurement is

$$E_r, gK_r \qquad \text{if } g\Gamma_n \text{ is not known.} \qquad (1.7.9)$$

In the case that in a given resonance a particular channel dominates, the kernel becomes proportional to the width of the other one,

$$\Gamma_n \gg \Gamma_\gamma \implies K_r \propto g_J\Gamma_\gamma \qquad (1.7.10)$$

$$\Gamma_n \ll \Gamma_\gamma \implies K_r \propto g_J\Gamma_n \qquad (1.7.11)$$

and thus information on individual parameters can be extracted. It must be noted here that, for astrophysical applications, the desired value is the MACS, which is an integrated value of the cross section. Thus, for nuclides with the resolved resonance region coincident with the neutron energy range of astrophysical interest, the knowledge of the resonance area might be sufficient.

Finally, R-matrix codes like SAMMY or REFIT [59] are based on resonance shape fitting of experimental data. By evaluating how accurate is a set of parameters in the whole range of the resonance, it is more selective on the parameters, and thus yields more accurate results than resonance area analysis alone. In addition, if parameters are already known, effective information on the sample physical characteristics can be extracted. Such procedure, in fact, has been applied to the analysis of the ^{204}Tl(n, γ) data, and it is discussed in detail in chapter 7.

Chapter 2

Measuring technique

2.1 Capture reaction detection techniques

In order to determine a capture cross section experimentally, it is necessary to measure the number of capture events produced by the interaction of a known neutron beam with the sample of interest. One of the common ways of counting capture reactions is by detecting the prompt gamma rays emitted by the de-excitation of the compound nucleus. However, the latter is a random process which involves the emission of a random number of gamma rays, with a myriad of possible energy combinations. Whereas counting properly the capture cascades is already a challenging task, the rejection of the gamma rays not coming from capture events –also known as *background*– is equally important. Over the years, two main techniques have been developed, which depict different strategies of counting capture cascades and minimizing the background. Both techniques are routinely employed at n_TOF.

- The **Total Energy Detection** technique (TED) is based on the use of low detection efficiency detectors, so on average only one gamma, at most, of the cascade is detected. The response function of the setup is conveniently manipulated so the cascade detection efficiency becomes proportional to the total energy of the cascade. This turns the efficiency independent of the energy of the photon detected, or the de-excitation path. The detectors are usually liquid scintillators, employing light materials like deuterated benzene (C_6D_6), especially chosen for its extremely low neutron detection efficiency.

This makes them the best option for measurements with samples with high scattering-to-capture ratios. The TED technique, employing a set of four C_6D_6 detectors, was the one employed in this work. As such, it will be described in detail in section 2.2.

- The **Total Absorption** technique involves the use of a 4π array of BaF_2 detectors (known as the Total Absorption Calorimeter, TAC), for a combined detection efficiency close to 100% [60]. Thus, the TAC works by detecting, ideally, all the gamma rays of the cascade. Adding all signals with the appropriate time coincidence, one can construct a deposited energy histogram like the one shown in Figure 2.1, which shows real capture in a ^{197}Au sample. A peak appears around the total cascade energy, whose integral is proportional to the number of capture events. Additional cuts in deposited energy and crystal multiplicity allow to discriminate capture events from signals coming from the background or other reaction channels. The high efficiency of the technique makes it very well suited for very low mass samples, but comes at the expense of also increasing considerably the neutron sensitivity of the setup. As a consequence, it makes it less convenient for target nuclei with high scattering-to-capture ratios. Furthermore, very radioactive may induce very high levels of signal pileup. Unfortunately, due to background and electric noise issues, at the time of the experiment the TAC of n_TOF could only be used reliably up to 10 keV of neutron energy. This severely limited its usefulness for measurements in the neutron energy range of astrophysical interest at this facility.

- An evolution of the TED is the **i-TED** technique, which is currently being developed for future experiments at n_TOF [62, 63]. It is based on applying the TED technique to a set of detectors with Compton imaging capabilities. Such a setup can discriminate, by means of advanced gamma ray imaging algorithms, between those signals coming straight from the sample, and those background signals arriving from elsewhere in the experimental hall. With this, it aims to reduce considerably the photon background caused by secondary capture of scattered neutrons, which in several cases is the dominant source of background for neutron energies beyond 100 eV [64]. Hence, due to its superior signal-to-noise ratio, i-TED is specifically designed to study sam-
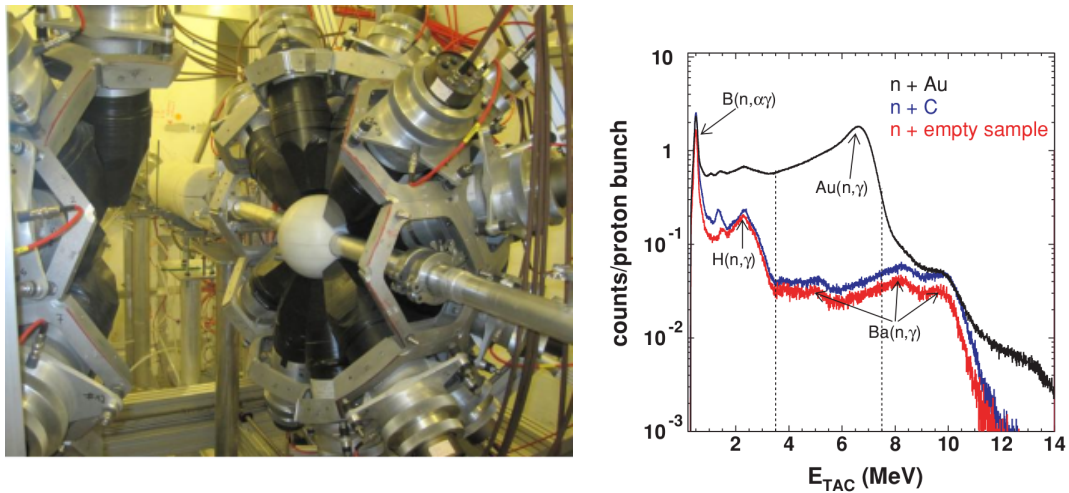
Figure 2.1: *Left: the Total Absorption Calorimeter of n_TOF. Right: $^{197}Au(n,\gamma)$ energy deposition spectrum measured with the TAC, showing the capture peak and several intrinsic background components. Figure extracted from [61].*
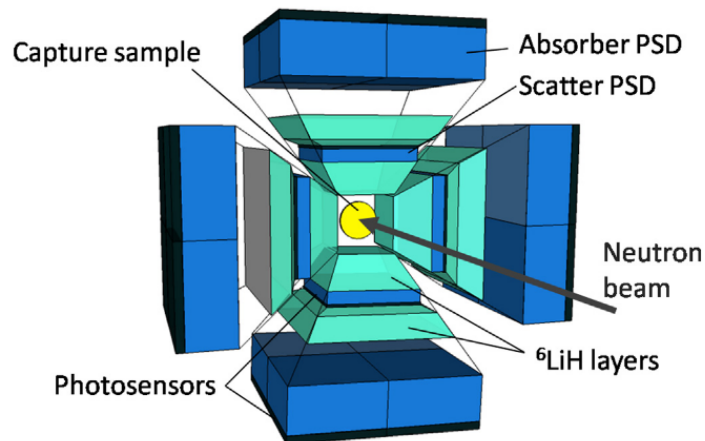
Figure 2.2: *Left: Diagram showing the concept of a 4π i-TED detector, surrounding a cylindrical sample in the centre. The several assemblies of scatterer and absorber allow to use Compton imaging techniques to reconstruct the emission point of the gamma rays detected, which enables to discriminate between true capture gamma rays arising from the sample and background gamma rays coming the surroundings. Extracted from [62].*

ples of very low mass, such as radioactive samples, which can be produced only in minute amounts.

2.2   The Total Energy Deposition Technique

As stated in the introduction, the TED technique is based on two principles. In the first place, it requires the use of low efficiency detectors, which guarantees that only one gamma ray of the cascade is detected:

$$\varepsilon^{\gamma} \ll 1 \ . \tag{2.2.1}$$

The efficiency for detecting a capture cascade, ε^c, can be expressed mathematically as the complementary probability of *not* detecting any of the $j = 1, \ldots, N$ gammas of which is composed the cascade:

$$\varepsilon^c = 1 - \prod_{j=1}^{N}(1 - \varepsilon_j^c) \ . \tag{2.2.2}$$

Being $\varepsilon^{\gamma} \ll 1$, if we expand equation (2.2.2) in power series, in the first degree approximation we have

$$\varepsilon^c \approx \sum_{j=1}^{N} \varepsilon_j^{\gamma} \ . \tag{2.2.3}$$

The efficiency of any detector, in general, has a dependence on the energy E_{γ} of the gamma ray detected. Therefore, without any further correction, the cascade detection efficiency ε^c would depend on the energy of that gamma ray detected, and consequently on the random cascade de-excitation path, biasing the capture counting results. The solution is to apply a second condition, which consists in imposing the proportionality between detection efficiency and energy of the gamma ray,

$$\varepsilon^{\gamma} = \alpha E_{\gamma} \ . \tag{2.2.4}$$

With this, the cascade detection efficiency becomes

$$\varepsilon^c \approx \sum_{j=1}^{N} \varepsilon_j^{\gamma} = \alpha \sum_{j=1}^{N} E_j^{\gamma} = \alpha E_C = \alpha(S_n + E_n) \ , \tag{2.2.5}$$

which means that the efficiency now depends only on the total cascade energy, and does not depend on the de-excitation path or the energy of the gamma ray detected. While the first condition can be easily achieved by employing a detector with the appropriate geometry and active material, the proportionality condition

is more difficult to achieve, as can be seen by the different approaches developed in the past and described below.

The origins of the modern TED technique can be traced back to the concept of the detector developed by Moxon and Rae in the early sixties [65]. In their approach, the response function of a small, plastic scintillator was manipulated to scale linearly with gamma ray energy. This was done by putting, in front of the detector, a thick slab of a low Z material that converted gamma rays to electrons. The main drawback was that, due to the particularities of the conversion process, the response of the detector was non-proportional for photons under 500 keV, which in fact is the energy range of most of the capture cascade gamma rays.

An alternative method, known as the Pulse Height Weighting Technique (PHWT), was first applied by Macklin and Gibbons to the measurement of neutron capture cross sections, thanks to an original suggestion by Maier-Leibnitz [66]. In this case, the proportionality condition is achieved by weighting the response function of the detector, signal by signal. The weight is given by a an energy dependent weighting function, specifically calculated for the setup.

The advent of the PHWT was a major step in the measurement of neutron capture cross sections, because it provides much greater flexibility in the election of the detection system and the rest of the experimental setup. The PHWT can be expressed mathematically in the following way. If we consider R_i^γ to be the discretized detector response function to a gamma ray of energy E^γ, where $i = 1, \ldots, N$ is the number of bins of R_i^γ, and we normalize it to the efficiency of detecting that gamma ray, we have $\varepsilon^\gamma = \sum_{i=1}^{N} R_i^\gamma$.

Then, the proportionality condition of equation (2.2.4) is achieved by weighting the response function,

$$\sum_{i=1}^{N} W_i R_i^\gamma = E^\gamma \,, \qquad (2.2.6)$$

where α in equation (2.2.4) has been chosen equal to 1 for convenience. Thus, the new, weighted efficiency is

$$\varepsilon_w^\gamma = \sum_{i=1}^{N} W_i R_i^\gamma = \alpha E_\gamma \,. \qquad (2.2.7)$$

2.3 Analytical Weighting Function (AWF)

In most cases, the WF is obtained by a least-squares fit of an analytical (polynomial) function to a discrete number of response functions for mono-energetic gammas in the energy range of interest. This energy range is basically defined by the neutron separation of the isotope under study, the maximum neutron energy covered in the experiment, and the instrumental resolution. Due to the practical difficulty of obtaining mono-energetic gamma ray sources in the whole energy required, the response functions are usually calculated with MC simulations. The PHWT, including the use of MC simulations to obtain the WF, has been thoroughly validated for capture measurements at n_TOF [67], and it was proved that the systematic uncertainty introduced by the technique was equal or lower than 2% RMS. A similar validation has been done for the GELINA facility as well [68].

Mathematically, the AWF can be expressed as

$$W_i(E_i) \approx \sum_k^l a_k E_i^k \ , \qquad (2.3.1)$$

where E_i is the energy of the bin i, and a_k coefficients are determined by least squares minimization of the expression

$$\min \sum_j^m \left(\sum_i^n \sum_k^l a_k E_i^k R_{i,j} - E_j^\gamma \right)^2 \qquad (2.3.2)$$

Usually the polynomial WF is approximated as a fourth or fifth degree, and the result is a monotonically increasing function. While this approximation usually works well for most situations, it has been shown that in some particular cases, like when working with lead or bismuth samples [31, 68, 69], this WF is not accurate enough. This is because the capture cross section of such nuclides is low, and being also dense and high Z materials, their scattering and gamma ray absorption coefficients are high.

In the first place, having low cross sections means that neutrons are captured homogeneously along the sample. Thus, a sizeable part of the capture gamma rays are emitted deep inside it, and must travel through millimetres of the material before escaping. In the process, a considerable number of them can be absorbed. Since the absorption rate is higher at lower gamma ray energies, much less low

energy photons manage to escape and reach the detectors. The consequence is that, below ~ 300 keV, the detection efficiency actually decreases. Such effect cannot be accounted for with the monotonically increasing polynomial WF. Consequently, the proportionality condition is not met at low energies. This leads to deviations of a few percent in the accuracy of the WF. An improvement in the analytical WF can be obtained if negative powers are added in the polynomial [68]. However, a more general approach can be applied, as reported in the following section.

2.4   Numerical Weighting Function (NWF)

The alternative approach [69, 31] consists in calculating the WF employing numerical methods, in a bin-per-bin basis. This method offers much more flexibility than the polynomial approach for obtaining the weights, and thus can produce more accurate results.

In the case of the thallium samples employed in this work, they were not especially thick or dense, and the cross section is orders of magnitude higher than that of lead or bismuth. Even in this situation, the NWF already showed an improvement over the AWF. However, the main source of low energy gamma absorption were the 2 mm lead foils put in front of the detectors to shield them from the ^{204}Tl enriched sample radiation (more details of the experimental setup will be given in the following chapters). The pronounced reduction in the efficiency at low energies caused by the foils made it highly convenient to resort to the numerical WF. A description of the method to obtain the WF by numerical means will be given in the following. Details of the NWF applied to the capture analysis will be given in section 5.1.

The numerical, or point-wise, approach consists in determining a solution W_i for the system of equations defined by

$$\sum_{i=1}^{N} R_{j,i} W_i = E_j, \tag{2.4.1}$$

where $R_{i,j}$ is the matrix containing the response functions of $i, \ldots, N$ bins to $j, \ldots, M$ gamma rays of energy E_j. This equation can be rewritten in vector notation as

$$\mathbf{R}\vec{W} = \vec{E} \ . \tag{2.4.2}$$

Obtaining a solution for $\vec{W}$ requires inverting the response function matrix $\mathbf{R}$,

$$\vec{W} = \mathbf{R}^{-1}\vec{E}, \qquad (2.4.3)$$

but this matrix, being normalized to the efficiency, is composed of small elements much smaller than 1. Inverting such a matrix is what is called an *ill-posed problem*, since finding an exact solution is impossible from the computational point of view (see section 2.2.2 from [69] for more details). On the other hand, an infinite set of approximate solutions exist, and one needs to find a method to determine the best of them. Following the procedure reported in [69], this is achieved also here employing the Tikhonov-Miller linear regularization method, which imposes a restriction in the number of possible solutions by using some kind of a priori expectation (or knowledge) about them. The principle of the method of regularization is the minimization, by Lagrange multipliers, of a quantity:

$$\chi^2 + \lambda\mathcal{B} \; . \qquad (2.4.4)$$

Where χ^2 is a measure of the agreement of a model solution to the data, $\mathcal{B}$ is a functional that measures the "smoothness" or "stability" of the solution, and λ is the Lagrange multiplier. $\mathcal{B}$ is defined as

$$\mathcal{B} = \vec{W}\mathbf{H}\vec{W}, \qquad (2.4.5)$$

where $\mathbf{H} = \mathbf{B^T B}$. Thus, if $\mathbf{B}$ is the $(N-1) \times N$ matrix

$$\mathbf{B} = \begin{pmatrix} -1 & 1 & 0 & 0 & 0 & 0 & 0 & \cdots & 0 \\ 0 & -1 & 1 & 0 & 0 & 0 & 0 & \cdots & 0 \\ \vdots & & & & \ddots & & & & \vdots \\ 0 & \cdots & 0 & 0 & 0 & 0 & -1 & 1 & 0 \\ 0 & \cdots & 0 & 0 & 0 & 0 & 0 & -1 & 1 \end{pmatrix} \qquad (2.4.6)$$

then $\mathbf{H}$ is the $N \times N$ matrix

$$\mathbf{H} = \mathbf{B^T} \cdot \mathbf{B} = \begin{pmatrix} 1 & -1 & 0 & 0 & 0 & 0 & 0 & \cdots & 0 \\ -1 & 2 & -1 & 0 & 0 & 0 & 0 & \cdots & 0 \\ 0 & -1 & 2 & -1 & 0 & 0 & 0 & \cdots & 0 \\ \vdots & & & & \ddots & & & & \vdots \\ 0 & \cdots & 0 & 0 & 0 & -1 & 2 & -1 & 0 \\ 0 & \cdots & 0 & 0 & 0 & 0 & -1 & 2 & -1 \\ 0 & \cdots & 0 & 0 & 0 & 0 & 0 & -1 & 1 \end{pmatrix} \tag{2.4.7}$$

A high value of $\mathcal{B}$ will mean that a solution $\vec{W}$ is unstable, in the sense that it oscillates greatly from one bin to the other, and could include negative weights as well. With the previous definition, the minimization principle becomes:

$$\chi^2 + \lambda\mathcal{B} = |\mathbf{R} \cdot \vec{W} - \vec{E}|^2 + \lambda\vec{W}\mathbf{H}\vec{W} \tag{2.4.8}$$

It can be shown (see [70], section 18.5) that this reduces to a linear set of equations,

$$(\mathbf{R^T R} + \lambda\mathbf{H})\vec{W} = \mathbf{R}^T\vec{E}\,, \tag{2.4.9}$$

which can be solved by standard LU decomposition. The λ prevents the problem to be ill-conditioned again.

In the end, by the minimization process we obtain the set of solutions, one for each possible value of λ. Each solution is a trade-off between minimizing the χ^2 i.e. obtaining the best possible agreement with the data, or minimizing the functional $\mathcal{B}$, which leads to the most stable solution. This can be readily seen when both quantities are represented for each λ, like in Figure 2.3. The solutions indicated with an arrow are those considered the "best" in the sense that they offer a compromise between stability of the solution and the agreement with the data. In practice, to avoid any unphysical results in the weighting of the signals, the additional requirement of an always positive WF has also been imposed, which puts a rather high constraint in the stability of the solution. This will be further discussed in section section 5.2, which deals with the application of the NWF to our capture measurements.
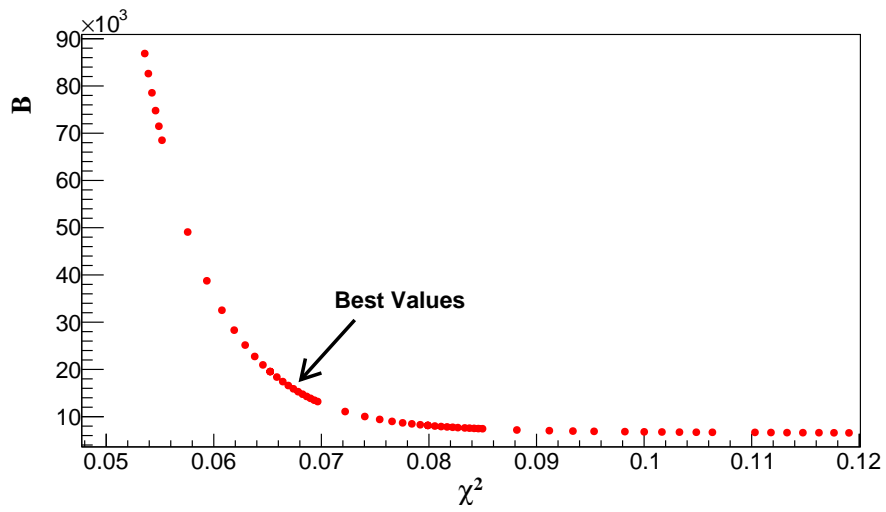
Figure 2.3: $\mathcal{B}$ versus χ^2 plot of several solutions obtained by varying λ.

Chapter 3

Experimental Setup

3.1 The n_TOF facility at CERN

The Neutron Time-Of-Flight facility, n_TOF, was established in 2001 at the European Organization for Nuclear Research (CERN) with the aim of producing pulsed neutron beams, with a wide energy range, for neutron cross section measurements.

At n_TOF, neutrons are produced by spallation reactions induced by a pulsed proton beam in a massive lead target. The proton beam has a time length of 7 ns RMS, and is accelerated up to 17 GeV by the Proton Synchrotron (PS) accelerator complex, shown in Figure 3.1. Protons are then shot against the target, where 300 neutrons per proton are produced on average [71]. There are two different types of proton beams provided by the PS:

- "Dedicated" beam, which is the beam specifically produced for n_TOF, with a nominal intensity of $7 \cdot 10^{12}$ protons per pulse.

- The so-called "parasitic" beam, which are a remanent from protons sent to other facilities, with a nominal intensity of $\sim 3 \cdot 10^{12}$ protons per pulse.

The highly energetic spallation neutrons emerging from the target are then moderated, acquiring in the process the desired white spectrum, from several GeV down to thermal energies. The beam is then collimated for a first time and, immediately afterwards, a magnet sweeps away the charged particles in the beam. Afterwards, a second collimator gives the beam its final shape. The aperture of this collimator can be chosen between a *small* one (18 mm), employed for cap-
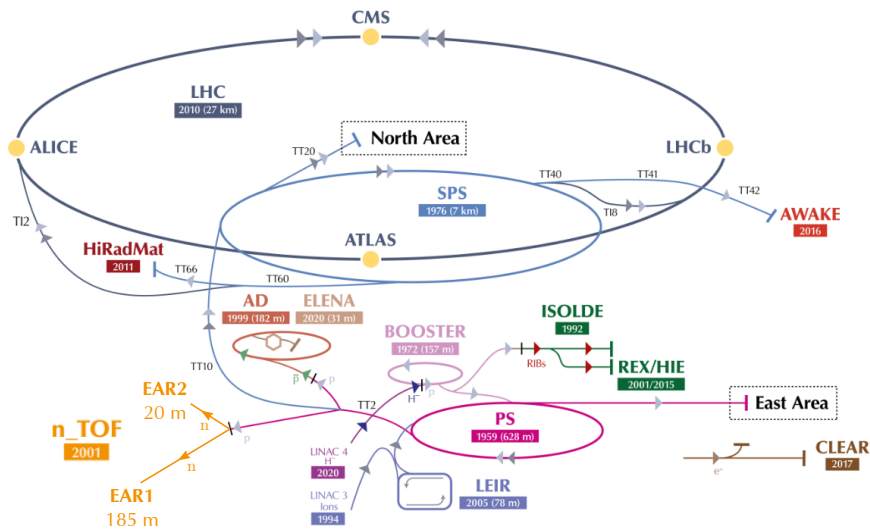
Figure 3.1: *Schematic view of the whole CERN accelerator complex in 2019. Protons are successively accelerated by the LINAC4 (up to 50 MeV), by the PS Booster (up to 1.4 GeV), and by the PS up to 17 GeV, before being shot against the n_TOF target (in the lower left part of the image).*

ture measurements, and a *big* one (80 mm), for fission measurements. Finally, the particle beam reaches the experimental areas, where measurements are performed.

As can be seen in the layout of the facility in Figure 3.2, at n_TOF there are two Experimental Areas (EAR): EAR1 was the first one operative, with a flight path length of 184 m; and EAR2, commissioned in 2014, which is situated vertically on top of the target, an has a flight path of 19 m. The shorter flight path results in a neutron flux 30 times higher than in EAR1, but comes at the expense of a lower neutron energy resolution, and of an increased background compared to EAR1. Hence, both areas have complementary features, which make each one of them suited for different experiments. Pictures of both areas can be seen in Figure 3.3.

n_TOF has several features that, all combined, make it exceptional for cross section measurements:

- n_TOF neutron beams have a very high instantaneous flux, which makes them especially suited for measurements that require a high signal to background ratio, like measurements of small quantities of radioactive samples.

- The high flux compensates for a repetition rate of, on average, 1.2 Hz, a
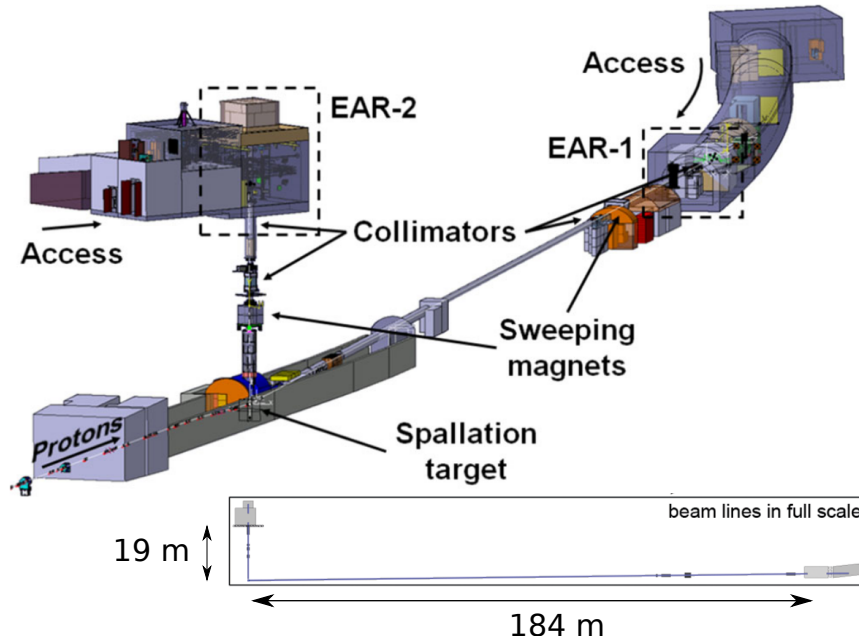
Figure 3.2: *Layout of the n_TOF facility, showing its two beam lines and the position of several other beam elements. A full scale profile view of both experimental areas is also shown (Extracted from [71] and [72], respectively.)*

feature of the working cycle of the PS. For several aspects the low duty cycle is also an advantage. It allows to perform measurements in a very wide range of neutron energies, from several hundred MeV down to the thermal point, without having any superposition between neutron pulses.

- In the case of n_TOF EAR1, thanks to the very long flight path a very high neutron energy resolution can be achieved. Specifically, $\Delta E/E$ lower or equal than 10^{-3} can be achieved up to 10 keV, and lower than $5 \cdot 10^{-3}$ up to an energy of 100 keV.

Most of the measurements performed at n_TOF are capture and fission experiments, mainly for nucleosynthesis studies in the field of astrophysics, and nuclear technology research [71]. Recently, measurements of (n,p) and (n,α) reactions for astrophysical studies [73, 74] and medical physics applications [75], have been carried out, as well. In its almost 20 years of existence, three main experimental campaigns have been conducted at n_TOF. Phase1, lasting from 2001 to 2004, was followed by the first long shutdown (LS1) of the CERN complex (2004-08),
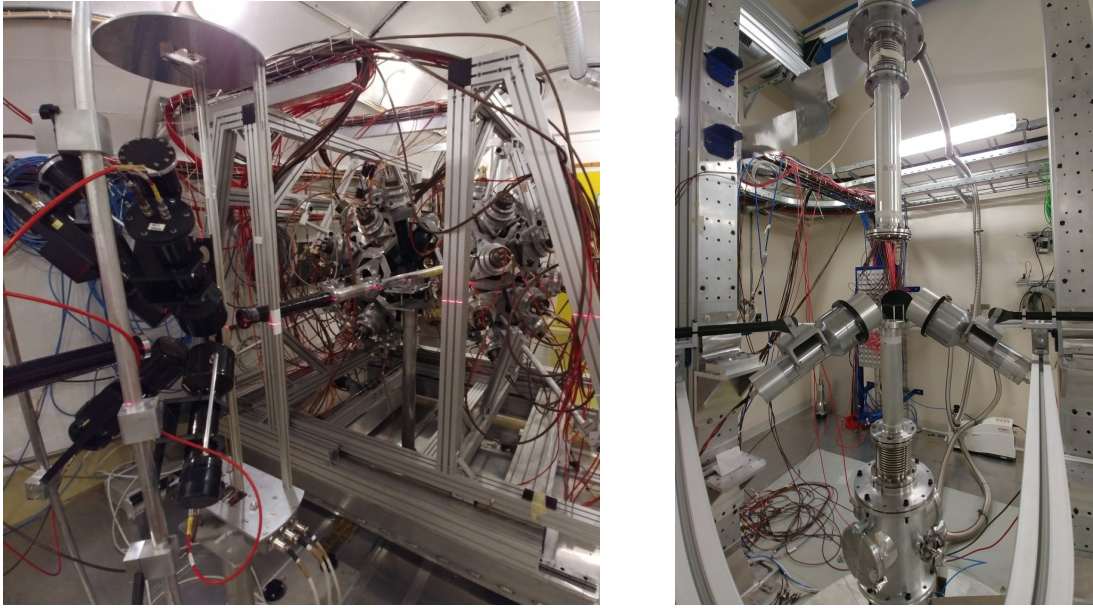
Figure 3.3: *Left: General view of the EAR1 beam line in 2018, with the latest C_6D_6 capture setup in the foreground, and the TAC behind it. In this picture, the beam enters the area from the left. Right: The vertical beam line of EAR2, with the three C_6D_6 capture setup employed in 2018. These are the BICRON C_6D_6 detectors used in the 2015 capture setup at EAR1 for the experiment presented in this work (see section 3.6 for details).*

during which a new cooling and moderator system was installed at n_TOF. The improvements included changing the moderator from natural water to borated water, which contributed to reduce considerably the gamma ray background of the facility. Experimental Phase2 ran from 2009 until the start of the second long shutdown LS2 (2012-13). During this stop, the second experimental area was built. Finally, Phase3 lasted from 2014 to 2018, during which the measurements reported in this work took place (summer of 2015). In 2018 the facility entered into long shutdown LS3, which is scheduled to end by 2021. Major upgrades in the facility are being carried out for the future Phase4. These include, among others, a new target and moderator ensemble, specifically designed for both experimental areas, and new irradiation facility very close to the target, also known as NEAR [76]. A list with all the reactions measured in each phase of n_TOF can be found in [71].
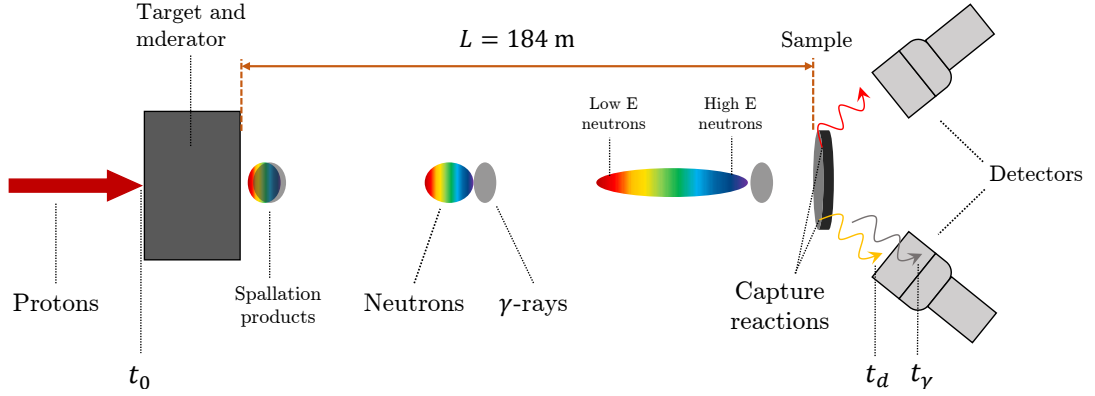
Figure 3.4: *Sketch representing the time-of-flight technique at the n_TOF facility.*

3.2   Time-of-flight technique

At a time-of-flight facility like n_TOF, the energy of the incoming neutrons is determined by measuring the time t they take to travel a fixed and well-known distance L, as illustrated in Figure 3.4. In our particular case, L is the distance from the target to the experimental areas. In the classical kinematics approximation, valid up energies of a few MeV, the kinetic energy E_n of a neutron travelling along L with speed v is given by the expression

$$E_n = \frac{1}{2}mv^2 = \alpha\frac{L^2}{t^2} \tag{3.2.1}$$

where, t is in μs, E_n in eV and L in m, the constant factor α assumes the value $\alpha = 72.29\frac{\sqrt{\text{eV}}\mu\text{s}}{m}$. The time-of-fight is calculated as $t = t_a - t_0 - t_t$, where t_a is the time of arrival of the neutrons, t_0 when the spallation reactions occur, and t_t is the time they spend travelling through the target and moderator. The time of arrival t_a is given by the time they induce a nuclear reaction. Or more specifically, by the time the secondary particles emitted after the reaction are detected, $t_d \approx t_a$. This is totally acceptable, since the timescale of nuclear processes, $\sim 10^{-15}$ s, is many orders of magnitude smaller than the minimum resolvable time-of-flight. However, very fast detectors and readout electronics are essential in order to minimize the offset between capture and detection. In order to determine t_0, it is exploited the fact that in the spallation reactions a large number of prompt gamma rays are produced. These photons induce a huge pileup signal in all sensitive detectors (see section 3.5). Since prompt gamma rays travel invariably at the speed of light, there

will be just an offset between the time they are detected and t_0, so $t_0 = t_\gamma - L/c$. Therefore, the final expression for t will be

$$t = t_d - t_\gamma + L/c\ - t_t. \tag{3.2.2}$$

In practice, the relation between neutron energy and t is obtained performing a "calibration" with resonances whose energy is very well known (see section 4.2 for details). In the process, the travel time through the target and moderator, t_t, is absorbed into the measured time t_m.

3.3 The neutron beam of n_TOF

3.3.1 Measurement of the neutron flux

In a capture experiment, an accurate knowledge of the absolute number and the energy profile of the neutrons impinging the sample under study is a basic requirement. In our particular case, the capture yield will be normalized to the yield of a reference sample at some specific neutron energy (a procedure described in detail in Chapter 4). Therefore, the most crucial aspect to be known independently is the energy dependency of the neutron *flux* [77]. Flux, in the context of n_TOF, refers the energy distribution, per unit surface, of the neutrons produced by each proton bunch.

The flux is measured by means of several neutron-converting reactions, whose cross sections are known accurately enough to be considered a standard in some energy range [78]. For a given reaction, the flux can be obtained by employing the following relation:

$$\phi(E_n) = \frac{C(E_n) - B(E_n)}{\varepsilon(E_n) \cdot \left(1 - e^{-n \cdot \sigma_t(E_n)}\right) \frac{\sigma_r(E_n)}{\sigma_t(E_n)}} \tag{3.3.1}$$

where C is the total number of counts per bunch, B the background contribution, n the areal density of the layer of converter, and σ_t and σ_r its total and reaction cross sections, respectively. At n_TOF, the flux was measured employing several independent detection systems in order to minimize the systematics effects related to each of them. These are:

- **Silicon Monitor (SiMon)**, which employs a foil of ^{6}Li as a converter. Four silicon semiconductor detectors placed out of the beam measure the products
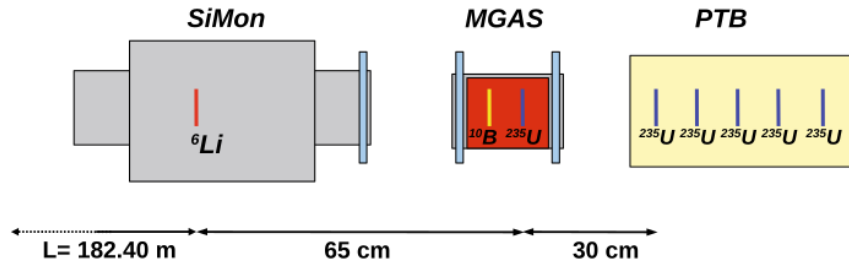
Figure 3.5: *Placement of the different detectors in the measurement of the flux with the small collimator.*

of the reaction ^{6}Li$(n, \alpha)^3$H. The SiMon is the detector commonly employed as flux monitor during capture cross section measurements [79].

- The **MGAS monitor detector** [80], which is a set of two MicroMegas gaseous detectors [81] enclosed in an aluminium chamber. Each detector employs a different neutron conversion reaction, which are ^{10}B$(n, \alpha)^7$Li and ^{235}U(n, f). The range of maximum accuracy for each reaction is different, and thus, with a combination of both, the full range from thermal up to 1 MeV of neutron energy can be covered. At n_TOF, MicroMegas based detectors have been employed, additionally, to measure the spatial profile of the beam [82] and for cross sections measurements like ^{33}S(n, α) [75].

- The **PTB fission chamber**, which is a calibrated ionization detector from the *Physikalisch-Technische Bundesanstalt* [83]. This consists of five platinum electrodes, with thin deposits of ^{235}U on both sides. The detector is considered a reference in the field of metrology due to its very good characterization, and was considered the reference measurement of the flux in the range from 1 to 10 MeV.

- a set of **Parallel Plate Avalanche Counters (PPAC)** [84, 85], which also employ the ^{235}U fission reaction. PPAC have unique features that make them very useful at n_TOF. Due to their almost total insensitivity to gamma rays, and their very fast response time, PPAC are almost unaffected by the burst of prompt gamma rays. This allowed to extend the flux measurement up to 1 GeV in neutron energy.

Measurements with SiMon, MGAS and PTB fission chamber were performed
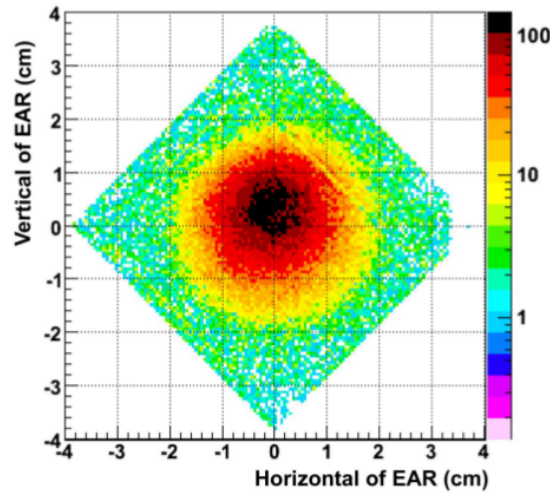
Figure 3.7: *Bidimensional profile of the n_TOF neutron flux in EAR1, obtained with the X-Y MicroMegas detector (extracted from [91])*

simultaneously employing the small collimator mode. The measurement with the PPAC was performed with the big collimator, and thus was carried out separately. The results of all measurements were combined and weighted appropriately to elaborate the so-called *Evaluated Flux* [77]. The PTB chamber value at thermal energy was used as an absolute normalization point. The systematic accuracy of the resulting flux, together with other parameters of interest, is reported in Table 3.1. The evaluated flux has been also compared to Monte Carlo simulations with the FLUKA [86], MCNPX [87] and Geant4 [88, 89] codes, for a very good general agreement [77, 90]. The evaluated flux is the one employed in this work.

The energy distribution of the evaluated flux per nominal proton bunch ($7 \cdot 10^{12}$ protons), in units of lethargy (i.e. neutrons/$d \ln E$), is shown in Figure 3.6. The absence of a peak at thermal energies is caused by the presence of ^{10}B in the moderator. Apart from that, the spectrum shows the characteristic evaporation peak in the MeV region. A relevant feature of the spectrum is the presence of several transmission "dips", associated to resonances of elements present in the aluminium alloys employed in the beam pipe windows. The strongest of them, at 6 keV, 35 keV and 80 keV correspond to ^{27}Al.
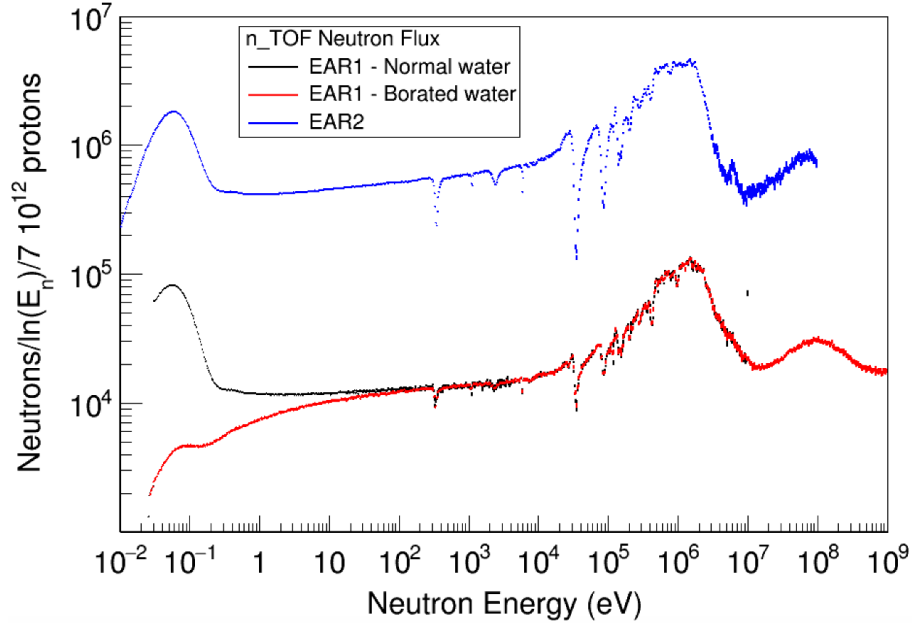
Figure 3.6: *Energy distribution of the flux in EAR1, for the configurations with normal water (before 2009, in black) and with borated water (after 2009, in red). For comparison, the evaluated flux of EAR2 is also plotted.*

Energy range	Neutrons/pulse	Eva. Flux unc. (%)	$\Delta E_n / E_n$
1 eV – 10 eV	$2.0 \cdot 10^4$	2	$3.2 \cdot 10^{-4}$
10 eV – 100 eV	$2.5 \cdot 10^4$	2	$4.3 \cdot 10^{-4}$
100 eV – 1 keV	$2.9 \cdot 10^4$	2	$5.4 \cdot 10^{-4}$
1 keV – 10 keV	$3.2 \cdot 10^4$	2	$1.1 \cdot 10^{-4}$
10 keV – 100 keV	$4.4 \cdot 10^4$	4-5	$2.9 \cdot 10^{-4}$

Table 3.1: *EAR1 values of the integrated number of neutrons per pulse, the uncertainty, and the resolution in neutron energy, of the evaluated flux for n_TOF. These values correspond to the neutron energy decades relevant for measurements of astrophysical interest.*

3.3.2   Neutron beam profile

The knowledge of the spatial profile of the neutron beam is of utmost importance when working with samples with radius smaller than the beam, because it crucially determines the intersection factor between the two. Furthermore, the profile has a dependency on the energy which also has to be taken into account. For this

purpose, a new X-Y MicroMegas was developed [91], which offered great precision 2D-imaging capabilities of the beam.

The beam bidimensional profile, depicted in Figure 3.7, presents a non-symmetrical shape, with a longer tail in the vertical downward direction. The measurement of the profile was found to be in good general agreement with MCNP and FLUKA simulations [91]. The profile in both axis can be approximated to a Gaussian distribution, with a nominal FWHM of 18 mm. From the validated simulations, the beam interception factors, for several standard sample geometries at n_TOF, were extracted.

3.3.3   The Resolution Function

The correspondence between the energy of the neutron and its time of arrival, however, is not a one-to-one relation. Neutrons with the same energy can arrive at different times, mainly because of the different paths they follow inside the spallation target and moderator until they arrive at the measuring point. Specifically, several experimental conditions contribute to this effect. First of all, the width of the proton pulses of the PS, equal to 7 ns RMS, which is in fact the absolute upper limit in the time resolution of the facility. In second place, the interaction of the neutrons with the different elements of the target-moderator assembly, and, finally, the time resolution of the detectors. The most important of them, however, is the moderation process. This effect is quantified in the *moderation length*, which is the distance that neutrons arriving with a given energy have travelled in the moderator. All these are included in what is called the Resolution Function (RF). The RF represents the distribution of arrival times that neutrons of the same energy E_n will have. It can be expressed alternatively in terms of neutron energy, time of flight or effective flight path:

$$R_E(E_n)dE_n = R_t(t)dt = R_L(L)dL \ . \tag{3.3.2}$$

The RF cannot be measured directly. Therefore, it is obtained by means of MC simulations, which include a fully detailed description of the target and moderator geometry [92]. In these simulations, performed independently with both the MCNPX and FLUKA codes, each neutron produced in the spallation process is followed in their path through the target and moderator. However, propagating
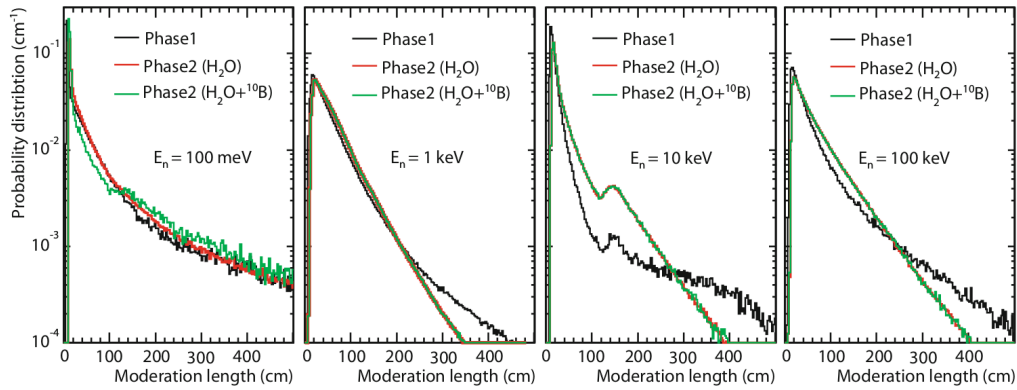
Figure 3.8: *The simulated probability distribution of the moderation length for neutrons of different energies, commonly known as the Resolution Function $R_L(L)$.*

the neutrons from there, up to the experimental hall –185 m away– by MC means would be totally impractical due to the computational time required. Thus, particle trajectories are calculated with a dedicated optical transport code. The accuracy of the resulting RF is validated by applying it to experimental data of narrow capture resonances, whose parameters are well established.

The RF for energies from epithermal to 100 keV is shown in Figure 3.8. It changes considerably from one order of magnitude to the other, and has a long tail because after each scattering interaction, the probability that the neutron exits with the right trajectory decreases exponentially. The RFs for the old configuration are also displayed, to highlight the important differences due to the features of the new assembly, like borated water.

More details of the n_TOF Resolution Function of EAR1 can be found in [92], and also in [90].

3.4　Proton beam monitors

The intensity of the proton beam sent to the lead target from the PS is constantly monitored during measurements. This is done by means of two devices:

- A **Beam Current Transformer (BCT)** which is situated in the proton line approximately 6 m before the n_TOF target. The BCT provides the reference beam intensity value employed at n_TOF, and the trigger signal for the start

of the acquisition system.

- A **Wall Current Monitor**, commonly known as **Pick-up** (or PKUP). This device is mounted immediately after the BCT and measures the instantaneous value of the proton beam current. It provides a signal whose area is proportional to the number of protons in each bunch, This information is incorporated in the data acquisition system (DAQ) of n_TOF.

3.5   The background at n_TOF

Apart from neutrons, during the spallation process there is a huge production of all kinds of particles. While all charged particles are swept away by the sweeper magnet, neutral particles are not.

Gamma rays are produced in vast amounts and represent an important source of background. Photons are also produced by capture of neutrons in any material intersecting the beam from the target until the measuring position at EAR1. Specifically, capture is particularly intense in the hydrogen of the water moderator, in the aluminium windows and pipes, and in the collimators. In the end, one can distinguish two components of the photon background, a prompt and a delayed one. Both of them have different times of arrival and energy distributions. These two components have been thoroughly studied through MC simulations of the spallation target of n_TOF [90].

3.5.1   The γ-ray flash

The prompt component is very sharp peaked, as it can be seen in Figure 3.9. It reaches the EAR1 between 614 ns –the time in which photons travel the 184 m– and less than 1 μs. These gamma rays have a hard spectrum, with its maximum in the MeV region and reaching up to several GeV. The prompt gamma rays are usually referred, in the context of n_TOF, as the *γ-ray flash*. It typically induces a huge signal in all sensitive γ-ray detectors, which usually saturates them for 2-3 μs. As was shown in section 3.2, this signal is employed to determine the initial time t_0 for the time-of-flight calculation. The saturation in the detectors due to the γ-flash usually sets the upper limit achievable in terms of neutron energy for most of them.
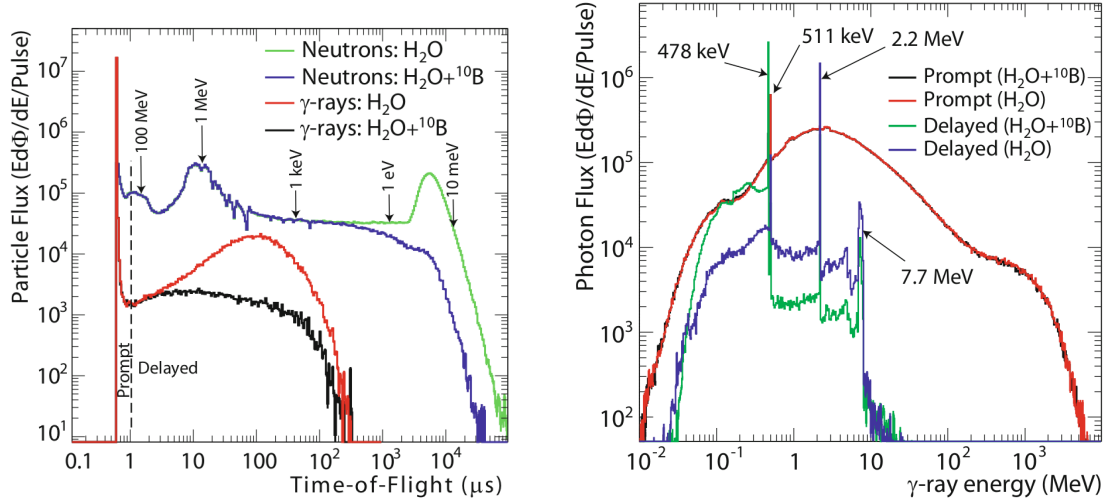
Figure 3.9: *Left: Time-of-flight distribution of the neutron and the in-beam gamma rays at the EAR1. The two components of the in-beam gamma rays are clearly distinguishable. The reduction of the delayed component due to the use of borated water is clear. Right: Energy distribution of the gamma rays, with prominent peaks due to capture in hydrogen and aluminium (2.2 MeV and 7.7 MeV), pair annihilation (511 keV), and $^{10}B(n,\alpha)$ reaction in boron (478 keV). Figures extracted from [92].*

3.5.2 Delayed background

For a capture experiment, the delayed γ-ray background is the most troublesome. These gamma rays, which arrive at times corresponding to the neutron energies of interest for most applications, can be scattered by the sample and then detected by the C_6D_6 detectors, without possibility to distinguish them from true capture γ-rays. As can be seen in Figure 3.9, the delayed spectrum is dominated by several capture gamma rays. Capture in the boron of the water moderator produces a very high peak at 478 keV due to the $^{10}B(n,\alpha)^7Li$ reaction. Capture in H and ^{27}Al produce much smaller peaks at 2.2 MeV and 7.7 MeV, respectively. In this sense, the use of a borated water moderator in practice shifts the energy distribution of the photon flux to lower energies. This is very convenient, since low energy photons are, in general, easier to reject.

A sizeable amount of gamma rays are also produced by neutrons, which are scattered by the sample and captured in any material around the experimental area, such as beam pipes, the detectors support structures, or other massive de-

tector elements, like the TAC. The detection of neutrons by the C$_6$D$_6$ detectors, called *neutron sensitivity*, is discussed in section 4.9. The capture of these neutrons produces gamma rays of up to several MeV depending on the capturing material. Thus they cannot be as effectively rejected as most of the in-beam gamma rays. In addition, the "neutron-induced" contribution is the dominant source of background for neutron energies above ~ 300 eV. An in-depth analysis of the scattered neutron background, by means of Geant4 MC simulations of the whole experimental area, can be found in [64]. As already mentioned in Chapter 2, alternative detection systems, such as i-TED [62, 63] have been proposed to reduce this type of background, and are under development.

3.6   C$_6$D$_6$ detectors for (n,γ) measurements

The capture measurements presented in this work were performed with four C$_6$D$_6$ liquid scintillation gamma ray detectors. The origin of these devices can be traced back to the non-hydrogenous C$_6$F$_6$ detectors originally employed by Macklin and Gibbons [66]. The C$_6$D$_6$ detectors possess several characteristics that make them especially well suited for neutron capture experiments:

- **Very low neutron sensitivity**. The use of deuterated benzene as scintillation material reduces considerably the neutron detection efficiency –also known as *sensitivity*– of these detectors, thanks to the low capture cross section of deuterium.

- **Low gamma ray detection efficiency**. The use of a light and low Z detection medium entails a maximum gamma ray detection efficiency of a few percent. Additionally, energy deposition at the photopeak is virtually non existent in these detectors. Nevertheless, low gamma ray efficiency is actually advantageous, since it is one of the requirements for applying the Pulse Height Weighting Technique (see section 2.2 for details).

- **Very fast response**. C$_6$D$_6$ detection signals have a rise time of ~ 3 ns and a FWHM of ~ 5 ns, which make them ideal for applications that require very high time resolution, like time-of-flight measurements.

The detectors are based on a commercial model produced by BICRON, modified

① mu metal

② quartz window
    of detector cell

③ aluminum cell

④ expansion volume
    (TEFLON tube)

⑤ glass tube of PM

⑥ electrodes of PM

⑦ quartz window of PM

⑧ carbon fiber cell

⑨ scintillator (C_6D_6)
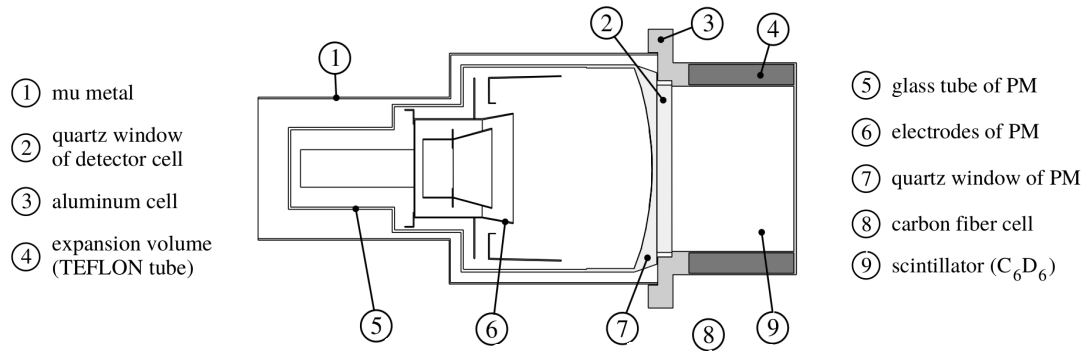
Figure 3.10: *Design of the BICRON C_6D_6 detectors, in its original form. Extracted from [93].*

in several aspects of its design to reduce the neutron sensitivity [93]. The changes include the use of thinner aluminium walls, and the modification of a Teflon tubing wound around the scintillation cell. The purpose of the latter was to act as expansion volume to the cell, but in its original form contributed notably to increase the neutron sensitivity. In addition, the original photomultiplier, which had a borosilicate window, was replaced by a Photonis XP1208 photomultiplier. The latter features a quartz window, avoiding the background contribution of neutron capture in boron.

The C_6D_6 setup employed for the ^{203}Tl(n, γ) and ^{204}Tl(n, γ) measurement campaigns is shown in Figure 3.11. The detectors were placed facing the sample and against the beam direction, with an angle respect to the beam of of $\sim$ 125°. De-excitation gamma rays arise from pure dipole transitions (see section 5.3), which have an angular distribution. The effect of the angular distribution in nuclides like the thallium isotopes, with a gamma ray multiplicity of 3-4, is not important, and eventually can be minimized at $\theta = 125°$, where the second order Legendre polynomial vanishes [29]. In addition, for gamma rays < 1 MeV, such angle reduces the in-beam photon background owing to the angular distribution of the Compton effect, which obeys the Klein-Mishima formula [94]. In order to reduce the huge low energy background caused by the activity of the ^{204}Tl sample, 2 mm thick lead foils were placed in front of each detector. The resulting reduction of the efficiency affected significantly the calculation and the performance of the weighting function (see Chapter 5 for details).
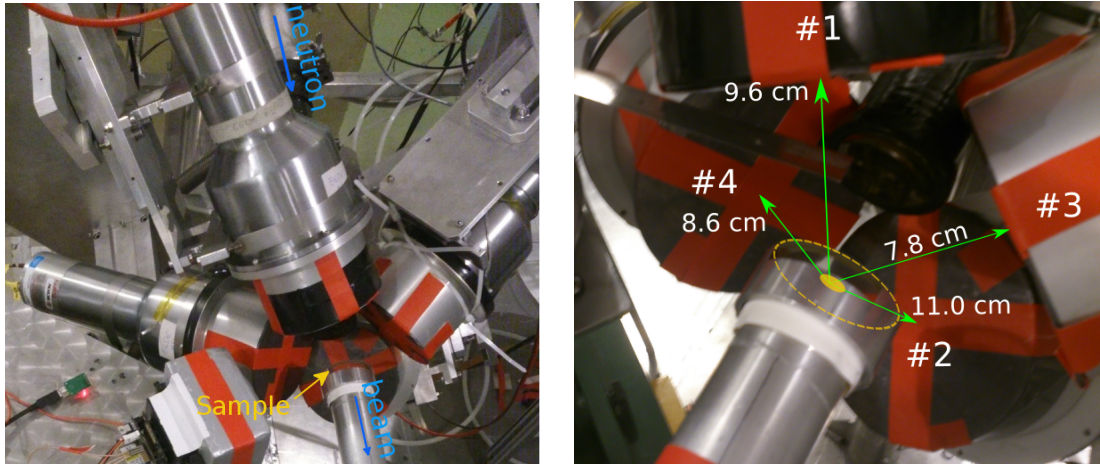
Figure 3.11: *Left: picture of the four C_6D_6 setup employed during the $^{203}Tl(n,\gamma)$ and $^{204}Tl(n,\gamma)$ campaigns. The beam direction is depicted by the blue arrows. The red tape was used to subject the lead covers to the detectors. The device in the bottom of the picture is an i-TED prototype (see chapter 2) which was tested in the middle of the campaign, but was not present during any of the data acquisition runs employed in the present work. Right: close-up of the four detectors. The green arrows represent (not in scale) the distance between the sample and the centre of the face of each detector, with the measured value also included. Since the sample is not visible in the original picture, for clarity purposes a sketch of the sample holder and the sample, in the position it would occupy, has been included.*

3.7 Data Acquisition System (DAQ)

The Data Acquisition System of n_TOF must serve to several needs [95]. In the first place, it must be capable of resolving very fast signals, like those from C_6D_6 detectors, separated by very short times-of-flight intervals. On the other hand, very high counting rates are often achieved, either from neutron-induced reactions of interest or from decay radiation of the radioactive samples under study. Related to this, some large detectors at n_TOF like the TAC require several dozens of channels working at the same time. Thus, the n_TOF DAQ must be fast, it must be flexible to manage dozens of different detectors, and finally, it must be able to manage all the amount of data produced, with data transfer peaks of several GB/s [96].

The DAQ of n_TOF is based on 12 bit flash-ADC digitizers from SPDevices, model ADQ412DC, which offers a sampling rate of up to 1 GHz, and a maximum

acquisition time window of 100 ms. In addition, they are equipped with an efficient zero-suppression algorithm, which eliminates data below a certain threshold defined by the user. This feature contributes to reduce considerably the amount of data recorded. The raw data from all detectors for several proton bunches (or "events") are stored together in a file in local computers. Every 10 proton bunches, the file is closed and automatically transferred to the CERN Advanced STORage manager (CASTOR) [97].

For the ^{204}Tl(n, γ) campaign, the very high counting rate induced by the sample activity led to the production of a huge amount of data. In order to reduce the size of the data files, it was necessary to optimize the configuration of the digitizers. The acquisition window was reduced to 14 ms, which in practice limited the lower neutron energy achievable to 1 eV. This was not a problem for the posterior analysis, since the first thallium resonance of either isotope is found at 37 eV. The sampling rate of the SiMon was also reduced to 56 MS/s. Finally, the size of the presample –the number of points recorded before the signal exceeds the zero-suppression threshold– and the postsample –the data recorded after the signal falls below the threshold– were both reduced to 256, down from 1024 and 2048, respectively.

In this way, it was possible to reduce the size of the raw data files to manageable values for the subsequent pulse shape analysis.

3.8 Pulse shape analysis routine

Once the raw digitized data is stored, it has to be processed in order to extract the relevant information of each signal. For this purpose, a generic routine was developed at n_TOF [98]. The main principles behind its design were:

- It was built to accommodate the wide variety of detectors employed at n_TOF, each one with its own signal characteristics.

- In order to comply with the previous need, it was made to require the smallest possible number of signal input parameters, which must be set externally by the user. In addition, it has a modular design which allows to select several options in each step of the routine.

- It is based on a pulse template adjustment procedure, also known as *pulse shape fitting.*

A very detailed description of all the steps of the routine, and the multiple features available, can be found in [98, 99]. The main stages of the algorithm are:

1. **Pulse recognition.** True pulses are identified by calculating the derivative of the signal and applying a multiple threshold crossing filter.

2. **Location of the γ-flash.** As explained in section 3.5.1, in most of the detectors, including C_6D_6, the γ-flash is employed to determine the t_0 for the time-of-flight measurement. Thus, the routine features several options to recognize it correctly and extract the γ-flash time, t_γ. For C_6D_6 the γ-flash is identified as the first signal crossing a very high threshold in amplitude.

3. **Baseline calculation**. For a proper determination of the amplitude and the area of the pulses, the baseline level must be determined accurately in order to subtract it. For the present analysis, the option of an adaptive baseline was chosen, calculated with the "moving maximum" technique (see [98] for details).

4. **Pulse shape fitting.** Once the baseline has been subtracted, the amplitude, the t_{TOF}, and the area of each pulse are obtained. Three methods are available to achieve that: searching for the signal highest point, parabolic fitting to the top of the pulse, and pulse shape fitting. For the latter, a "model" pulse shape is adjusted and fitted to each pulse by a least squares procedure. The model pulse shape must be provided by the user, and it is obtained by averaging a large number of pulses. The pulse shape fitting was the method employed in the present analysis.

3.8.1   Event building

The information of each signal –detector number, amplitude, time of arrival, area, among many other attributes–, together with the information of the event that generated it –number of event, proton intensity, γ flash time– is stored in a ROOT file [100], one for each data acquisition run. The signals belonging to each detector are stored as *entries* in a ROOT data structure called *TTree*. For a given entry,

every attribute of the signal is stored in a separate substructure of the TTree, called *TBranch*. The Tree/branch data structure of ROOT is specifically designed to provide a fast and flexible access to the specific properties of the signals. This, combined to its histogramming and plotting capabilities, allows to perform very quick preliminary analysis of the data. This is crucial in order to monitor all important aspects –detectors, samples, the neutron beam, etc.– during an ongoing measurement.

The pulse shape analysis and the production of the ROOT files is fully automated at n_TOF with the user required only to provide, in anticipation, the set of input parameters for the detectors of interest. Once completed, the output ROOT files are stored in CASTOR. These files are ready to be analysed for determining the capture reaction yield, a task which is described in the next chapter.

Chapter 4

Determination of the capture yield

In this chapter we will describe the several steps that have been followed to extract a reliable capture yield from the experimental data processed by the PSA routine. Details on each of the steps are particular to each sample under study, and hence will be discussed more in depth in the chapter devoted to each cross section measurement.

All the tasks described in this chapter were carried out by writing several ROOT [100] C/C++ programs, which performed the sorting of the experimental data, applied all the necessary cuts and correction factors, and produced the counting rate histograms for the analysis. A detailed description of the analysis routine is given in Appendix A.

The experimental yield

The final goal of the data reduction process is to obtain an experimental yield that can be fitted in order to extract the desired cross section, using the R-matrix formalism described in chapter 1. The experimental yield can be defined as the fraction of incident neutrons, N_n^I, that arrive at a certain time interval t_{TOF} in the sample, and undergo a radiative capture event which is measured by the detectors:

$$Y_{exp}(t_{TOF}) = \frac{N_n^C(t_{TOF})}{N_n^I(t_{TOF})} = \frac{C(t_{TOF})}{N_n^I(t_{TOF}) \cdot \varepsilon(A)} \ , \tag{4.0.1}$$

where $C(t_{TOF})$ are the number of counts registered in each detector at the given time-of-flight, and $\varepsilon(A)$ is the detection efficiency, which depends on the amplitude

A of the signals registered. A, expressed in units of ADC channels, is proportional to the energy deposited by a γ-ray in the detector volume, and thus the first step in the analysis is the determination of this relation. This procedure is described in section 4.1.

Since we are interested in a cross section expressed as a function of neutron energy E_n, it is necessary to perform a time-of-flight to neutron energy calibration, a procedure explained in section section 4.2.

The fraction of neutrons crossing the sample geometry, $N_n^I(t_{TOF})$, is calculated from the evaluated neutron flux ϕ_n [77] (see section 3.3.1 for details), which must be integrated over the sample surface exposed to the beam,

$$N_n^I(t_{TOF}) = \int_S \phi_n(t_{TOF})dS \; . \qquad (4.0.2)$$

In practice, $N_n^I = f_{bi} \cdot \phi_n$, where f_{bi} is the fraction of the total beam intercepted by the sample, also called *beam interception factor*. This is obtained from simulations for the typical circular geometries employed at n_TOF. The f_{bi} changes with the beam profile, which depends on the energy of the neutrons. However, in the energy range of 1 eV to 10^5 eV, the factor is practically constant [92]. The calculation of the interception factor for our particular case is explained with more detail in section 4.8.

Finally, the total counts registered in the detectors, $C(t_{TOF})$, include a certain number from several different sources of background, $B(E_n)$, which have to be carefully evaluated in order subtract them. The analysis of the background components is discussed in section section 4.7.

4.1   Deposited energy and resolution calibration

An accurate calibration of the C_6D_6 detectors in deposited energy is particularly important in the analysis of a capture experiment that employs the TED technique. This is because pulses are weighted according to their energy deposition and hence, an error in the calibrations turns into an error in the weight assigned to that pulse. Furthermore, the higher the energy of the pulse, the more sensitive is the PHWT to errors. In this respect, a smooth WF without strong oscillations is desirable. Otherwise, in the case of a erroneous determination of the pulse amplitude, the

abrupt variations in the $W(E_\gamma)$ function would magnify the bias in the weight assigned to the pulse.

There are a few important requirements for a proper calibration of C_6D_6 detectors:

- **Wide energy range**. C_6D_6 detectors must be calibrated in a wide energy range, corresponding to the range of the full de-excitation cascade of the nucleus under analysis. To achieve that, several monoenergetic gamma ray sources were employed: a ^{137}Cs, with a gamma ray photo-peak at 662 keV; a ^{88}Y source, which emits two gamma rays at 1836 and 898 keV; and an Am-Be source, in which a 4.438 MeV gamma ray is released due to the $^9Be(\alpha, n)$ reaction. Additionally, in order to have a reference at higher energies, closer to the S_n of the thallium isotopes, the deposited energy spectrum of capture in ^{197}Au, with and endpoint at 6.512 MeV [101], was also routinely employed in the calibrations. The latter was employed as a substitute for a Cm-C source unavailable at the time, which emits a gamma ray of 6.13 MeV.

- **Periodicity**. Calibrations must be done periodically in order to detect any possible shift in the energy-amplitude relation over the course of the experiment. This is especially important for experiments with highly radioactive samples, because the performance of the photomultiplier can change under conditions of high counting rates. Furthermore, a constant, low amplitude background can induce an apparent shift in the gain of the detector due to pileup effects. For both reasons, specific calibrations for the ^{204}Tl measurement were performed, with the sample present in the beam position.

- **Dedicated calibration curves**. Due to the aforementioned importance of the calibration at higher energies, the type of calibration curve must be chosen carefully. The shape is usually different for each detector, and it can also vary in time for the same detector. Additionally, a linear relation, especially in the high energy range, was not possible most of the times. Double linear, parabolic, and double parabolic curves were employed instead. When using two calibrations, the separation between the low and high energy one was set at the energy of the Am-Be peak.

- **Simulations.** The most accurate way to calibrate the detectors is to per-
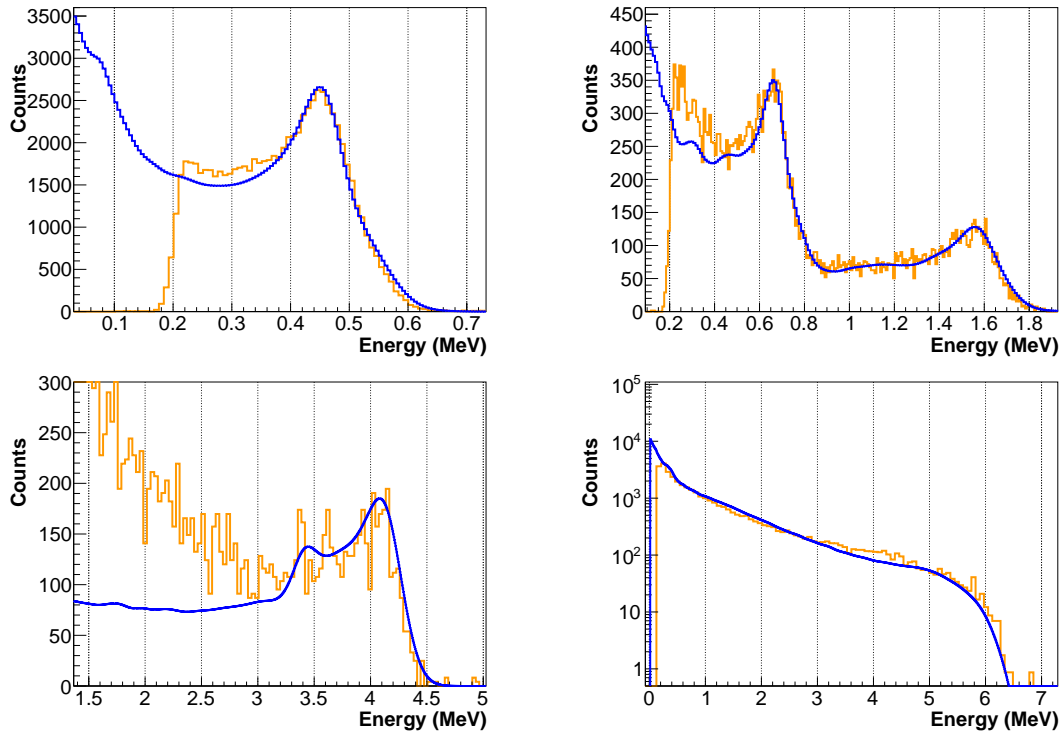
Figure 4.1: *Experimental (orange) versus simulated (blue) energy deposited spectra in $C_6D_6\#4$, for the July 14 calibrations. The sources are the ^{137}Cs gamma ray at 662 keV (top left), the two gamma rays of ^{88}Y at 1836 and 898 keV (top right), the Am-Be (bottom left), and the deposited energy spectrum at the 4.9 eV $^{197}Au(n,\gamma)$ resonance, with $S_n = 6.512$ MeV.*

form simulations of the response functions of the detectors to the gamma ray sources employed in the experiment. This is especially convenient because C_6D_6 detectors have no photo-peak, and the broad Compton edge must be employed instead. Monte Carlo simulations were performed with the Geant4 toolkit [88, 89], and featured a detailed reproduction of the capture setup implemented before in a previous measurement [102, 103]. The resulting simulated deposited energy spectra are convoluted and simultaneously fitted to the measured spectra, in order to determine the calibration coefficients.

An example for a calibration of $C_6D_6\#4$, employed for the $^{203}Tl(n,\gamma)$ campaign is shown in Figure 4.1. For these calibrations a single parabolic polynomial was employed.

4.2   Time-of-flight to neutron energy calibration

An accurate determination of the relation between the time of arrival of the neutrons at the sample position and their energy is essential to obtain the correct energy dependent cross section. In the approximation of the classic kinematics, the energy of the neutrons E_n is related to the travelled time by the relation

$$E_n = \frac{1}{2}m_n v^2 = \alpha^2 \frac{L^2}{t^2}, \ \ \alpha = 72.2977\frac{\sqrt{eV}\mu s}{m} \tag{4.2.1}$$

where L stands for the effective flight path travelled by the neutrons from the emission point to the sample. However, as we saw in the discussion of the Resolution Function in chapter 3, the moderation path of neutrons in the target and moderator is a distribution that changes considerably from one order of magnitude of E_n to the other. A first approximation is to calculate an average moderation length for each energy, $\Delta L(E_n)$, so L can be expressed as the sum of two terms,

$$L(E_n) = L_0 + \Delta L(E_n), \tag{4.2.2}$$

where L_0 is the fixed, geometric distance from the outer face of the target-moderator ensemble to the sample position. From MC simulations of the whole facility, a simple relation of ΔL with the energy has been determined,

$$\Delta L = 0.101\sqrt{E_n} \ . \tag{4.2.3}$$

With this, the effective flight path L can be obtained in a two step process. An approximate E_n is first obtained with the fixed L_0, $\Delta L(E)$ is calculated, and the E_n is recalculated again with the effective $L(E_n)$ from equation (4.2.2). However, this procedure must be done signal by signal, which would increase considerably the computational time dedicated of the data sorting. Alternatively, it can be shown that the addition of an energy dependent ΔL is equivalent to add a constant time offset in the denominator in equation (4.2.1). Thus,

$$E_n = \frac{1}{2}m_n v^2 = \left(\frac{72.2977L_0}{t + t_0}\right)^2. \tag{4.2.4}$$

The L_0 geometrical distance is calculated by using well-known low energy resonances up to 60 eV of ^{197}Au, because at those energies the ΔL correction is negligible. The calibration has been tested with several other resonances, from 60

eV up to 10 keV, with and without the corrections. In the end, no correction was applied, since only this way an accuracy equal or better than 0.1% was achieved in all resonances. The shift in the peak energy resonance at higher energies is corrected eventually by the use of a numerical resolution function in the analysis of the yield (see section 4.6). In any case, beyond 10 keV neutron energy it is also the Resolution Function, as the dominant source of resonance broadening, that limits the maximum achievable energy resolution, with $\Delta E_n/E_n \geq 1.1 \times 10^{-3}$ [92].

4.3   Consistency checks between detectors

The first step in the analysis process was to perform a preliminary list of checks and crosschecks among detectors to ensure the consistency of the data registered by each of them.

Monitoring of the gain shifts

- **C_6D_6 detectors gain**. The use the PHWT to apply the TED technique makes this a critical check to be performed. A change of unknown origin in the gain of a detector will result in an error in the weight assignment, which will be directly propagated into the capture yield. Therefore, if an important shift in gain is found for a detector during several runs, the decision is to exclude those data from the final analysis.

- **SiMon detectors gain**. The deposited energy spectra of the four silicon detectors is shown in Figure 4.2, for four separated runs of the experimental campaign. The gain of the detectors remains stable throughout the measurement. Due to the nice separation from the alpha particles and background component, only the counts in the triton peak are considered for counting rate monitoring. Thus, only counts between channels 1500 and 2700 were selected.

Monitoring of the detector counting rate

The stability of the counting rate of the different detectors was checked to identify variations during the course of the measurement. Because this checks are particular
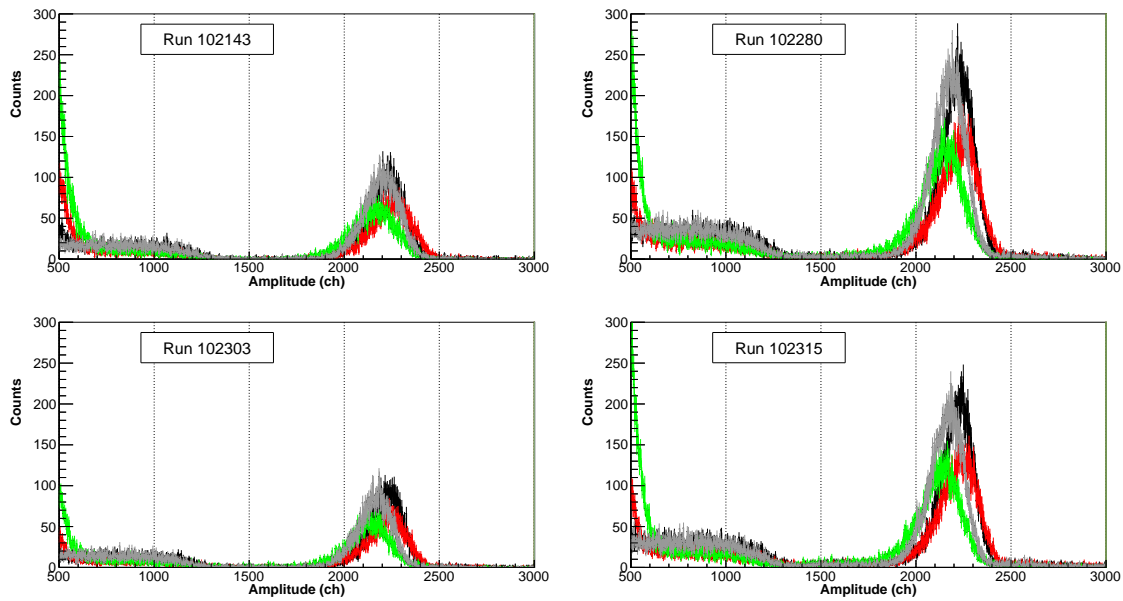
Figure 4.2: *Energy deposition in the four SiMon detectors, for different runs along the measurement.*
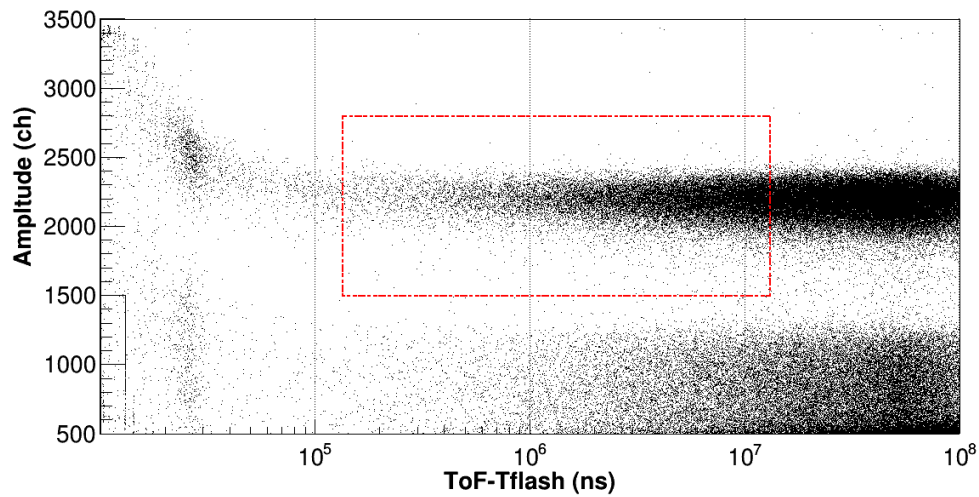
Figure 4.3: *SiMon counting rate distribution, as a function of amplitude and time-of-flight, for run 102280. The cut employed in both magnitudes is highlighted by the red square.*

to each experimental run, they will be only briefly described here, and the plots will be shown in the chapters devoted to the analysis of each measurement (in sections 6.2.2 and 7.4, respectively).

- **Ratio of C_6D_6 detectors over the SiMon**
  This check is performed to ensure the stability of the gamma ray counting rate per incident neutron. Due to the reliability of the SiMon detectors, variations in one or more detectors would reveal changes in the efficiency of the detection setup. Such changes could be related to the performance of the C_6D_6 detectors, or to the position of the sample. On the other hand, a similar variation in all four detectors could indicate issues in the SiMon detectors. The amplitude and time window cuts of the SiMon were selected by inspection of the plot in Figure 4.3. The time-of-flight window corresponds to energies from 1 eV to 10 keV, while the cut in amplitude corresponds, as before, to the triton energy deposition.

- **Beam intensity monitoring**
  The evaluated neutron flux is employed to calculate the yield for both the sample under analysis and the reference sample. Therefore, the ratio of neutrons per proton must be experimentally checked to be constant for all samples in the measurement campaign. In case of variations in the ratio, hypothetical problems of the SiMon detectors could be identified by comparing this ratio with the C_6D_6/SiMon. Once this possibility had been discarded, a variation in the SiMon/BCT ratio could be explained by:

  i) A real variation in the neutron intensity, which could be produced, for instance, by changes in the position where the proton beam hits the spallation target. In that sense, tests have been conducted recently that report that shifting a few mm the position results in a variation in the neutron intensity of up to a few %.

  ii) An error in the reported BCT intensity of the proton beam. Such situation would also lead to a variation in the ratio of the PKUP area over the BCT value.

  If variations in the SiMon/BCT between different samples are identified, they must be corrected appropriately. The same SiMon/BCT ratios are used to

calculate a beam intensity normalization factor f_{si}, which will be described with more detail in section 4.5.

4.4 Determination of the threshold in deposited energy

A threshold in signal amplitude must be applied when sorting the processed data to eliminate as much as possible low background signals which do not come from capture events. Possibly, the most important source of very low amplitude signals is the electric noise inherent to any electronic equipment. Another source of spurious signals, which has been observed in different C_6D_6 detectors at n_TOF, are the low amplitude signals that appear as a rebound or "echo" signal of a real high amplitude signal. These are believed to come from possible issues in the photomultiplier, or possible impedance mismatches in the signal transmission chain, including the voltage divider [104, 105]. The time distribution of these signals peaks around a few hundreds of nanoseconds, but they hardly appear exactly at the same time. Thus, discriminating them by pulse shape fitting techniques is not feasible.

On the other hand, approximately 40% of the capture signals deposit an energy lower than 0.6 MeV, so one must choose a threshold high enough to avoid most of the background, while keeping it as low as possible to minimize the loss of capture counting statistics. For the case of the $^{203}Tl(n,\gamma)$ the main concern was to ensure that most of the false echo signals were rejected, which was accomplished with a digital threshold of 250 keV.

In the case of the $^{204}Tl(n,\gamma)$ campaign, due to the intense sample activity, the threshold had to be set at a higher energy. The optimum value was determined as the one maximizing the signal-to-noise ratio in the capture resonances. Further details can be found in Chapter 7.

4.5 Correction factors to the experimental yield

At this point, it is opportune to rewrite equation (4.0.1) in terms of E_n and E_{dep}^{γ},

$$Y_{exp}(E_n) = \frac{C(E_n) - B(E_n)}{N_n^I(E_n) \cdot \varepsilon(E_{dep}^{\gamma})} \; . \qquad (4.5.1)$$

As was explained in Chapter 2, the dependency of the detection efficiency on the energy of the incoming gamma ray is resolved by applying the PHWT. The

weighted counting rate can be then expressed as

$$C_w(E_n) = \sum_{E_{dep}} W(E_{dep}) \cdot C(E_n, E_{dep}) \,, \qquad (4.5.2)$$

and thus the experimental yield becomes

$$Y_{exp}(E_n) = \frac{C_w(E_n) - B_w(E_n)}{N_n(E_n) \cdot (S_n + E_n)} \,. \qquad (4.5.3)$$

The absolute detector efficiencies $\varepsilon(E_{dep})$ are still required to calculate the WF. They are obtained from detailed simulations of the capture setup, in a procedure described in detail in Chapter 5. Even this simulations are as close to the real setup as possible, there still could be small discrepancies in variables which are difficult to control. Some of these could be the relative distances between each detector and the sample, the detector exact orientation, or the real volume of the active liquid scintillator, just to name a few. On top of that, although the shape of the flux is stable and well known, there could be small, periodic oscillations in the number of incident neutrons at a given energy.

All these issues are circumvented by normalizing the yield to a reference sample, whose cross section is known as accurately as to be considered a standard. The normalization procedure employed in this work is the **saturated resonance method**, described more in detail in section 4.11. The normalization is directly applied to the yield as a the normalization factor, $\boldsymbol{f_{sat}}$. Other corrections may arise due to particularities of each sample, which must be addressed separately:

- **Threshold correction factor, $\boldsymbol{f_{th}}$.** This correction arises due to the necessity of applying a threshold in deposited energy. It compensates for the number of capture cascades that are lost under the threshold, which might differ between the sample under study and the normalization sample. The factor is obtained by means of dedicated simulations of capture cascades. The correction also compensates for all those capture events lost due to emission of internal conversion electrons (ICE) in the de-excitation process. The threshold correction factors are obtained by applying the WF to simulated capture cascades, a procedure discussed in depth in chapter 5.

- **Neutron sensitivity correction factor, $\boldsymbol{f_{ns}}$.** The f_{ns} can be important for some resonances with very high Γ_n, since this can artificially increase the

capture yield due to the neutron sensitivity of the experimental setup. The f_{ns} is further discussed in section 4.9.

- **SiMon renormalization factor, $\boldsymbol{f_{si}}$.** In case that a discrepancy in the neutron counting rate per proton is observed between the normalization data runs and any other runs, it is necessary to renormalize the evaluated neutron flux accordingly. The renormalization is always performed by the f_{si}, which is obtained from the SiMon/BCT counting rate ratio,

$$f_{si} = \frac{C_{Au}^{sm}/BCT_{Au}}{C_{x}^{sm}/BCT_{x}} \ . \qquad (4.5.4)$$

The particular values of the f_{si} for each x sample are given in the chapters dedicated to the analysis of the ^{203}Tl(n,γ) and ^{204}Tl(n,γ) measurements.

All in all, the final experimental yield can be expressed as:

$$Y_{exp}(E_n) = f_{sat} \cdot f_{th,ice} \cdot f_{si} \cdot f_{ns} \frac{C_w(E_n) - B_w(E_n)}{f_{bi} \cdot \phi_n(E_n) \cdot (S_n + E_n)} \ . \qquad (4.5.5)$$

4.6 Resolution function

An accurate description of the RF is essential for a reliable analysis of the capture yield in the resolved resonance region, because the RF starts to be the dominant source of broadening at a few keV. In addition, it shifts the centre of the resonance, slightly affecting the time-of-flight to neutron energy conversion.

The yield in a resonance with neutron energy E_n can be written as

$$Y(E_n) = \int Y(t_{TOF}) R(E_n, t_{TOF}) dt_{TOF} \qquad (4.6.1)$$

The RF is included directly into the SAMMY code employed for the analysis of the yield (see section 4.12). In Phase1, an analytical RF [92, 106], derived from neutron production and transport calculations, was used with satisfactory results. For Phase2, a numerical and more accurate RF, also obtained from simulations, was determined [90, 92], and this is the RF employed in this work.

4.7 Background subtraction

The subtraction of the background is a very important and delicate step towards the obtention of the capture yield. As discussed in section 3.5, the gamma ray

background at n_TOF comprises several contributions, which have to be evaluated carefully for each sample and nuclide under analysis.

- In the case of radioactive samples, the **intrinsic activity background** is evaluated by simply recording data without beam. The signals from the radioactive decay are registered at a constant rate. Thus, in a time-of-flight histogram with logarithmic binning, they have a smooth linear distribution, which can be readily subtracted from the capture spectrum with a negligible uncertainty.

- The **background from scattered gamma rays** is evaluated experimentally using a natural lead sample in the target position. Natural lead, especially its most abundant isotope ^{208}Pb (50%), has low neutron interaction cross sections, and as a dense and high Z material, it is a strong gamma ray scatterer.

- The **background caused by secondary capture of scattered neutrons** is assessed by using a natural carbon (graphite) sample as target. ^{nat}C is a strong neutron scatterer due to its low Z and a total cross section totally dominated by the elastic channel. On the other side, as a low density and low Z material, it is practically transparent to gamma rays.

- A further contribution to the overall background comes from the natural radioactivity emanating from the walls of the experimental hall. This contribution is generally negligible when compared to the other sources of background listed above.

In experiments with nuclides that have a high elastic cross section, the gamma rays emitted in the secondary capture of scattered neutrons dominate the background over a large neutron energy range [64]. In those situations, the ^{nat}C time-of-flight spectrum can be used to analyse the background over a large neutron energy span. This was the case for the ^{203}Tl sample. In other cases, like for the ^{204}Tl measurement, the main source of background was due to reactions in the sample container. In this situation, the background was evaluated with a "dummy" sample of the container.

In order to subtract the background, its spectrum must be weighted with the same weighting function as the sample under analysis. A detailed description of

the background subtraction process for each thallium sample will be given in the corresponding analysis chapter.

4.8   Beam Interception factor

The samples studied in this work had a nominal geometry of 5 mm. The beam interception factor, f_{bi}, for 5 mm diameter samples was calculated from the f_{bi} at 20 mm, which is accurately known to to be 0.68 from MC simulations of the facility. For that purpose, it was assumed that for two similarly thin samples of the same material, it holds the relation

$$\frac{f_{bi}(\phi_{5mm})}{f_{bi}(\phi_{20mm})} = \frac{C_w(\phi_{5mm})}{C_w(\phi_{20mm})} \ . \tag{4.8.1}$$

The weighted counting rate C_w is employed in order to correct for any small difference in the detector efficiencies caused by the different radii of the samples. The counting rate at the saturated resonance at 4.9 eV of ^{197}Au was used, since its value can be accurately measured in the resonance plateau. From equation (4.8.1), $f_{bi} = 0.0717$ was obtained.

It must be noted that, for 5 mm diameter samples, the alignment of the sample with respect to the beam could have a strong impact. Given the sharp peak profile of the beam, a misalignment of 1-2 mm could produce a substantial reduction of the neutrons intersecting the sample. However, this uncertainty can be minimized by fixing the relative position of the sample under study and the reference sample along the experiment. That being said, the normalization to a reference sample made the accurate determination of the interception factor less of an issue. In the end, what really mattered was to avoid any difference in the relative positions between the ^{197}Au and the ^{203}Tl samples.

4.9   Neutron Sensitivity correction

As discussed in chapter 3, the neutron sensitivity of the modified BICRON C_6D_6 detectors employed in the capture measurements is very low. However, when measuring capture in nuclides with very high elastic cross section, the probability that a count registered by the detectors originates from a contaminant neutron capture in the detector itself might not be negligible.

The probability that, in resonance at a given energy, a signal in the detectors is due to a neutron rather than a gamma ray from the capture cascade can be expressed as

$$P_{ns} = \left(\frac{\varepsilon_n}{\varepsilon_c}\right) \cdot \left(\frac{\Gamma_n}{\Gamma_\gamma}\right), \tag{4.9.1}$$

where ε_n is the neutron detection efficiency of the setup, ε_c is the capture cascade detection efficiency, and Γ_γ and Γ_n are the probabilities that a neutron is captured or scattered, respectively, at that resonance.

It is convenient to rewrite the previous equation in terms of $\varepsilon_n/\varepsilon_\gamma$, which is the neutron sensitivity as defined in Ref. [93]. The reported value at a neutron energy of 10 keV was $\varepsilon_n/\varepsilon_\gamma = 6.1 \cdot 10^{-4}$, which was adopted as an acceptable overall average for the range of energies from 1 eV to 30 keV. However, the value was corrected to take into account the decrease in ε_γ due to the use of the lead foils on the detectors. For that it was assumed that the absorption of neutrons in the 2 mm foils is negligible, owing to the very low capture cross section of lead. If ε'_γ is defined as the gamma ray efficiency of the shielded C_6D_6 setup, we have

$$\left(\frac{\varepsilon_n}{\varepsilon'_\gamma}\right) \approx \left(\frac{\varepsilon_\gamma}{\varepsilon'_\gamma}\right)\left(\frac{\varepsilon_n}{\varepsilon_\gamma}\right) = 7.9 \cdot 10^{-4} . \tag{4.9.2}$$

With this, equation (4.9.1) can be rewritten as

$$P_{ns} = \left(\frac{\varepsilon'_\gamma}{\varepsilon_c}\right) \cdot \left(\frac{\varepsilon_n}{\varepsilon'_\gamma}\right) \cdot \left(\frac{\Gamma_n}{\Gamma_\gamma}\right). \tag{4.9.3}$$

For the calculation, the gamma ray detection efficiencies ε_γ and ε'_γ where those corresponding to photons of 600 keV. Values for ε'_γ, ε_γ and ε_c were obtained by means of Geant4 simulations of the capture setup, which yielded $\varepsilon'_\gamma = 0.0170(2)$, $\varepsilon_\gamma = 0.0221(2)$ and $\varepsilon_c = 0.0273(2)$ (more details on the cascade simulations can be found in chapter 5). The final correction to the capture yield, f_{ns}, will be

$$f_{ns} = \frac{1}{1 + P_{ns}} \tag{4.9.4}$$

The factor f_{ns} was calculated and applied resonance by resonance in the yield analysis (in chapter 6 and 7, respectively).

4.10 Pileup

The so-called pileup effect occurs when two signals are registered within a given time τ, in such way that the PSA routine cannot resolve them as separate signals, and thus they are identified as a single one. This results in the loss of the second count and, most probably, in a wrong measurement of the amplitude of the first signal. Due to the use of the PHWT, this would lead, in turn, to a wrong weight assignment, and a bias into the final cross section.

The time τ mimics to a large extent the dead time of a detection system. Therefore, dead-time models can be used to correct for this pileup effect. Two ideal models of dead-time behaviour can be distinguished: *paralyzable* and *non paralyzable* systems [107].

In a nonparalyzable system, every time that a signal is recorded, the detector is assumed to be *dead* for the time τ. Events occurring during that time are lost, and have no effect on the behaviour of the detector. In this situation, if m is the measured counting rate, the fraction of all time the detector is dead is given by $m \cdot \tau$. Then, if n is the real counting rate, the rate of lost counts is $n \cdot m \cdot \tau$. On the other hand, this rate can also be expressed simply as $n - m$, and thus,

$$n - m = mn\tau \implies n = \frac{m}{1 - m\tau} \tag{4.10.1}$$

In the case of the paralyzable system, the situation is more complicated. The dead time is not constant, but depends on the real counting rate, and thus the later can only be evaluated numerically from the expression

$$m = ne^{-n\tau} . \tag{4.10.2}$$

The data processing system employed in this work can be compared to a paralyzable system. One can suppose the hypothetical case of an extremely high counting rate, where signals pileup for a prolonged time. The routine would be unable to separate them, and hence it would identify them as a single one for the whole time span. In fact, something similar to this happens during the γ-flash.

For low detection rates, when the condition $n \ll 1/\tau$ holds, the true rate in a paralyzable can be approximated to the nonparalyzable case, and thus expression equation (4.10.1) can be applied to the capture counting rates measured with C_6D_6 detectors to correct for this pileup effect.

In our particular case, we would like to apply the correction to weighted counting rates. Provided that the dead time τ is independent of the amplitude of the registered pulse, it can be shown [69] that the real weighted counting rate C_w can be obtained applying equation (4.10.1) to the measured weighted counting rate M_w,

$$C_w(E_n) = \frac{1}{1 - \tau M_w(E_n)} M_w(E_n) \tag{4.10.3}$$

where $1/\left(1 - \tau M_w(E_n)\right) = f_p(E_n)$ is defined as the pileup correction factor. In the present analysis, the correction due to pileup has been determined to be negligible for the case of the 4.9 eV resonance of ^{197}Au, which in practice has the highest counting rate of all measurements, including the ^{204}Tl data acquisition.

However, in the ^{204}Tl case pileup can lead to apparent changes in the gain of the detectors. Capture –or high energy calibration– gamma rays can be frequently piled up together with the low amplitude signals produced by the activity of the sample. This leads to an increase in the amplitude of the signals over all the energy spectrum, and hence to an apparent decrease in the gain of the detectors. Variations in the gain of the detectors along the ^{204}Tl(n, γ) measurement will be further discussed in section 7.2.

4.11   Saturated resonance normalization method

As introduced earlier in this chapter, the normalization to a standard sample is a necessary procedure when determining the experimental capture yield. It allows to cancel out most systematic errors, that are difficult to control in absolute terms.

The normalization is performed by measuring a sample of the same exact diameter as the sample under analysis. Provided that the experimental setup and the neutron flux are the same, any experimental deviation will affect both samples by similar amounts, and thus will cancel out.

A reference sample, of thickness n at/barn, is chosen so that it has a resonance with accurately known –and very high– cross section, and where capture is the dominant process. Thus, $\Gamma_\gamma \gg \Gamma_n$ and $\sigma_t \approx \sigma_\gamma$. As a result, $n\sigma_\gamma$ will be very large, and the theoretical yield can be approximated as follows:

$$Y_{th} = (1 - e^{n\sigma_t})\frac{\sigma_\gamma}{\sigma_t} \approx \frac{\sigma_\gamma}{\sigma_t} \approx 1 \ . \tag{4.11.1}$$

This so-called thick-sample approximation means that all incoming neutrons are captured and the yield reaches its maximum value. Hence, it is said that the yield "saturates" at the resonance. In wide and high cross section resonances, this produces a structure similar to a plateau, where the yield can be determined accurately. It is opportune to say that, while we just applied the "thick" approximation, the sample is actually chosen to be the thinnest possible, in order to limit the self-absorption of cascade gamma rays, and to reduce the sample-induced scattering background. The saturated resonance employed in this work was the 4.9 eV resonance of ^{197}Au, in a sample with thickness $7.7 \cdot 10^{-4}$ atoms/barn. With this, all the aforementioned requirements were met.

To obtain the normalization constant A_n for each detector, the experimental yield $Y_{exp}(E_n)$ of ^{197}Au is then fitted with SAMMY in the saturated resonance. This can be expressed as

$$Y_{exp}(E_n) = A_n \cdot Y_{th}(E_n) \ , \tag{4.11.2}$$

where A_n is the only free parameter of the fit. Deviations from unity in the normalization constant can be interpreted as a measure of the overall error in the determination of the absolute yield. The corresponding normalization factor to apply to the sample under analysis will be $f_{sat} = 1/A_n$.

4.12   Capture yield analysis: the SAMMY code

The analysis of the cross section in the Resolved Resonance Region was performed with the code SAMMY [57]. This is a code, developed at the Oak Ridge National Laboratory (ORNL), that applies the R-matrix formalism to the analysis of time-of-flight experiments of neutron induced reactions. The code implements Bayes' equations to obtain, from a set of initial input resonance parameters, the final set of parameters that best fit the experimental data. SAMMY incorporates several versions of R-matrix theory. The recommended, and the one employed for this work, is the Reich-Moore approximation (see section 1.6.4), due to its accuracy. Other formulations are the single level (SLBW) and Multilevel Breit-Wigner (MLBW), which are only included for compatibility with nuclear evaluation data originally elaborated with them.

SAMMY includes corrections for several important experimental conditions, which are described below.

4.12.1 Self-shielding and multiple scattering correction

The total theoretical capture yield Y_{th} can be described as the sum of several contributions. These contributions are related to the number of scattering interactions that a neutron undergoes in the sample before being captured,

$$Y_\gamma = Y_0 + Y_1 + Y_2 \ldots \tag{4.12.1}$$

Depending on the total cross section, the Y_0 can be affected by the self-shielding effect, which is the observed reduction in the capture cross section caused by the attenuation of the beam in the same sample. Thus, the probability that a neutron is captured at given depth z in a sample of thickness L can be expressed as the probability of interaction times the capture probability, that is,

$$\frac{n}{L} \cdot e^{-n\sigma_t \frac{z}{L}} \cdot \sigma_\gamma dz \ , \tag{4.12.2}$$

which integrated over the thickness L of the sample, gives the Y_0 capture term

$$Y_0 = (1 - e^{-n\sigma_t}) \cdot \frac{\sigma_\gamma}{\sigma_t} \ . \tag{4.12.3}$$

However, the probability of capture after one or more scattering interactions is considerably more complex. It involves an increasing number of integrations in order to evaluate the angular direction and spatial position after each elastic scattering. Such integrations require detailed knowledge of the sample geometry. SAMMY features analytical models for the single and the multiple scattering events. In the latter, it assumes that after two scatterings, the position and direction distributions of the neutrons in the sample are uniform.

Self-shielding and multiple scattering effects have a strong dependency on the geometry of the sample, and thus are usually referred to as thickness effects.

4.12.2 Doppler broadening

The observed experimental broadening of nuclear resonances due to the thermal motion of the nuclei is called Doppler –or thermal– broadening. Several broadening models are included in SAMMY, of which the Free Gas Model (FGM) is the one

employed in this work. This model assumes that the target nuclei have the velocity distribution of an ideal gas, that is, a Maxwell-Boltzmann distribution. With a few approximations [54] the broadened cross section can be expressed as

$$\sigma_D(E) = \frac{1}{\Delta_D\sqrt{\pi}} \int \exp\left[-\left(\frac{E'-E}{\Delta}\right)^2\right] \sqrt{E'}\sigma(E')dE', \qquad (4.12.4)$$

which implies a Gaussian broadening of the cross section, with a width given by

$$\Delta_D = \sqrt{\frac{4m_n EkT}{M/m}} \; , \qquad (4.12.5)$$

where m is the neutron mass, M the target nucleus mass, and kT the temperature in units of energy.

4.12.3   Multi-nuclide sample analysis

Usually, the samples in a capture experiment contain multiple isotopes of the same element, and the additional presence of other chemical impurities. Both circumstances were present in the ^{204}Tl sample employed in the ^{204}Tl(n, γ) measurement. SAMMY is prepared to include several nuclides to account for their contribution in the analysis of the measured capture yield. The parameters necessary for the analysis –spin groups, nuclear masses and radius– must be specified for each nuclide. The abundances must be expressed in atomic fraction.

4.12.4   Analytical backgrounds

An analytical background is usually implemented in SAMMY for the capture analysis. Four energy dependences can be specified for the background, with the total being the sum of them,

$$B_T(E) = B_a + B_b/\sqrt{E} + B_c\sqrt{E} + B_d e^{-B_f/\sqrt{E}} \; . \qquad (4.12.6)$$

The user can provide the parameters B_a to B_f in the input files. In the present work only a constant "redualsidual" background was employed for the yield analysis, since the experimental background had been previously evaluated and subtracted for each of the isotopes under study (see section 6.5 and section 7.6 for details).

4.12.5   Maxwellian averaged cross section (MACS)

The relevant input for astrophysical s-process calculations is the cross section averaged by the maxwellian energy spectrum of neutrons at stellar temperatures (MACS), already introduced in chapter 1. SAMMY features the option to calculate it by reconstructing the cross section from the resonance parameters, and integrating numerically the expression

$$\left\langle \sigma(E)\sqrt{E} \right\rangle_{kT} = \frac{2}{\sqrt{\pi}} \int_0^\infty \sigma_\gamma(E) E \frac{e^{-E/kT}}{(kT)^2} \qquad (4.12.7)$$

for a set of thermal kT energies provided by the user. Additionally, SAMMY features the possibility to add pointwise cross sections for energies higher than those described by the resolved resonances. As the kT energy increases, the contribution to the average of the energies much higher than the peak increases considerably. These cross sections must be provided separately, in the ENDF File 3 format. SAMMY can provide the covariance matrix for the MACS by propagating the uncertainty in the resonance parameters. However, not all resonance parameters can be included, which could lead to an underestimation of the uncertainty. An alternative method to obtain the uncertainties was developed in this work, which is based on obtaining the MACS distribution at each kT temperature by Monte Carlo sampling of the resonance parameters. More details are given in section 6.7.

Chapter 5

Calculation of the Weighting Function

The first part of this chapter will be dedicated to describe in detail the calculation of the weighting function and the effects of the use of lead shields in the experimental setup. In the second part, we will focus on the Monte Carlo cascade generator and the simulations of the capture cascades. These are not only necessary to evaluate the uncertainty of the weighting function, but also can to estimate the systematic error introduced by several sources of experimental error. The different systematic uncertainties will be analysed and quantified individually.

5.1   Calculation of the Weighting Function

5.1.1   Monte-Carlo simulations of the experimental setup

The most convenient way of obtaining the detector response functions employed for the WF calculation, is by means of detailed MC simulations of the whole capture setup. These simulations must include every element susceptible of interacting with the γ-ray and particles produced in the de-excitation cascades. Indeed, the weighting function is unique for each combination of detector and sample under analysis.

The simulations have been carried out employing the Geant4 simulation framework [88, 89], using the geometry of the C_6D_6 setup of n_TOF implemented in a previous work [102, 103]. The experimental setup reproduced in the simulations
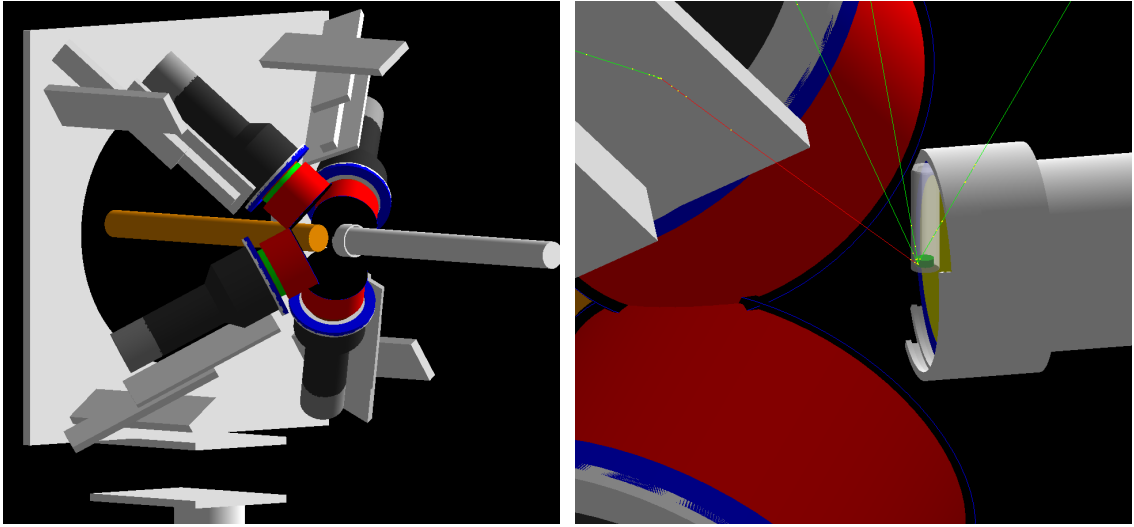
Figure 5.1: *Geant4 simulation of the n_TOF EAR1 C_6D_6 experimental setup. Left: General view of the detectors and the different detector supports and structural elements. Right: Close-up of the ^{204}Tl sample as included in the WF and capture simulations, with traces of photons (green) and secondary electrons (red) emitted in a simulated capture event.*

is shown in Figure 5.1. The deposited energy distribution in the sensitive volume of the detectors was obtained for a set of gamma rays from 0 to 8 MeV, in the case of ^{203}Tl and ^{197}Au. For ^{204}Tl, the simulation covered 0 to 9 MeV, owing to the higher neutron separation energy of 7.546 MeV of the latter. The increment in the photon energy was of 50 keV, and thus a total of 160 response functions were obtained for the first two samples, and 180 for the ^{204}Tl case. The response functions were recorded in histograms with a bin size of 10 keV, and the maximum energy recorded was 9 MeV for ^{197}Au and ^{203}Tl, and 10 MeV for ^{204}Tl.

For each gamma ray energy, 10^7 photons were emitted sequentially, with the point of emission in the sample determined, in the radial axis, by a gaussian distribution to match the neutron beam profile. In the beam axis, photons were emitted following a negative exponential distribution, in order to take into account the *self-shielding effect*, which is the reduction of the beam intensity due to the neutrons already captured or scattered in the sample. As outlined in chapter 2, the use of a relatively thick sample with a high Z, and the lead foils placed in front of the detectors, were the main challenges in this particular WF calculation. Both could increase dramatically the absorption of gamma rays, especially at low energies. In

order to evaluate the impact of each factor separately, the set of response function were obtained also for the case without the shields, and for the ^{197}Au and the ^{203}Tl samples. It is assumed that the self-absorption effects were similar between the ^{203}Tl and the ^{204}Tl-enriched sample.

In Figure 5.2, three comparisons have been drawn. In the first two plots, the response functions for the cases of the gold sample, with and without the foils, are shown. In the middle, those for the gold and thallium sample, without the foils; and in the bottom ones, the same, but with the foils in place. In the first case, the effects caused by the shield can be clearly observed. The reduction in the C_6D_6 detection efficiency of a 150 keV gamma is very large, from 2.9% down to 0.07%, a factor of 40. However, the efficiency quickly increases to 0.7% for 250 keV gamma rays, and for 1 MeV photons almost equals to the non shielded case, 1.5% vs 1.7%. This is explained by the fact that between 0.1 MeV and 1 MeV, the γ-ray absorption coefficient of lead and thallium drops by more than two orders of magnitude. Finally, beyond 5 MeV, the efficiency is actually higher when employing the foils. This is ascribed to a substantial pair-production in the foils, evidenced in the much higher 0.511 MeV Compton edge counting rate, and the reduced Compton edge associated to the full energy peak. Thus, the foils act as "converters" of higher energy γ-rays into lower energy ones, for which the detection efficiency is higher, smoothing the overall deposited energy spectra.

The effect produced by the ^{203}Tl sample is basically the same, albeit less pronounced. All in all, the effect of the shield dominates and thus the efficiency for both samples is similar (see bottom panels in Figure 5.2). At low energies, the added contribution of the self-absorption of capture gamma rays in the thallium sample reduces the efficiency to only 0.04%.

5.2   The Weighting Function

The weighting function was calculated with both the numerical and the polynomial methods in order to study the performance of the different approaches in our particular case. Only weighting functions calculated for the setup with the lead foils will be discussed in the following, since they were part of the final setup of the experiment.

An example of both types of WF is represented in Figure 5.3, for the case of
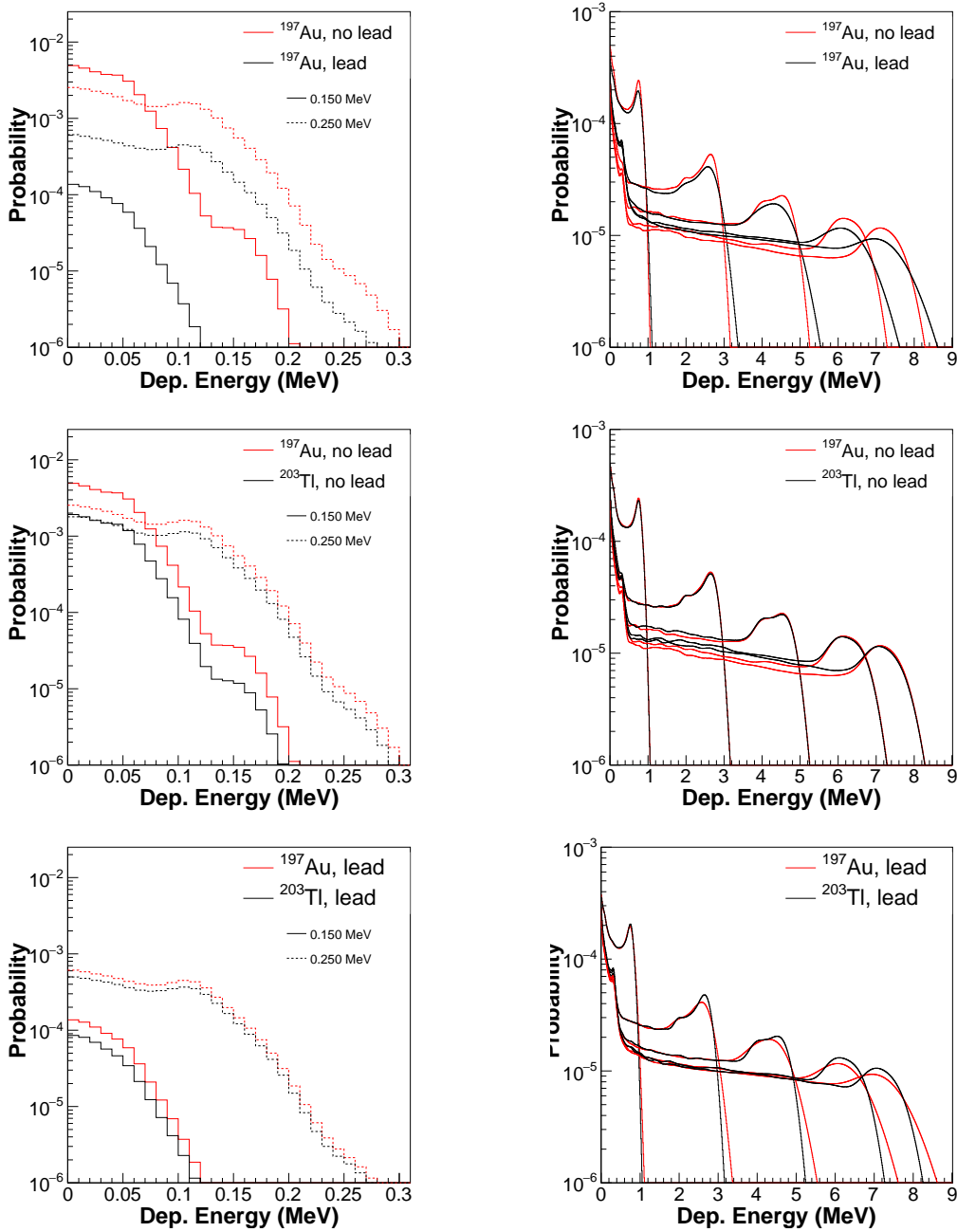
Figure 5.2: *Comparison of the RF of $C_6D_6\#1$ to the γ-rays emitted by the ^{197}Au sample with and without lead foils (top plots), ^{197}Au and ^{203}Tl without the foils, and ^{197}Au and ^{203}Tl with them. The γ rays shown are those of 0.15 and 0.25 MeV (left plots) and 1, 3, 5, 7 and 8 MeV (right plots)*

^{203}Tl sample and $C_6D_6\#1$. The regularization parameter λ was chosen as to have only positive weights (see section 2.4), which also led to a smoother function. For comparison, a numerical weighting function with a tighter constrain on the χ^2 is also plotted, showing pronounced oscillations. A polynomial of fifth order was employed for the calculation of AWF.

The goodness of the WF can be quantified by calculating the ratio

$$\frac{\sum_i W_i R_{i,j}}{E_j^\gamma} \tag{5.2.1}$$

for every gamma ray energy E_j^γ. In the ideal case of a perfect WF, the ratio should be unity for every E_j^γ. The results of the test for both the numerical WF (NWF) and the analytical WF (AWF), obtained for $C_6D_6\#1$ and the ^{203}Tl sample, are plotted in Figure 5.4. Above 500 keV, the accuracy of the NWF is remarkable, with an RMS of 0.3%. In comparison, the AWF shows more pronounced oscillations, and a worse RMS of 1%. Between 150 keV and 500 keV, even though the numerical still outperforms the polynomial, its accuracy also decreases notably. Finally, below 150 keV, both weighting functions fail similarly to reproduce the proportionality condition.

The overall RMS error is 14.8% for the AWF and 12% for the all-positive NWF, which represents a moderate improvement of 19%, but still a very high value. It must be noted that with the lower χ^2 NWF also represented in Figure 5.3 (dotted line), the RMS is reduced to 5.6%. The accuracy of both NWF in determining the number of capture cascades will be compared in section 5.3.2. A comparison of the detector efficiency before and after applying the corresponding NWF to the ^{197}Au and the ^{203}Tl samples is shown in Figure 5.5.

An important conclusion drawn from this comparison, is that, despite the fact that the proportionality condition fails below 250 keV, the weighted efficiency is very similar for both samples. That means that, when the correction for the missing cascades below threshold is calculated, the bias introduced by the weighting function will be similar for both samples. Therefore, provided the ^{203}Tl yield is normalized to that of ^{197}Au the effect should largely cancel out. Given the overall best performance of the NWF, it was the one employed for all the samples in the final analysis.
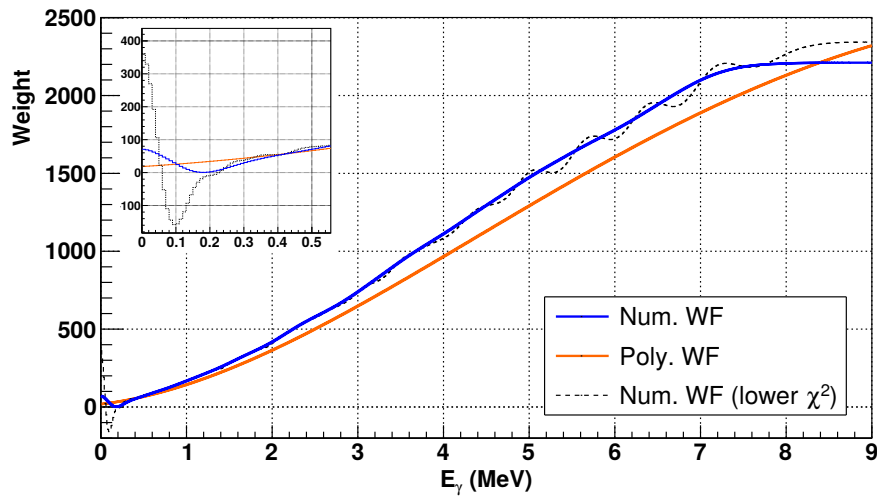
Figure 5.3: *Plot of the Numerical WF (blue), the polynomial WF (orange), and the Numerical WF with a tighter constraint on the χ^2.*
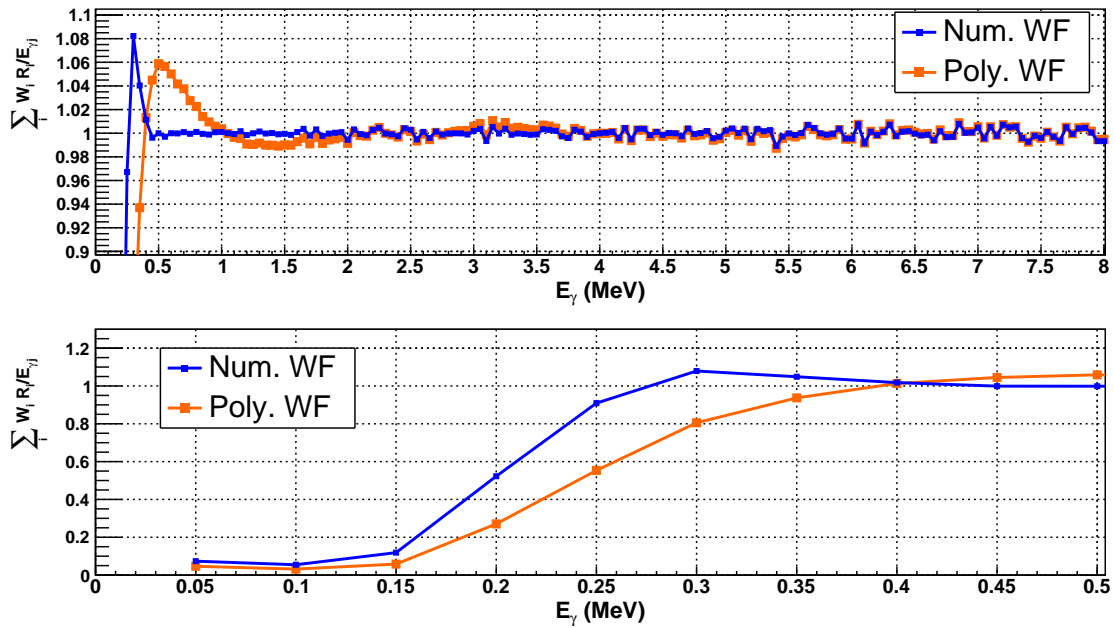
Figure 5.4: *Top: Comparison between the residuals of the numerical WF (in blue) and the analytical or polynomial (in orange). Bottom: same as top, in the energy range from 50 keV to 500 keV.*
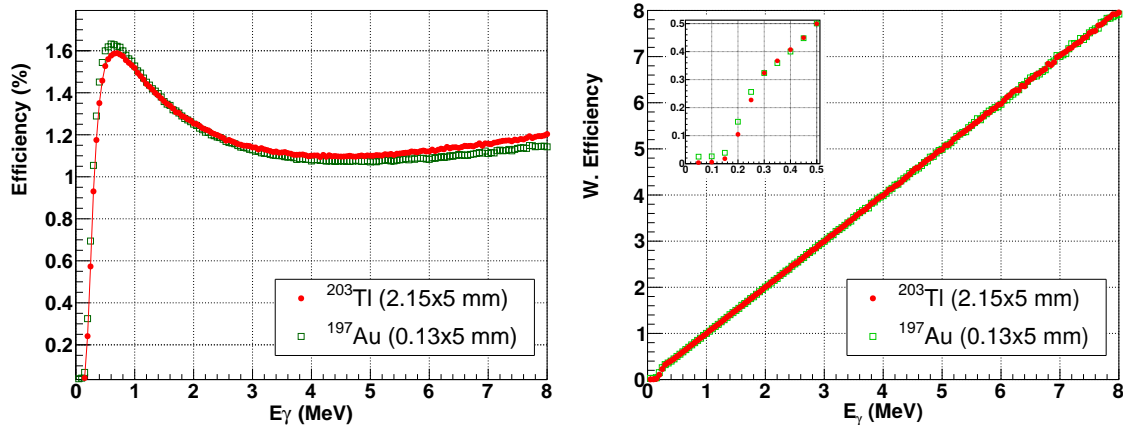
Figure 5.5: *Left: detection efficiency of $C_6D_6\#1$ for gamma rays from 50 keV to 8 MeV. Right: weighted efficiency in the same range.*

5.3 Simulations of the capture cascades

5.3.1 Capture cascades generator

De-excitation capture cascades were generated by means of the code CAPTU-GENS, which is based on the code reported in Ref. [108]. CAPTUGENS works by splitting the capture cascade in two parts, as it is represented in Figure 5.6:

- In the lower range of excitation energies, from the ground state up to a certain cut energy E_{cut}, the level scheme is composed by levels for which the energy, spin, and the transition energies and probabilities are known experimentally. Such data is obtained from nuclear structure databases, as ENSDF [109].

- At excitation energies higher than E_{cut}, and up to the neutron separation energy level E_C, the energy level scheme is derived from level density parametrizations (LDP), and the gamma ray transitions are calculated from parametrized photon strength functions (PSF).

Several models of the level density parametrization exist, and in the code were incorporated the Constant Temperature (CT), and the Back-shifted Fermi Gas Model (BSFG) [110], and a combination of both, known as the Gilbert-Cameron formula (GC) [111]. The BSFG was the one employed in this work.

The electromagnetic transitions included in the code are the Giant Electric Dipole Resonance (E1 GDR), the Giant Magnetic Dipole Resonance (M1 GDR),

and the E2 Giant Quadrupole Resonance (E2 GQR). Many types of PSF exist to describe the electromagnetic transitions, of which the Single Particle, Lorentzian and Generalized Lorentzian are featured in the program. The latter was the one employed for the E1, and the standard Lorentzian for the M1 and E2. The expressions for each PSF were adopted from Kopecky and Uhl [112]. For some nuclides, a better description of the E1 transition is obtained if a second small resonance, commonly called "pigmy" resonance, is included in the PSF. For this reason, the option to add a second (Generalized) Lorentzian is also available in CAPTUGENS.

An important feature of the code is the inclusion of the Conversion Electron (CE) process. In this, an electromagnetic transition is substituted by the release of one ore more atomic electrons. The CE process is more relevant at low transition energies, closer to the binding energies of the K, L and M shell electron bands. In order to include the CE process in the generation of the cascades, the energy of the different electron shells, the fluorescent yields and the internal conversion coefficients (ICC) must be introduced.

Figure 5.6: *Scheme of the MC cascade generation method employed in CAPTUGENS.*

Once the full excitation level scheme is produced, cascades are generated by Monte Carlo sampling, starting from the excitation energy corresponding to the capture energy $E_C = S_n + E_n$ of the compound nucleus. The output of the code is a file with the number of photons (and CE electrons, if present) emitted in each cascade, and the energy of each particle. This file can be directly used as input in simulations of the capture setup.

5.3.2 Uncertainty of the WF: weighted sum of cascades

The accuracy of the PHWT can be assumed to be 2% or better [67], if the uncertainty ascribed to the WF used to weight the capture events is negligible and well under control. Hence, for a setup involving elements that affect considerably the response functions of the detectors, it is important to evaluate the uncertainty of the WF.

To this aim, the previous Geant4 model was employed to simulate the emission of capture cascades. The total energy of the cascade is always E_C, so the sum over the k number of gamma rays of a large number N of cascades will be given by $\sum^k E_k^\gamma = NE_C$. The time scale of the de-excitation process is much lower than the time resolution of our detection system, and thus we can assume that the gamma rays of each cascade are emitted simultaneously.

For each detector, the corresponding response function histogram to the sum of all the gamma rays would be $R_C = \sum_k R_{i,k}$, with i representing the i-bin of the histogram. If W_i is the weighting function calculated for this setup, by the PHWT principles it should be fulfilled that

$$\sum_k \sum_i W_i R_{i,k}^\gamma = \sum_k E_k^\gamma = NE_C \tag{5.3.1}$$

$$\sum_i W_i R_i^C = NE_C \tag{5.3.2}$$

It derives that any deviations of the weighted sum $\sum_i W_i R_i^C$ from NE_C can be understood as the error introduced by the weighting function W_i. Equation (5.3.1) –which in the following shall be referred to as the *weighted sum of cascades test* or WSCT– is a very powerful tool. It can be used to estimate, by means of the capture cascade simulations, the impact of many sources of systematic error, which otherwise would be very difficult to quantify experimentally.

The accuracy of the weighting function was tested for each sample, and each detector, employed in this analysis, with the results summarized in Table 5.1. A similar average accuracy of around 1% was achieved for all samples. In addition, differences in each detector, between the [197]Au and [203]Tl samples, and between the [203]Tl and the [204]Tl enriched sample, were always below the 1% level. Thus, we concluded that the use of the PHWT did not introduce any significant bias in the determination of the capture yields.

Sample	$C_6D_6\#1$	$C_6D_6\#2$	$C_6D_6\#3$	$C_6D_6\#4$
^{197}Au	0.982(1)	0.995(1)	0.990(1)	0.989(1)
^{203}Tl	0.989(1)	0.993(1)	0.991(1)	0.992(1)
^{204}Tl	0.995(1)	0.990(1)	0.992(1)	0.986(1)

Table 5.1: *Weighted sum of cascades obtained for the four C_6D_6 detectors, for the ^{203}Tl and ^{197}Au samples.*

Finally, differences between the NWF represented in Figure 5.3, which employed different regularization parameters, were studied. Improvements of $0.3\% - 0.7\%$ were randomly found when employing the low χ^2 solution, which had a much lower RMS at low gamma ray energies. It was concluded that the contribution of medium to high energy gamma rays in the cascade is clearly dominant, and in that region, both NWF offer similarly good results. Therefore, the always positive solution was the one employed in the final analysis.

5.4   Estimation of systematic errors

A detailed description and quantification of the most important sources of systematic errors which can be evaluated employing the WSCT is provided below.

5.4.1   Correction for the lost cascades under the digital threshold

A large number of gamma ray interactions in the C_6D_6 deposit a small energy. Consequently, a sizeable amount of capture events will deposit energy below the digital threshold. This leads to a reduction in the measured counting rate. In order to account for all those missing counts, a correction factor, F_{th}, must be applied. Because of the normalization to a reference sample, it is necessary to know the correction factor for both the sample under analysis, and the normalization sample. This is because their capture spectra might have different deposited energy distributions, and thus the number of cascades lost under the threshold could vary

accordingly. The correction factor F_{th} is given by

$$F_{\text{th}} \equiv \frac{\sum\limits_{i=0}^{\infty} W_i R_i^C}{\sum\limits_{i=\text{th}}^{\infty} W_i R_i^C}, \qquad (5.4.1)$$

where $\sum\limits_{i=0}^{\infty} R_i^C$ is the full detector response to the simulated cascades, and $\sum\limits_{i=\text{th}}^{\infty} R_i^C$ is the response truncated by the threshold, being $i = th$ the histogram bin corresponding to the threshold energy E_{th}.

The final threshold correction factor to the yield , defined as f_{th}, is expressed as

$$f_{\text{th}} = \frac{F_{\text{th}}^A}{F_{\text{th}}^R} \qquad (5.4.2)$$

where A refers to the sample under analysis, and R to the reference normalization sample.

5.4.2 Correction for internal conversion electrons (CE)

In a minority of cases, the energy of a de-excitation transition is released by the emission of an electron from the innermost shells of the atom, instead of a gamma ray. It is followed by the emission of a low energy X-ray, due to electron shell reconfiguration. The involved transitions are of low energy (< 300 keV), and thus the CE process leads to a moderate decrease in the number of very low energy gamma rays emitted. On the other hand, most of the internal CE are stopped in the sample itself or in the detector case, depositing very low energy in the detectors, or none at all. In this way, a certain number of cascades will go undetected, leading to an underestimation of the capture yield.

In order to better isolate the contribution of the CE, simulations of the setup were performed without the lead shields. The effect was quantified with the ratio

Sample	$C_6D_6\#1$	$C_6D_6\#2$	$C_6D_6\#3$	$C_6D_6\#4$
^{197}Au	1.015(1)	1.019(1)	1.012(1)	1.020(1)
^{203}Tl	1.019(1)	1.012(1)	1.020(1)	1.012(1)

Table 5.2: F_{ce} factors of the four C_6D_6 detectors, for the ^{203}Tl and ^{197}Au samples.

$F_{ce} = \sum_i W_i R_{i,noce}^C / \sum_i W_i R_{i,ce}^C$, where $R_{i,ce}^C$ and R_{noce}^C are the simulated response function to 10^7 cascades generated with and without conversion electrons. The results are reported in Table 5.2. The missing cascades due to IC electrons are at most 2% of total, averaging 1.6% for both the ^{197}Au and the ^{203}Tl samples. Interestingly, the proportion of energy emitted only by gamma rays is $\sum^k E_k^\gamma / E_C = 0.985$. This matches exactly the previous correction due to conversion electrons, and consequently the ratios $\sum_i W_i R_{i,ce}^C / \sum^k E_k^\gamma$ are very close to unity. We deduce that virtually none of the emitted electrons deposit energy in the detectors, and thus it is confirmed that the energy of those transitions is effectively lost.

5.4.3 Gamma ray summing in each detector

One of the principles of the PHWT is that at most one gamma ray of the cascade is detected per capture event. It is possible, however, that more than one gamma ray of the same cascade is detected at the same time and in the same detector, a phenomenon known as gamma ray summing. In such event, the registered energy deposition of the two –or more– gamma rays is added, and is weighted correspondingly. Although the probability of such an event is very low due to the intrinsic low efficiency of our whole detection setup, it is still convenient to quantify the overestimation in the yield caused by this effect, and correct for it. This can be done by obtaining the weighted response functions to all the gamma rays emitted sequentially by the 10^7 cascades, and comparing it to the simultaneous emission case. Any excess over unity of the ratio $F_{sim} = \sum_i W_i R_{i,sim}^C / \sum_i W_i R_{i,seq}^C$ shall be ascribed to γ-summing events. In order to isolate the summing effect from other possible sources of error, the simulations were performed with a setup that did not include the lead shields or IC electrons. In Table 5.3, the ratios F_{sim} of the four C_6D_6 detectors are listed, for the ^{203}Tl and the gold samples. The correction averages 0.5%, and it is $\leq 0.7\%$ in all cases.

Sample	C_6D_6#1	C_6D_6#2	C_6D_6#3	C_6D_6#4
^{197}Au	1.004(1)	1.006(1)	1.003(1)	1.007(1)
^{203}Tl	1.002(1)	0.999(1)	1.002(1)	1.006(1)

Table 5.3: F_{sim} factors of the four C_6D_6 detectors, for the ^{203}Tl and ^{197}Au samples.

5.4.4 Summing between detectors

The multiple cascade detection can happen also between different detectors. This effect can be directly evaluated trough the MC simulations of a large number of cascades, simply by counting coincidences between two detectors for each event. In this way, the probability of multiple detection of the same cascade by different detectors was estimated to be of 1.2% for gold, and 0.5% for ^{203}Tl. The differences can be attributed to the higher multiplicity of the gold cascade, and its softer cascade spectrum. If C_w is the total counting rate of the four detectors, and P_c the coincidence probability, we have that the corrected counting rate is

$$C'_w = C_w(1 - P_c/2) . \tag{5.4.3}$$

The correction to the counting rate is 0.997 for ^{203}Tl, and 0.994 for ^{197}Au. Thus, the final correction to the normalized ^{203}Tl yield would correspond to 1.003. This is almost ten times less than the accuracy of the whole weighting procedure, and hence it will not introduce any significant bias in the final results.

Detector cross-talk

Finally, a multiple detection event can also take place due to backscattered photons from one detector to another, an effect called detector *cross-talk*. This effect is already taken into account in the simulations of the detector response functions performed to obtain the WF, which include all detectors.

5.5 Global correction factor

It is convenient –and more realistic– to define a global correction factor, which includes all the corrections described in the above list. In line with previous definitions, this factor, F_{glob}, is defined as

$$F_{glob} = \frac{\sum_i W_i R^C_{i,noce,noth}}{\sum_i W_i R^C_{i,ce,th}}, \tag{5.5.1}$$

with the correction factor applied to the yield of the sample under analysis,

$$f_{\text{th}} = F^A_{glob}/F^R_{glob} . \tag{5.5.2}$$

The specific global correction factors for the ^{203}Tl and the ^{204}Tl measurements are reported and discussed in the respective analysis chapters 6 and 7.

5.6   2D Weighting function

As it has been explained in section 5.1.1, the self-absorption of the cascade gamma rays in the sample is already considered in the sim- ulations of the response functions. Although acceptable as a first approximation, in real- ity the self-absorption depends on the depth of emission of the γ-rays in the sample.

Figure 5.7: *Probability of γ-ray emis- sion as a function of the depth of emis- sion, for very different capture cross sections. Figure extracted from [61].*

It can be seen in Figure 5.7 that the gamma ray emission probability across the sample thickness is very dependent on the cross section. In a strong resonance, the high cross section implies that most of the cap- tures will be produced in the very first few μ of sample thickness. Instead, for low cross section resonances, captures will be much more homogeneously distributed along the sample. Considering that the four C_6D_6 detectors are positioned on the side of the incoming neutron beam, the self-absorption will be more pronounced for low cross section resonances.

Therefore, to account for all the possible depths of emission of the gamma rays, it would be necessary to calculate a weighting function –with the corresponding response functions– ideally for each possible value of the cross section. However, the usual procedure is to consider only the case of either a high or a low cross section resonance.

In the end, whether the single depth of emission approximation is good enough depends on the physical characteristics of the sample material, namely density and atomic number. For low Z or low density materials, the photon self-absorption will be low in general, whatever the emission profile is. On the other hand, in materials with low capture cross sections the gamma emission profile will be mostly homo- geneous along the sample, and self-absorption will be similar for all resonances. Therefore, the effect can be relevant for specific nuclides, which have both a high

Figure 5.8: *Left: ghe bidimensional weighting function calculated for the ^{203}Tl measurement. Right: projection of the 2DWF of the highest and lowest cross section cases.*

Z and high cross section resonances. This is exactly the case for ^{203}Tl and also for ^{204}Tl, as predicted by the evaluations.

However, simulating all response functions for every cross section value was not feasible, and thus it was necessary to perform an approximation. This consisted in calculating the WF only for the two extreme cases: a high cross section and a low one. The rest of weighting functions were obtained interpolating (or extrapolating) linearly using the evaluated cross section data from ENDF/B-VIII.0. In this way a bidimensional Weighting Function (2DWF) is obtained, which includes the additional dependency on the capture cross section. A plot of the 2DWF can be seen in Figure 5.8. The 2DWF has been projected in the E_γ axis, for the illustrative cases of the low and high cross sections.

In the present work, the 2DWF was employed only for the ^{203}Tl measurement, owing to the exact knowledge of its physical properties. However, it was not used in the ^{204}Tl analysis, due to the limited knowledge of the geometry and capture cross section. The methodology of the 2DWF can be especially useful for the analysis of stable, thick samples, like the natural Tl sample employed in the ^{205}Tl(n, γ) measurement performed at n_TOF in 2018 [45].

Chapter 6

^{203}Tl capture cross section measurement

In this chapter we will cover in detail the ^{203}Tl(n, γ) measurement and the subsequent data analysis, which will follow the general procedure described in Chapter 4. Owing to the fact that the mass and the size of the sample are accurately known, one can effectively apply the gold saturated resonance method, and thus systematic uncertainties can be kept under control. This is essential in order to extract reliable resonance parameters, which will be used in the posterior ^{204}Tl(n, γ) analysis.

6.1   Experiment

The sample used for the experiment was a cylindrical pellet of Tl$_2$O$_3$, measuring 5 mm in diameter and 2.15 mm in thickness, with a total mass of 260 mg. It was enriched up to 99.5%, and thus the content of ^{203}Tl was 232 mg. The main motivation for using such a small sample was to have it identical to the one that was irradiated in the reactor for the ^{204}Tl enrichment. The capture measurement was performed in two blocks of runs, separated by 14 days, including a long data taking with the ^{204}Tl enriched sample in between. Right after the ^{203}Tl data acquisition, capture on the gold sample was measured for yield normalization. Two main sets of energy calibrations with γ-rays were conducted: one just before the ^{203}Tl was put in beam, and one right after the gold runs.

A summary of the different data acquisition runs for the ^{203}Tl measurements

	^{203}Tl	^{197}Au
Mass (mg)	232.3(1)	50.0(1)
Enrichment (%)	99.5	Pure
Diameter (mm)	5.05(1)	5.01(1)
Thickness (mm)	2.15(1)	0.13(1)
Atomic thickness (at./barn)	$1.72(1) \cdot 10^{-3}$	$7.79(3) \cdot 10^{-4}$
Protons	$6.27 \cdot 10^{17}$	$2.03 \cdot 10^{17}$
Runs	102141-102147	102308-102311
	102280-102307	102314-102319

Table 6.1: *Summary of the beam statistics allocated to the ^{203}Tl and the ^{197}Au samples in the ^{203}Tl(n,γ) measurement.*

	^{nat}C	^{nat}Pb	Empty frame
Protons	$1.69 \cdot 10^{17}$	$2.46 \cdot 10^{17}$	$2.40 \cdot 10^{17}$
Runs	102342-102351	102326-102341	102098-102100, 102257-102266
			102274-102277

Table 6.2: *Summary of the statistics for the samples used for estimating the background for the^{203}Tl(n,γ) analysis.*

is presented in Tables 6.1 and 6.2. The total amount of protons for the whole set of measurements were $1.59 \cdot 10^{18}$, of which $6.27 \cdot 10^{17}$ were allocated to the ^{203}Tl sample. Considering an average daily beam delivery of $1.1 \cdot 10^{17}$ protons at n_TOF, that quantity corresponds to approximately 5.5 days of full beam. Background measurements amounted to $6.54 \cdot 10^{17}$ protons, distributed among different samples:

- Empty frame: An aluminium support ring with a thin layer of mylar foil attached to it. It is identical to the support employed for the ^{203}Tl sample. These runs were used to estimate the background caused by the presence of the beam.

- ^{nat}Pb: A lead sample with natural isotopic composition, with the same geometry as the ^{203}Tl sample. These runs were used to estimate the additional

background caused by in-beam gamma rays scattered by the sample. Lead is
employed due to its high density and high Z, similar to thallium.

- ^{nat}C: A graphite sample, with identical geometry. Used to evaluate the gamma
  background arising from neutron scattered in the sample. These neutrons,
  after being thermalized in the experimental area structures and walls, are
  finally captured, producing additional background gamma rays.

6.2   Data reduction

6.2.1   Initial calibrations

The ^{203}Tl measurement was split in two blocks, with a long ^{204}Tl data taking in
between. Thus, it was necessary to perform a careful analysis of the data, in order
to identify possible effects in the detectors caused by the high counting rate of the
^{204}Tl sample activity or other similar experimental effects.

The first basic step in the data reduction was the time-of-flight to neutron en-
ergy calibration of the facility, a procedure described in detail in section 4.2. Once
a time to energy calibration was obtained, a preliminary sorting of the data was
done to check the consistency between the data from dedicated and parasitic pro-
ton bunches. A comparison of the counting rate spectra produced by both types of
beam can be seen in Figure 6.1. A prominence with higher counting rate than the
background, from 600 and 900 eV, can be seen in the parasitic spectrum, which
is clearly not present in the dedicated data. This disturbance was probably due
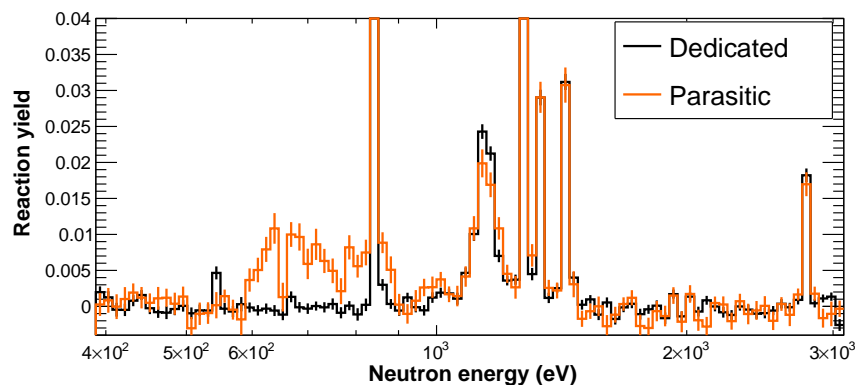
Figure 6.1: *Reaction yield comparison between the parasitic and the dedicated data.*
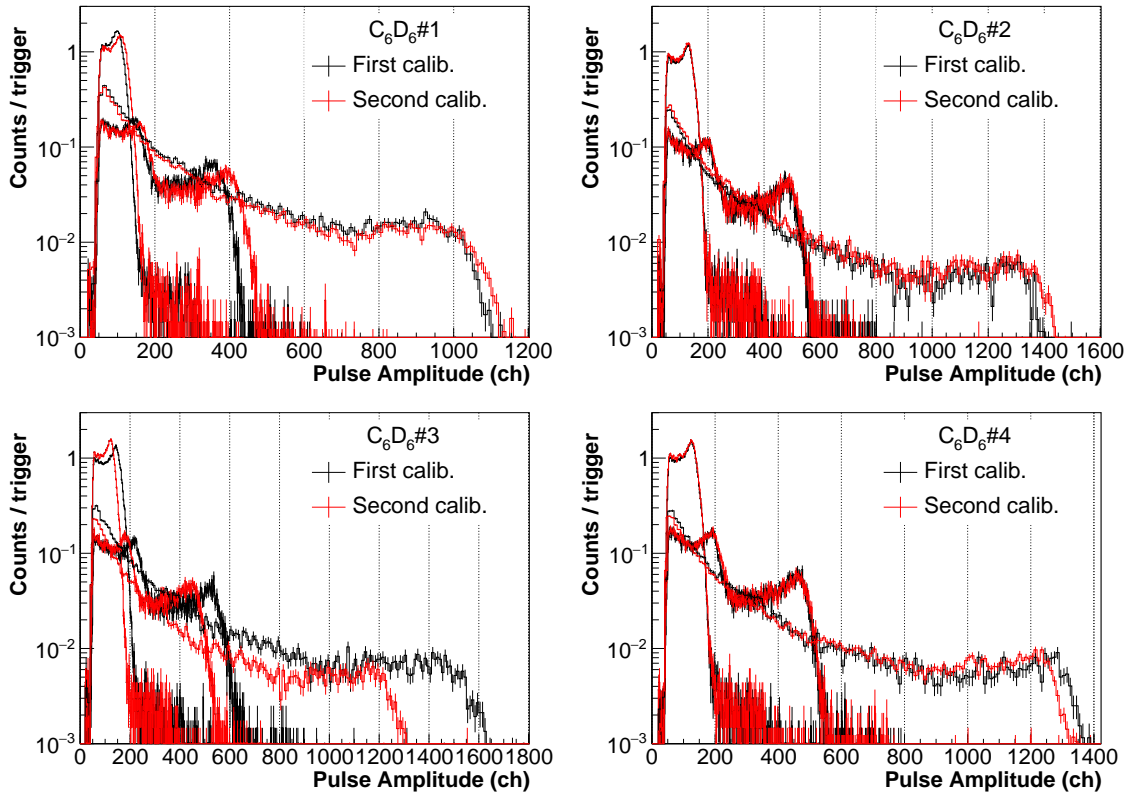
Figure 6.2: *Deposited energy spectra of the three calibration sources employed in the two full calibrations of the $^{203}Tl(n,\gamma)$ measurement in the four C_6D_6 detectors.*

to a wrong determination by the PSA of the time stamp for the gamma-flash of parasitic bunches of low intensity. However, it was not possible to improve the PSA performance to overcome such effect. To prevent any bias in the cross section due to this structure, it was decided to exclude parasitic data for the final analysis, leaving the final proton statistics at $5.1 \cdot 10^{17}$. The next essential step in the analysis was calibration in deposited energy for the C_6D_6 detectors. In Figure 6.2 it is shown the raw amplitude spectra of three calibration sources, as measured by the four C_6D_6 detectors, for the two main calibrations performed during the measurement. Whereas $C_6D_6\#2$ shows a rather stable behaviour, there is a pronounced increase in gain of $C_6D_6\#3$. Besides, the variation increases with the deposited energy, from 14% at low energies ,up to 22% at the 4.4 MeV energy of the Am-Be. $C_6D_6\#1$ showed variations of the gain as well, although much less pronounced than in $C_6D_6\#3$, while $C_6D_6\#4$ was very stable. A possible explanation to this
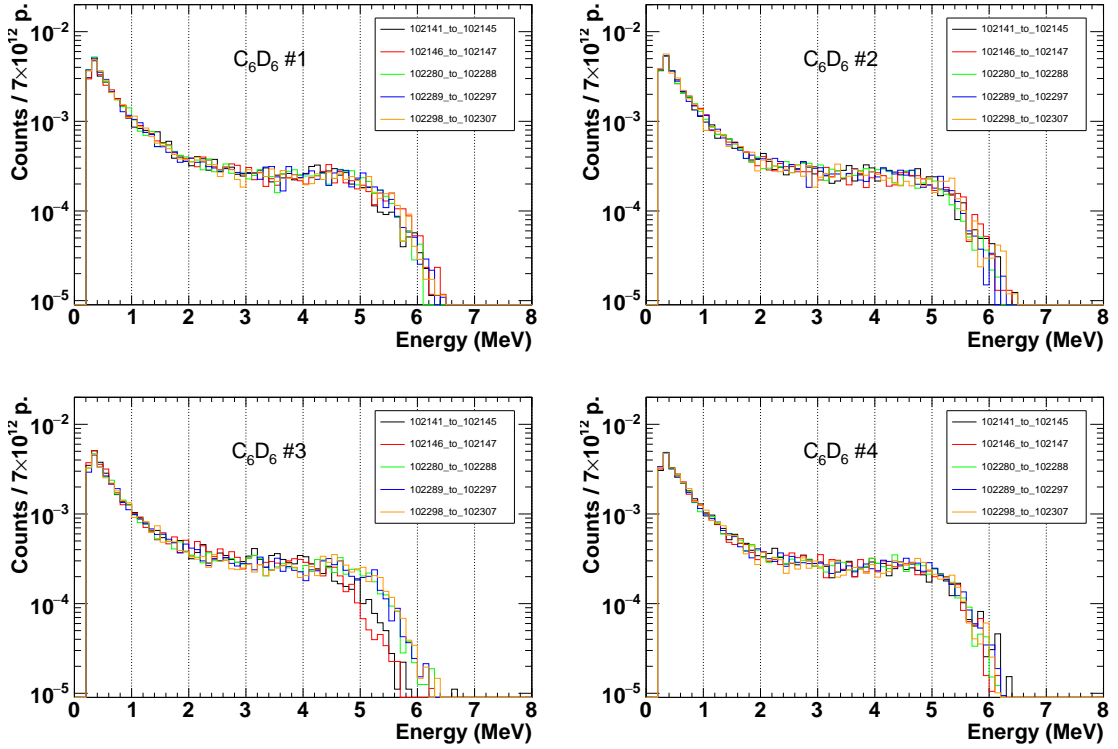
Figure 6.3: *Energy deposition in the four C_6D_6 detectors, for different runs along the measurement.*

behaviour could be the stability issues found in the HV power supply that powered the C_6D_6#1 and #3. Issues with the gain could also explain the abnormally huge number of counts seen in both detectors in some isolated runs during the measurement. Incidentally, this power supply failed a few days after the end of the ^{204}Tl(n, γ) campaign.

6.2.2 C_6D_6 performance monitoring

The calibration of the C_6D_6 detectors allowed to investigate the gain stability of the four C_6D_6 detectors along the whole data acquisition. This was done by comparing the energy deposition, in the resonance at 236 eV, at different times during the measurement. A satisfactory agreement was found for all detectors but C_6D_6#3. As it can be observed in Figure 6.3, its deposited energy spectrum shows significant fluctuations in the first runs of the measurement. To avoid a systematic

bias in the data analysis due to this effect, it was decided to discard all $C_6D_6\#3$ data recorded from run number 102141 to 102147. Following the monitoring of the gain, the stability of the counting rate along the measurement was checked for all detectors, as can be seen in Figure 6.4. In order to reduce statistical fluctuations, signals are integrated over 100 proton bunches. To exclude as much background as possible, it is convenient to consider only counts coming from the time-of-flight window of interest for the analysis. In the case of ^{203}Tl, a time-of-flight window was selected that covered the range of the resolved resonance region, up to 35 keV. For the gold sample, one is mainly interested in the yield at the saturated resonance, and therefore, the window was set at the 4.9 eV resonance. By comparing the different counting rates, it can be seen that, between the first $\sim$20000 events and the rest of the campaign, there is a discrepancy in the average beam intensity delivered and the value reported by the BCT. The difference is clearly visible in all four C_6D_6 detectors, which discards any issue with the detectors or the SiMon. In fact, the C_6D_6/SiMon ratio is considerably stable during all the measurement. The variation was also noticeable in the PKUP monitor.

The discrepancy was further investigated by comparing the SiMon/BCT ratio for different samples of the campaign. In the bottom plot of Figure 6.4, the ^{203}Tl ratio is compared to that of ^{197}Au and ^{nat}C. The ratio of gold matches the ratio for the second bunch of ^{203}Tl runs, while the ^{nat}C matches exactly that of the first ^{203}Tl runs. In this situation, a beam intensity renormalization factor f_{si}, described in section 4.5, was employed to normalize the SiMon/BCT ratio of all samples to that of ^{197}Au. In practice, the factors, which are listed in Table 6.3, are applied directly to the counts registered in each detector during the data sorting.
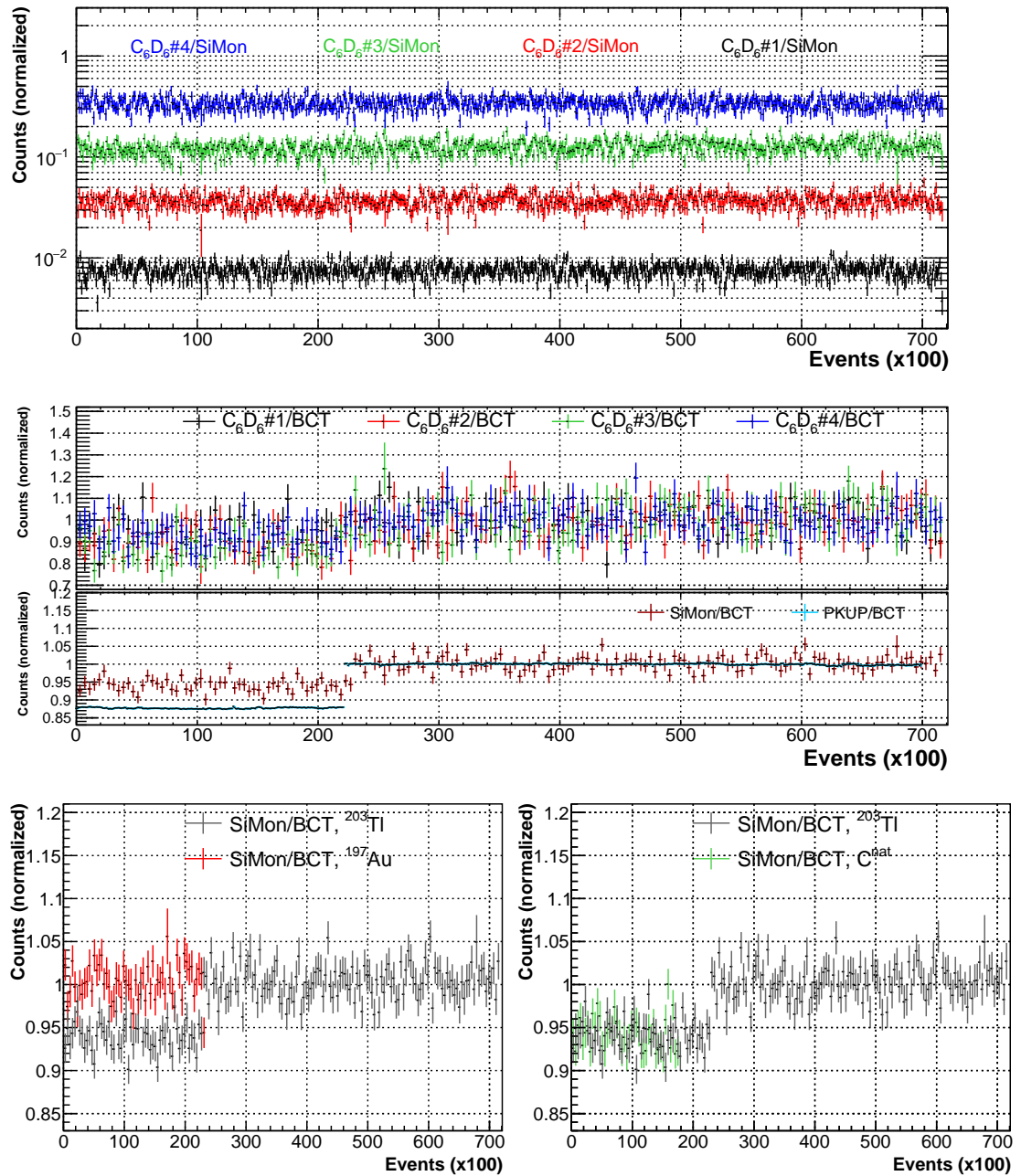
Figure 6.4: *(Top) Counting rate for the C_6D_6 detectors and the monitoring devices during the $^{203}Tl(n,\gamma)$ data taking. (Middle) Ratio between C_6D_6 detectors and the SiMon counting rate for the measurement. (Bottom) The SiMon/Proton Intensity ratio for the ^{203}Tl run, compared to the gold and the ^{nat}C, which has been used as the background sample.*

Sample	f_{si}	Runs
^{203}Tl	1.065	102141 to 102147
	1	102280 to 102307
^{197}Au	1	all
^{nat}Pb	1.069	all
^{nat}C	1.064	all
Empty frame	1.074	all

Table 6.3: *Summary of the beam statistics of the f_{si} factors employed in the ^{203}Tl(n,γ) analysis.*

6.3 Simulations of the ^{203}Tl(n,γ) capture cascades

As explained in section 5.3, simulations of the capture cascade must be performed to account for some relevant experimental effects that are not included in the saturated resonance method. The capture cascade generator employed works by splitting the cascade into two parts. The low energy part corresponds to the range of excitation energies where levels are experimentally known. The high energy part is included by means of a statistical nuclear model. The transition from one regime to the other is defined by an energy cut value, E_{cut}. The choice of E_{cut} requires a careful study of all the information available on the excited energy levels and emitted gamma rays of the compound nucleus, as it is described below. A measurement of the gamma ray capture spectrum of natural thallium was performed
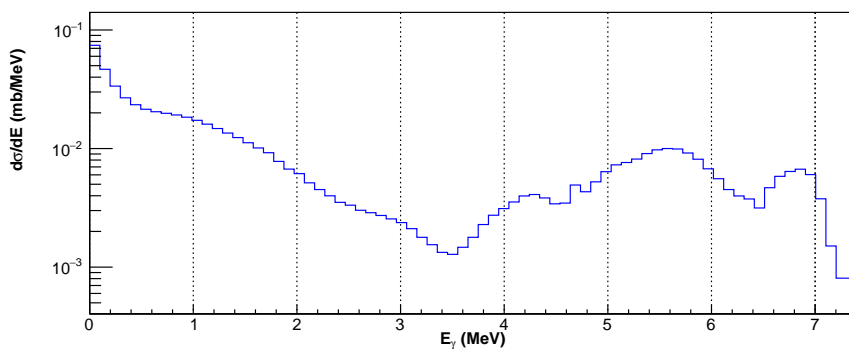
Figure 6.5: *Prompt gamma ray spectrum following the capture of 0.5 MeV neutrons in ^{nat}Tl as measured in Ref. [113].*

by Voignier et al. [113]. The resulting distribution showed an uncommon shape, as can be seen in Figure 6.5. It features a deep valley between 2 and 5 MeV, a small peak around 4.5 MeV, and then a prominent peak close to 7 MeV. This spectrum can be compared to the deposited energy spectrum in the C_6D_6 for the measurement at n_TOF(Figure 6.6). The comparison is only qualitative, because of the presence of ^{205}Tl capture gamma rays, and the different response function of C_6D_6 detectors and the Compton-suppressed NaI detectors employed in Ref. [113]. Nevertheless, the flat behaviour of the C_6D_6 response function between 2 and 5 MeV seems compatible with the low number of gamma rays between those energies.

For the discrete part of the capture cascade of the ^{203}Tl(n,γ) reaction, the experimental data provided in the ENSDF database was employed, which is based on the results of a thermal neutron capture experiment conducted at the Budapest reactor facility [114]. This is, most probably, the source used by the RIPL-3 database as well (Capote et al. [115]), since both databases are almost identical. Up to the level at 1.74 MeV information on energy levels, photon transition energies and intensities, is provided in both databases. Beyond that energy, there are several additional levels listed in both, but there is almost no information about transition gamma rays and probabilities, except for the full neutron separation energy at 6.656 MeV [101]. For the statistical part of the cascade, the Fermi Back-Shifted Gas model (FBSG) was chosen. The values of the main parameters of the model, which are the level density, a, and the shell correction energy, δ_{eff}, are listed in Table 6.4.

The performance of the model can be evaluated by calculating the total cumulative number of levels, N_l, as a function of the excitation energy U, and comparing it to the experimental value. The N_l between 0 and a certain U_0 is calculated by integrating the level density $\rho(U)$,

$$N_l = \int_0^{U_0} \rho(U)dU \ , \tag{6.3.1}$$

where $\rho(U)$ is the parametrization adopted by Dilg et al. [110]:

$$\rho(U) = \frac{1}{12\sqrt{2}} \frac{1}{\sigma a^{1/4}} \frac{\exp\left[2\sqrt{a(U - \delta_{eff})}\right]}{(U - \delta_{eff} + t)^{5/4}} \ . \tag{6.3.2}$$

	Reference	Value(s)		
Level density, a_0 (MeV^{-1})	[116]	11		
Excitation energy shift, δ_{eff}	[117]	-1.23		
Strength Functions		E_0 *(MeV)*	Γ_0 *(MeV)*	σ_0 *(mb)*
E1$_{\text{GDR}}$	[118]	13.63	3.82	382.22
E1$_{\text{pigmy}}$	[118]	5.2	1.0	36.0
M1	RIPL-1 [119]	6.96	4.00	1.12
E2	RIPL-1 [119]	10.70	3.66	4.88

Table 6.4: *Summary of the BSFG model parameters, and the gamma strength functions, employed in this work.*
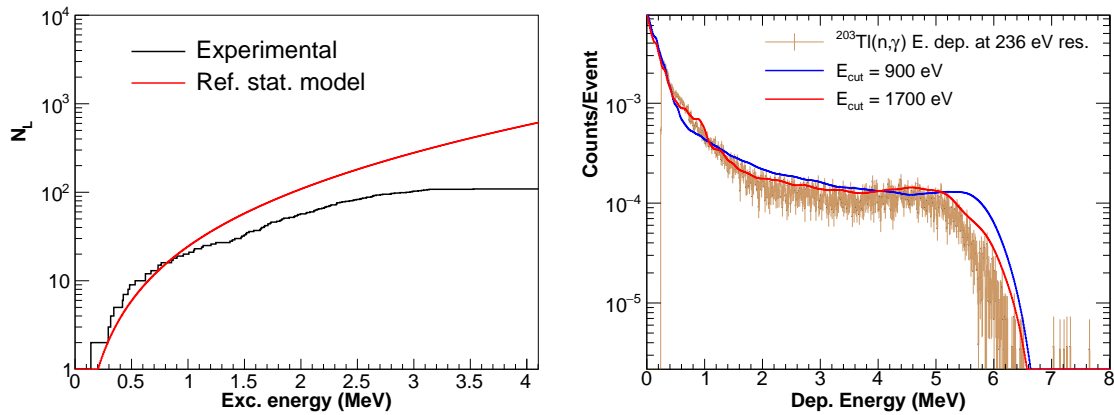
Figure 6.6: *Left: Comparison of the experimental and the theoretical N_l, the latter calculated with the parameters of Table 6.4. Right: The experimental deposited energy spectrum compared to the simulated, for different E_{cut} energies.*

In this expression, t is the thermodynamic temperature determined from the relation $U - \delta_{eff} = at^2 - t$, and σ is the level density spin parameter, which is taken to be $\sigma \approx 0.015A^{5/3}\ t$. The comparison between the model and the experimental N_l is plotted in Figure 6.6. The number of experimental levels starts to be lower than the predicted from 1 MeV, and from 3.2 MeV it barely increases. This could be ascribed to a real decrease in the number of excited levels, like Figure 6.5 would suggest. However, it could be also due to number of levels not observed in measurements.

For the E1, M1 and E2 photon strength functions, due to the absence of ex-

perimental information, it was necessary to resort to evaluations and theoretical parametrizations. The E1 photon strength function employed was taken from Kim et al. [118]. This E1 features a peak energy and width quite similar to the recommended by RIPL, but the σ_0 is 37% lower. Additionally, they also include a second small ("pigmy") resonance at lower excitation energy. Concerning the M1 and E2 strength functions, owing to their much weaker intensities, the authors did not work on new parameters, and thus were used the values calculated from the global theoretical parametrizations from RIPL-1 (Kopecky [119]).

The accuracy of the different elements in the statistical model was tested by comparing the experimental deposited energy spectrum in the C_6D_6 in a strong resonance, with the simulated detector response function to 10^7 capture cascades generated randomly. The cutoff energy E_{cut} and the parameters of the pigmy resonance were fine-tuned in order to improve the agreement with the experimental spectrum. This two parameters were found to have a high impact in the shape of the spectrum. The final E_{cut} was set at 1.74 MeV of excitation energy, where the last level with knwon gamma ray transitions lies. Additionally, as can be seen in Figure 6.6 (right plot), it produces a much better agreement compared to a lower cutoff such as 900 keV. The latter produces a spectrum harder than the experimental, which led us to assume that the statistical model, at least between 1 an 1.7 MeV, is overestimating the number of excitation levels. Concerning the pigmy resonance, the best agreement was found for $E_0 = 5.2$ MeV and $\sigma_0 = 60$ mb. Hereafter, these parameters will be referred to as the *reference* model.

6.4   Capture cascade parameters and threshold correction factors

It is worth emphasizing that the purpose of matching the experimental capture cascade spectrum is not to seek for the most physically true and accurate cascade model for ^{203}Tl(n,γ). This is because C_6D_6 detectors, with their null photopeak efficiency and low resolution, are not the best tool to perform gamma ray spectroscopy. The aim is rather to have a model that reproduces well enough the experimental capture spectra, in order to estimate realistically the threshold correction factors. Additionally, by changing some of the parameters, its is possible

to estimate an uncertainty for the correction factors. The threshold correction factors for the ^{203}Tl(n, γ) measurement are $f_{glob} = F_{th,ice}^{203\text{Tl}}/F_{th,ice}^{197\text{Au}}$ (see details in section 5.5), where $F_{th,ice}$ accounts for the non measurable fraction of the response function due to the threshold, and the emission of conversion electrons,

$$F_{th,ice} = \frac{\sum\limits_{i=0}^{\infty} W_i R_i^C}{\sum\limits_{i=th}^{\infty} W_i R_i^{C,ice}} \ . \tag{6.4.1}$$

The factors for the four C_6D_6 detectors are listed in Table 6.5, for the deposited energy threshold of $E_{th} = 250$ keV selected for the ^{203}Tl(n, γ) measurement. Since the ^{197}Au cascade has a higher level density, with more low energy transitions than ^{203}Tl, more cascades are lost under the threshold. Thus the final correction for the ^{203}Tl normalized yield is less than unity.

Following the same procedure, several model parameters were investigated in order to estimate the uncertainty and to study the sensibility of the threshold correction to the cascade model itself. These are listed below:

1. Reference model with the pigmy resonance suppressed.

2. Reference model with the pigmy parametrized like in Ref. [118], with $E_0 = 5.6$ MeV.

3. Reference model with the σ_0 of E1 transitions increased to the value of the RIPL parametrization.

4. Reference model with σ_0 of M1 transitions increased by a factor of 20.

For comparison, the simulated response functions of $C_6D_6\#4$ for the different models are plotted in Figure 6.7. Although in the higher energy range there are some

	$C_6D_6\#1$	$C_6D_6\#2$	$C_6D_6\#3$	$C_6D_6\#4$
$F^{197\text{Au}}$	1.094(1)	1.100(1)	1.092(1)	1.088(1)
$F^{203\text{Tl}}$	1.071(1)	1.071(1)	1.064(1)	1.055(1)
$\mathbf{f_{th}}$	**0.979(1)**	**0.974(1)**	**0.975(1)**	**0.970(1)**

Table 6.5: *Correction due to missing cascades under the threshold for the ^{203}Tl and the ^{197}Au samples, and the resulting threshold correction factors to the yield, with $E_{th} = 250$ keV.*

Model	$C_6D_6\#1$	$C_6D_6\#2$	$C_6D_6\#3$	$C_6D_6\#4$
Reference model f_{th}	0.979(1)	0.974(1)	0.975(1)	0.970(1)
1. No pigmy	-0.3(1)%	-0.3(1)%	-0.3(1)%	-0.6(1)%
2. Kim et al.	0.1(1)%	0.1(1)%	< 0.1(1)%	0.1(1)%
3. Enhanced $\sigma(E1)$	1.0(1)%	1.1(1)%	< 0.1(1)%	0.5(1)%
4. Enhanced $\sigma(M1)$	0.9(1)%	0.7(1)%	0.1(1)%	0.9(1)%

Table 6.6: *Deviations of the different test models f_{th} with respect to the reference f_{th}.*

differences, in the low energy part, where counting rate is more than 10 times higher, differences are smaller. Consequently, deviations in the threshold correction factor are of 1.1% in the worst case, and in most cases below 1%, as can be seen in Table 6.6. In view of this situation, the systematic uncertainty associated to the statistical model was estimated as 1%.
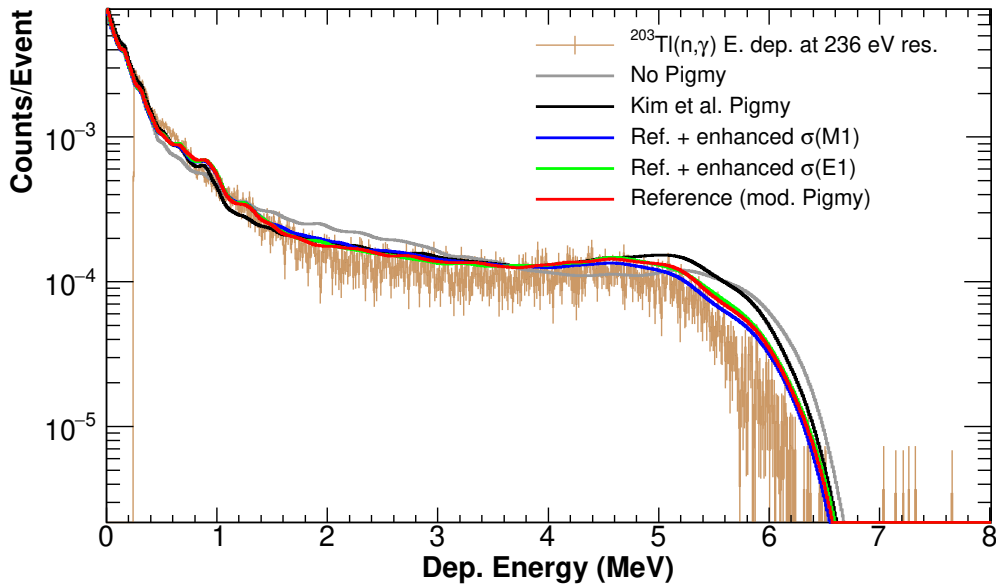
Figure 6.7: *Comparison, for $C_6D_6\#4$, between the experimental capture spectrum for the resonance at 236 eV (light brown) and the simulated response function to several cascade models, described more in detail in the text.*
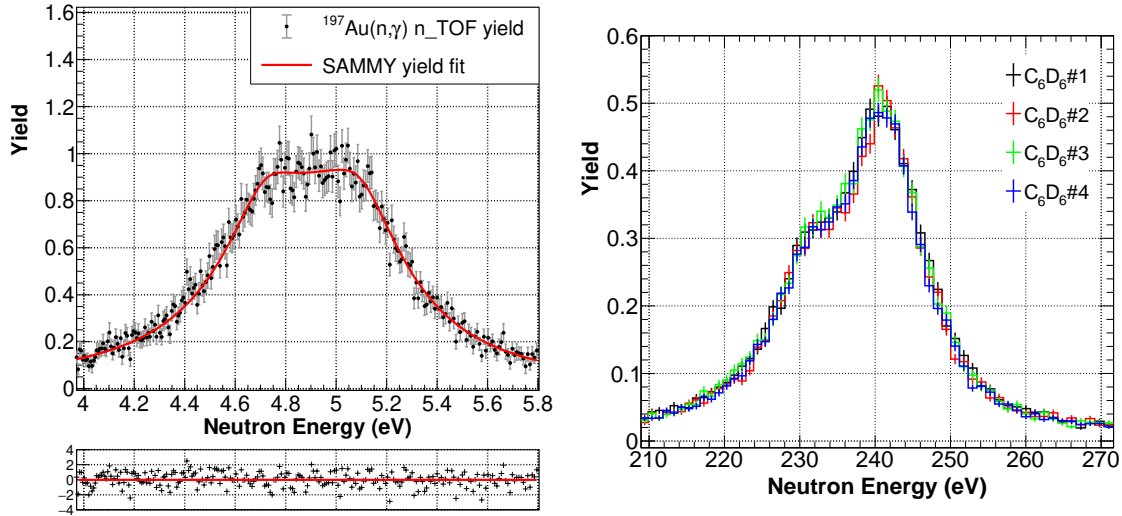
Figure 6.8: *Left: for each detector, the normalization constant A_n is obtained by fitting the 4.9 eV resonance of gold. Right: the normalized yield for all detectors, in the 236 eV resonance of ^{203}Tl.*

6.5 Yield normalization and background subtraction

At this point, it is convenient to recall the expression of the experimental capture yield introduced in section 4.5:

$$Y_{exp}(E_n) = f_{glob} \cdot f_{sat} \cdot f_{si} \cdot f_{ns} \frac{C_w(E_n) - B_w(E_n)}{f_{bi} \cdot \phi_n(E_n) \cdot (S_n + E_n)}. \tag{6.5.1}$$

f_{bi} has been already calculated in section 4.8. The neutron sensitivity correction factors f_{ns}, which are specific for each resonance with very large Γ_n will be discussed in the next section, where resonances are analysed individually.

Hence, the final steps to obtain the final capture yield were related to the normalization and background subtraction. In order to apply the saturated resonance technique, the yield at the 4.9 eV resonance of gold is analysed with SAMMY to extract the normalization constant A_n, from where $f_{sat} = 1/A_n$ (see left plot in Figure 6.8). In Figure 6.8 the normalized yield for all four detectors, in the 236 eV resonance of ^{203}Tl, is plotted. The normalized yield for the ^{203}Tl, the ^{nat}C and the empty frame is plotted in Figure 6.8 for $C_6D_6\#1$.

Based on the fact that ^{203}Tl has an elastic cross section several times that of capture, it can be assumed that most of the background was produced by neutrons
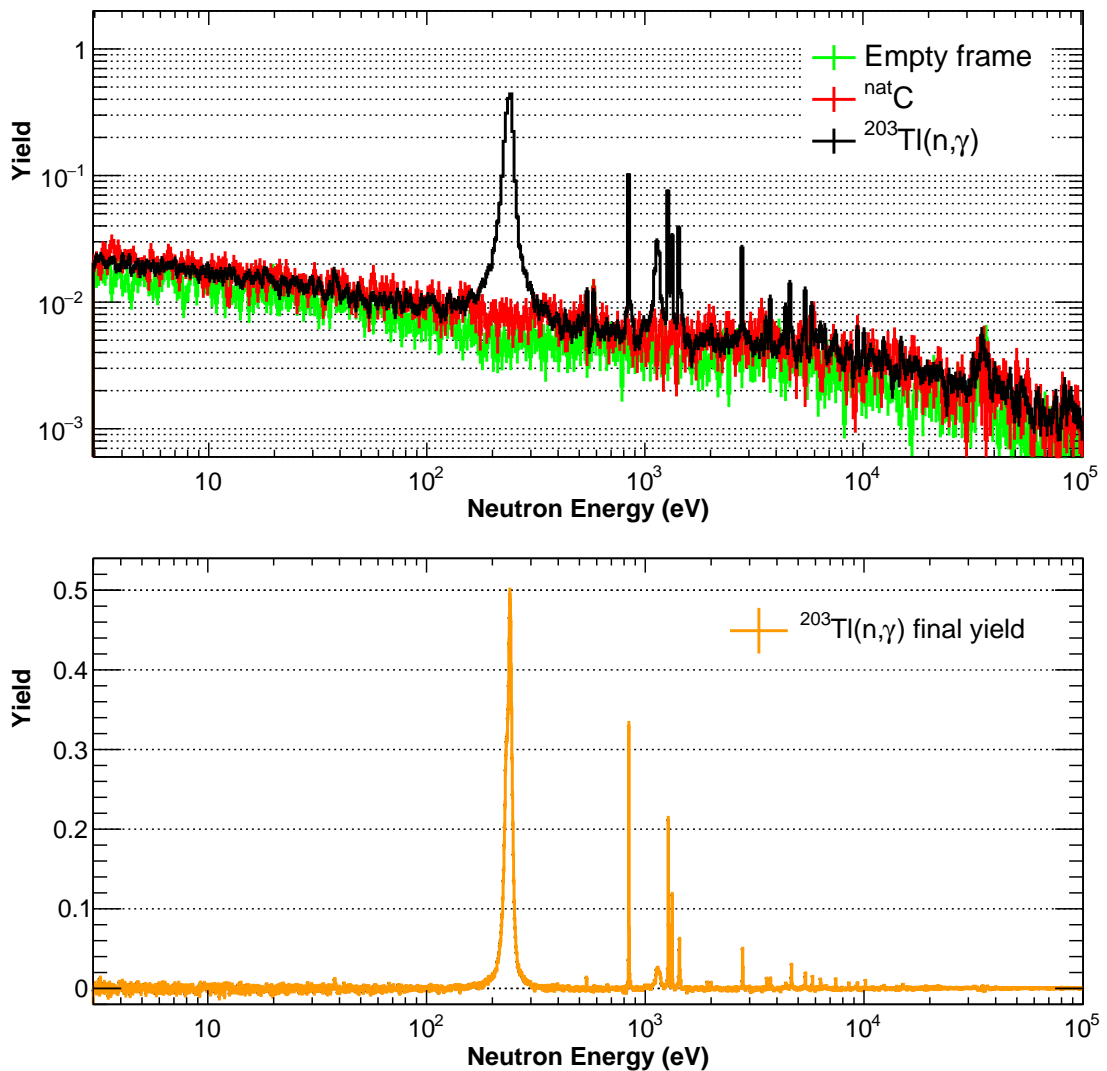
Figure 6.9: *Top: Yield of ^{203}Tl and the different backgrounds in the full neutron energy range, measured by $C_6D_6\#1$. Bottom: the final yield, averaged over the four detectors.*

scattered by the sample and subsequently captured in the surrounding materials. For this reason, the ^{nat}C sample was best suited for the background subtraction. Indeed, once properly scaled to account for the different atomic thickness and Z, the ^{nat}C spectrum matched remarkably well the ^{203}Tl yield at low energies and in the valleys between resonances.

The scaling factor for ^{nat}C was calculated in the lower neutron energy part of the spectrum, because in that region there are no capture resonances of ^{203}Tl.

Additionally, due to the low sample mass, the $1/v$ component of the capture probability was considered negligible. Thus, it was assumed that the signals in that region are mainly coming from the aforementioned background. Once the background was subtracted from the yield of each detector, they were all summed and averaged. The final capture yield, as depicted at the bottom of Figure 6.9, was ready for the capture resonance analysis.

The systematic error due to the averaging procedure was estimated by doing a preliminary fit of the 236 eV resonance with SAMMY for each detector separately. The relative standard deviation was found to be 1.5%, which was the figure adopted as the uncertainty of the averaging procedure.

6.6 ^{203}Tl(n,γ) R-matrix analysis in the Resolved Resonance Region

6.6.1 Preliminary discussion

A detailed description of the resonance analysis is presented here, including a comparison of the new data with previous experiments, and with the JEFF-3.3 [120] and ENDF/B-VIII.0 [121] evaluations. The analysis in the RRR was made on an individual resonance basis up to neutron energies of about 16 keV, and on broader energy intervals (2-3 keV) beyond that energy. It was used as starting point resonance data provided by the JEFF-3.3 nuclear data evaluation, since it extends up to 100 keV. Besides, it was checked that for almost all resonances, the JEFF kernels were identical to the data measured in the ^{203}Tl(n, γ) measurement performed at ORNL in 1976 by Macklin and Winters [122] (referred from now on as "ORNL"), later corrected due to a systematic error in the data analysis [123]. This turned out to be very useful, because many low amplitude resonances were observed in that experiment, but not in the present measurement. This is to be ascribed to the much larger sample used at ORNL. In that experiment, the sample consisted of a square with a thickness of $7.5 \cdot 10^{-3}$ atoms/barn, which corresponds to 38 grams of ^{203}Tl$_2$O$_3$. Such figures correspond to 4.4 times the atomic thickness, and almost 150 times the mass, of the sample used in the n_TOF measurement. When available, the parity assignment and $g\Gamma_n$ from the transmission measurement performed at the Columbia University cyclotron at the Nevis Laboratories [124] were adopted as initial values. In those resonances where it was available, it was preferentially employed, as initial values, the parity assignment and the $g\Gamma_n$ from the transmission measurement performed at the Columbia University cyclotron at the Nevis Laboratories [124]. Also the uncertainty of $g\Gamma_n$ was set to the reported value from the transmission data.

Capture resonances measured at ORNL, and not visible in the n_TOF data, were considered compatible with the data if they fell inside the background fluctuation, whose range has been assessed to be of $\pm 2\sigma_{res}$, where σ_{res} is the residual in sigma units, i.e. $\sigma_{res} = (Y_{exp} - Y_{th})/\sigma_{exp}$. In other words, any evaluated resonance deviating more than $2\sigma_{res}$ interval from the experimental data will be either excluded or its magnitude artificially reduced, in order to fall into the compatibility

range. (Resonance parameters from the past measurements may be referred to as Γ_x^{Trans} and Γ_x^{ORNL}, respectively).

The criteria employed to define new resonances was that, at low neutron energies, a peak must comprise at least 3 consecutive points that deviate more than $2\sigma_{res}$ from the background level. At higher neutron energies (> 15 keV) a lower number of bins per decade had to be employed most of the time, and thus 2 points were deemed enough.

The fits have been performed following a general set of rules:

- The energy of the resonance was determined in a preliminary fit of both E_n and the Γ_γ, or Γ_n if it is considerably smaller than Γ_γ.

- To obtain the correlated uncertainty for both Γ_γ and Γ_n widths, both have been taken as free fit parameters in SAMMY for all resonances but the one at 842 eV. For those with high statistical accuracy, all possible spin assignments, compatible with the parity provided, have been tried. Finally, the one producing the best fitting results, while being compatible with the $g\Gamma_n$ of the transmission measurement, was chosen. If there was still ambiguity, the one providing a Γ_γ closer to the evaluated Γ_γ was selected.

- For low kernel resonances the evaluated spin group is used, and for compatible resonances, all parameters were left without modification.

In some cases, for example when both parameters have a similar magnitude, it was useful to investigate whether a possible correlation between Γ_γ and Γ_n existed. This was done by plotting the chi-squared for each possible combination in a wide range of Γ_γ and Γ_n values. If a correlation exists, these plots allow to see that similar fitting results can be obtained with very different sets of parameters. SAMMY tends to minimize the chi-square test, which could lead to parameters that disagree with experimental data. This procedure was developed and applied in a previous work [103].

6.6.2 The residual background in SAMMY

The background subtraction procedure described in section 6.5 successfully eliminated most of the background from the capture yield. However, the presence of a small, residual background could still be identified when analysing the data with

SAMMY. This background was quantified by fitting the yield –previously rebinned to 1500 bins per decade– in the valleys between resonances at lower energies. A constant background of $2 \cdot 10^{-4}$ was found, and was applied to all the resonance fits.

However, due to the nature of the subtraction process the residual background might fluctuate as well. At high energies, with increasing statistical uncertainty and the increased proximity between resonances, it is more complex to fit properly the background. Therefore, in order to evaluate the impact of variations in the residual, a second fit of the most prominent resonances was performed without it. Results are further discussed in section 6.6.4.

6.6.3   Resonance analysis

235 eV resonance

This is the strongest resonance in ^{203}Tl. In a previous experiment performed in the 1960s in the USSR [125], it was the only distinguishable level. However, the values reported correspond to a much broader resonance and consequently with a much lower amplitude. This can be ascribed to the low neutron energy resolution of that measurement. From the transmission experiment, $g\Gamma_n = 3.0(3)$ eV and $\Gamma_\gamma = 0.80(20)$ eV were reported for this resonance, with quantum numbers $J = 1$ an $l = 0$. This important level was not observed at ORNL due to their cut-off at neutron energies below 3 keV. From the analysis of the n_TOF data, and thanks to the high neutron energy resolution at EAR1, one can affirm that the true energy of the resonance is 235.7 eV, lower than the evaluated value of 238 eV reported in [124]. The previous bias in the resonance energy can be most probably ascribed to the the very prominent multiple scattering peak that appears at higher energies. In a measurement with low energy resolution, it could be mistaken as the peak of the resonance.

According to the SAMMY multiple scattering parametrization model, this peak is produced by neutrons that are scattered two or more times in the sample before being captured (see Figure 6.10). This is caused by the fact that Γ_n is more than six times the value of Γ_γ, which makes such a phenomenon quite probable. In detail, the neutron arrives at a certain time at the sample, corresponding to an energy higher than the resonance one. In the ensuing elastic scatterings it loses the right

amount of energy –due to recoil of the sample nuclei– to fall in the energy range of the resonance. Owing to the much smaller time scale of the nuclear scattering process, the multiple scattering capture peak will appear at approximately the time when the neutron entered the sample, plus the time corresponding to the average distance travelled between collisions. Multiple scattering effects directly depend on the physical attributes of the sample –that is, length, radius and atomic thickness. Thus, they may be also referred to as *thickness effects*.

Γ_γ and Γ_n obtained from the analysis of the n_TOF data are 634(7) meV and 3813(10) meV, respectively. The latter corresponds to a $g\Gamma_n$ of 2.86(1), very close to the transmission value but 30 times more precise.

842 eV

This resonance was determined to be an *s*-wave in the transmission experiment, and with spin $J = 1$, in agreement with our analysis. An important feature is that $\Gamma_\gamma \sim \Gamma_n$, and the Γ_γ vs Γ_n plot shows a pronounced correlation between the
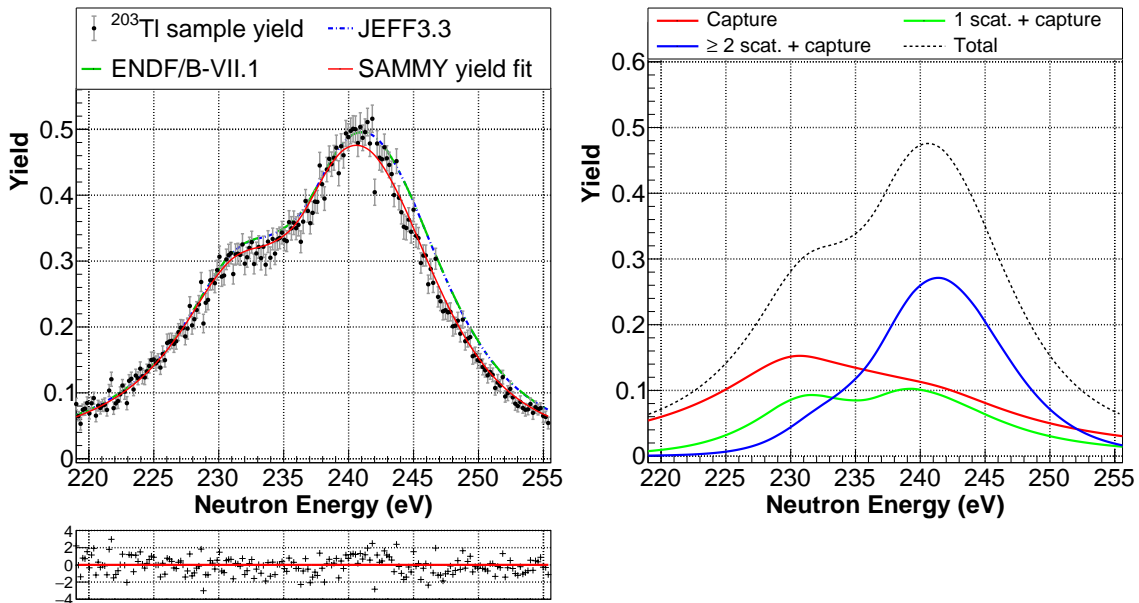
Figure 6.10: *Analysis of the 236 eV resonance. (Left) Fit of the yield with SAMMY and comparison to evaluations. (Right) Plot of the different multiple scattering contributions to the final experimental yield for the sample measured at n_TOF.*

parameters (see Figure 6.11). It can also be observed that the minimum calculated by SAMMY is obtained with a Γ_n systematically lower than the transmission value, well outside the uncertainty range. In this situation, it was considered convenient to use the transmission Γ_n value directly, including its uncertainty, which is also plotted in Figure 6.11. This constraints the range of the possible Γ_γ considerably, and the resulting fits still maintain a reasonable agreement with the data. The Γ_γ paramter and its associated uncertainty was obtained by a series of Monte Carlo SAMMY runs, where the Γ_n value was sampled from a normal distribution, with its mean at Γ_n^{Trans}, and the standard deviation given by $\sigma(\Gamma_n^{Trans})$. Due to the shape of the correlation, the resulting distribution of Γ_γ values is asymmetric, with the mode of the Γ_γ distribution bigger than the mean value. The mean of the distribution was chosen as the recommended value for Γ_γ, with the uncertainty given by the standard deviation, resulting in $\Gamma_\gamma = 557(34)$ meV.

1137 eV

The broad shape of this resonance indicates that this is an s-wave, with $\Gamma_\gamma \ll \Gamma_n$ (Figure 6.12). Any spin different than $J = 0$ produced a resonance with a shape
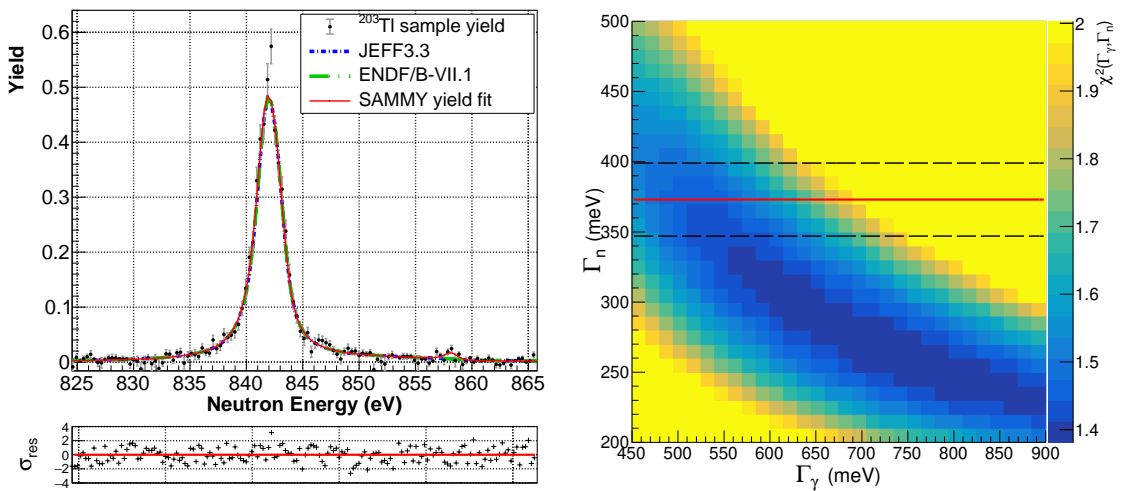
Figure 6.11: *Analysis of the 842 eV resonance. (Left) Fit of the yield with SAMMY and comparison to evaluations. (Right) 2D plot of the χ^2 variation as a function of Γ_γ and Γ_n; the solid red line and the dashed lines correspond to $\Gamma_n^{Trans} \pm \sigma(\Gamma_n^{Trans})$*
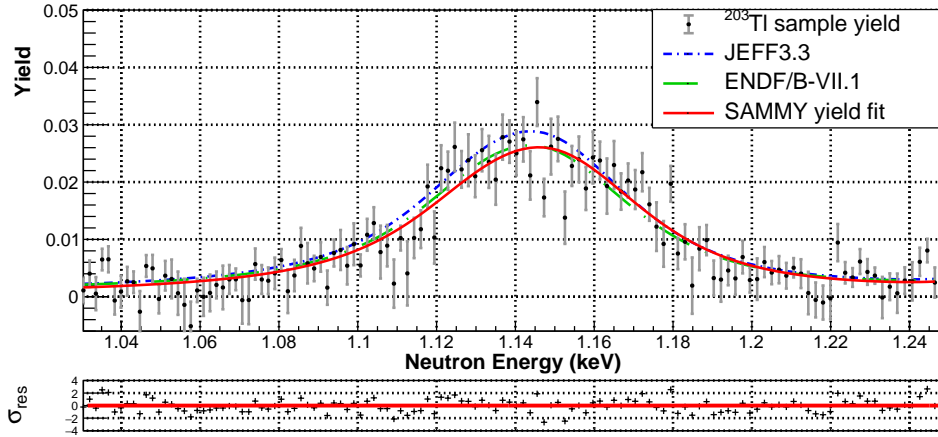
Figure 6.12: *SAMMY fit of the yield for the 1137 eV resonance*
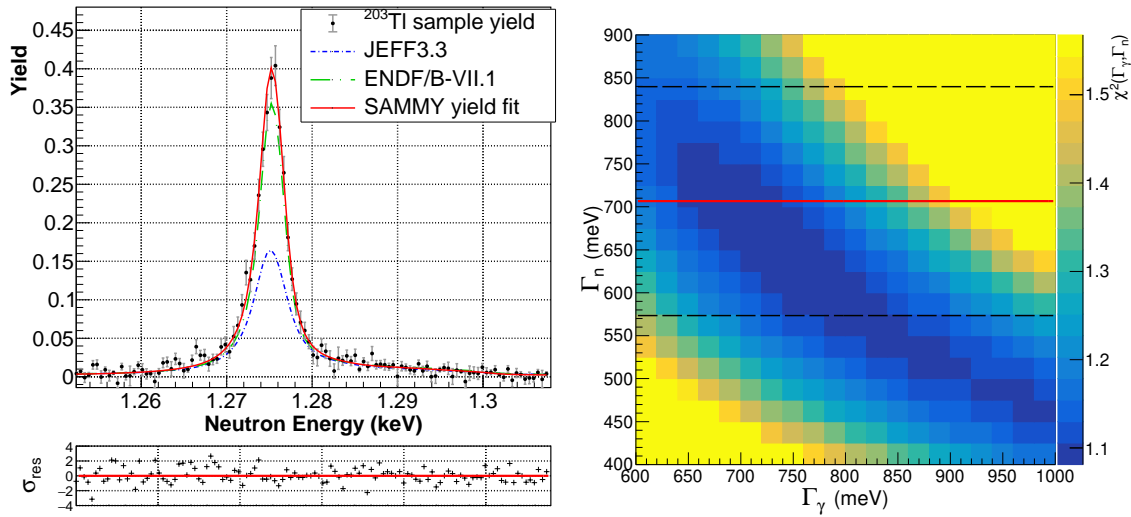
Figure 6.13: *Analysis of the 1275 keV resonance. (Left) Fit of the yield with SAMMY and comparison to evaluations. (Right) 2D plot of the χ^2 variation as a function of Γ_γ and Γ_n. The solid red line and the dashed lines correspond to $\Gamma_n^{Trans} \pm \sigma(\Gamma_n^{Trans})$.*

not in agreement with the data. Owing to the relatively high Γ_n value of ~ 46000 meV, the neutron sensitivity correction factor for this resonance was of 3.5%. Γ_γ was found to be 634(19) meV.
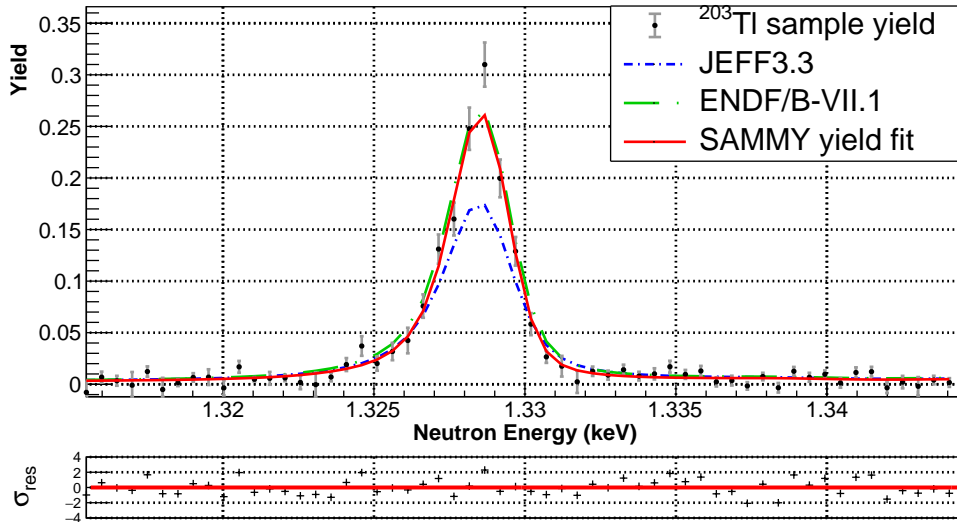
Figure 6.14: *SAMMY fit of the yield of the 1328 eV resonance*

1275 eV

This $J = 1$, s-wave resonance, features $\Gamma_\gamma \sim \Gamma_n$, and shows an important correlation between the parameters as shown in the χ^2 plot in Figure 6.13). In this case, the best fit with SAMMY yields a value of $\Gamma_n = 643(66)$ meV, compatible with the transmission result of $707(133)$ meV. The corresponding radiative width is $\Gamma_\gamma = 831(84)$ meV. Comparing the new fit with the evaluated data the agreement with ENDF is almost perfect (see Figure 6.13), while JEFF notably underestimates the cross section providing a radiative kernel that is 50% lower than the measured one.

1328 eV

This is a positive parity resonance as determined by the transmission measurement. A $g\Gamma_n$ almost equal to the one found there is obtained for $J = 1$ (unlike for the case with $J = 0$). The corresponding Γ_γ is $406(100)$ meV. The fit of the experimental data is shown in Figure 6.14.

1432 eV

This resonance was determined to be an s-wave with $J = 1$ in the transmission measurement, with g$\Gamma_n = 2.1(0.2)$ eV. In the present data analysis better results were obtained with $J = 0$. To clarify the situation, it was decided to look at the Γ_γ vs Γ_n plot for both the $J = 0$ and $J = 1$ cases. In both, the minimum χ^2 is outside the range of the transmission measurement, although a slightly better agreement is obtained for $J = 0$. With this assignment, the Γ_γ of the minimum is more in line with the Γ_γ obtained for other $\Gamma_\gamma \ll \Gamma_n$ resonances, and with the value recommended value by Mughabghab [116]. Thus $J = 0$, $\Gamma_\gamma = 623(24)$ and $\Gamma_n = 6729(328)$ are considered the best parameters for this resonance. As can be seen in the plot of the resonance (Figure 6.15), both nuclear data libraries overestimate the cross section remarkably, producing a kernel that is 3.4 times the one found in this work.

1.8 to 2.2 keV

Both l-wave resonances stated by the transmission experiment in this range have been observed, at 1917 eV and 2002 eV. In the data there seems to be another small resonance close to the first one, at 1914 eV. However, in the ^{204}Tl sample yield, with much higher statistics, this resonance was not observed, and thus its existence was discarded. Concerning the comparison with evaluated data, both libraries overestimate both resonances.

2789 eV

This level was found to be $J = 1$ and $l = 0$ as established before [124]. Best fit parameters yielded $\Gamma_\gamma = 506(25)$ meV and $\Gamma_n = 3456(221)$ meV values, compatible with the transmission measurement, which yielded $\Gamma_\gamma^{Trans} = 600(180)$ meV and $\Gamma_n^{Trans} = 3600(200)$ meV.

3 to 4 keV

A strong p-wave $J = 1$ resonance at 3585 eV was observed (see Figure 6.17) with $\Gamma_n \ll \Gamma_\gamma$. The result is that the kernel is mostly dependent on the neutron width, and Γ_γ is difficult to assess accurately, $\Gamma_\gamma = 1270(563)$. The Γ_n obtained is fully
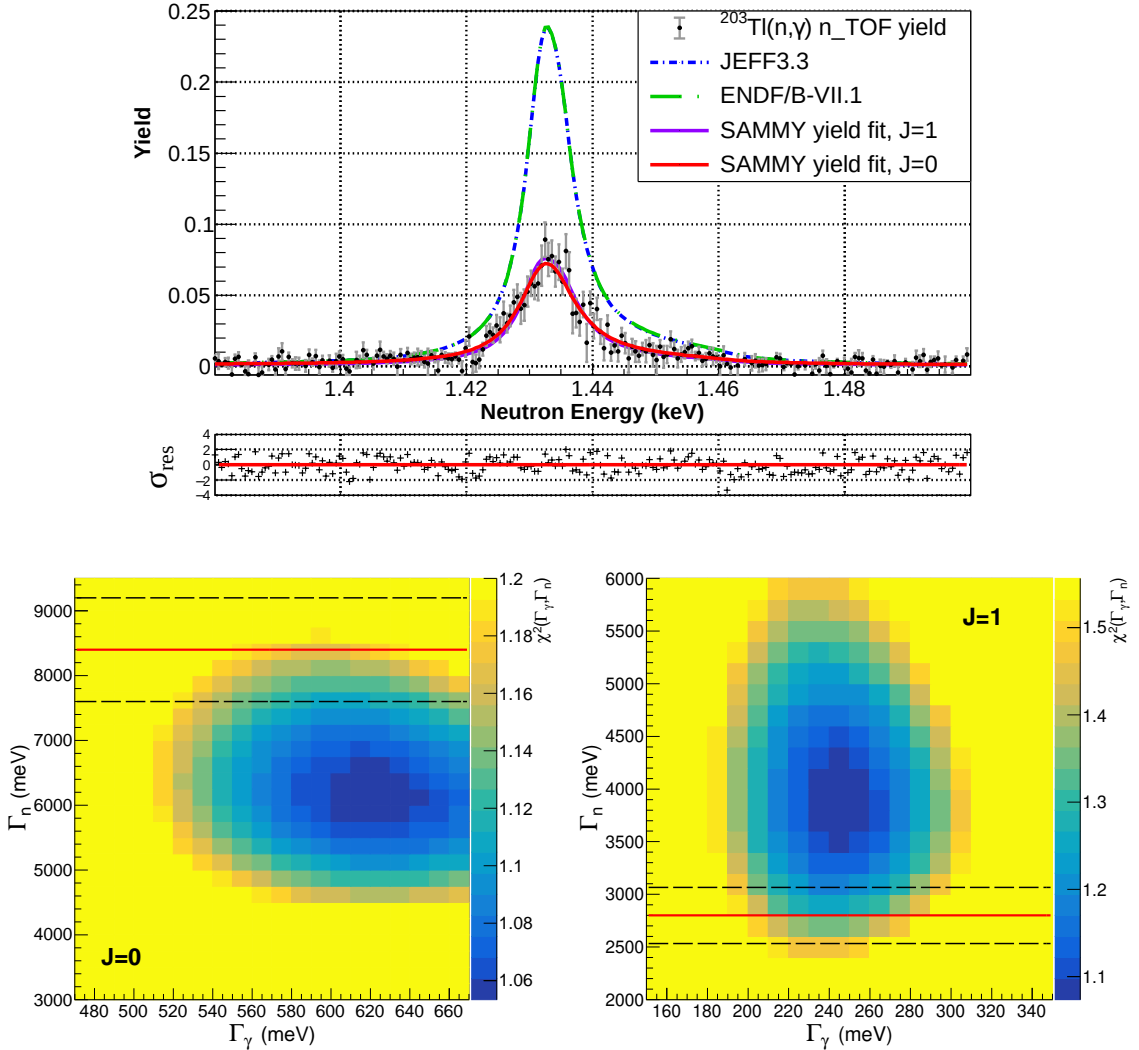
Figure 6.15: *(Top) SAMMY fit of the 1432 eV resonance, with both the fits with J=0 and J=1 represented. (Bottom) the respective χ^2 plots, J=0 and J=1.*

compatible with Γ_n^{Trans}. Another important resonance was observed at 3731 eV. This is an s-wave, with $J = 0$, and $\Gamma_\gamma \ll \Gamma_n$. The resulting Γ_γ is 739(76). Two, much smaller resonances were observed by Macklin at 3551 eV and 3902 eV [122], which are also included in the evaluations. These resonances were not observed in this work, most possibly due to the small sample used here. However, they have been included in the analysis since their presence is compatible with our data.
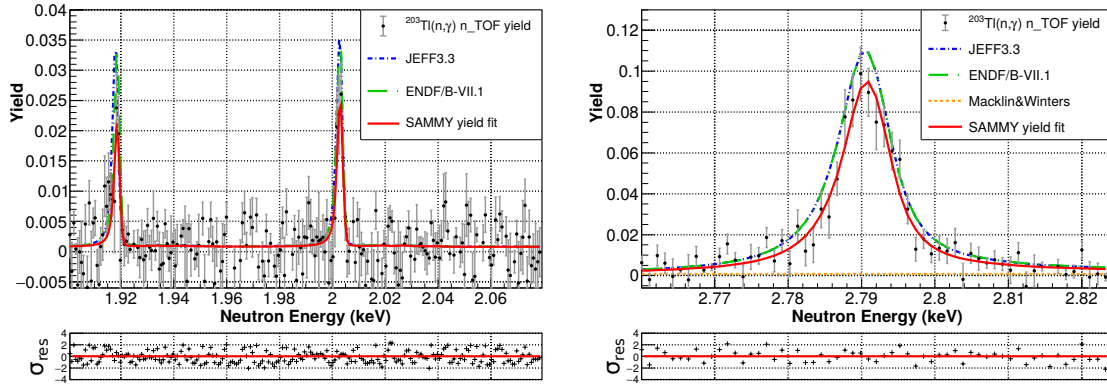
Figure 6.16: *Yield fit for the resonances at 1917 eV and 2002 eV (left), and at 2789 eV (right)*

4 to 5 keV

In this range there are two important s-wave resonances at 4398 eV and 4659 eV, plus a low-kernel one at 4785 eV. The first two are broad resonances due to the high neutron width of $\Gamma_n = 62894(6866)$ and $\Gamma_n = 12398(1019)$ meV. Both values are in agreement with those established in the transmission measurement of 64000(8000) meV and 14667(2667) meV, respectively. In this situation it was opportune to calculate the correction factor due to the neutron sensitivity of the detection setup, which resulted in a 3.4% correction in the first case, and a negligible correction of less than 1% in the second. Final radiative widths were 885(115) meV and 768(45) meV. It is important to note here that both kernels are considerably lower than those measured at ORNL. Consequently, our results are also below what is reported in both evaluations: 10% lower in the 4400 eV resonance, the one with the highest Γ_n, and 11% in the 4659 eV resonance. On the other hand, having $\Gamma_n \gg \Gamma_\gamma$ means the radiative kernel is for the most part only dependent on Γ_γ ($K_r \approx g\Gamma_\gamma$), so that any increase in the counting rate at the resonance due to background would entail a direct increase in the Γ_γ measured. Therefore, one can hypothesize that the difference in Γ_γ could be a consequence of the higher neutron sensitivity.

Specifically, the differences could be ascribed to underestimation of the neutron-induced background in the previous experiments. For example, Macklin and Winters report a 1.5% figure for a setup which was significantly more sensitive to
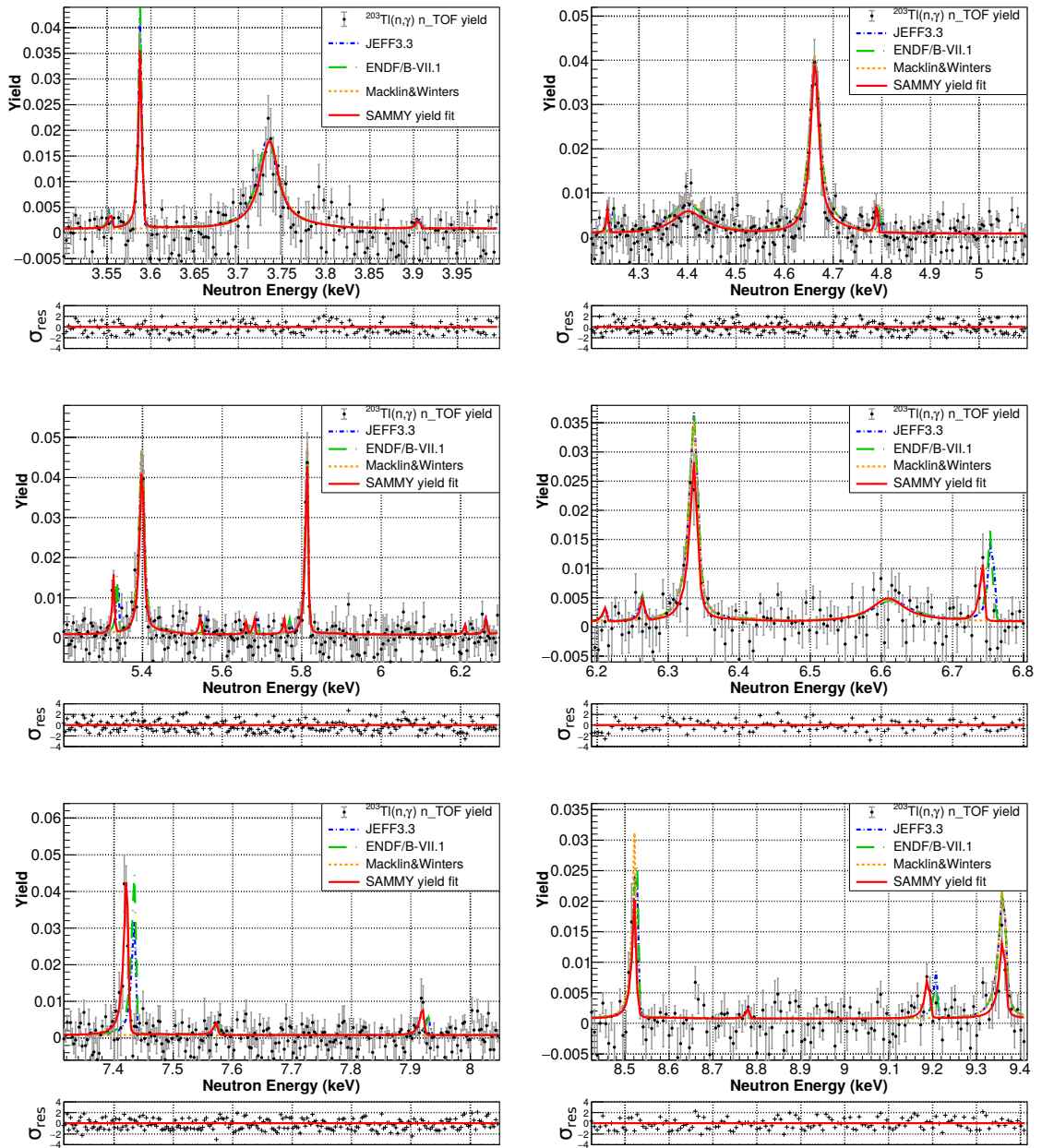
Figure 6.17: *Yield fit for the resonances between 3.5 keV and 9.5 keV.*

neutrons than the one used here. The neutron sensitivity of the n_TOF setup – design specifically to minimize it– can be as high as a few percent, and has been evaluated through detailed MC simulations [93].

5 to 6 keV

The main resonances in this range have been found to be a p-wave $J = 0$ resonance at 5323 eV, and two stronger resonances, both s-waves of $J = 1$, at 5395 eV and 5808 eV. In all three cases, the fits are in good agreement with transmission data. Resulting Γ_γ values are, respectively, 292(73) meV, 638(49) meV and 440(56) meV. In addition to these resonances, a few other low amplitude ones, found at [122] and considered compatible with the n_TOF data, are included in the analysis.

6 to 7 keV

The most intense resonance in this range is a $J = 1$, s-wave at 6331 eV, with Γ_n in agreement with the transmission data, and $\Gamma_\gamma = 441(49)$ meV. A very broad, $J = 0$, s-wave resonance is present at 6606 eV, whose high Γ_n value of 48286(7692) meV yields a correction due to neutron sensitivity of 2.5%. After applying the correction, the resulting Γ_γ is 582.5(177) meV. Still another narrow resonance, with a smaller kernel, is observed at 6736 eV (see Figure 6.17).

7 to 9 keV

The resonance at 7413 eV was classified as a p-wave in the transmission measurement, and at ORNL its total spin was determined as $J = 2$. In any case, all three possible spin assignments were tried, 0, 1, and 2. Both $J = 1$ and $J = 2$ produce good results, and a $g\Gamma_n$ value compatible with the transmission measurement. Finally, $J = 2$ was chosen on the basis that if Γ_n is fixed to the transmission value, the resulting Γ_γ was closer to the recommended value. In any case, changing the spin does not really affect the final radiative kernel, since the difference is around 1%. The value, 311(38) meV, is well in agreement with the ORNL value and ENDF library, and a 50% bigger than the evaluated in JEFF-3.3. Another important resonance appears at 8513 eV. This is reported to have positive parity in Ref. [124]. The situation is similar to the previous resonance, this time with $J = 0$ or $J = 1$ as possible total spin values. Looking at the Γ_γ vs Γ_n plots, the correlation is weak. Using the same criteria for Γ_γ like in the previous case, $J = 1$, $\Gamma_\gamma = 322(52)$ meV and $\Gamma_n = 2041(590)$ meV were obtained. This spin assignment also coincides with the ORNL measurement. Again, the final kernel difference is of 1%, and therefore a different spin assignment would not affect appreciably the result reported here.

Finally, a smaller resonance has been analysed at 7910 eV, and three other minor resonances observed at ORNL have been included as compatible.

9 to 10.5 keV

In the transmission measurement it was determined that the resonance at 9351 eV was an s-wave with $J = 0$, while at ORNL was found determined to be $J = 1$. In this measurement, setting $J = 0$ produces results which are not compatible with the reported $g\Gamma_n = 4(1)$ eV from transmission [124]. On the other hand, the assignment of $J = 1$ at ORNL yields good agreement, with $\Gamma_\gamma = 415(68)$ meV and $g\Gamma_n = 4.1(1.0)$ eV. The p-wave at 10.17 keV presents $\Gamma_\gamma \sim \Gamma_n$ and an important correlation between parameters. The spin is determined as $J = 1$ since using $J = 0$ and $g\Gamma_n$ from the transmission value requires a very high Γ_γ parameter. Both resonance parameters are fitted together with $J = 1$, obtaining $\Gamma_\gamma = 565(126)$ meV and $g\Gamma_n = 1.2(0.8)$ eV.

10.5 to 13.5 keV

The most important resonance in this range is found at 10.97 keV. Its spin and parity were determined in the transmission measurement to be 0^+. This has been confirmed here, with a compatible $g\Gamma_n$. However, its measured kernel is around 54% lower than the value reported at ORNL, as can be seen in Figure 6.18. A second resonance at 12.37 keV was also fitted, confirming as well the $J^\pi = 1^+$ assignation from transmission. In this case the kernel value was 35% lower than the result from ORNL, but compatible within the uncertainty.

14 keV to 17 keV

Major resonances were measured at 14.50 keV and 15.10 keV. For the first one, $J = 0$ was excluded due to disagreement with the data, while $J = 2$ requires a Γ_γ much higher than the expected. Therefore, $J = 1$ was chosen, though the low statistics did not allow to determine it unequivocally. In the case of the second one, an s-wave, $J = 1$ gave a better agreement with the established $g\Gamma_n$ value, and a $\Gamma_\gamma = 712(131)$ meV. An assignment of $J = 0$ would require a very high Γ_γ of 2113(556) meV.
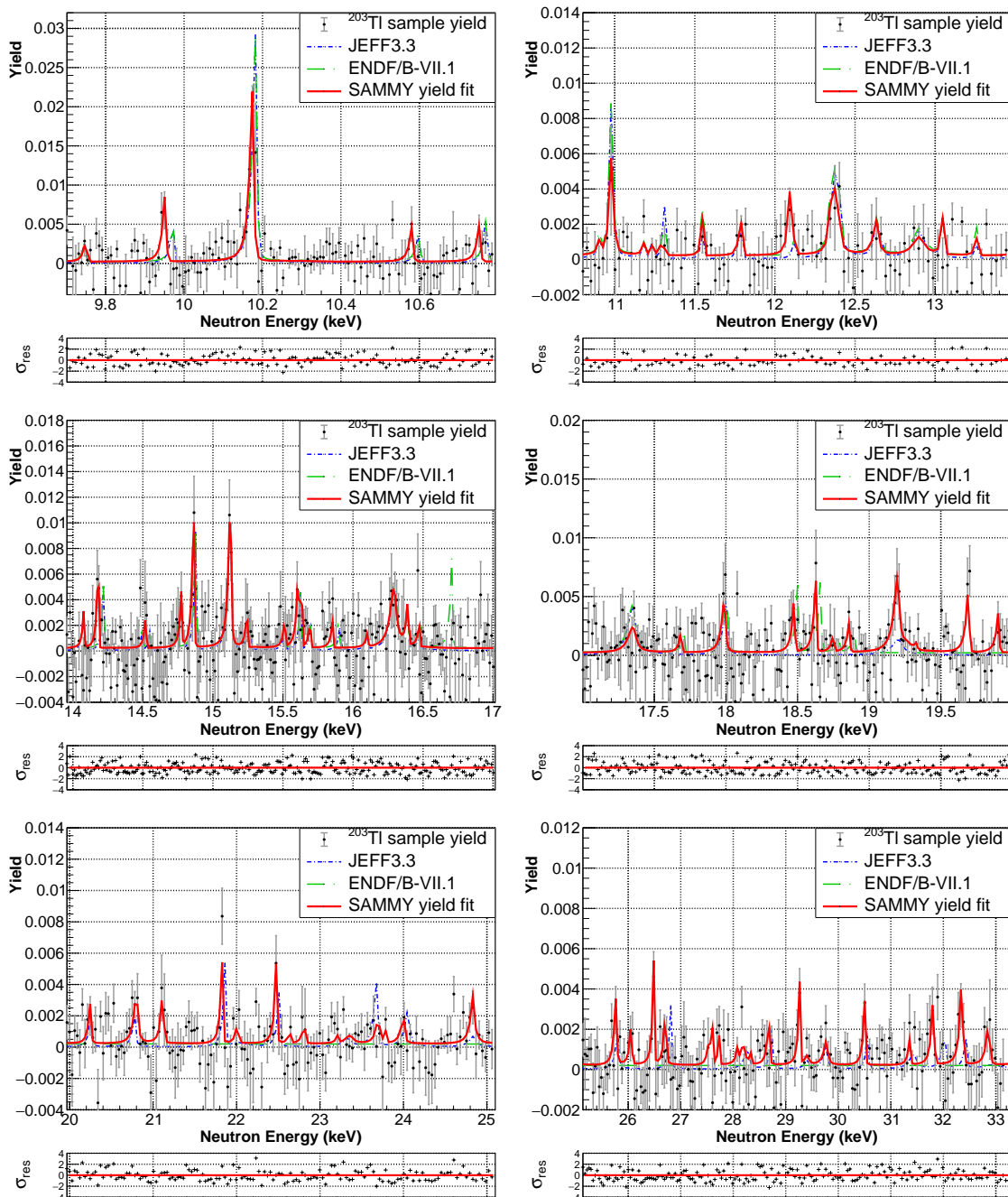
Figure 6.18: *Capture yield R-matrix fit for the resonances between 9.7 keV and 32 keV.*

17 to 20 keV

Two *s*-wave resonances were analysed in this energy range. The first one, at 17.96 keV, has been determined to be $J = 1$ since this fit has the best agreement with

the $g\Gamma_n$ value from transmission. The second one, at 19.17 keV, was determined to have $J^\pi = 0^+$. However, in our measurement the only way to be in agreement with their $g\Gamma_n$ was for $J = 1$. In this range, the increasing statistical uncertainty makes it not feasible to analyse (beyond simple identification) some s-wave resonances with a relatively high kernel, like those at 18.44 keV and 18.60 keV.

20 to 32.5 keV

The level at 19.17 keV was the highest energy resonance measured in the transmission measurement for which $g\Gamma_n$ was reported. Therefore, from 20 keV up to the last observed resonance at 32.80 keV, resonances were fitted in this work using only the parameters from the libraries, with both Γ_γ and Γ_n free to vary. In addition, the high statistical uncertainty leads to a very low precision in determining the resonance parameters. Thus, only the kernel information is considered meaningful in this range of energies. Macklin and Winters reported a resonance at 23.70 keV and $K_r = 554(30)$. This has not been found in our data, or at least does not have the stated magnitude, since the peak of the resonance would be more than 4σ above our background level. Thus, its magnitude was reduce to 220 meV, which would be compatible with our sensitivity level.

General remarks

A total of 56 resonances were resolved and analysed in the capture data from n_TOF. The full list of resonances measured in this analysis can be found in appendix B. The list also includes the resonances measured at ORNL, which were too weak to be observed here with our small sample measurement.

The energy of all resonances has been found to be systematically lower than the values reported in the experiment at ORNL. Looking at some narrow resonances in energies below 10 keV, the shift is quite constant, of around 0.15%. If one considers higher energy resonances, with lower statistics, the shift is, at most, of 0.2%. This can be explained by the fact that in the results from ORNL report the peak of the resonance as the resonance energy, while SAMMY includes the shift introduced due by the resolution function. As one goes up in neutron energy the influence of the RF is higher, and the shift of the peak becomes more visible.

In Figure 6.19 the new kernels found here are compared with previous exper-
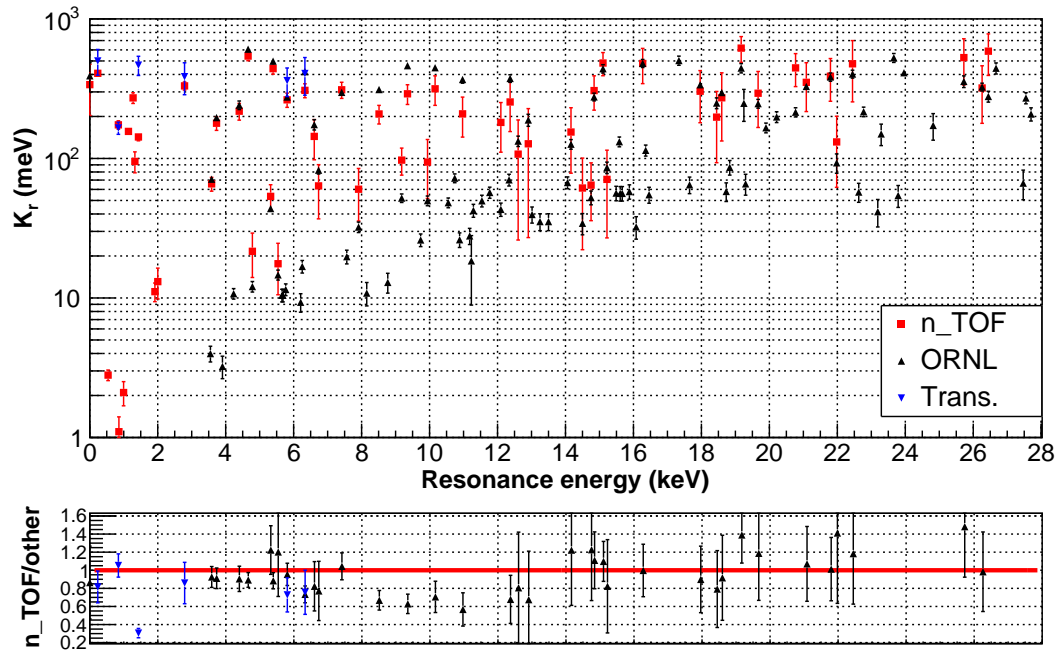
Figure 6.19: *^{203}Tl (n,γ) n_TOF kernels compared to ORNL results, and the transmission performed at the Nevis Laboratories.*
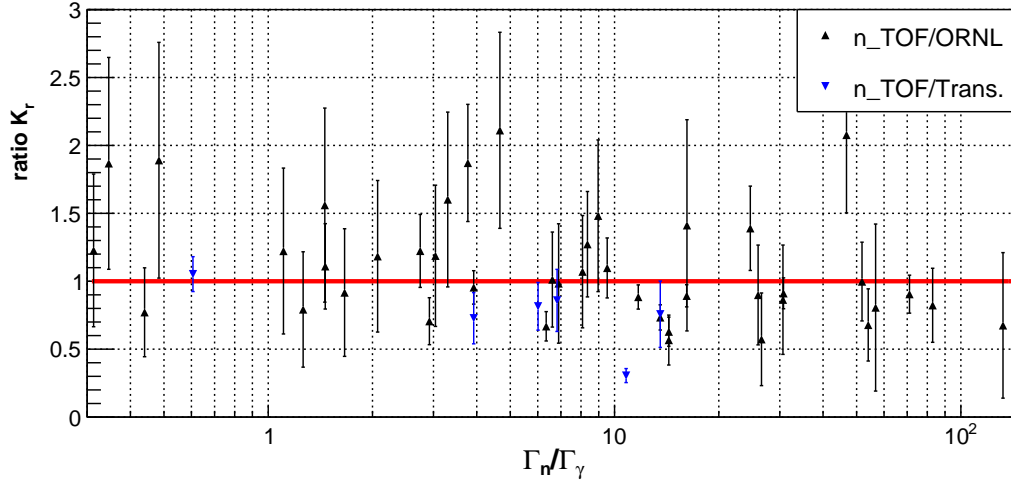
Figure 6.20: *Ratio of n_TOF resonance kernels compared to previous experiments as a function of Γ_γ/Γ_n*

iments up to 32 keV. Focusing in the range up to 13 keV, the lower statistical uncertainty of the strongest resonances allows to see that the new kernels are con-

sistently lower than those reported for the ORNL measurement. More specifically, for resonances with a statistical uncertainty lower than 15% –which are concentrated in the 3.5 keV to the 6.3 keV range– the n_TOF/ORNL ratio of the kernels is quite consistent, averaging 0.91(10). In particular, a smaller trend can be observed in large kernel resonances between 8.5 and 11 keV. The present kernels for this resonances are consistently lower, around 30%–40% approximately, than the respective kernels at ORNL. This could be another indication of a systematic effect related to the neutron sensitivity of the ORNL capture setup.

Incidentally, below a neutron energy of 3.5 keV, where there is no data available from ORNL, both evaluations present important deviations from the experimental data for almost every resonance, especially in the range between 900 eV and 2 keV. This trend in the reduction of the kernels is perhaps better visualized if one looks at the plot of the ratio of the kernels vs Γ_n/Γ_γ, in Figure 6.20. As the ratio between parameters increases, the ratio for most of the resonances is under unity, especially for those with the lowest statistical uncertainty. Since most of these resonances are s-waves, with $\Gamma_n \gg \Gamma_\gamma$, it is expected that the reduction in the radiative kernels should be accompanied by a reduction in the average partial radiative width. $\langle\Gamma_\gamma\rangle$ is obtained by fitting to a constant the Γ_γ values for resonances with $\Gamma_n > 10 \cdot \Gamma_\gamma$, resulting in $\langle\Gamma_\gamma\rangle = 675(53)$ meV. Compared to $\langle\Gamma_\gamma\rangle = 689$ meV from ORNL, this means a reduction of only 2%. However, there is a high uncertainty in the average, ascribed to the difficulties in analysing the broad ($\Gamma_n \gg \Gamma_\gamma$) levels with the present statistics. An additional source of uncertainty might also come from the neutron sensitivity corrections applied to these resonances.

Finally, as can be seen in the yield in Figure 6.9, the low mass sample and low statistics hampers any analysis of the cross section of the RRR and the URR at higher energies than 32 keV.

6.6.4   Systematic uncertainty estimation

As mentioned in section 6.6.2, several resonances were analysed without any residual background, to study the impact in the determination of the resonance area. In Table 6.7, the increments in the radiative kernels for some prominent resonances are listed. The impact of the absence of a residual background is higher as one increases in neutron energy and the amplitude of the resonance decreases. Due to

					Uncertainty due to background				
E_n res. (eV)	236	1137	2789	4667	8512	10166	15102	19170	22400
ΔK_r (%)	0.3	1.9	1.4	1.9	4.2	7.3	7.6	7.2	7.2

Table 6.7: *Variation of the yield due to elimination of the residual background. The results were adopted as the associated systematic uncertainty, σ_{backg}, introduced by the background subtraction process.*

Source of uncertainty	σ_{sys} (%)
PHWT [67]	2
Statistical model of the capture cascade	1
Flux [77]	2
Residual background	0.3 to 7.6
Normalization	1
Yield spread between detectors	1.5
Detector gain shifts	2
Total	**4.0 to 8.6**

Table 6.8: *Assessment of the different sources of systematic uncertainty of the ^{204}Tl(n,γ) measurement.*

the constant and systematic nature of this error, it was adopted as the uncertainty introduced by the background subtraction procedure, and directly added into the uncertainty budget.

The rest of sources of systematic uncertainty considered for the ^{203}Tl(n,γ) analysis are listed in Table 6.8, and have been discussed in the corresponding sections. Due to the variation of the uncertainty associated to the residual background in SAMMY, the systematic uncertainty has been calculated separately for different neutron energy ranges.

6.7 MACS calculation

As described in chapter 1, during s-process conditions neutrons are thermalized at the stellar temperatures of the environment. Therefore, the energy dependent cross section must be folded by the Maxwellian spectra of the neutrons at those temperatures, T:

$$\langle\sigma v\rangle_{kT} = \frac{\langle\sigma v\rangle}{v_T} = \frac{2}{\sqrt{\pi}} \frac{\int_0^\infty \sigma(E_n) \cdot E_n \cdot e^{-E_n/kT} dE_n}{\int_0^\infty E_n \cdot e^{-E_n/kT} dE_n} \ . \tag{6.7.1}$$

The maxwellian spectrum is a continuous distribution, and extends well beyond its peak energy. It can be seen in Figure 6.21 that this effect is more pronounced as the kT value increases. Therefore, to obtain a reliable MACS it is necessary to have cross section information up to energies, ideally, much higher than the peak.

Up to 35 keV, which comprises most of the RRR, the new n_TOF data can be complemented with the ORNL data for the missing levels (see appendix B). However, from 35 keV up to 200 keV, the only available source of data are the evaluations. As it can be seen Figure 6.22, there are important differences between the last versions of JEFF-3.3, ENDF/B VIII.0 and TENDL-2017.

In ENDF, the RRR ends at 19 keV, and beyond an average cross section is provided.

Figure 6.21: *Maxwell-Boltzmann distributions at temperatures $kT = 8$ keV (red) and $kT = 30$ keV (blue).*

In order to check the accuracy of this average cross section, it has been compared to the average experimental cross section (i.e. n_TOF plus ORNL reuslts) in the range from 19 keV to 35 keV. The result is that ENDF overestimates it by 27%. This confirms the tendency seen in the individual resonance analysis, where ENDF also overestimated most of the kernels under 10 keV. On the other hand, JEFF-3.3, which is based in the TENDL-2015 evaluation, provides resonances calculated with statistical Hauser-Feshbach models up to 100 keV, and an average cross section up to 200 keV. It is worth recalling here that predictions based on statistical averages are less reliable closer to the neutron shell closure numbers. There, the level density drops sharply, and the cross section becomes more sensitive to individual resonances.

Figure 6.22: *The cross section of $^{203}Tl(n,\gamma)$ in the range from 20 keV to 100 keV, as predicted by ENDF/B VIII.0, JEFF-3.3 and TENDL-2017.*

Another remarkable feature is that JEFF and TENDL-2017 include only three resonances between 35 keV and 45 keV, which are the highest energy ones observed in the transmission measurement. Due to the low number of resonances, compared to energies up to 35 keV, it is assumed that most levels in the range were not resolved. This is confirmed after plotting the cumulative number of resonances as a function of neutron energy for the JEFF-3.3 evaluation, shown Figure 6.23. The slope is roughly constant from 0 to 35 keV, and then suddenly decreases. From 45 keV to 100 keV, the slope recovers again. This may indicate that the number of resonances has been parametrized in order to reproduce the experimental resonance spacings.

Beyond 45 keV TENDL-17 provides an average cross section, which is consistently about 20% lower than ENDF in the whole energy range up to 1 MeV. From 100 keV to 200 keV, the average cross section in JEFF-3.3 is identical to TENDL-17.

In view of these findings, revised versions of the evaluations were elaborated, to harmonize them with the experimental data:

- In the case of TENDL-2017, the average cross from 45 keV to 200 keV was extrapolated down to 35 keV.

- In the case of JEFF-3.3, new artificial resonances were added in the 35 keV

to 45 keV range, using the average resonance spacing at lower (or higher) energies. The amplitude of these resonances was modelled to those in the > 45 keV range.

- For ENDF/B VIII.0, the average cross section from 35 keV to 200 keV was scaled down by a factor of 0.73, as observed in the comparison with the experimental data.

The MACS has been calculated in the 5 keV to 60 keV range for each evaluation, using in all cases the experimental data (n_TOF + ORNL) for energies below 35 keV. The uncertainty of the parameters is propagated into the MACS calculation by Monte Carlo sampling. Both resonance parameters are assumed to have normal distributions, with a standard deviation equal to the corresponding error. Each parameter for each resonance is sampled randomly, and the MACS ins calculated. After several thousand calculations, a gaussian distribution of the MACS is obtained at each energy, which is fitted to obtain the desired uncertainty. The

Figure 6.23: *Experimental cumulative number of resonances, up to 35 keV, compared to the JEFF-3.3 evaluation for energies > 35 keV.*

reliability of the procedure is checked by comparing the mean of the MACS with the value obtained with the direct calculation of SAMMY. Based on the uncertainty quoted by Macklin and Winters [122], a 10% uncertainty is adopted for the resonance parameters extracted from JEFF-3.3.

The results of the three MACS are plotted in Figure 6.24. This plot includes, for comparison, other MACS distributions. These are the MACS calculated only with the unmodified ENDF evaluation, which is the recommended by the provisional Kadonis v1.0 database, and the results from ORNL, which correspond to the recommended MACS in the current Kadonis version (v0.3). Additionally, the contribution of the n_TOF data alone, and of the combined n_TOF + ORNL data, are also shown in the plot.

The first important observation is that, between the three cases calculated with the experimental data, the difference at 8 keV is only around 1%, which is

Figure 6.24: *MACS of the reaction $^{203}Tl(n,\gamma)$ for the different cross section models tested. n_TOF+ ORNL refers to the cross section from this work with added ORNL data for the missing levels, up to 35 keV.*

Model	Source of cross section		MACS (mb)	
	< 35 keV	> 35 keV	8 keV	30 keV
MACS 1	n_TOF+ ORNL	JEFF-3.3	325.7(16.4)	111.5(7.9)
MACS 2		reduced ENDF	329.0(16.5)	130.8(9.2)
MACS 3		TENDL-17	329.6(16.5)	136.3(9.6)
Recommended			**327.7(18.5)**	**123.9(22.0)**

Table 6.9: *Summary of the different MACS evaluated in this work.*

totally compatible with the respective calculated uncertainties. This underlines the importance of the new results in determining precisely the cross section at low energies. In fact, the resonances measured in this work contribute to 87% of the MACS at 8 keV. ^{13}C-pocket nucleosynthesis takes place at a range of temperatures corresponding to 8 keV to 10 keV of thermal energy. Therefore, the final conclusion is that, for ^{13}C-pocket nucleosynthesis calculations, the choice of the evaluation for energies > 35 keV should not have a relevant impact in the final abundance patterns, even when using ENDF for the high energy part.

Compared to the previous experimental data of ORNL, the inclusion of the levels below 3 keV in neutron energy leads to a MACS consistently higher as we go down in neutron spectrum energy. At 5 keV, the MACS of the present work is 33% higher than the ORNL value. However, at 10 keV, the MACS reported at ORNL is already 12% higher than the one obtained here. This could be a direct consequence of the systematically lower resonance kernels between 8 keV and 10 keV of the present work. The consequence is that the present MACS has a rather different distribution between 5 keV and 10 keV, with a more pronounced decreasing slope between 5 keV and 10 keV.

Concerning the nuclear data evaluations, the MACS at 8 keV obtained with ENDF/B VIII.0 original data is the recommended cross section by the provisional Kadonis v1.0. The new results suggest that it overestimates the MACS by 17%. This is ascribed mainly to the general overestimation in the cross section from 1 to 35 keV, especially due to the average cross section in the 18-35 keV range. It is concluded that the present ENDF evaluation, at least up to 35 keV, is not in agreement with experimental data and thus should not be employed for nucleosynthesis calculations. At 30 keV, the differences at energies higher than 35 keV among the evaluated cross sections have a higher impact in the MACS. The statistical resonance model of JEFF-3.3 provides the lowest MACS of 112 mb, whereas the average cross section of TENDL-17 yields 137 mb, a 22% difference. In between, a MACS of 132 mb is obtained with the reduced ENDF version, a quantity totally compatible with the reported by Macklin and Winters at ORNL of 124 mb.

In view of the results, a recommended value of the MACS at 30 keV has been calculated as the average of the three experimental–plus–evaluation cross sections, 124.5(18.1). For the uncertainty, it was adopted as a realistic value the difference between the highest –TENDL-17– and the lowest –JEFF-3.3. The recommended value matches exactly the 30 keV MACS of Macklin and Winters. Such coincidence could be explained assuming that the contribution of < 3 keV resonances, not measured at ORNL, compensates for the general overestimation of observed in the ORNL radiative kernels of the larger resonances.

Chapter 7

^{204}Tl capture cross section measurement

This chapter will be devoted to discuss in depth all aspects concerning the ^{204}Tl(n, γ) cross section measurement. Most steps of the data reduction process are equivalent to those followed for the ^{203}Tl(n, γ) analysis. However, the high activity of the sample and the uncertainties in its mass and spatial distribution needed additional preparations before the experiment, and required special attention in several aspects during the analysis. Specifically, much care has been put into the background subtraction process and the normalization of the yield.

7.1 Preparation for the experiment

7.1.1 Sample production and characteristics

The ^{204}Tl enriched sample was produced in the framework of a collaboration between CERN, the institute Laue Langevin (ILL, Grenoble, France) and the Paul Scherrer Institute (PSI, Villingen, Swizterland) [34]. The seed sample, prepared at PSI, was a 252 mg pellet of Tl_2O_3, amounting to 225 mg of thallium. This was enriched up to 99.5% in ^{203}Tl. The pellet was irradiated with thermal neutrons for 56 days in the experimental reactor at ILL. The final isotope distribution was calculated from the initial seed composition and the neutron irradiation parameters. The abundances of the most important nuclear species present in the sample at the time of the experiment are summarized in Table 7.1. The total amount of

	^{204}Tl	^{203}Tl	^{204}Pb	^{205}Tl	^{60}Co	Total
Conc. (%)	3.99(4)	93.2(5)	1.9(4)	0.89(4)	$1.53(1) \cdot 10^{-5}$	99.98
Mass (mg)	8.98(5)	210(1)	4.34(5)	1.99(5)	$3.44(1) \cdot 10^{-5}$	225(1)
Activity (Bq)	$\mathbf{1.54 \cdot 10^{11}}$	–	–	–	$3.73 \cdot 10^{5}$	$1.54 \cdot 10^{11}$

Table 7.1: *The composition of the ^{204}Tl enriched sample, including the most important impurities for the experiment and the posterior analysis, at the time of the experiment (June 2015). Values are calculations based on the initial seed composition and the time of irradiation.*
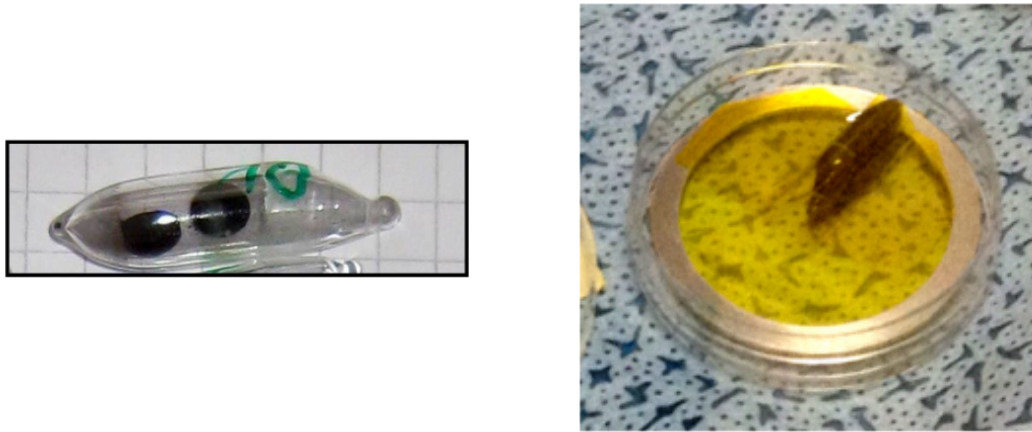
Figure 7.1: *Left: The Tl_2O_3 pellet had already broken in two pieces before the irradiation in the neutron reactor. Right: The sample after irradiation, already fixed on the aluminium ring by means of kapton foils. The inner walls of the capsule had totally blackened.*

^{204}Tl was 9 mg, which corresponded to an enrichment of 4%. The rest of the sample was mainly ^{203}Tl (210 mg, 93%), with small amounts of ^{204}Pb, the daughter isotope of ^{204}Tl, and ^{205}Tl. Finally, the presence of 373 kBq of ^{60}Co is ascribed to the activation, during irradiation in the reactor, of a small cobalt impurity (< 0.3 ppm) in the ^{203}Tl oxide seed sample. The consequences of the ^{60}Co impurity for the measurement and the analysis will be discussed in detail in section 7.5.

Prior to irradiation, the sample was enclosed in a small quartz capsule, which was sealed upon moulding in order to avoid any dangerous loss of material during and after the irradiation. The quartz capsule had an approximately cylindrical shape (see Figure 7.1), with a length of 3 cm, an external diameter of 10 mm, and 1 mm thick walls.

7.1.2   Gamma ray scanning of the sample

After production in the ILL reactor, it was necessary to evaluate the physical state of the sample after a 55 days long irradiation. The reason behind this was that the ^{203}Tl pellet, which had been produced by pressing of a powder, had already broken in two pieces before the experiment, which were loosen inside the quartz container (Figure 7.1, left). It was unknown whether, in the harsh conditions of constant heat and neutron irradiation in the reactor, it could have broken further, or even pulverized. Another, perhaps more important concern was that the sample could have adhered to some parts of the capsule, which could remain out of the beam during the experiment.

At n_TOF, sample holders are usually aluminium rings, with a diameter of 6 cm. When in position, the centre of the ring is aligned to the centre of the neutron beam. The quartz container was attached to the aluminium ring with kapton tape –right picture of Figure 7.1–, so the top of the capsule laid in the centre of the ring. Due to the longer size of the capsule compared to the radius of the neutron beam –approximately 1.7 cm–, a sizeable part of the capsule would remain outside the beam. It was possible that portions of the sample, due to the heat, had adhered to those parts of the capsule staying out of the beam.

However, it was impossible to inspect visually the interior of the quartz container, because the irradiation in the reactor had turned it totally black opaque. Furthermore, close manipulation was not convenient due to the very high contact dose of 620 mSv/h, and of 18 mSv/h at 10 cm. Therefore, it was necessary to devise a remote method to characterize the geometry of the sample. For this purpose, a gamma ray imaging device, or scanner, was designed and build. This device, which could be operated remotely, exploited the very high decay radiation of the sample to image its spatial distribution. Detailed pictures of the scanner, taken during the sample characterization and depicting its main components, can be seen in Figure 7.2.

The scanner had two main parts. There was a fix base aluminium structure, at the end of which the imaging system was mounted. This consisted of a NaI gamma ray detector, shielded with thick blocks of lead on all sides. The block on the front had a 4 mm diameter circular window, and was designed to fit, on the external face, a pinhole (1 mm) tungsten collimator. In this way, the detector acted like a

collimated gamma ray camera, with a spatial resolution calculated to be ~ 2 mm at the face of the detector.

The second part of the scanner mas movable, and consisted of an aluminium bar, which was free to slide on the base structure, and at the end of which a lift table was mounted. This had been adapted, in such way its elevation could be adjusted remotely by means of a 2 m long screw. Finally, on top of the table lift, an aluminium sample holder was placed, which had been specifically designed to fit securely the ^{204}Tl sample. Live close images of the latter during operation were obtained by means of a webcam attached at the end of the scanner structure.

The smooth sliding of the aluminium bar allowed precise positioning, in steps of 1 mm, in the horizontal direction. In the vertical axis, the table lift was adjusted in steps of quarter of a full turn of the screw, which corresponded approximately to 2 mm. In this way, the scanner permitted a detailed two-dimensional mapping of the distribution of the material inside the capsule. In addition, the operation could be performed manually from a 2 m distance from the sample, where the gamma ray dose was low enough for prolonged safe stays.

Scans were conducted with the capsule both in horizontal and vertical orientations. From an initial position, data was taken in regular steps in the horizontal direction. After a full horizontal scan, the sample was lifted and the procedure repeated. The step in the horizontal direction was 3 mm for the sample in horizontal orientation, and 2 mm for the vertical direction. Results of the vertical scan are shown in Figure 7.3.

The latter features the measured distribution of the ^{204}Tl material inside the capsule, plotted on top of a 2D cross sectional view of the n_TOF beam, obtained independently with a μ-Megas detector [82]. A schematic view of the aluminium ring external border and the capsule is included, as a size reference. The procedure was successful in revealing that most of the sample was concentrated in a single piece, which apparently was still free to move inside the capsule. With the capsule in vertical position, it laid close to the bottom of the container. However, a small fragment of the sample had adhered to the other end of the quartz capsule (i.e. the closest part to the aluminium ring). This part would remain out of the beam during the measurement. The final conclusion drawn was that, provided the capsule was in vertical position, most of the sample would lie close to the centre of the beam, which enabled the measurement of ^{204}Tl(n, γ).
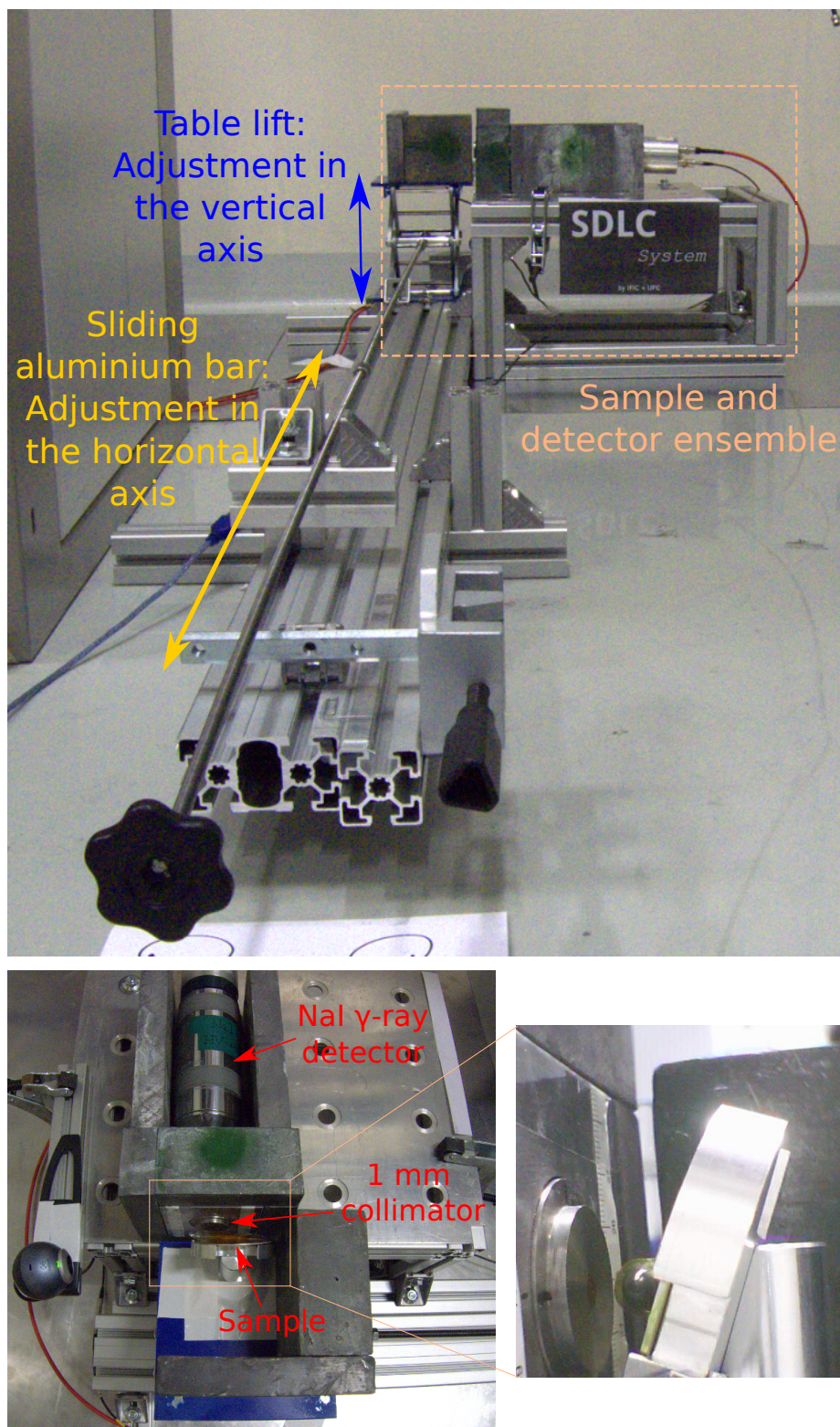
Figure 7.2: *Top: General view of the gamma ray scanner. Bottom left: Top view of the detection part of the device. The detector was shielded with thick lead blocks, including a top foil removed for the picture. Bottom right: Detail view of the sample, in horizontal orientation, during a scan run.*
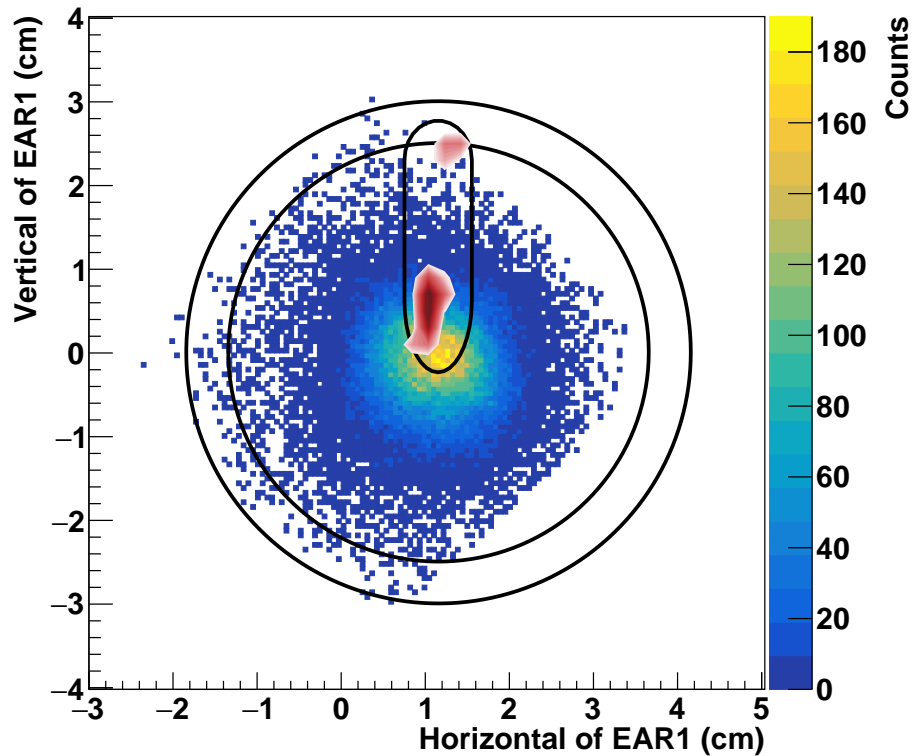
Figure 7.3: *2D Plot of the n_TOF beam profile. The sample distribution determined with the scanner is plotted in red/pink tones, the darker tones indicating the zone with the highest measured activity. The contour of the aluminium ring and the capsule are plotted in thick black lines.*

On the basis of the ratios of activity of both fragments, we estimated that the bigger fragment contained between 70% and 80% of the sample. The atomic thickness is one of the key parameters for calculating the cross section. Such uncertainty in the mass irradiated during the experiment is one of the main challenges in the analysis of the data. To overcome this problem, a specific normalization method was devised, which is described extensively in section 7.10. It allowed to determine an *effective* mass for the reliable analysis of the capture yield. This method also permitted to estimate the corresponding systematic error associated to the uncertainty on the sample mass.

	^{204}Tl	Dummy	Beam off
Mass (mg)	$\mathbf{9 \pm 1}$	-	-
Enrichment (%)	4	-	-
Protons	$1.82 \cdot 10^{18}$	$7.13 \cdot 10^{17}$	-
Runs	See Table 7.3	102101-04, 102129-33 102352-66	102059, 102073, 102152, 102179,102192-93, 102200-02, 102253

Table 7.2: *Summary of the beam statistics for the ^{204}Tl sample, and those employed to estimate the background for the ^{204}Tl(n, γ) analysis.*

7.2   Experiment

Once the ^{204}Tl-enriched sample was put in the n_TOF beam a series of preliminary data acquisition runs were taken in order to perform the final adjustments in the experimental setup and the DAQ system parameters. The data produced in these runs turned to be of impractical use, due to the huge photon emission derived from the activity of the sample. On top of that, there was a real concern that the amount of signals would lead to pile-up and detector dead time issues.

As mentioned in section 3.6, to deal with this problem lead foils of 2 mm in thickness were positioned in front of each detector. This shielding was successful in reducing the amount of low energy gamma rays being detected, decreasing the detection efficiency below 250 keV down to negligible values (see section 5.1.1 for details). This led to huge reduction of the background, but this improvement came at the expense of reducing the capture yield detection efficiency. In any case, the reduction in background led to a much improved signal-to-noise ratio, which outweighs the reduction in the absolute yield statistics.

The data acquisition for the ^{204}Tl(n, γ) measurement was distributed in two main blocks of runs, which are listed in Table 7.2. The photon background induced by the interaction of beam particles in the quartz capsule was evaluated employing an empty quartz container. The other main source of background was caused by the activity of the sample itself, and was measured simply by acquiring data without beam (in the following, these runs will be also referred to as *beam-off* runs). Measurements of both backgrounds were distributed along the course of the campaign.

Date	Run type	Runs
Jun 26 – 3 jul	^{204}Tl-enriched sample	102031-47, 102058, 102064-69
Jul 3	Calib: ^{88}Y, Am-Be, ^{60}Co	102070-73
Jul 3 – Jul 6	^{204}Tl-enriched sample	102075, 102078-79, 102081-82
Jul 17	Calib: ^{88}Y, ^{60}Co	102151-52
Jul 17 – Jul 29	^{204}Tl-enriched sample	102153-78, 102183-91, 102195-98, 102203-06,
		102225-35, 102237-41, 102243-50
Jul 29	Calib: ^{88}Y,Am-Be, ^{60}Co	102251-53

Table 7.3: *Timeline of the ^{204}Tl*(n, γ) *measurement. For clarity purpose background measurements have not been included.*

7.3   C$_6$D$_6$ calibration in deposited energy

Already during the time of the experiment, a prominent peak around 950 keV was observed in the deposited energy spectrum of all C$_6$D$_6$ detectors, for both runs with and without beam. The peak was identified as the overlapping of the Compton borders of the two gamma rays produced by the decay of ^{60}Co, which have energies of 1.17 MeV and 1.33 MeV. This was confirmed by Geant4 simulations of the response of the detector setup to a ^{60}Co source. The signals produced by the ^{60}Co gamma rays were the main source of background above 800 keV. However, the ^{60}Co in the sample could be exploited as an additional, always present, calibration source. This turned out to be very helpful as a "low" energy point, since both the 667 keV peak of the ^{137}Cs source, and the first peak at 898 keV of the ^{88}Y source, were buried under the continuum of signals from the decay of ^{204}Tl.

Thus, for the energy calibration of the C$_6$D$_6$ detectors were employed the second peak of ^{88}Y (1.84 MeV), the ^{60}Co embedded in the ^{204}Tl sample, and the Am-Be source. Additionally, as a high energy calibration point, the ^{203}Tl(n, γ) deposited energy spectrum was used. For the latter, a selection in TOF corresponding to the 235.7 eV resonance was made. The endpoint of this spectrum –prior to detector resolution broadening– corresponds to the Compton edge of the neutron separation energy of ^{204}Tl, equal to 6.656 MeV. An example of a calibration for C$_6$D$_6$#3, using the four gamma ray energies, is shown in Figure 7.4. Due to the activity of the sample, background subtraction was necessary in the case of the 235.7 eV resonance capture spectrum. The latter was assessed by averaging the
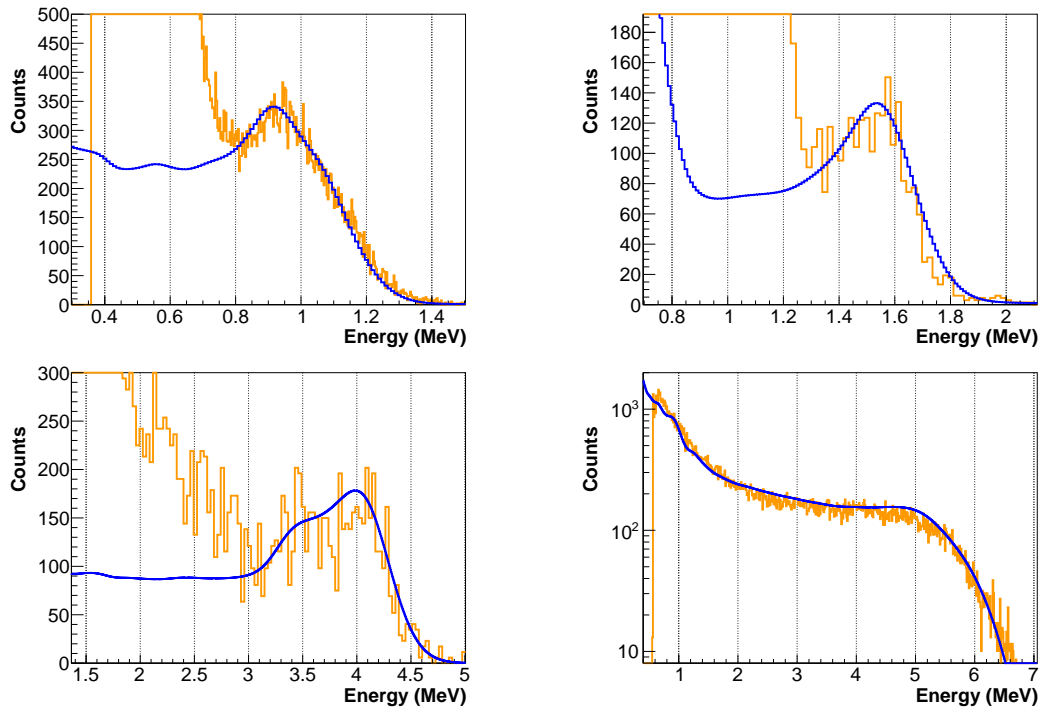
Figure 7.4: *Experimental (orange) versus simulated (blue) energy deposited spectra in $C_6D_6\#3$, for the July 3rd calibrations. The sources are the sample-embedded ^{60}Co (top left), the second peak of ^{88}Y (top right), the Am-Be (bottom left), and the 235.7 eV ^{203}Tl capture resonance spectrum.*

deposited energy spectra of background signals recorded before and after the 235.7 eV resonance.

Calibrations were performed during the first block of runs (runs 102070-102073, *July 3rd* calibrations), before the second block (runs 102151-52, *July 17th*), and after it (runs 102251-53, *July 29th*). When using external sources, the sample was kept in beam position in order to account for possible gain variations in the detectors caused by the very high counting rate.

The calibration runs from July 29th were immediately followed by calibrations without the ^{204}Tl sample in the beam position, employing the ^{88}Y source. Thus, a direct comparison could be done to study the immediate effect of the high counting rate in the gain of the detectors. The results are plotted in Figure 7.5. In all detectors, the presence of the sample led to a general increase in the gain of the detectors, evidenced as a shift in the position of the ^{88}Y second peak. The magnitude of the shift is small in $C_6D_6\#1$, and moderate in $C_6D_6\#2$ and $C_6D_6\#4$.
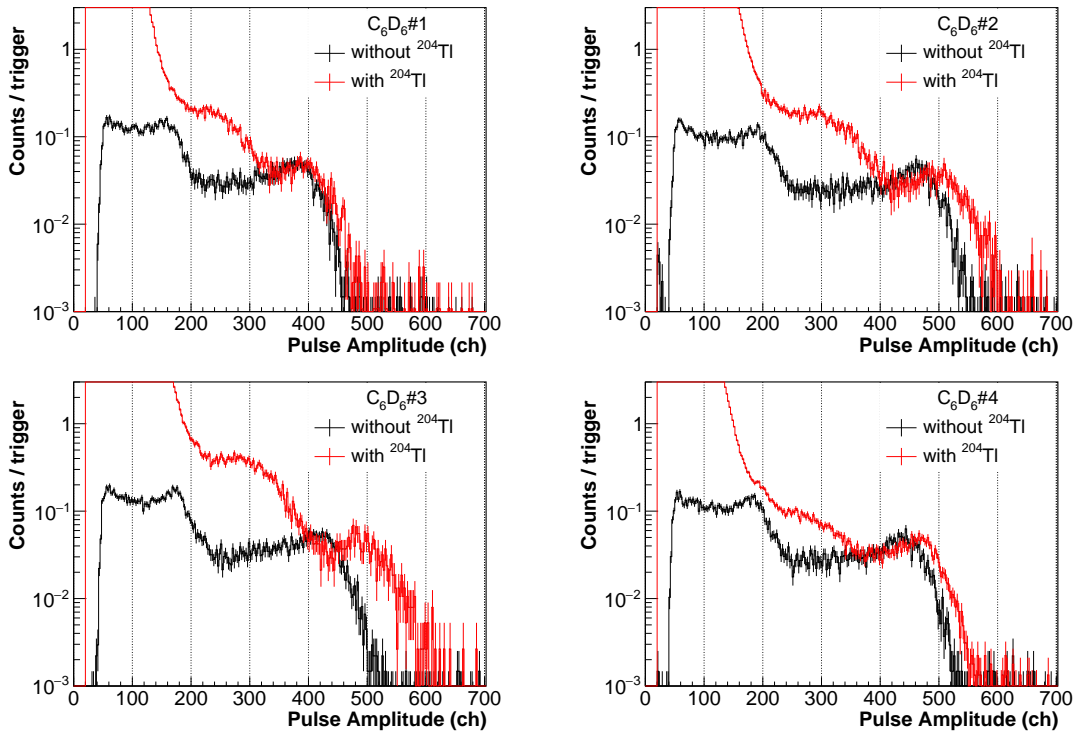
Figure 7.5: *^{88}Y measured spectra in the July 29th calibrations. In red, with the ^{204}Tl in the beam position, and in black, without the sample.*

However, it is particularly high in $C_6D_6\#3$, with a 16% shift in amplitude at the energy of the peak. Such a strong effect underlines the need for dedicated and periodic calibrations along the course of the ^{204}Tl(n, γ) data acquisition run.

7.4   Gain and counting rate monitoring

After the energy calibration of the detectors, the next step was to check the stability of the gain and the counting rate along the measurement. Thanks to the periodic calibrations, gain variations were kept under control for C_6D_6 #1, #2 and #4, as can be seen in Figure 7.6. Like in the case of the ^{203}Tl(n, γ) measurement, $C_6D_6\#3$ showed noticeable gain fluctuations, especially for runs between 102168 and 102198. In these runs there was a decrease in the gain of approximately 3%. However, due to the low number of runs involved, and the small fluctuations, it was decided not to discard the data of $C_6D_6\#3$ for the final analysis. Instead, the systematic uncertainty associated to gain fluctuations of that detector was
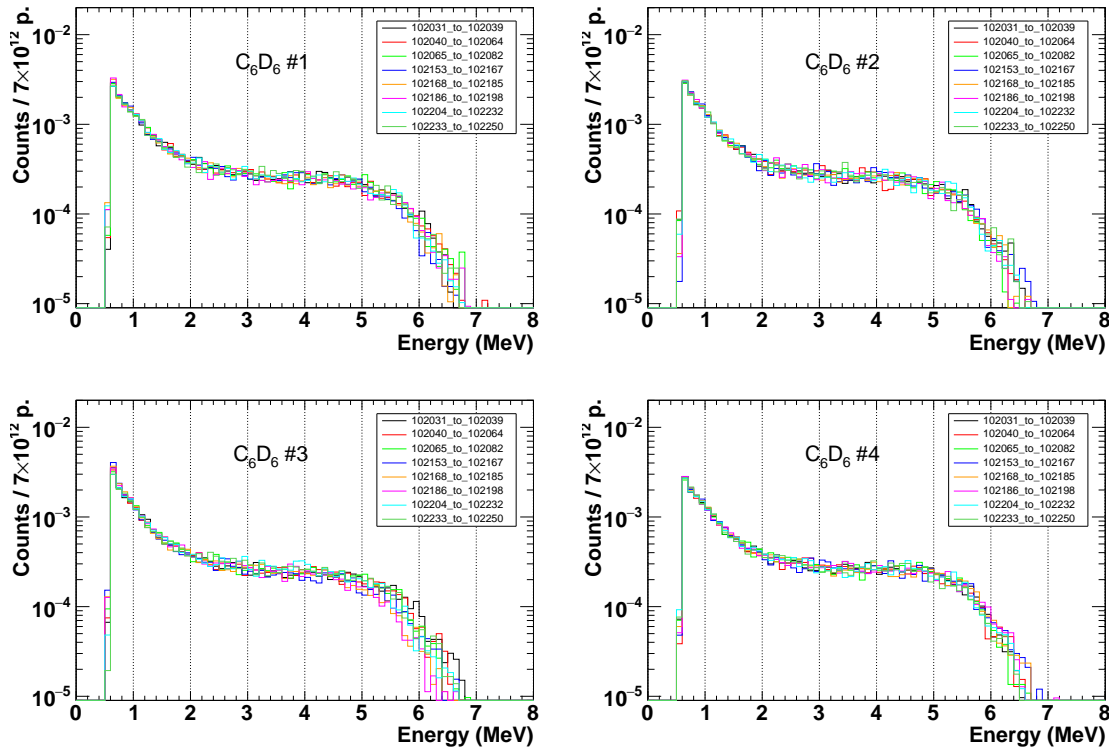
Figure 7.6: *Energy deposition in the four C_6D_6 detectors, for different runs along the measurement.*

increased accordingly.

The second step in the analysis was to validate the consistency of the data recorded in the detectors by means of counting rate crosschecks between them. Because the counting rate was overall dominated by the sample background, the checks were obtained for a time-of-flight window limited to a capture resonance. Exploiting the 93% content in ^{203}Tl of the sample, the 235.7 eV resonance of ^{203}Tl was employed for this task, since it has the highest counting rate of all observed resonances. As it can be seen in Figure 7.7, the C_6D_6/SiMon ratio was mostly stable for all four detectors through most of the measurement. However, between events #80000 and #145000, corresponding to the start of run #102204 and run #102153, a slight increase in the counting rate of C_6D_6#3 and #1 can be observed, of around 6%. In both cases, it was the first run after the sample had been placed back in the beam position. A very similar trend is observed also in the C_6D_6/BCT ratios for those two detectors, but not in the SiMon/BCT ratio. This implies that

Sample	f_{si}	Runs
^{204}Tl, Dummy	1.068	all
^{203}Tl	1.065	102141 to 102147
	1	102280 to 102307
Empty frame	1.074	all

Table 7.4: *List of the f_{si} factors empoyed in the ^{204}Tl(n, γ) analysis.*

the issue was most probably related to a slight variation in the position of the sample, thereby changing the efficiency of the setup.

Because the variation was moderate, for a limited time and in only two detectors, no correction was applied in this case, since the error introduced in the final total yield was estimated to be 1%, much less than the statistical uncertainty.

In addition, a substantial decrease in counting rate was observed for the last $\sim$ 10000 events. This decrease was quite consistent across all of the detectors, between 14% and 17% in both the C_6D_6/SiMon and the C_6D_6/BCT ratios. However, there is no appreciable change in the SiMon/BCT ratio. The latter is displayed in dark grey at the bottom panels of Figure 7.7. This leads to the conclusion that the issue is most probably not related to the beam, but rather to the experimental setup. Since the cause of this variation could not be precisely identified, and owing to the small fraction of statistics affected, it was decided to completely discard those runs from the final analysis.

Finally, as mentioned above, the SiMon/BCT ratios for the different samples of the campaign are plotted at the bottom panels of Figure 7.7. It can be seen that the ratio between the ^{204}Tl capture and the dummy background measurement is the same. However, when compared to the second bunch of runs of the ^{203}Tl(n, γ) measurement, the ^{204}Tl ratio is noticeably lower. More interestingly, the difference found here is almost the same than that found between the first and second bunches of runs in the ^{203}Tl campaign, around 6% (see section 6.2.2). This is an additional indication of the existence of some underlying systematic related to the value reported by the BCT. In any case, like in the ^{203}Tl analysis, the SiMon/BCT of the ^{197}Au runs was taken as reference for all measurements, and thus it was necessary to apply a correction factor f_{si} to all the ^{204}Tl sample and dummy data, as reported in Table 7.4.
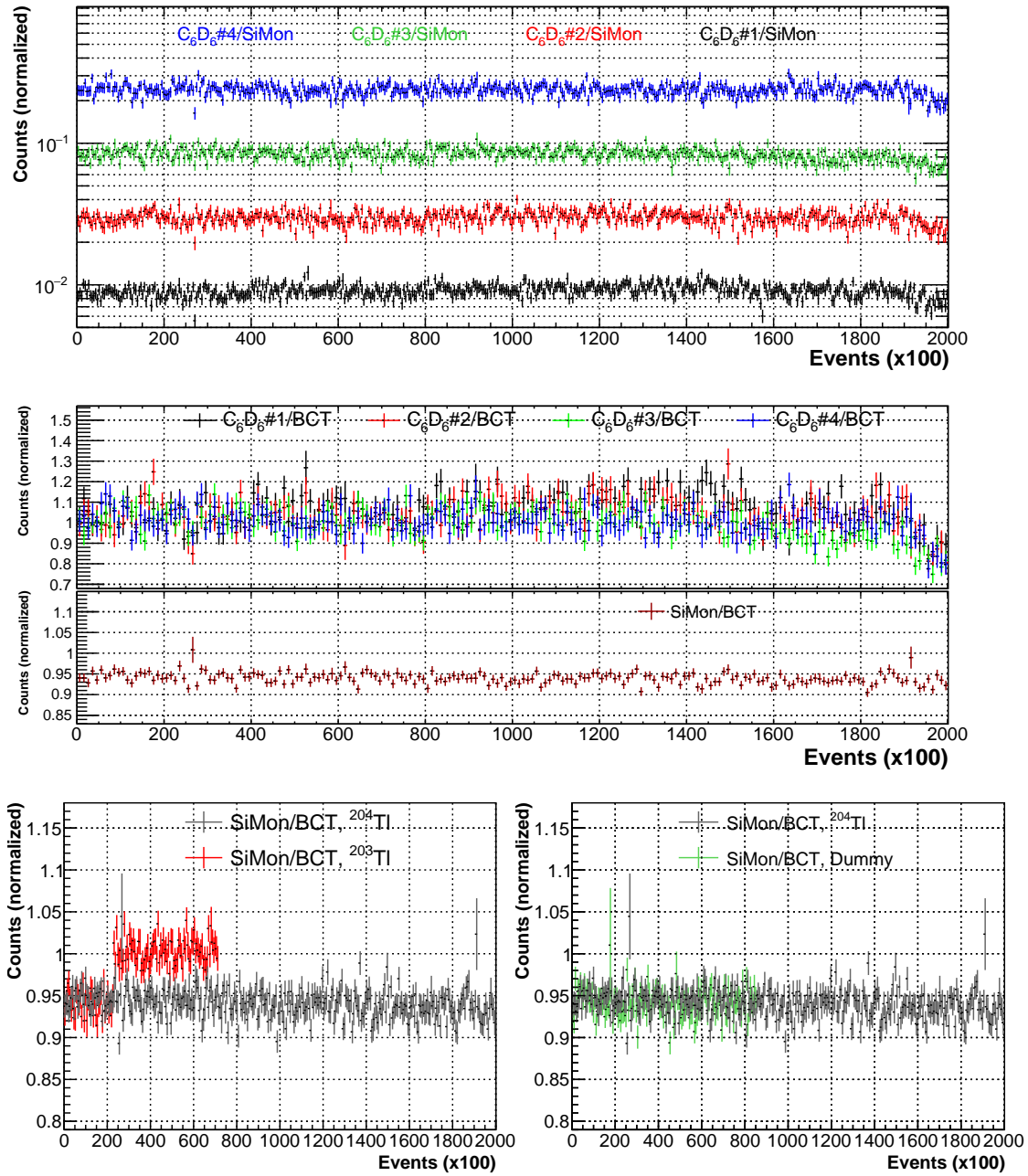
Figure 7.7: *(Top) Raw counting rate for the C_6D_6 detectors and the monitoring devices during the $^{204}Tl(n,\gamma)$ measurement, averaged per 100 events. (Middle) Ratio between C_6D_6 detectors and the SiMon counting rate. As an example, $C_6D_6\#2$ counting rate has been fitted to two constants to show the difference in the last ~ 20000 events. (Bottom) The SiMon/Proton Intensity ratio for the $^{204}Tl(n,\gamma)$ runs (in black), compared to the ^{203}Tl employed for normalization, and the dummy container, which has been used as the background sample.*

7.5   Selection of the deposited energy threshold

Due to the activity of the sample, the subtraction of the background constitutes one of the most delicate steps in the analysis of the ^{204}Tl(n, γ) data. Also, a careful determination of the best threshold energy, E_{th}, must be done in order to find the best trade-off between background rejection and detection efficiency. Although most of the beta radiation emitted by ^{204}Tl is stopped in the quartz container, the electron stopping process produces a huge amount of bremsstrahlung radiation, which has a continuum distribution with a maximum energy equal to the maximum beta energy, which is 763 keV. This corresponds to a Compton edge of 572 keV. Considering that double and even triple Compton coincidences are probable because of the high activity, and the broadening due to the resolution of the detectors, the background from the ^{204}Tl decay will extend up to 1 MeV or more (see Figure 7.8). However, beyond ~ 780 keV the signals from the decay gamma rays of ^{60}Co become the dominant source of background, as already seen in section 7.2. In the end, the whole background caused by the sample activity (referred hereafter as *sample-induced* background, B_{SI}) extends up to 1.4 MeV.

In this scenario, two options were considered for the background rejection. Either putting a very high digital threshold, to eliminate all the SI background
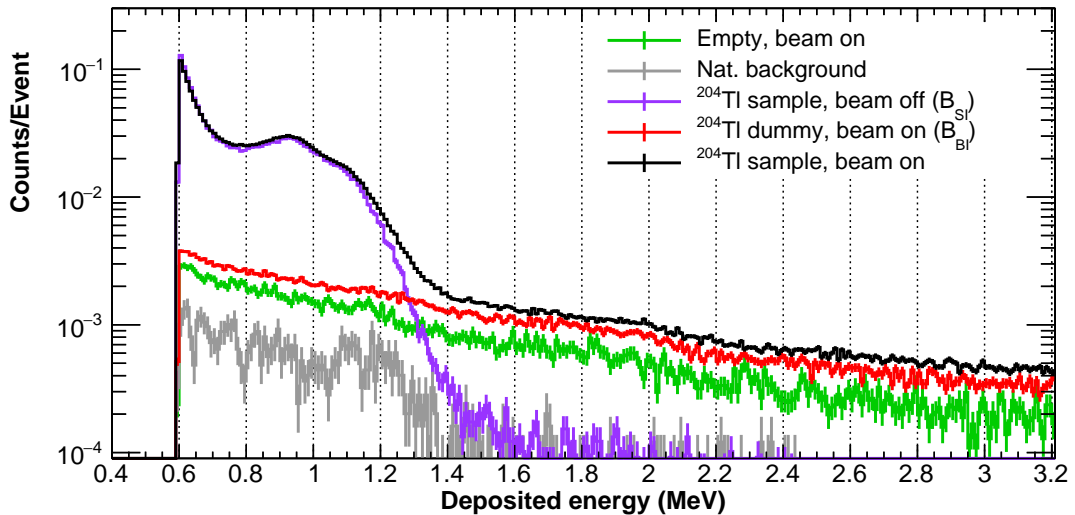
Figure 7.8: *Gamma ray deposition energy in $C_6D_6\#2$, in the range 0.4 to 3.2 MeV, for the different measurements of the ^{204}Tl(n, γ) campaign.*

Threshold (keV)	Counts	S/N	C. norm to 600 keV	S/N norm. to 600 keV
$600 - B_{SI}$	11026(119)	15.71(62)	1	1
600	12602(112)	5.25(12)	1.14(2)	0.33(2)
$850 - B_{SI}$	10372(106)	15.86(64)	0.94(1)	1.01(6)
850	10807(104)	9.56(30)	0.98(1)	0.61(3)
1600	8751(94)	14.83(63)	0.79(1)	0.94(5)
2500	7289(85)	17.35(87)	0.66(1)	1.10(7)

Table 7.5: *The signal-to-noise analysis for the ^{204}Tl resonance at 122 eV. For $E_{th} = 600$ keV and $E_{th} = 850$ keV both cases with background subtraction $(-B_{SI})$ and without it are reported.*

Threshold (keV)	Counts	S/N	C. norm to 600 keV	S/N norm. to 600 keV
$(600 - B_{SI})$	860(45)	1.97(14)	1	1
600	1421(38)	1.37(6)	1.65(10)	0.70(6)
$(850 - B_{SI})$	782(119)	2.00(13)	0.91(6)	1.02(10)
850	941(31)	1.65(9)	1.09(7)	0.84(7)
1600	663(26)	2.02(14)	0.77(5)	1.03(10)
2500	557(24)	2.18(17)	0.65(4)	1.11(11)

Table 7.6: *Same as Table 7.5, for the ^{204}Tl resonance at 915 eV.*

directly, or using a low threshold, applying afterwards a subtraction of the beam off data. To determine the best strategy, we used $C_6D_6\#1$ data to obtain the signal-to-noise ratio and the absolute number of counts of the most important $^{204}Tl(n,\gamma)$ resonances, for several values of the threshold from 600 keV to 2500 keV. For the thresholds with $E_{th} < 1000$ keV, the beam off background data B_{SI} was subtracted. The background level at the resonance was calculated by interpolation. The results for the ^{204}Tl resonance at 122 eV and 915 eV are shown in Table 7.5 and Table 7.6 respectively, for several values of E_{th}.

Comparing high and low thresholds, it can be seen that a moderate improvement of the S/N ratio, in the best case of 10%, can be achieved at the expense of a remarkable reduction in statistics of 34%. In addition, for low energy thresholds the use of the background subtraction provides a much better S/N, as expected. At the 915 eV resonance, the S/N relation is much lower in general, and thus the improvement caused by the subtraction is less pronounced. In any case, low

thresholds still outperform the higher ones. Therefore, a 600 keV threshold with dedicated beam off background subtraction was chosen for the final data reduction.

7.6   Background subtraction

After the deposited energy threshold was selected, the next step is to subtract the background for each detector separately. As already outlined in section 7.2, apart from the sample-induced background, the other relevant background component is that produced, directly or indirectly, by beam particles scattered in the sample (*beam-induced* background, B_{BI}) and the quartz container.

Gamma rays from decay reactions are emitted –and detected– at a constant rate over time. In neutron energy histograms, due to the logarithmic binning employed, they will take the form of smooth negative exponentials. Hence, in principle, beam-off data might be subtracted directly. However, it was observed that, in some detectors, at low neutron energies the beam-off spectra registered more counts than the beam-on histograms. The change in the counting rate was produced, most probably, by small, temporal variations in the gain for some specific beam off runs. Due to the very high counting rate at low deposition energies, even a very small reduction in gain would lead to high fluctuations in the counting rate. Furthermore, the lack of gamma ray sources with energies lower than 900 keV makes the calibrations less reliable at those energies. The consequence is that, the lower the threshold is, the bigger are the discrepancies between beam-off and beam-on data. This is the main reason why a threshold lower than 600 keV has not been considered for the analysis.

The beam-off data has been renormalized by scaling it by a factor k, using the ^{204}Tl beam on data as a reference. However, for this purpose it is necessary to estimate reliably the beam-induced background. This has been done by means of selections in deposited energy. As it is shown in Figure 7.8, the number of counts of the B_{SI} (violet line) drops sharply above 1.6 MeV. On the other hand, those of the dummy sample have a rather flat and smooth energy distribution, with an important contribution up to several MeV. Additionally, the time distribution of the beam-induced background remains almost identical from 5 eV to 100 keV when raising the threshold, as demonstrated in Figure 7.9. Thus, by sorting the dummy data with a threshold of ≥ 1.6 MeV, one can obtain a meaningful neutron energy distribution of the sample dummy alone, and its relation to the ^{204}Tl(n, γ)
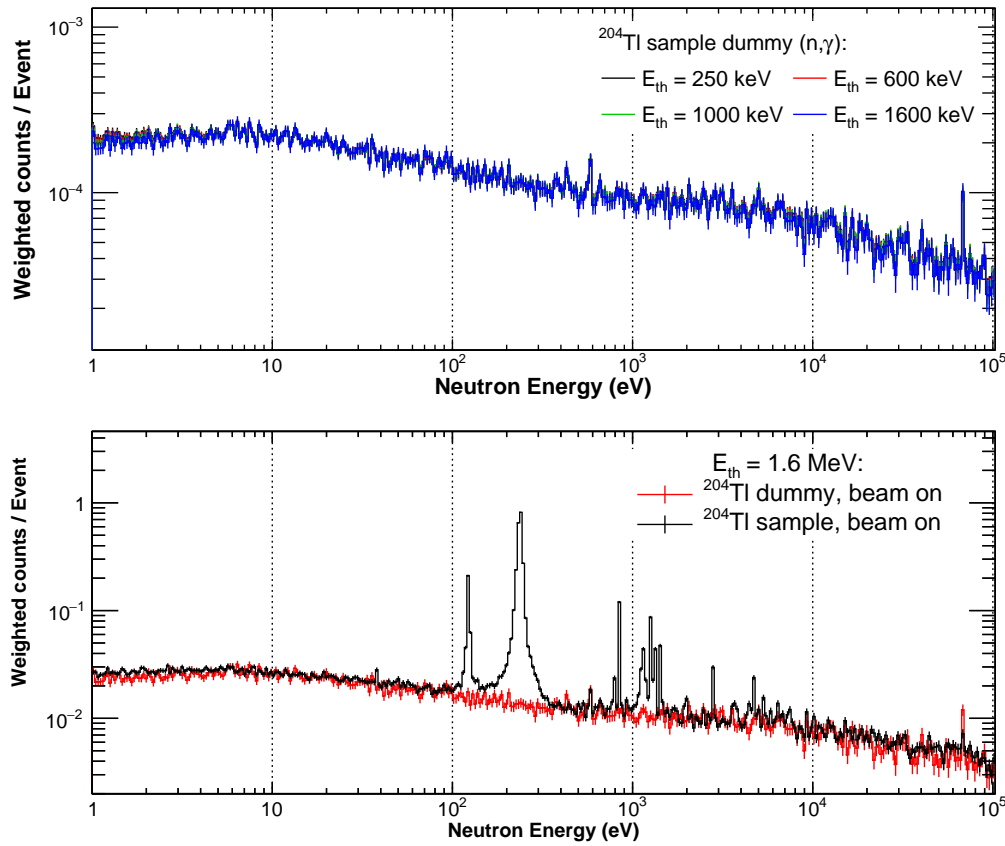
Figure 7.9: *Top: Neutron energy distribution of the ^{204}Tl sample dummy signals, for different values of the deposited energy threshold. The spectra have been normalized to the counting rate in the 5 eV to 30 eV range. Bottom: The ^{204}Tl sample and the ^{204}Tl dummy neutron energy spectra, with $E_{th} = 1.6$ MeV. Both measured with $C_6D_6\#1$.*

histograms.

In the bottom panel of Figure 7.9, the neutron energy histograms of the ^{204}Tl sample and the dummy sample are plotted, with a threshold of $E_{th} = 1.6$ MeV. It can be seen that the dummy sample matches nicely the capture spectrum in the valleys between resonances, and especially in the 5 to 30 eV region, far from the capture resonances. Therefore, it is assumed that the dummy is a good estimation of the beam-induced background. Now, we can proceed again with the beam-off scale factor calculation. Two assumptions can be made:

- At low neutron energies, on the basis of what has been discussed in the previous paragraph, we assume that all signals in the interval 5 to 30 eV are

background, so $C_{tot} \approx B_{tot}$.

- In that same interval, the total background, B_{tot}, can be decomposed as

$$B_{tot} = k \cdot B_{SI} + B_{BI} - B_{nat}, \qquad (7.6.1)$$

where k is the scale factor we need to determine, and B_{nat} is the spectrum of the natural background of the facility.

This is accomplished by solving iteratively the equation $C_{tot} - kB_{SI} \approx B_{BI}$ for k in the 5 to 30 eV interval. Once k is obtained, the beam off spectra are scaled and subtracted from the capture spectra. If the latter matches the shape of the B_{BI}, it will imply that equation (7.6.1) holds, and thus, the above assumptions can be validated.

The result of the subtraction procedure is shown in Figure 7.10, for $C_6D_6\#4$, as an example. The blue histograms are the ^{204}Tl sample capture spectra, with the activity subtracted. Far from resonances, they match the shape of the dummy spectra remarkably well, which can be viewed as a consistency proof of the whole beam-off subtraction procedure. We can proceed then to subtract the B_{BI} to obtain the radiative capture counting rate.
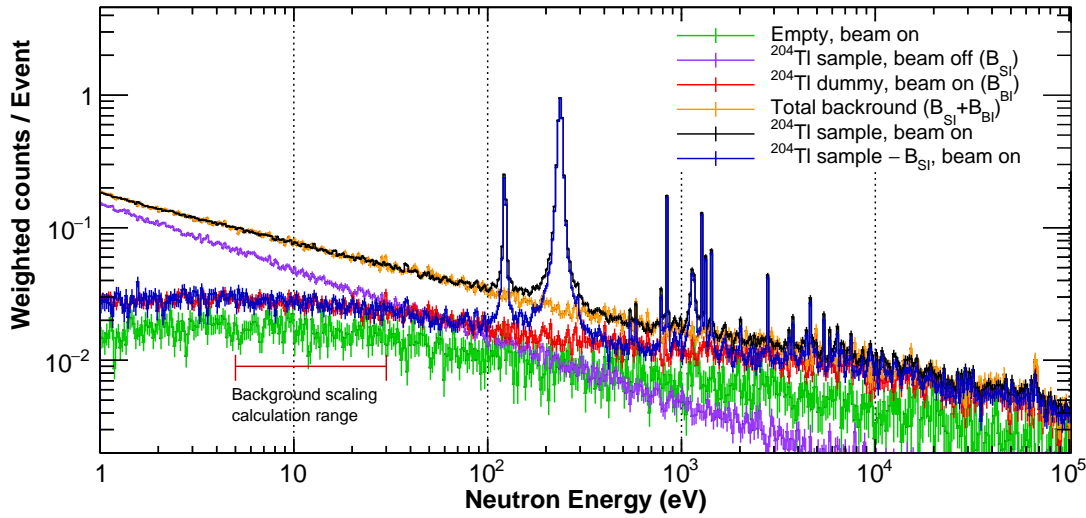
Figure 7.10: *Neutron energy histograms of the $^{204}Tl(\text{n}, \gamma)$ campaign, measured by $C_6D_6\#4$. The beam-off scale factor applied* k *was 0.982. The ^{204}Tl beam-off has been plotted as measured (violet), without applying factor* k*, in order to display the issues concerning the beam off counting rate (1–5 eV region). However,* k *has been applied for the total background addition (in orange). A reference to the energy range employed for the calculation of* k *is also included (dark red segment).*

7.7   Simulation of the ^{204}Tl capture cascades

As seen in the ^{203}Tl(n, γ) analysis, the impact in the capture yield of several sources of systematic error can be estimated by means of simulations of a large number of randomly generated ^{204}Tl cascades. To this aim, one has to determine, previously, a set of cascade parameters which accurately reproduce the experimental capture spectra.

In the absence of previous capture experiments on ^{204}Tl, all the experimental information on the excited levels and photon transitions of the compound nucleus, ^{205}Tl , comes from experiments performed directly on its ground state, which is stable. They consisted of gamma ray spectroscopy measurements from inelastic reactions such as ^{205}Tl(γ, γ'), ^{205}Tl($n, n\gamma'$) and others. In the end, we relied mainly on the ^{205}Tl(γ, γ') measurement reported in [126], which is available in the ENSDF database. The reason was that the electromagnetic transition intensities provided therein are normalized to 100 excitations of ^{205}Tl induced by monochromatic γ-rays of 7.646 MeV. This is comparable to have the intensities normalized to 100

^{205}Tl(n, γ) reactions, which is the format used in the MC code of this study, since the S_n of ^{205}Tl is 7.5460(5) MeV [101].

There is a big gap in the number of observed levels between the one at 3.288 MeV and the full excitation energy at 7.646 MeV. Existing levels in that range are considered to be missing due to the increasing difficulty to observe higher energy gamma transitions, and therefore it was decided to use the statistical model from a cut off energy of 3.28 MeV. Concerning the latter, the Back-Shifted Fermi Gas Model employed requires two parameters, the level density a_{ld}, and the shell correction energy, δ_{eff}. Unfortunately, in the references employed in the ^{203}Tl analysis there are no recommended values for ^{205}Tl, since calculations are based on the number of levels beyond the neutron separation energy (i.e. capture resonances). To estimate both parameters, they were empirically adjusted in order to match the experimental number of levels, N_l. As a first input, the shell correction was set arbitrarily to -0.8 MeV, a value lower than the recommended value for ^{204}Tl or ^{206}Tl. The adoption of this value was motivated by the predicted systematic trend that shows that odd-even nuclei have lower shifts energies compared to odd-odd nuclei, especially in the $200 < A < 210$ mass region (figure 2 in [117]). In order to obtain an acceptable fit, an extremely low value of the level density was required, in line with the low number of experimental levels incorporated in the simulations (Figure 7.11). Even though there is a pronounced drop in a_{ld} close to the double shell closure at ^{208}Pb, it still seems unrealistically low. In this highly uncertain scenario, the most practical way to proceed was to directly investigate how important variations in a_{ld} impact the threshold correction factors, and how they compare to the experimental ^{204}Tl(n, γ) spectrum. This is reported in the next section.

Concerning the different photon strength functions (SF), the parameters for M1 and E2 transitions were the same as in the ^{203}Tl(n, γ) analysis. Those for the E1 strength, instead, were obtained by interpolating from the very similar values reported in [118] for ^{204}Tl and ^{206}Tl, which include identical pigmy resonance parameters. These approximations are not unreasonable, since SF parameters are usually parametrized as a function of the atomic mass A. Furthermore, in the analysis of the ^{203}Tl cascade we already observed important variations in these parameters. Although such variations affect moderately the shape of the cascade, their impact in the calculated threshold correeection factor, f_{th}, is negligible. Three models, with $a_{ld} = 7, a_{ld} = 5$, and $a_{ld} = 0.8$ have been calculated and simulated. The results are plotted in Figure 7.12. Whereas there are differences at high de-

posited energies, the spectra are almost identical under 1.2 MeV. This is most probably due to the fact that we are using the same experimental data for the low lying levels. For comparison, the experimental capture spectrum at the 122 eV resonances has also been included in Figure 7.12). In the case of $a_{ld} = 5$ and $a_{ld} = 0.8$ cases the agreement with the experimental spectrum is acceptable up to 5 MeV. Important discrepancies appear beyond 5-6 MeV, where the simulated spectrum extends visibly further than the experimental. This discrepancy could be ascribed to hypothetical missing levels –and the corresponding transitions– in the range 4 to 7.6 MeV. The final parameters employed for the capture cascade simulations are summarized in Table 7.7.

7.8   Estimation of the uncertainty related to threshold correction factors

The threshold in the pulse height spectra has an important impact in the data analysis. An increasing threshold value implies a correspondingly high loss of counts in the deposited energy spectrum. A particular feature of the ^{204}Tl analysis was that gold was not used as reference for the capture yield normalization. Instead, capture in the embedded ^{203}Tl in the sample was employed, as it will be discussed
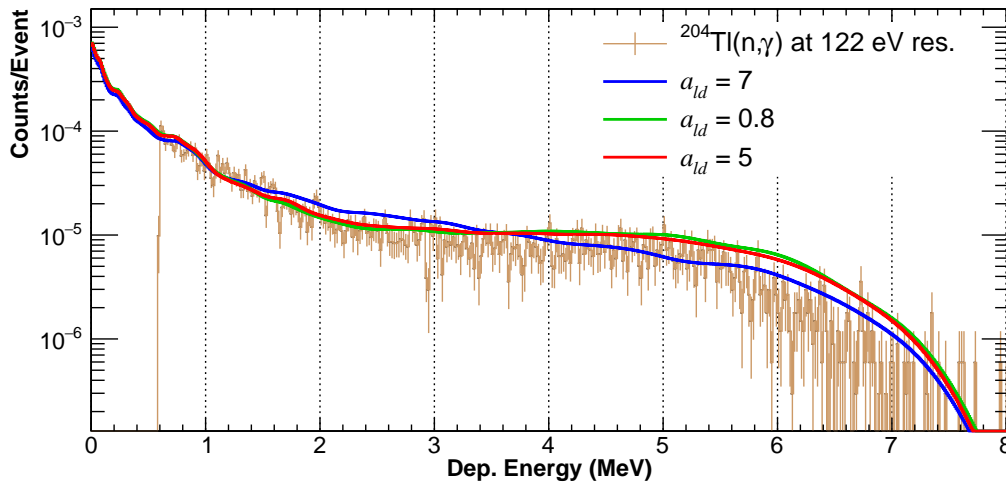
Figure 7.12: *The $C_6D_6\#1$ simulated response function to different $^{204}Tl(\mathrm{n},\gamma)$ cascades models, in which the level density a_{ld} has been varied.*

	Reference	Value(s)		
Level density, a_{ld} (MeV^{-1})	[116]	5.0		
Excitation energy shift, δ_{eff}	[117]	-0.8		
Strength Functions		E_0 *(MeV)*	Γ_0 *(MeV)*	σ_0 *(mb)*
E1$_{GDR}$	[118]	13.66	3.82	382.22
E1$_{pigmy}$	[118]	5.2	1.0	36.0
M1	RIPL-1 [119]	6.96	4.00	1.12
E2	RIPL-1 [119]	10.70	3.66	4.88

Table 7.7: *Summary of the BSFG model final parameters, and the gamma strength functions, employed in the ^{204}Tl(n, γ) gamma cascades simulations.*

in full detail in section 7.10. Hence, the threshold correction factors to the ^{204}Tl yield had to be with respect to ^{203}Tl, that is:

$$f_{th,ce} = F_{th,ce}^{^{204}\text{Tl}} / F_{th,ce}^{^{203}\text{Tl}} \ , \tag{7.8.1}$$

where $F_{th,ice}$ is the factor which corrects for the cascades missing under a given threshold. Simulations of the capture cascade of both nuclides, and of the C_6D_6 response functions, are essential to assess the factors F_{th}. (Note: for simplicity in the notation, all factors reported as F_{th} and f_{th} hereafter include the effect of conversion electrons).

Based on the goodness in reproducing the experimental spectrum, the case with $a_{ld} = 5$ was chosen as the most representative, and used for the final f_{th} employed in the yield calculation. The final correction factors are reported in Table 7.8. This factors include the correction due to conversion electrons, as well. It is remarkable

	C_6D_6#1	C_6D_6#2	C_6D_6#3	C_6D_6#4
$F_{th}^{^{204}\text{Tl}}$	1.119(1)	1.105(1)	1.108(1)	1.109(1)
$F_{th}^{^{203}\text{Tl}}$	1.135(1)	1.129(1)	1.131(1)	1.126(1)
f_{th}, $a_{ld} = 5$	1.006(1)	0.993(1)	1.003(1)	1.012(1)

Table 7.8: *The correction factors F_{th}, with a 600 keV threshold, for the ^{204}Tl and the ^{203}Tl capture cascades. In the third row, the resulting ^{204}Tl yield threshold correction factors, $f_{th} = F_{th}^{^{204}\text{Tl}}/F_{th}^{^{203}\text{Tl}}$. The model employed for the ^{204}Tl has $a_{ld} = 5$, the one chosen as reference.*

	$C_6D_6\#1$	$C_6D_6\#2$	$C_6D_6\#3$	$C_6D_6\#4$
f_{th}, $a_{ld} = 5$	1.006(1)	0.993(1)	1.003(1)	1.012(1)
$a_{ld} = 0.8$ rel. diff. (%)	-1.1	-1.4	-1.5	-1.5
$a_{ld} = 7.0$ rel. diff. (%)	-2.7	-0.4	-1.3	-1.9
Average rel. diff. (%)	-1.9	-0.9	-1.4	-1.9

Table 7.9: *Correction factors f_{th} for the reference case with $a_{ld} = 5$, and the relative deviations of the models with $a_{ld} = 0.8$ and $a_{ld} = 7.0$ with respect to the reference model. In the latter the statistical error is less than 0.1%.*

that the number of missing cascades is virtually the same for all detectors except for $C_6D_6\#4$, which in any case shows a maximum deviation of 1.2%. This results are ascribed to similarities in the shape of the de-excitation cascades of ^{203}Tl and ^{204}Tl. The consequence is that, in practice, the correction factor for each isotope cancel out, leading to an overall void correction in the yield due to these effects. This also indicates that the choice of ^{203}Tl as reference in this measurement was a good election from the point of view of the systematic uncertainties.

To study the influence of the level density a_{ld} the threshold corrections were obtained also for the cases with $a_{ld} = 7$ and $a_{ld} = 0.8$. This alternative statistical models seen in the previous section do show slightly larger deviations from unity, as reported in Table 7.9. These variation are, on average, of 1.4% for $a_{ld} = 0.8$, and of 1.6% for $a_{ld} = 7$. In some particular case, the variation reaches 2.7%. In this situation, we considered that a 1.5% figure provides a fair estimation of the systematic error in the correction factor due to the uncertainty in the statistical model. It is worth remarking that the uncertainty in the correction factors is directly propagated into the yield.

Figure 7.11: *Comparison between the experimental and the theoretical cumulative number of levels N_l, the latter calculated with $d_{eff} = -0.8$ MeV.*

The deposited energy spectrum of the other two resonances at $E_n = 789$ eV and $E_n = 915$ eV has also been simulated and compared to the experimental
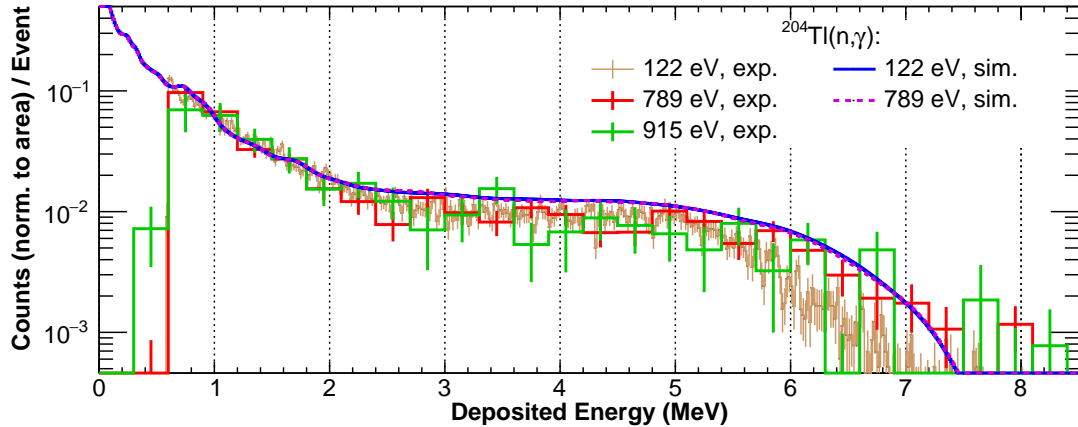
Figure 7.13: *The $C_6D_6\#1$ simulated response function to different $^{204}Tl(n,\gamma)$ cascades models, in which the level density a_{ld} has been varied extensively.*

results. The results can be seen in Figure 7.13. Both are predicted to have $l = 0$, $J = 5/2^+$ by the JEFF3.3 and ENDF/B-VIII.0 evaluations –which are based on TENDL-2015–, and also by TENDL-2017. Thus, their spectra should be very similar. After background subtraction, the data of the four C_6D_6 detectors has been added together to improve the statistics for the higher energy resonances. The same has been done for the simulated spectra. Once normalized to the capture area of each resonance, the spectra match each other precisely up to 5 MeV. Although statistical fluctuations beyond that point hinder a more in-depth analysis, the 789 eV spectrum seems to extend visibly higher in energy than the 122 eV resonance.

7.9 Estimation of the systematic uncertainty due to the sample geometry and position

The uncertainty on the exact geometry, and in general, of the sample conditions, may have an impact on the weighting process, and the errors associated to it. Changes in the density, or in the shape along the beam axis, could introduce changes in the neutron self-shielding and in the gamma ray absorption profiles. In addition, the detection efficiency would decrease in the same way for all four detectors. Variations in the vertical axis with respect to the beam could be higher due to the longer size of the container, and to the Gaussian profile of the neutron beam. These variations would lead to an increase in efficiency in a pair of detectors,

and a decrease in the others. It is a matter of study whether these variations would cancel out when adding the yield of the four detectors, since the relative distance to the sample is different for each of them. .13 In all cases, uncontrolled changes in the detection efficiency with respect to the nominal geometry, would introduce errors in the weighting procedure. To evaluate and quantify these errors we have employed again the test of the weighted sum of cascades. The procedure consisted in performing Geant4 simulations of 10^7 capture cascades with several different sample geometries, and then applying to them the WF calculated with the nominal or reference geometry, which is the one employed in the data analysis. Deviations are quantified by means of the weighted sum of cascades equation, $\sum_{i=0}^{\infty} W_i R_i^C / N E_C = 1$, and normalized to the results obtained with the reference WF.

The cases studied were based on what was observed in the scanning procedure, and on reasonable virtual hypothetical situations considering the rough irradiation conditions, and the sample geometry. They were:

1. A case in which 60% of the sample mass was in the fragment covered by the beam, whereas the rest was in the piece not covered. This is considered a lower bound on the main fragment mass, based on the scan measurement (section 7.2). The reference sample thickness has been decreased accordingly, to keep the density constant (referred as case 1b, case 1a being the nominal sample and position).

2. Two cases where the cylindrical sample inside the quartz capsule is in vertical position, coaxial with the beam: one with the nominal mass and thickness, and the other one with the values reduced to 60% of the nominal ones (cases defined as 2a and 2b).

3. A case with a degraded sample, turning it to a powder, with a much lower density, that has settled in the bottom of the capsule. Thickness has been increased to keep the mass constant to 60%.

4. An extreme version of the previous case, in which the sample had pulverized and adhered around the capsule walls. A thin cylindrical shell is employed for modelling this situation.

The results of the tests are summarized in Table 7.10, reported as the percentage variation with respect to the nominal geometry. A simple reduction of the

Geometry	Nominal (1a)	1b	2a	2b	3
ρ (g/cm^3)	6.03	6.03	6.03	6.03	1.036
Thickness (cm)	0.215	0.129	0.215	0.129	0.4
$C_6D_6\#1$	0.976(1)	-0.4	0.4	-0.2	1.7
$C_6D_6\#2$	0.982(1)	1.0	-1.7	-1.1	-2.5
$C_6D_6\#3$	0.979(1)	0.0	0.1	-0.8	1.1
$C_6D_6\#4$	0.974(1)	0.1	-2.3	-2.7	-1.9

Table 7.10: *Summary of results of the geometry tests. The values of the nominal configuration are the ratio $\sum_{i=0}^{\infty} W_i R_i^C / N E_C$, while the rest as the % deviation respect to them.*

sample mass (case 1b) produces differences in the weighted sum of the capture cascades of, at most, 1% (for $C_6D_6\#2$). Differences are negligible for the other detectors.

On the other hand, for cases 2a, 2b and 3, an important underestimation is observed in the number of detected cascades by $C_6D_6\#2$ and $C_6D_6\#4$. What all these geometries have in common is that the sample extends along the Y-axis, and thus the same happens with the emission profile. Since $C_6D_6\#2$ and $C_6D_6\#4$ are positioned under the beam plane, the distance to the emission point of the cascade increases, and thus the detection efficiency is reduced. The effect in $C_6D_6\#1$ and $C_6D_6\#3$ is the inverse, albeit somewhat less pronounced.

This combined effect is especially notorious in the low density case (3). The latter condition leads to a more homogeneous emission profile along the sample, yet increasing the distance to $C_6D_6\#2$ and $C_6D_6\#4$. In turn, the overestimation in $C_6D_6\#1$ and $C_6D_6\#3$ becomes now also relevant.

In summary, a systematic uncertainty of 2% for the capture was ascribed to the geometry effects of the capture sample.

7.10 ^{204}Tl(n,γ) normalization

As explained in chapter 4, to apply effectively the saturated resonance method it is necessary to have exactly the same experimental setup for the reference sample and the sample to measure. Unfortunately, these requirements are not met for the ^{204}Tl-enriched sample (see section 7.1). In second place, the exact orientation of
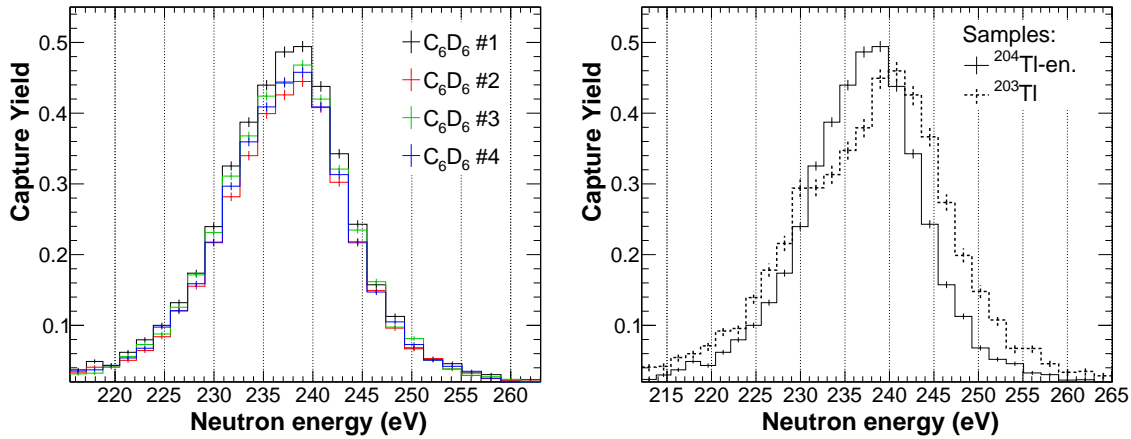
Figure 7.14: *Left: Capture yield of the four C_6D_6 detectors for the ^{204}Tl-enriched sample data, in the 236 eV ^{203}Tl resonance. All the correction factors obtained ^{203}Tl(n,γ) analysis, with a threshold of 600 keV. The histograms have been rebinned to 600 bins per decade to reduce the statistical fluctuation. Right: Comparison of the yield of the ^{203}Tl sample and the ^{204}Tl-enriched in the 236 eV resonance, for C_6D_6#1.*

the fragment is not known either, nor the exact relative position of the sample with respect to the beam. Assuming a cylindrical pellet perpendicular to the beam, with its centre lying in the beam axis –which is the *nominal* geometry employed in the Geant4 simulations– the beam interception factor f_{bi} would be very different to that of the ^{197}Au and the ^{203}Tl samples, and the related systematic error would be large.

This statement is demonstrated in Figure 7.14. The histograms in the left plot are the capture yield with the ^{204}Tl sample, in the 236 eV ^{203}Tl resonance, as measured by the four C_6D_6. They have been obtained with the same f_{bi}, and the correction factors (f_{sat}, f_{th}) as calculated for the ^{203}Tl(n, γ) measurement, but with a 600 keV threshold. Discrepancies between detectors are important, up to 14% betwen C_6D_6#1 and C_6D_6#2, in contrast with what was observed in the ^{203}Tl(n, γ) analysis (see Figure 6.8). This basically shows the inadequacy of applying directly the saturated resonance method in the context of the ^{204}Tl(n,γ) experiment.

This is further confirmed when comparing the present yield with that of the ^{203}Tl sample, as can be seen in the right plot of Figure 7.14 for C_6D_6#1. Especially prominent are the differences, not only in amplitude, but also in shape and width in the 236 eV resonance. In the case of the enriched sample, the resonance is nar-

rower, and the multiple scattering peak appears less defined. Since the strongest resonances are very sensitive to the geometric parameters of the sample (due to the multiple scattering effect), this can be considered a direct proof of the physical differences between samples. In this respect, with the yield depending on geometric parameters largely unknown, the possibility of direct re-normalization to the ^{203}Tl yields, via resonance integrals, did not appear feasible either. However, the radiative kernel –or equivalently the area–, being only dependent on Γ_γ and Γ_n, must be the same, regardless of the sample characteristics.

Thus, a method based on in-sample ^{203}Tl resonances kernel normalization was developed. By "fixing" the parameters for a few resonances, SAMMY can be employed to obtain a *unique* set of values for the unknown parameters required for a reliable analysis of the capture yield. These are:

i) the atomic thickness, n.

ii) the geometrical dimensions of an "effective" cylindrical sample, that is, length (or thickness), t, and radius, r. The former, for a given atomic thickness, determines the density of the sample.

iii) the normalization constant, A_n.

It is meant, by unique, that the geometric parameters are the same for the four detectors. In this way, at the end of the process all four yields can be added together for the final yield analysis. The procedure was possible, in particular, thanks to the new or updated ^{203}Tl(n,γ) resonance data obtained in Chapter 6. Specifically, several resonances under 3 keV, those measured with good precision for the first time, were employed. Unfortunately, the resonance with the second highest amplitude, at 842 eV, had to be avoided since it would overlap with a possible ^{204}Tl resonance predicted by JEFF-3.3 between 830 and 850 eV.

Recalling equation (4.12.1), the total theoretical capture yield can be described as the sum of several contributions, related to the number of scattering interactions a neutron undergoes in the sample before being captured,

$$Y_\gamma = Y_0 + Y_1 + Y_2 \dots \tag{7.10.1}$$

The correction for one scatter before capture, Y_1, and for two ore more scatters Y_2 are evaluated analytically by SAMMY, which requires detailed knowledge of the sample geometry and its relative position respect to the beam (see section III.D

in [57] for a detailed description). In the case of ^{203}Tl, except for the very strong resonance at 236 eV, second and third order MS corrections can be neglected for all resonances in first approximation, and thus, $Y_\gamma \approx Y_0$.

Considering a sample of thickness n, of total and capture cross sections σ_t and σ_γ. Y_0 is the fraction of neutrons captured in the first interaction, which can be expressed as the product of the neutrons that do *not* traverse the sample, and the probability of them being captured,

$$Y_0 = (1 - e^{-n\sigma_t}) \cdot \frac{\sigma_\gamma}{\sigma_t} \ . \tag{7.10.2}$$

By multiplying by the atomic thickness n, the expression can be rewritten as

$$Y_0 = n \cdot F \cdot \sigma_\gamma \ , \tag{7.10.3}$$

where F is the so-called self-shielding factor, caused by the attenuation of the beam in the sample:

$$F = \frac{(1 - e^{-n\sigma_t})}{n \cdot \sigma_t} \ . \tag{7.10.4}$$

Since the factor F depends on the total cross section, at the centre of a resonance the neutron flux, and thus the yield, will be reduced more than in the resonance wings. The observable we are going to employ for the normalization is the resonance integral. In that case we have to integrate equation (7.10.3),

$$A_{Y_\gamma} = n \int F(E, n)\sigma_\gamma(E) dE \ . \tag{7.10.5}$$

The integrand should be evaluated numerically at once, which is what SAMMY does when applying the self-shielding corrections. Here, we can approximate F to an effective value for the whole resonance area, which requires averaging F over its cross section,

$$\overline{F}(n) = \frac{\int \sigma_\gamma(E)F(E)dE}{\int \sigma_\gamma(E)} \ . \tag{7.10.6}$$

Hence the yield integral becomes,

$$A_{Y_\gamma} = n \cdot \overline{F}(n) \cdot A_r = n \cdot \overline{F}(n) \cdot g \frac{\pi}{k_n^2} K_r \ . \tag{7.10.7}$$

On the other hand, the experimental yield, prior to normalization, is obtained with the usual expression, for the ^{203}Tl(n, γ) yield,

$$Y_{exp}(E_n) = f_{glob} \cdot f_{si} \cdot f_{ns} \frac{C_w(E_n) - B_w(E_n)}{f_{bi} \cdot \phi_n(E_n) \cdot \left(S_n^{204\text{Tl}} + \left(S_n^{204\text{Tl}}/S_n^{205\text{Tl}}\right) \cdot E_n\right)} \ , \tag{7.10.8}$$

with $S_n^{204\text{Tl}} = 6.656$ MeV, and $E_{th} = 0.6$ MeV.

Fitting the experimental yield with SAMMY to extract the normalization parameter can be interpreted as imposing the equality

$$f_{nor} \cdot Y_{exp}(E_n) \equiv Y_\gamma(E_n), \qquad (7.10.9)$$

where $f_{nor} = 1/A_n$. In terms of resonance integrals this last expression is equivalent to

$$f_{nor} \cdot A_{Y_\gamma} = n \cdot \bar{F}(n) \cdot A_r(\Gamma_\gamma, \Gamma_n) \ . \qquad (7.10.10)$$

Let us suppose that the last equation holds perfectly for atomic thickness n. Now, we can change n in SAMMY by a factor, that is, $n' = \alpha \cdot n$, which leads to a different $F(n)$, $\bar{F}' = \beta \cdot \bar{F}$. By the previous equation, $f_{nor}A_{Y_\gamma} = \alpha\beta \cdot n\bar{F}A_{r1}$. SAMMY should be able to perform a perfect fit again just by scaling the normalization factor as $f'_{nor} = f_{nor}/\alpha \cdot \beta$, leaving all resonance parameters fixed.

The situation changes if we employ in the fit a second resonance, with a different cross section. The self-shielding factor of this second resonance will vary in a different way when changing the atomic thickness. Thus, $\bar{F}'_{r1} = \beta\bar{F}_{r1}$ and $\bar{F}'_{r2} = \delta\bar{F}_{r2}$, with $\beta \neq \delta$. Equation (7.10.10), with the initial atomic thickness n, now is

$$f_{nor}A_{Y_\gamma} = n\left(\bar{F}_{r1}A_{r1} + \bar{F}_2 A_{r2}\right) \ . \qquad (7.10.11)$$

This equation, for the case of the different thickness n', turns into

$$f_{nor}A_{Y_\gamma} = \alpha\beta n\left(\bar{F}_{r1}A_{r1} + \frac{\delta}{\beta}\bar{F}_{r2}A_{r2}\right). \qquad (7.10.12)$$

From this last expression, in order to recover equation (7.10.11) by scaling f_{nor}, it is required that $\delta = \beta$, which is not the case. Hence, we would obtain a less accurate fit of both resonances. We can conclude that, if one knows accurately the cross section for a few resonances, it is possible to determine, unambiguously, an atomic thickness that produces the best fit of the resonances.

The dependence of resonance area ratios with the atomic thickness is the main principle behind the Neutron Resonance Capture Analysis (NRCA) technique [127], which has been used to characterize the elemental composition of materials with great accuracy and precision [128].

In the previous hypothetical case of areal density n', if we allow now the code to fit freely the parameters of both resonances, we will obtain the corresponding new

kernel $K'(\Gamma'_\gamma, \Gamma'_n)$. Then, we can quantify the error introduced due to the change in atomic thickness by calculating a Root Mean Square (RMS) error of the new kernels respect to the reference kernel values,

$$x_{rms}(K'_i \dots K'_k) = \sqrt{\frac{1}{k} \sum_i^k \left(\frac{K_i - K'_i}{K_i} \right)^2},$$ (7.10.13)

However, we still need to determine some sort of effective physical dimensions of the sample, besides n. For that, it is necessary to include in the procedure a resonance where thickness effects are so strong that the MS contribution to the yield is significant,

$$Y_\gamma = Y_0(n) + Y_{ms}(n, r, t),$$ (7.10.14)

where Y_{ms} are the multiple scattering contributions, r is the radius of the sample and t is its physical thickness. The 236 eV resonance in ^{203}Tl(n, γ) seems particularly well suited for this purpose. Thus, by fitting the experimental yield in that resonance, we should be able to provide, at least, some constraint on the geometrical parameters, and an additional confirmation of the areal density determined by the RMS calculation.

In practice, the whole procedure consisted in fitting the ^{204}Tl sample yield data with SAMMY, for a wide range of values of the atomic thickness n, the physical dimensions t and r, and the normalization constant f_{nor}. The χ^2 of each fit was employed as a measurement of the accuracy of the set of parameters. Since the code does not weight the data points when calculating the χ^2, those between resonances were was excluded from the fit. This was done in order to avoid reducing artificially the χ^2 with background data, which fluctuates around zero.

The resonances employed, which were always fitted together at once, were those at 236 eV, 1275 eV, 1432 eV and 2789 eV. Although the resonance parameters were free to vary, their initial uncertainty was set to the previously determined experimental values.

As stated above, the 236 eV resonance, due to its great amplitude and width, was well suited to study the thickness effects. For the same reason, it has a very strong influence in the global χ^2 calculation. Consequently, we assume that the χ^2 values should provide the desired constrain in the r and t parameters.

In this way, for every set of input parameters we obtained a χ^2 and a x_{rms} value. These data can be represented graphically using bidimensional histograms,
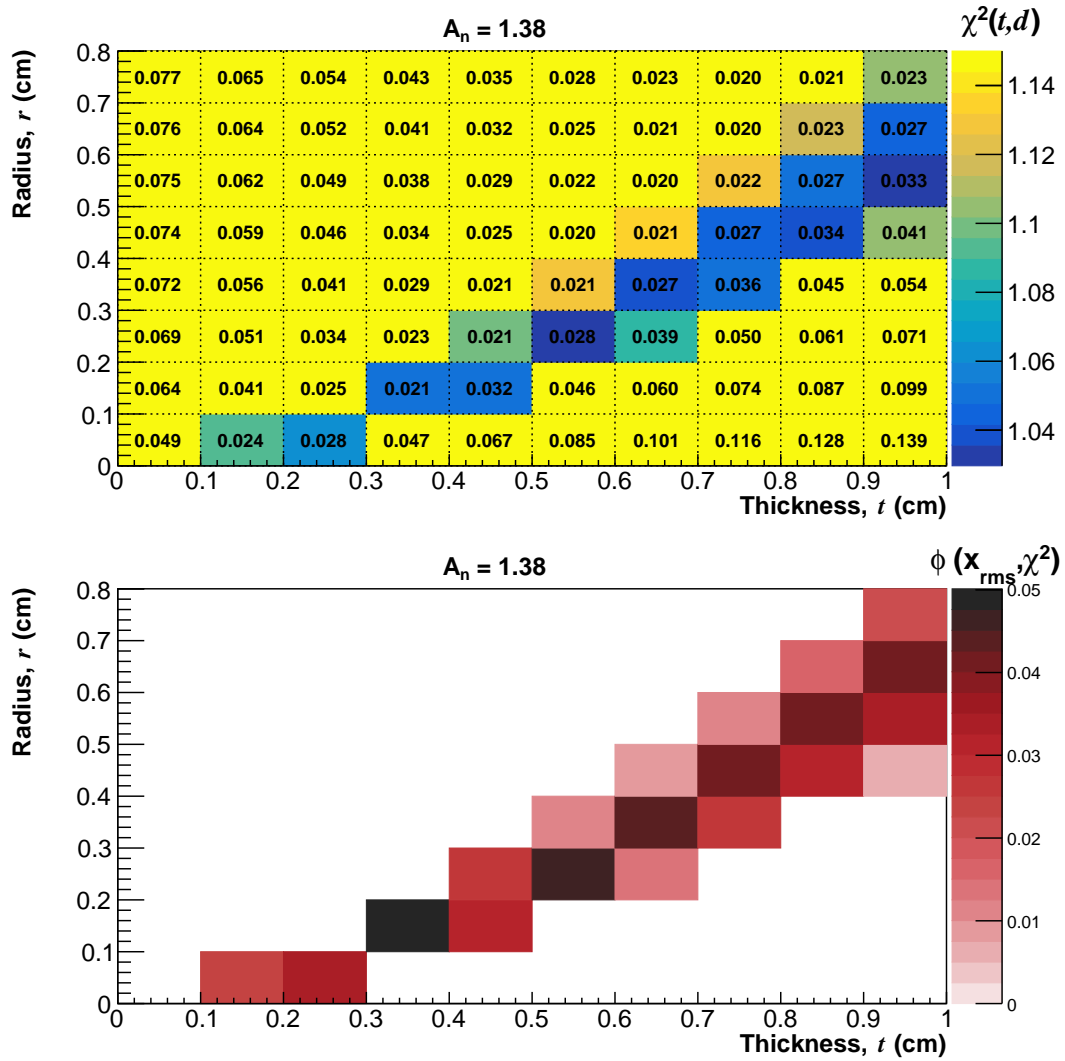
Figure 7.15: *Top: The χ^2 of the SAMMY fits as a function of the macroscopic thickness and the radius of the sample, for a normalization constant $A_n = 1.38$. In each bin, the corresponding x_{rms} of the fit is reported. Bottom: The figure of merit ϕ calculated for the same parameter space of the top figure. Only positive values of the ϕ are reported, which are those that represent an improvement over the chosen thickness (l) and radius (r). This example corresponds to $C_6D_6\#1$ and $n = 8.0 \cdot 10^{-4}$ atoms per barn*

.

like the one shown in the top panel of Figure 7.15. In it, for a given normalization value, the χ^2 is plotted as a function of the thickness (x-axis) and the radius (y-axis). The x_{rms} for each combination is written inside each bin. These plots are

useful to observe a favoured range of geometric parameters, which is common to almost all normalizations. In fact, an approximately linear dependency on both the thickness and the radius is obtained. However, the plots do not enable us to determine directly, and unambiguously, which set provides the best combination of the chi-squared and the x_{rms}.

This has been achieved, instead, by defining a figure of merit (FOM) ϕ, as a function of both quantities,

$$\phi(x_{rms}, \chi^2) = \frac{x_{rms} - x_{rms}^{max}}{x_{rms}} \cdot \frac{\chi^2 - \chi_{max}^2}{\chi^2} \ , \qquad (7.10.15)$$

where x_{rms}^{max} and χ_{max}^2 are the values of both quantities taken as an arbitrary upper limit for the calculation. Provided that the goal is to minimize both, a fit will be an improvement when both factors of the product are negative, which leads to a positive ϕ. Hence, the higher is the relative reduction of both the chi-squared and the x_{rms}, the higher is the value of the ϕ, thereby providing a hierarchy of fits. In the bottom panel of Figure 7.15 the corresponding figure of merit, as a function of t and r, has also been included. This plot allows to see, more clearly, that fits with similar accuracy are obtained with rather different geometric combinations.

In this situation, we proceeded by using the normalization that offered the best figure of merit for each detector, regardless of the geometry. Once normalized and averaged over the four detectors, the yield was fitted again. This time, the aim was to determine the best geometric parameters among those combinations which scored high in the figure of merit test.

The whole process has been repeated for several values of the atomic thickness n. The χ^2 and x_{rms}, for every combination of n, t, and r tested, are plotted in Figure 7.16.

The first observation that can be made is that x_{rms} improves as the size of the sample decreases, with the best results overall obtained with $t = 2$ mm and $r = 1$ mm. On the other hand, the χ^2 shows an inverse trend, with better results obtained as the size increases. In any case, we consider that the increase in χ^2 is modest compared to the gain in x_{rms}. Similar low x_{rms} values were obtained between $7 \cdot 10^{-4}$ atoms/barn and $8.5 \cdot 10^{-4}$ atoms/barn. The uncertainty of x_{rms} was minimum at $n = 8.0 \cdot 10^{-4}$ at./barn, resulting in $x_{rms} = 0.013(10)$. Thus, that was the atomic thickness adopted for the ^{204}Tl analysis.

It was equally important to estimate the uncertainty in the determination of
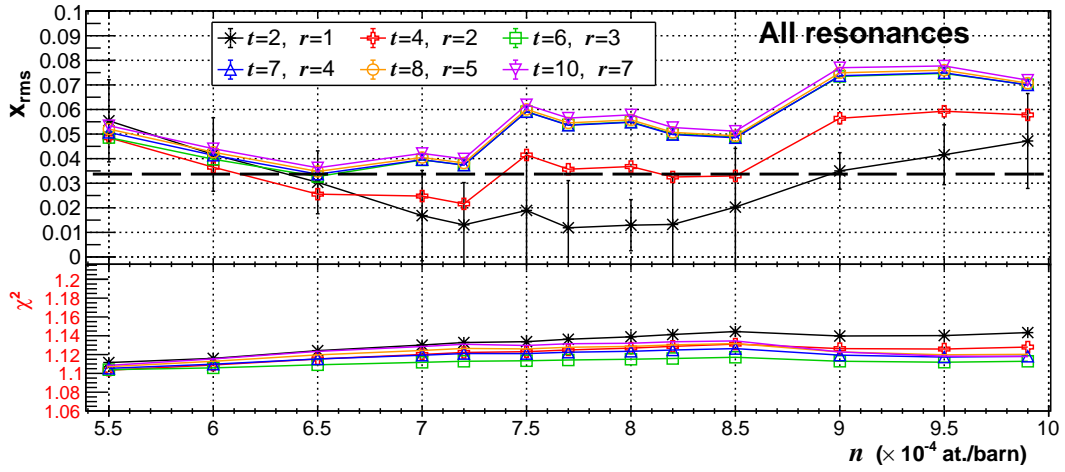
Figure 7.16: *Values of the x_{rms} (top) and the χ^2, obtained when fitting simultaneously the ^{203}Tl resonances at 236 eV, 1432 eV and 2789 eV, as a function of the atomic thickness n.*

these parameters. It was considered as compatible all atomic thickness values whose x_{rms} value was within the range defined by twice the error associated to the minimum x_{rms}. This methodology yields a the final value for the atomic thickness of $n = 8.0(1.5) \cdot 10^{-4}$. Concerning the dimensions of the sample, we adopted the figures of $t = 2(2)$ cm and $r = 1(1)$ cm, owing to the consistently better results provided by the combinations $t = 2$, $r = 1$ and $t = 4$, $r = 2$.

The atomic thickness of $n = 8.0(1.5) \cdot 10^{-4}$ corresponds to 47(9)% of the atomic thickness of the sample right after production and before the irradiation. The latter is assumed to be $1.72 \cdot 10^{-3}$ at/b, equal to that of the sample employed in the ^{203}Tl analysis. It is important to recall that the above determination corresponds to the part of the sample that interacts with the neutron beam, and thus can be seen as a lower limit of the sample thickness.

Several causes could explain these differences. After the pellet breaking and the posterior irradiation, the sample might have presented irregularities and inhomogeneities, whereas the SAMMY sample is a perfect and homogeneous cylinder. In addition, while in SAMMY the sample and neutron beam are concentric, the real sample might be displaced from the centre (see Figure 7.3), and with its axis non parallel to it. Any of these circumstances would lead to a reduction of the real neutron flux traversing the sample.

The same arguments can be applied to explain the difficulties in fitting accu-

	SAMMY sample mass (g)		
t (mm), r (mm)	$n = 6.5 \cdot 10^{-4}$	$n = 8.0 \cdot 10^{-4}$	$n = 9.5 \cdot 10^{-4}$
2, 1	0.015	0.019	0.022
4, 2	0.062	0.076	0.090
6, 3	0.139	0.170	0.202
7, 4	*0.246*	*0.303*	*0.360*
8, 5	*0.385*	*0.474*	*0.562*

Table 7.11: *Masses of the SAMMY-effective samples, for the geometric parameters by means of the x_{rms} and χ^2 minimization process.*

rately the tip of the 236 eV resonance. Under the SAMMY model, it was necessary to considerably reduce the atomic thickness, which comes at the expense of increasing x_{rms}. In this situation, it was assumed that the discrepancies in the peak of the resonance –and thus in the χ^2– are mostly a matter of a different combination of single and multiple scattering events, although the overall resonance area should be approximately the same.

Variations in the scattering components could be also caused by the possible eccentricity of the sample respect to the neutron beam. This would lead to a profile of the neutron beam intersecting the sample differently than that of the ideal SAMMY case. An equivalent effect could be caused by possible sample inhomogeneities.

Another constraint on the geometrical parameters can be obtained by calculating the mass of each geometric configuration. In Table 7.11 we have reported those corresponding to the best performing geometries, calculated for the adopted thickness and the maximum and minimum of its uncertainty range. Given the distribution of the sample in the capsule (see Figure 7.3) we have excluded those geometries which result in masses 90% or higher of the total. Following this criteria, all geometries with $t > 6$ mm and $r > 3$ mm have been discarded, leaving as possible the combinations $t=2$, $r=1$; $t=4$, $r=2$; and $t=6$, $r=3$ (all in mm).

The determination of the geometric parameters, and its associated uncertainties, allowed one to evaluate the systematic error introduced by the normalization process in the ^{204}Tl resonance analysis. To such aim, the kernel of the ^{204}Tl resonance at 122 eV was obtained for the same range of atomic thicknesses as in
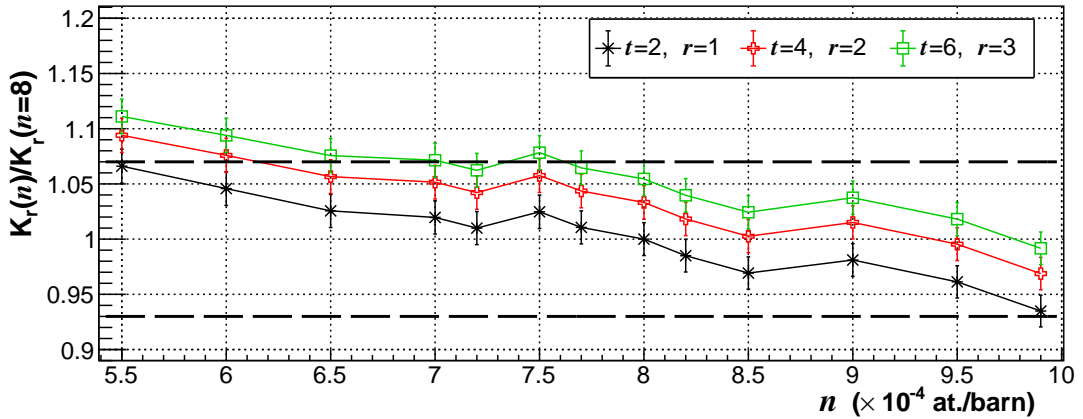
Figure 7.17: *The kernel of the 122 eV ^{204}Tl resonance, plotted as a function of the atomic thickness n, and normalized to the value corresponding to $n = 8 \cdot 10^{-4}$ atoms/barn. The black dotted lines highlight the $\pm 7\%$ adopted range of uncertainty.*

Figure 7.16. The results, normalized to the value of the reference geometry (t=2 mm, r=1 mm and $n = 8.0 \cdot 10^{-4}$ atoms per barn), are plotted in Figure 7.17. In the range defined by the respective uncertainties of n, t, and r, the relative variation of the kernel is approximately $\pm 7\%$. Therefore, this was the quantity assumed as a reasonable estimation of the normalization systematic error. Even though we have been able to provide a set of effective geometric parameters, at this point it is important to emphasize that we are not trying to determine the real physical dimensions of the sample. In the first place because, as mentioned earlier, we have only information of the fraction of sample interacting with the beam. However, we do not know what the fraction exactly is, nor its interaction factor with the beam. In second place, the limitations of the analytical model of the multiple scattering used by SAMMY limit the possible sample geometry to a cylinder.

Finally, the definition of the figure of merit is totally arbitrary, as it is the adopted criterion to choose the final parameters as those that score the highest ϕ, or alternatively the lowest x_{rms}. For all these reasons, it is more accurate to claim that we have obtained an effective "SAMMY-equivalent" of the sample.

Despite all the uncertainties regarding the geometry of the sample, the systematic error introduced by the normalization procedure has been estimated at 7%. Except for the two strongest resonances, that figure is lower than the predicted statistical uncertainty in the ^{204}Tl capture resonance kernels.
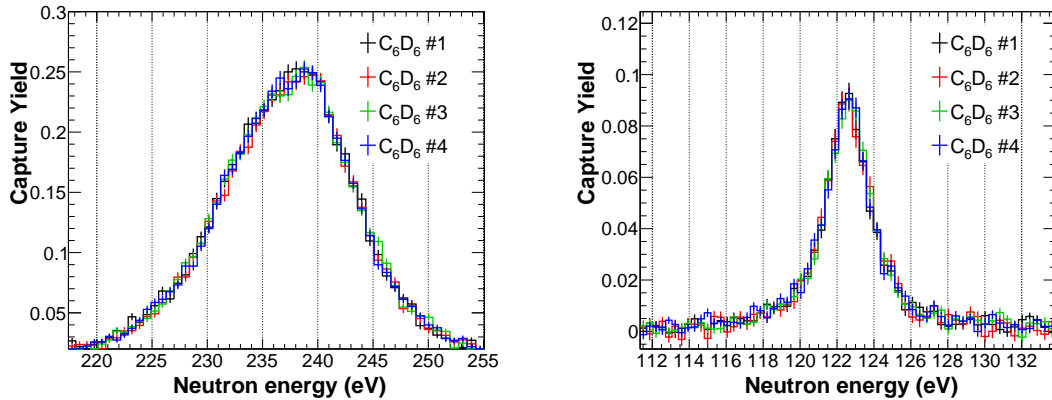
Figure 7.18: *Left: Capture yield of the four C_6D_6 detectors for the ^{204}Tl-enriched sample data, in the 236 eV ^{203}Tl resonance (left), and the ^{204}Tl 122 eV resonance (right). All the correction factors obtained ^{203}Tl(n,γ) analysis, with a threshold of 600 keV.*

A_n				Geometry		
C$_6$D$_6$#1	C$_6$D$_6$#2	C$_6$D$_6$#3	C$_6$D$_6$#4	t (mm)	r (mm)	n (at/barn)
1.38	1.44	1.12	1.28	2(2)	1(1)	$8.0(1.5) \cdot 10^{-4}$

Table 7.12: *The normalization constants and the geometric parameters employed in the final analysis of the ^{204}Tl capture analysis.*

Concerning possible thick-sample effects affecting the determination of the kernels, we do not expect their contribution to the yield to be relevant, due to the low content of ^{204}Tl. Thus, we conclude that, by means of the normalization procedure developed, an accurate determination of the ^{204}Tl resonance parameters should be possible.

The final parameters resulting from the normalization process are summarized in Table 7.12. With $f_{nor} = 1/A_n$, the ^{204}Tl yield can be expressed as (recalling equation (7.10.8)),

$$Y_{exp}^{^{204}\text{Tl}}(E_n) = f_{nor} \cdot f_{glob} \cdot f_{si} \cdot f_{ns} \cdot \frac{C_w(E_n) - B_w(E_n)}{\phi_n(E_n) \cdot (S_n + E_n)} \tag{7.10.16}$$

where $S_n = 7.546$ MeV and $th = 0.6$ MeV. Figure 7.18 shows the normalized yield of each detector in the 236 eV ^{203}Tl resonance, and in the 122 eV ^{204}Tl resonance.

7.11 ^{204}Tl(n,γ) resonance analysis

In the following pages the R-matrix analysis of the ^{204}Tl yield, in the energy range from 100 eV to 5 keV, is presented. New resonances assigned to ^{204}Tl but whose existence is dubious due to the low statistics, have been reported as *tentative* in the final list of resonances, in Table 7.16.

Plots of all ^{204}Tl resonances fitted are also shown, which include comparisons with the evaluated libraries, and with all other isotopes in the sample, including ^{203}Tl –with the updated resonance data from the present work– and ^{204}Pb. As in the previous chapter, a plot of the residual in sigma units, i.e. $\sigma_{res} = (Y_{exp} - Y_{th})/\sigma_{exp}$, is also featured. In some specific situations, a second σ_{res} plot is included. The latter corresponds to the fit of the ^{203}Tl and other impurities data in the ^{204}Tl-enriched yield, and it is employed to highlight the presence of a tentative ^{204}Tl resonance.

Concerning the evaluations, both JEFF-3.3 and ENDF/B-VIII.0, which are the latest editions of both libraries, include an evaluated cross section of ^{204}Tl(n,γ) based on the TENDL-2015 calculation [129]. Two subsequent editions of TENDL have been published, TENDL-17 and TENDL-19. While the former lists resonances up to 10 keV in neutron energy, the latter does only covers up to 5 keV. Up to this energy, however, the number, energy, and radiative width of the levels is the same in both editions. Hence, due to its higher range, we decided to employ the 2017 edition in the comparisons with the experimental data.

The resonance at 122.5 eV is the first, and strongest, ^{204}Tl resonance observed. This resonance was observed in a transmission measurement performed in the Materials Testing Reactor (MTR) of the Idaho National Laboratory in 1968 [130]. In the present experiment, by its width we deduce it is an s-wave. The spin and parity predicted by TENDL, $J^{\pi} = 5/2^+$, offers marginally better fit results than any other combination featuring either $l = 1$ or $J = 3/2$. All combinations of spin and parity tested are listed in Table 7.13. Concerning the magnitude of the kernels, changing only the spin to $J = 3/2$ leads to a 1% increase in the kernel, still within the uncertainty. If the parity is changed, both $J^{\pi} = 5/2^-$ and $J^{\pi} = 3/2^-$ lead to slightly higher variations, of 2% and 2.5%, respectively. Regarding the comparison of the new experimental data with the TENDL evaluations (Figure 7.19), an important reduction of 46% in the gamma width leads to a reduction in the kernel of 35%. The resonance parameters correlation test has been performed for

J	l	Γ_γ (meV)	Γ_n (meV)	K_r (meV)
5/2	0	406(5.6)	1769.3(32.4)	198.2(2.3)
3/2	0	745.6(20.3)	1534.3(47.6)	200.7(4.2)
5/2	1	415.9(5.7)	1768.6(32.7)	202(2.3)
3/2	1	762.5(20.8)	1521.1(48.4)	203.2(4.3)

Table 7.13: *The different combinations of J and l tried for the 122 eV resonance.*

J	l	Γ_γ (meV)	Γ_n (meV)	K_r (meV)
5/2	0	765(49)	7330(796)	416(24)
3/2	0	1227(83)	6961(811)	417(25)
5/2	1	770(50)	7369(805)	418(25)
3/2	1	1232(84)	6983(817)	419(25)

Table 7.14: *The different combinations of J and l tried for the 789 eV resonance. Differences in K_r are minimum and within the uncertainty.*

$J^\pi = 5/2^+$, and is plotted in Figure 7.19 (bottom). Γ_γ and Γ_n present no visible correlation.

The second ^{204}Tl resonance observed (Figure 7.20) appears at 788.5(3) eV. This resonance was the last reported in the transmission measurement of 1968, but with its neutron energy not accurately determined. In this case the area is 22% higher than the evaluations. Due to $\Gamma_n \approx 10 \cdot \Gamma_\gamma$, the variation is caused by an equally higher experimental radiative width. As in the previous case, several combinations of J and l were fitted, this time showing no significant variation in the resonance kernel (Table 7.14). A look at the Γ_γ vs Γ_n plot shows that the parameters are mostly non correlated.

For the ensuing resonances, due to their low yield, and thus high statistical uncertainty, neither the spin and parity check, nor the parameter correlation analysis, were performed. New resonances were arbitrarily fitted to $J = 5/2$ or $J = 3/2$, and were all considered s-waves, based on the assumption that most ^{204}Tl p-waves must be too weak to be detected.

Two criteria were established in order to determine when a structure in the data could be considered a new ^{204}Tl resonance: first, that the data points show a resonance-like structure deviating positively, with any point around a 2-σ interval
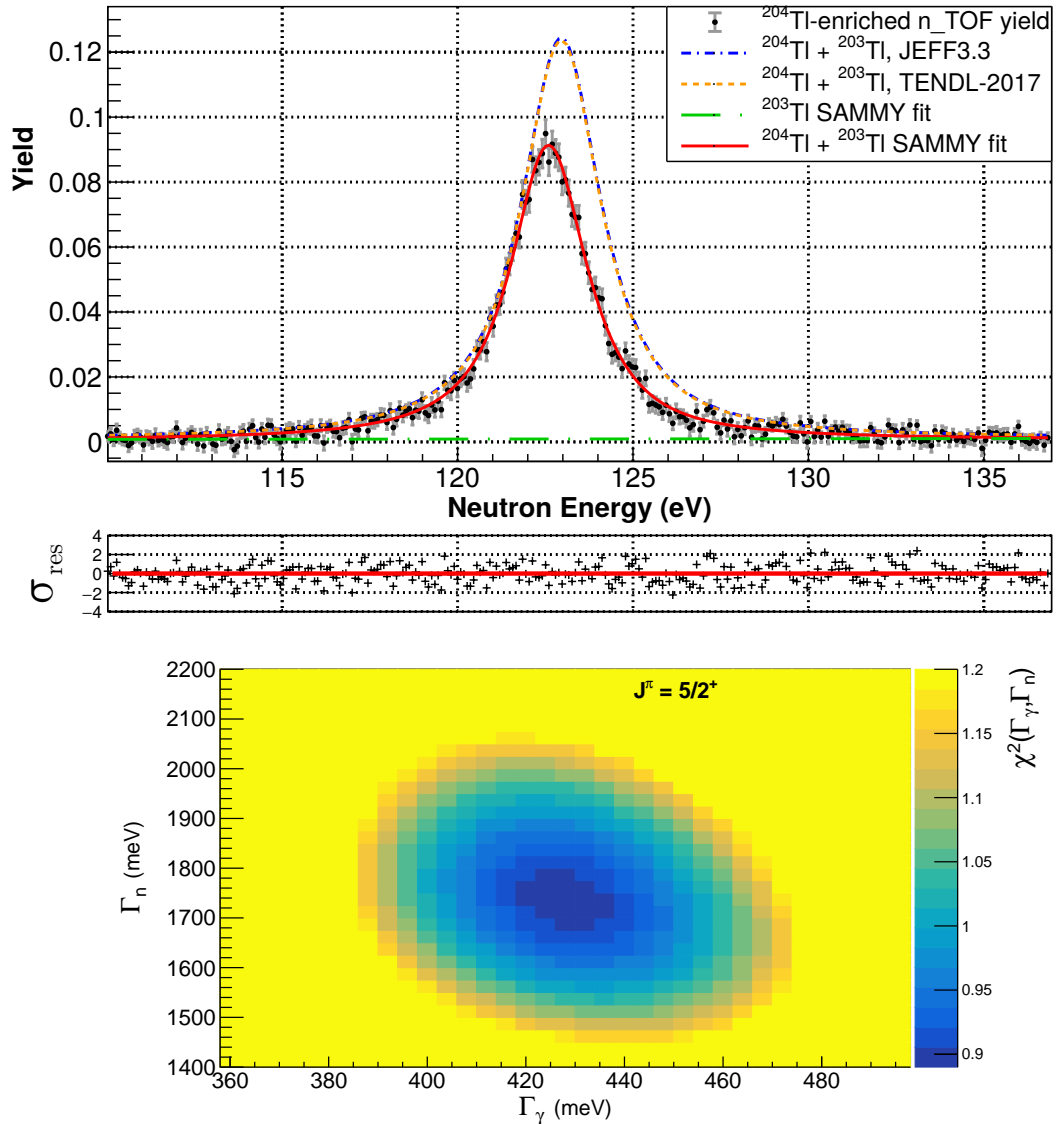
Figure 7.19: *Top: fit of the 122 eV capture resonance of ^{204}Tl, compared to JEFF-3.3 (TENDL-15) and TENDL-17. Bottom: Γ_γ vs Γ_n correlation plot of the same resonance, for $J^\pi = 5/2^+$. No apparent correlation is observed.*

if possible; secondly, that the candidate was observed consistently in the data when employing different number of bins per decade. Those resonances which fulfilled these criteria, but their existence was still dubious, were given the status of *tentative* in the final review of this work.

In JEFF-3.3 (i.e. TENDL-15) a resonance at 841 eV is listed. This would co-
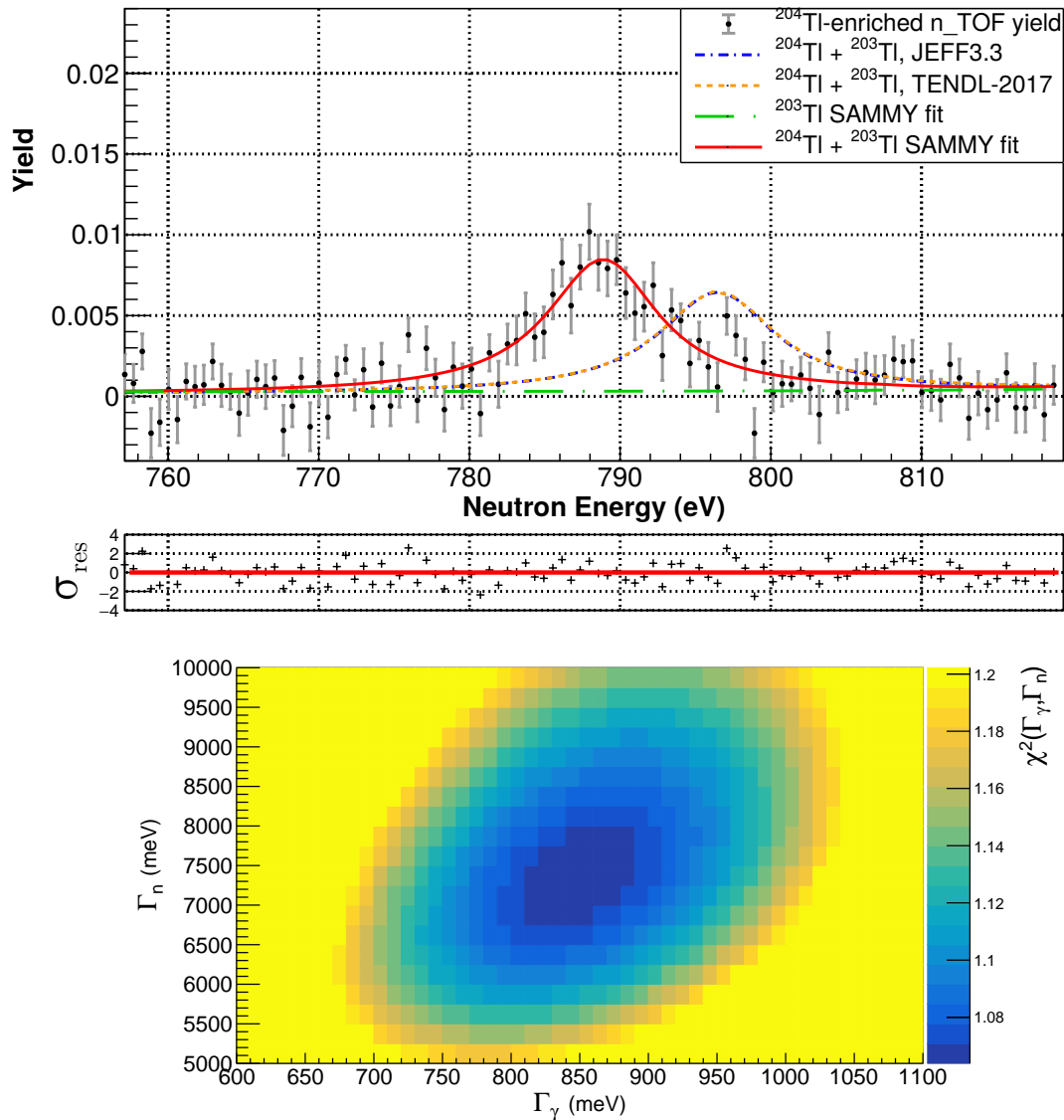
Figure 7.20: *Top: fit of the 789 eV capture resonance of ^{204}Tl, compared to JEFF-3.3 (TENDL-15) and TENDL-17. Bottom: Γ_γ vs Γ_n correlation plot of the same resonance, for $J^\pi = 5/2^+$. No relevant correlation is observed.*

incide exactly in energy with the much more intense 841 eV resonance of ^{203}Tl, hampering its proper identification and analysis. In this case, we proceeded by fitting the ^{203}Tl resonance, whose kernel is known with a 5% precision. If an accurate fit was achieved without increasing much the kernel, we would assume that there is no ^{204}Tl resonance. Otherwise, a significantly bigger kernel would be an

Combination	^{203}Tl res. K_r	^{204}Tl res. K_r	χ^2
Fit ^{203}Tl only	144.9(4.6)	–	1.03
Fit ^{203}Tl and ^{204}Tl	144.4(4.8)	13(25)	1.03
Fixed ^{203}Tl, fit ^{204}Tl	142.4(9.0)	101(27)	1.09
Fit ^{203}Tl, fixed ^{204}Tl JEFF-3.3	152.8(6.0)	141	1.11

Table 7.15: *Different cases tested in the range of the 841 eV ^{203}Tl resonance.*
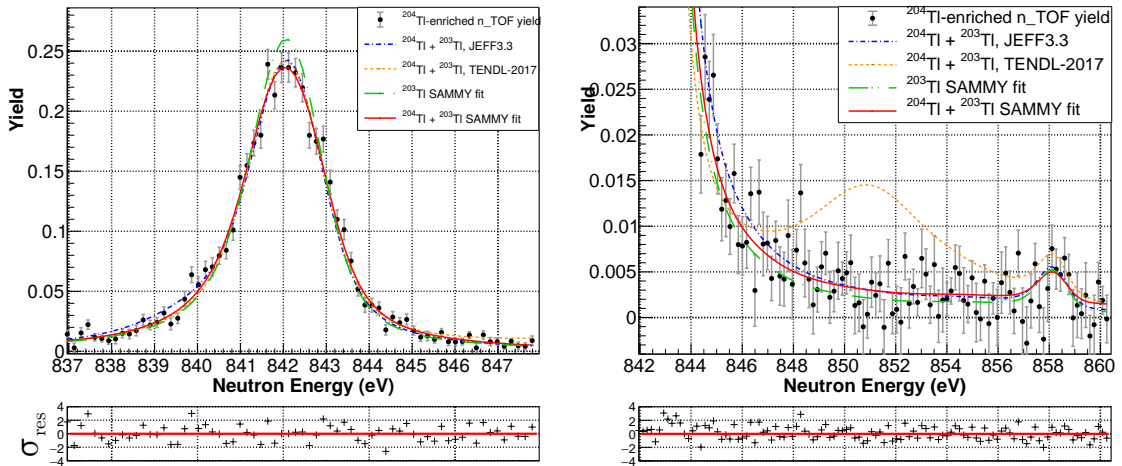
Figure 7.21: *In red, fit of the 842 eV capture resonance of ^{203}Tl, compared to the plot (dash green line), of the resonance data of the main impurities (^{203}Tl and ^{204}Pb), and the libraries.*

indication of the presence of a resonance. In all cases, the quality of the fit was taken into account as well.

The kernel of the 842 eV ^{203}Tl has been fitted and then compared to the reference value, which has been scaled to compensate for the different S_n, that is $K_{204} = (S_n^{203}/S_n^{204}) \cdot K_{203}$.

The results are summarized in Table 7.15. When fitting the ^{203}Tl resonance alone, we obtain a kernel which is totally compatible with the reference value. In other words, the resonance is successfully fitted without the need of an extra ^{204}Tl, which means that either it has very low amplitude, or, more likely, it does not exist. If a candidate ^{204}Tl is fitted jointly with the ^{203}Tl resonance, the ^{203}Tl area is unchanged, and the resulting ^{204}Tl resonance becomes very wide, with a very low kernel. The high uncertainty in the latter, twice its value, suggests that
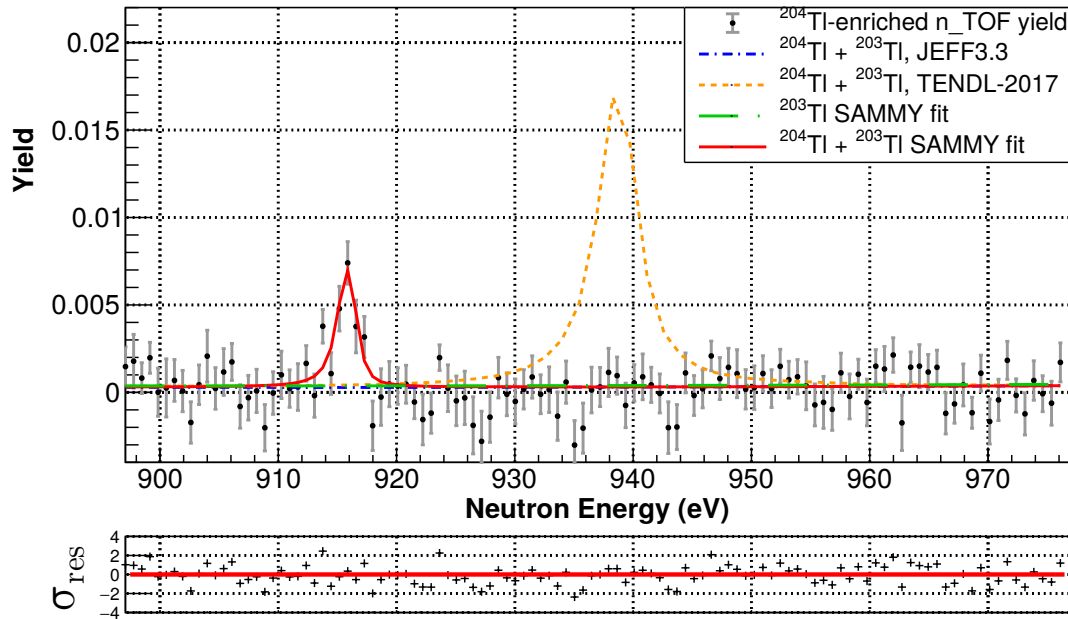
Figure 7.22: *Fit of the 915 eV capture resonance of ^{204}Tl, compared to JEFF-3.3 (TENDL-15) and TENDL-17.*

its contribution to the fit is minimum compared to the ^{203}Tl resonance. Finally, if the ^{203}Tl is fit while the ^{204}Tl candidate is fixed to the JEFF-3.3 parameters, the χ^2 of the fit increases considerably. The resulting fit, which can be seen in Figure 7.21, contributed to higher values of the yield between 838 and 840 eV.

We concluded that we can not either confirm nor deny the existence of the ^{204}Tl resonance as quoted in TENDL-15 or JEFF-3.3. Thus, it will not be included in the final list of resonances of this work. However, the resonance parameters will be reduced in order to match the best fit of the experimental data reported in Table 7.15.

Finally, in the right plot of Figure 7.21, it can be clearly seen that the resonance at 850 eV predicted by TENDL-17 does not exist, or does not seem to have the reported intensity.

The next ^{204}Tl resonance has been found at 915.4(2) eV. As can be seen in Figure 7.22, TENDL-17 had predicted the existence of a resonance relatively close, but with a kernel six times higher.

The resonances predicted at 1080 eV (TENDL-17) and 1127 eV (JEFF-3.3) are
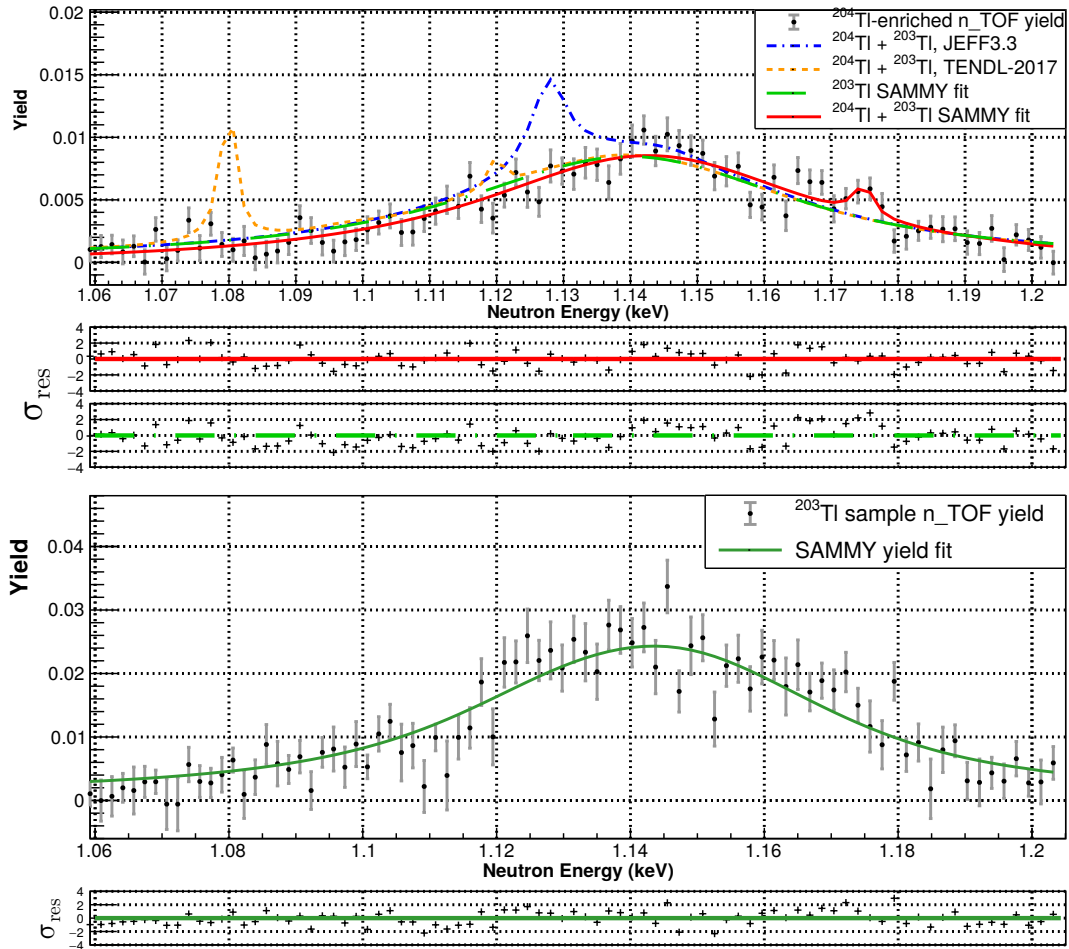
Figure 7.23: *Top: fit (in red) of the data in the range of the 1137(1) ^{203}Tl resonance, compared to the JEFF-3.3 (TENDL-15) and TENDL-17. Below are the relative error plots corresponding to the ^{204}Tl fit (red), and the ^{203}Tl and other impurities fit (dashed green), curves. A comparison of both hint the presence of the 1174(1) resonance. is , compared to JEFF-3.3 (TENDL-15) and TENDL-17.*

either not present, or their intensity is much lower than stated. As it is presented in Figure 7.23, a structure around ∼1175 eV, with a few points deviating more than a 2-σ_{res} relative error, has been fitted as a tentative candidate for a ^{204}Tl resonance, leading to an improvement of the χ^2 of the fit. However, the alleged resonance at 1175 eV is quite sensible to the exact energy parameters of the underlying 1137 eV ^{203}Tl resonance. As an example, the best fit in the range is obtained with a small variation of ∼ 3 eV in the energy of the broad ^{203}Tl resonance, respect to
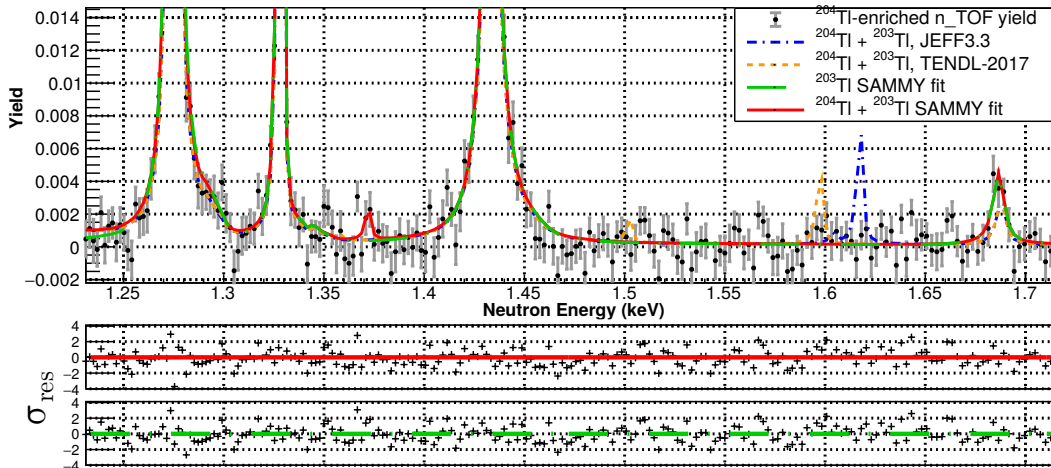
Figure 7.24: *Fit of the enriched sample yield data from 1.25 to 1.7 keV, compared to the ^{203}Tl and impurities data (dashed green line), and the JEFF-3.3 (TENDL-15) and TENDL-17 libraries.*

the reference value. This shift is enough to imply an important reduction of the kernel of the alleged 1175 eV resonance. For this reason, the latter was given the *tentative* status. The values quoted in the final list of resonances in Table 7.16 correspond to the best fit results in this region for both resonances.

1.2 to 1.7 keV

In this range (see Figure 7.24) no clear resonance belonging to ^{204}Tl has been observed, including those predicted by each library around 1600 eV. The resonance observed at 1689 eV is attributed to be the lowest energy resonance of ^{204}Pb [33], the daughter isotope of ^{204}Tl.

1.7 to 2.5 keV

A new ^{204}Tl resonance has been observed at 2017 eV (see Figure 7.25), very close to a ^{203}Tl at 2002 eV, but clearly resolvable thanks to the high energy resolution of n_TOF. Its K_r has been found to be 233(77) meV. Additionally, a low yield resonance has been fitted at 2267(2) eV. The latter was given the *tentative* status.
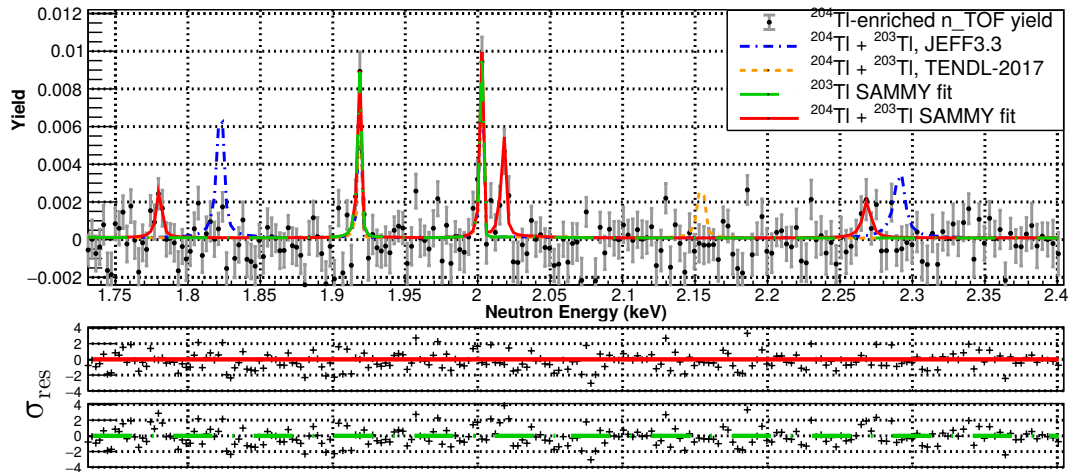
Figure 7.25: *Fit of the enriched sample yield data from 1.75 to 2.4 keV, compared to the ^{203}Tland impurities data (dashed green line), and the JEFF-3.3 (TENDL-15) and TENDL-17 libraries.*

2.4 to 2.8 keV

Candidates for possible ^{204}Tl resonances were fitted at 2595(1) eV and at 2708(1) eV (Figure 7.26). The structure observed around 2480 eV is believed to be the second strongest ^{204}Pb resonance. Related to this, the alleged ^{204}Tl resonance at 2708(1) eV would coincide with another level from ^{204}Pb. In this case, however, the ^{204}Pb resonance has a cross section more than 10 times less than the resonance at 1689 eV, which would make it too weak to be detected in this measurement. Thus, one can assume that it belongs to ^{204}Tl.

3.2 to 4 keV

Several resonances attributed to ^{204}Tl have been observed in this neutron energy range. Resonances at 3522(1) and 3657(1) appear distinctive enough to be regarded as ^{204}Tl resonances, as can be seen in Figure 7.27. Instead, those levels at 3267(1) and 3979(1) have been given the tentative status.

Beyond 4 keV, the decrease in the amplitude of the resonances, together with the higher background fluctuation and the bigger bin size, allowed us to identify only one more candidate for a ^{204}Tl resonance, at 5471(3) eV, shown in Figure 7.28. The large energy gap from the previous at 3979 eV probably indicates that some resonances in between could not be detected. In addition, resonances predicted by
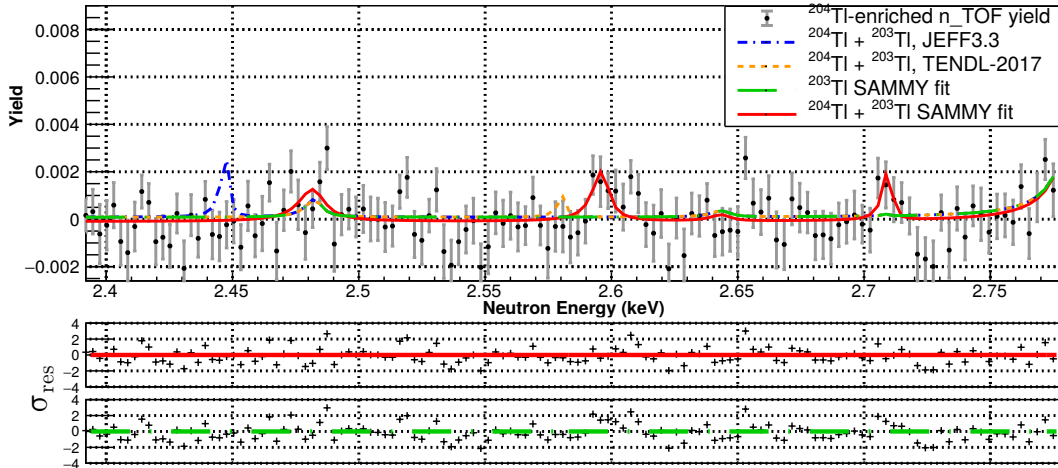
Figure 7.26: *Fit of the enriched sample yield data from 2.4 to 2.8 keV, compared to the ^{203}Tl and impurities data, and the JEFF-3.3 (TENDL-15) and TENDL-17 libraries.*
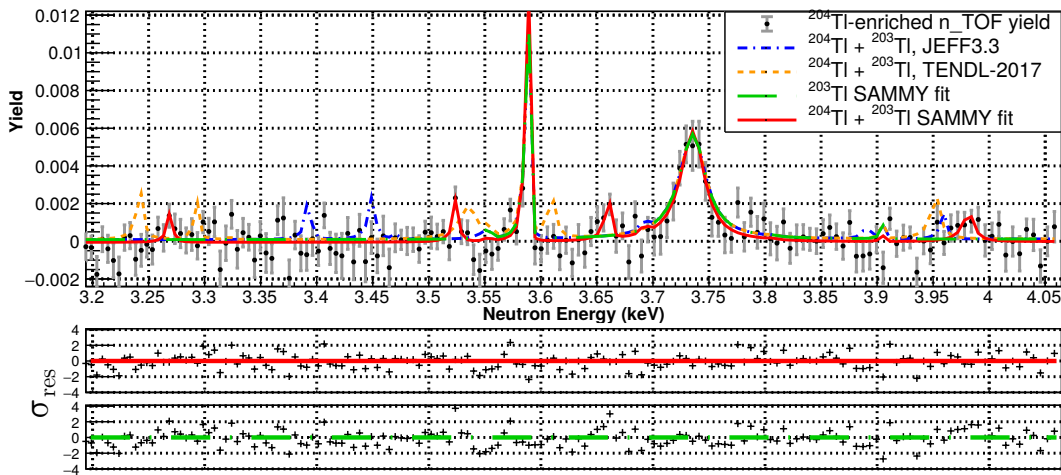
Figure 7.27: *Fit of the enriched sample yield data from 3.2 to 4 keV, compared to the ^{203}Tl and impurities data, and the JEFF-3.3 (TENDL-15) and TENDL-17 libraries.*

different TALYS calculations fall below the background fluctuation range, making no longer possible to confirm their existence.

General remarks

Despite the challenging conditions of the measurement, we were able to determine, for the first time, the presence of thirteen ^{204}Tl resonances, which are listed in
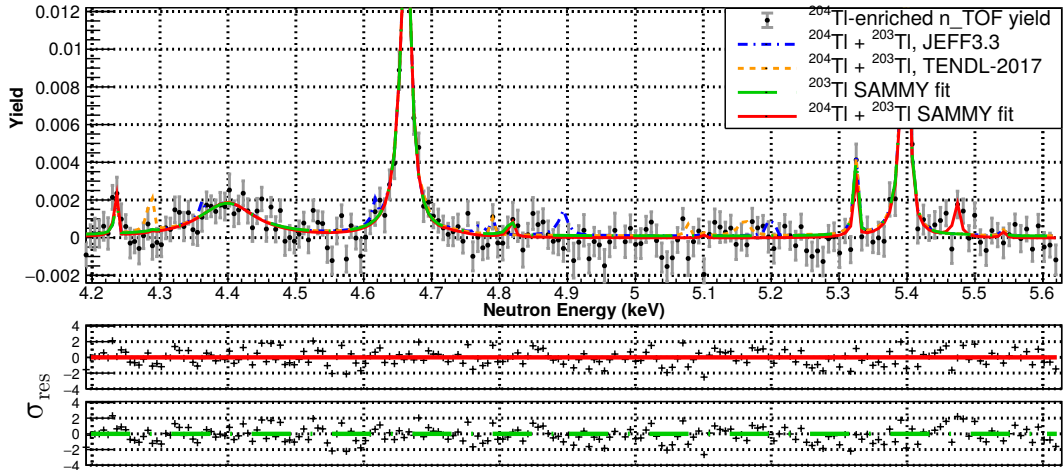
Figure 7.28: *Fit of the enriched sample yield data from 4 to 5.6 keV, compared to the ^{203}Tl and impurities data, and the JEFF-3.3 (TENDL-15) and TENDL-17 libraries.*

Table 7.16. This analysis also enabled to determine, up to ~ 5 keV in neutron energy, all the resonances from calculations which are not compatible with the experimental data within our sensitivity range.

It is difficult to determine how many levels fall below the measurement threshold in this experiment. We can use as a reference the different TALYS calculations. Up to 3 keV, in this work we found 10 levels, which compares quite favourably against the 12 listed by JEFF-3.3 (i.e. TENDL-2015), and the 13 by TENDL-2014. However, many more levels might be missing if the comparison is done with the latest 2017 and 2019 versions, which include 35 levels. However, most of these are very low amplitude l-waves

In any case, the new data on the low neutron energy resonances should provide valuable information, and tighter constrains, for future calculations of the cross section, and for astrophysical calculations, as discussed in section 7.12.

7.11.1   Systematic uncertainty estimation

The sources of systematic uncertainty considered for the ^{204}Tl(n, γ) analysis are summarized in Table 7.17. The values reported have been either discussed in the respective sections, or are directly quoted from references. The systematic uncertainty has been already applied to the MACS calculations described in the next section.

E_n (eV)	J	l	Γ_γ (meV)	Γ_n (meV)	K_r (meV)	Notes
122.49(0.01)	5/2	0	426.6(6.7)	1725(37)	205.2(2.7)	
788.5(0.3)	5/2	0	853(55)	7477(813)	459(27)	
915.4(0.2)	5/2	0	912(440)	183(31)	92(15)	
1174.3(1)	3/2	0	245(88)	1714(1387)	86(28)	*Tentative*
1371.5(0.8)	5/2	0	90(42)	1463(1225)	51(23)	*Tentative*
1779.5(0.8)	5/2	0	242(81)	2725(1848)	133(42)	
2016.7(0.5)	5/2	0	654(226)	1509(1063)	274(88)	
2267.6(1.9)	5/2	0	372(144)	4278(3060)	205(74)	*Tentative*
2594.6(1.4)	5/2	0	564(211)	7214(4713)	314(110)	*Tentative*
2707.8(0.9)	5/2	0	331(207)	857(793)	143(75)	*Tentative*
3267.4(1.3)	5/2	0	348(208)	5205(3675)	196(110)	*Tentative*
3522.3(1.3)	5/2	0	1047(700)	1251(1007)	342(177)	
3657.3(1)	5/2	0	781(276)	3263(2671)	378(123)	
3979.3(1.4)	5/2	0	1218(512)	17130(10749)	682(269)	*Tentative*
5470.8(3.4)	5/2	0	1669(802)	7758(5524)	824(342)	*Tentative*

Table 7.16: *List of all the ^{204}Tl resonances found in this work.*

Source of uncertainty	σ_{sys} (%)
PHWT [67]	2
Geometry uncertainty to WF	2
Statistical model of the capture cascade	1.5
Flux [77]	2
Background subtraction	2
Normalization	7
Detector dep. energy calibrations	3
Total	**9**

Table 7.17: *Assessment of the different sources of systematic uncertainty of the ^{204}Tl(n,γ) measurement.*

7.12   Maxwellian averaged cross section calculations

The calculation of the averaged cross section at the stellar temperatures of the s-process nucleosynthesis is the last step of the capture analysis work. The activation of the ^{204}Tl branching point happens already during the ^{13}C pocket nucleosynthesis events, at kT thermal energies of 8 keV. However, it is especially strong during He flash-burning in the thermal pulses, where the thermal conditions can reach 30 keV, leading to neutron fluxes of $10^{10} - 10^{11}$ cm^{-3} [23]. As it was already shown in the previous chapter, the maxwellian spectrum of the neutrons at that temperature extends well beyond 30 keV. Thus, for an accurate determination of the MACS it is necessary to know the capture cross section, ideally, up to several hundred keV.

In this work, we were able to measure ^{204}Tl resonances from 100 eV up to 5 keV. In addition, it is reasonable to assume that many of the levels in that range were undetectable. Nevertheless, the measured resolved resonances are also those with the highest amplitude, and thus they have an important contribution to the MACS.

In this situation, we proceed by first evaluating the impact of the new experimental results in the MACS at 1 keV. In order to have a realistic estimation of the cross section at higher neutron energies, the experimental data has been supplemented with the evaluated libraries TENDL-17 and JEFF-3.3 (the latter based on TENDL-15). It is interesting to compare both libraries in terms of number and type of the resonances. In the range of 100 eV to 5 keV, the number of s-wave resonances provided in both is similar. In this sense, the analysis was very useful to provide upper bounds to the amplitude of several s-wave resonances predicted by both libraries. Therefore, it is assumed that the experimental data, with the corrected resonances from the evaluations, provides a reasonable estimation of the s-wave resonance contribution to the MACS at 1 keV.

Concerning p-wave resonances, whereas TENDL-17 lists 32 $l = 1$ levels, JEFF-3.3 includes only 3. All these levels were included in the comparison with the experimental yield in the previous section (figures 7.24 to 7.27), where they were, in fact, too weak to be resolved. Despite that, by calculating the MACS with both evaluations it is possible to quantify the overall contribution of p-wave resonances.

In Figure 7.29, the results of several MACS calculated with SAMMY are shown, plotted in the range 1 to 8 keV. The MACS represented are those obtained by employing only the resonances from this work (Table 7.16), the MACS obtained with
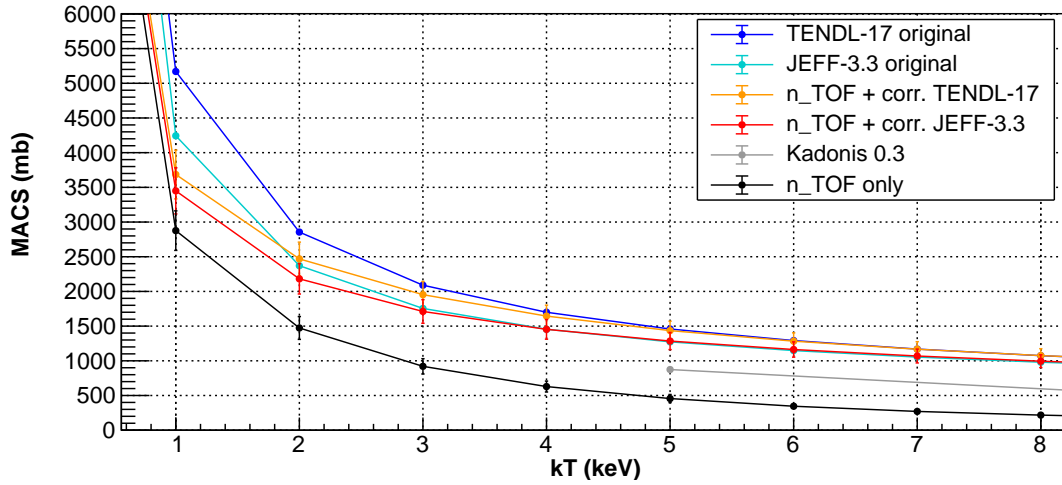
Figure 7.29: *MACS of ^{204}Tl(n, γ) in the range 1 to 8 keV. In blue and cyan, the cross section obtained with the original versions of the evaluations. In orange and red, the corrected versions, which include the new experimental data and reduced versions of some predicted resonances. In grey, the recommended MACS by the Kadonis v0.3 compilation. And in black, the direct contribution to the MACS of the results presented in thsi work.*

Source	MACS at 1 keV (mb)
TENDL-17	5170
JEFF-3.3	4243
n_TOF + corr. TENDL-17	3686(352)
n_TOF + corr. JEFF-3.3	3450(332)
n_TOF only	2877(285)

Table 7.18: *Values of the stellar ^{204}Tl(n, γ) cross section at kT = 1 keV of the MACS shown Figure 7.29.*

the original TENDL-17 and JEFF-3.3 compilations, and those MACS obtained by combining the new resonances with the corrected versions from both libraries (hereafter referred to as *corrected* versions). For comparison, the values of the MACS recommended by the Kadonis v0.3 compilation [39] are also plotted. These values are directly quoted from a theoretical calculation by Bao et al. [131].

For those MACS which included the experimental data, the uncertainty was calculated by means of the MC method employed in the MACS calculation of the ^{203}Tl(n, γ) analysis. As in there, the uncertainty given to the resonance parameters
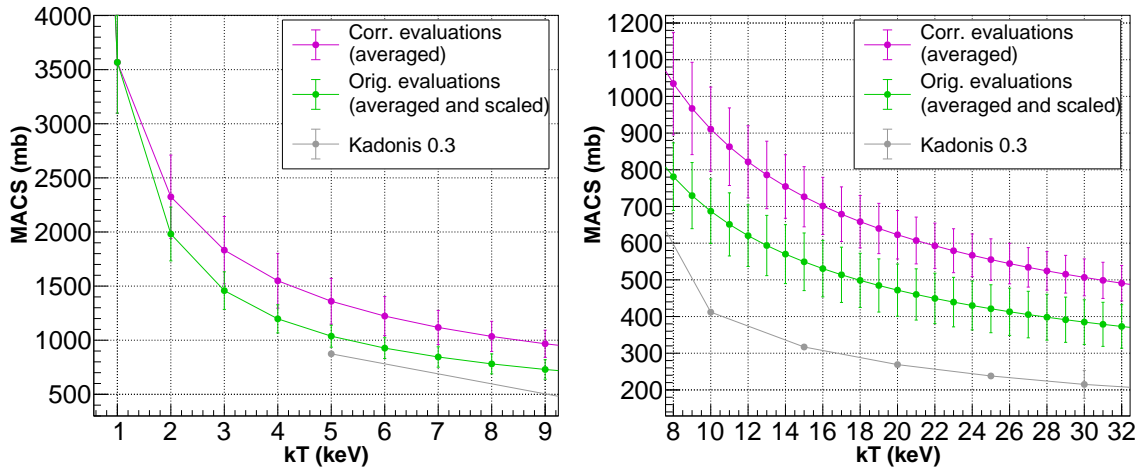
Figure 7.30: *In magenta, the MACS of ^{204}Tl(n,γ) obtained by averaging the corrected evaluations (orange and red distributions in Figure 7.29). In green, the MACS obtained by averaging the original evaluations, and scaling them to the value of the corrected average at 1 keV.*

	MACS at 8 keV	MACS at 30 keV
Average of corrected eval.	1035(140)	507(50)
Average of scaled eval.	**781(92)**	**385(61)**

Table 7.19: *Averages, at kT = 8 keV and kT = 30 keV, of the ^{204}Tl(n,γ) stellar cross sections calculated with the corrected nuclear data evaluations, and with the default evaluations normalized to the 1 keV value of the respective corrected version.*

of the evaluations was 10%.

The inclusion of the new experimental data led to an important reduction in the 1 keV MACS of 28% for TENDL-17, and of 19% for JEFF-3.3. In both cases, the contribution of the experimental resonances is high, of 78% and 83%, respectively. Consequently, the TENDL/JEFF ratio has been reduced to 7% in the corrected versions. This difference was of 22% in the original libraries. As the peak energy increases, the contribution of the new results logically decrease, and at 8 keV the corrected versions produce almost identical results as the original evaluations.

Therefore, the new measurement was useful in setting tighter lower and upper bounds at low thermal energies. In the first case, an absolute low limit to the MACS was obtained via the direct measurement of the resonances that contribute the most to it. In the second case, it limited the contribution of those resonances

predicted by the evaluations, which however were not directly measured in this work.

An estimation of the MACS at higher energies was obtained by extrapolating the results at 1 keV. The extrapolation has been performed by scaling the whole MACS distribution of each evaluation by a fixed factor. This factor has been calculated by normalizing the 1 keV MACS of each evaluation to the 1 keV MACS of the corresponding corrected version. In this way, we are adopting the average level density predicted by TENDL models, and assuming that the aggregated correction in the cross section would be similar to the one observed at the 1 keV point.

Upper and lower bounds were estimated by normalizing the distributions to the values defined by the uncertainty range of the corrected $\langle\sigma\rangle_{1keV}$ versions of Figure 7.29. Finally, the scaled MACS distributions of the evaluations have been averaged to produce a single distribution.

The results of the extrapolation are plotted in Figure 7.30. In the MACS at 8 keV and 30 keV MACS, the normalization led to a substantial reduction of 32(8)%, respect to the average value of the MACS predicted by the libraries. The resulting MACS are 781(92) at $kT = 8$ keV, and 385(61) at $kT = 30$ keV.

The MACS at 5 keV obtained with the extrapolation is compatible with the value calculated by Bao et al. However, as the energy of the neutron spectrum increases, the distributions diverge from each other considerably. This discrepancy, most probably caused by the different statistical models employed in the determination of the capture resonances, is not resolvable within the present work. However, if the extrapolation described above is reasonably accurate, it would lead to a considerable increase in the MACS compared to Kadonis v0.3.

In summary, the higher value of the ^{204}Tl MACS is expected to contribute to a significant reduction of the s-only ^{204}Pb abundance. However, a quantitative assessment of this effect needs to be evaluated by means of a stellar model for a thermally pulsating asymptotic giant star. On one hand, ^{204}Pb is produced only by the branching at ^{204}Tl because it is shielded from the r-process by ^{204}Hg. On the other hand, ^{204}Pb is not affected by the α-recycling beyond ^{209}Hg, nor by the radiogenic contribution from the Th/U decay chains.

Since the ^{204}Tl branching is very sensitive to the thermal conditions, the new MACS in combination with suitable stellar models can provide a new insight into the strong temperature and neutron density fluctuations characteristics of TP-AGB stars.

Conclusions and outlook

The aim of this work was to perform, for the first time ever, a capture experiment on the s-process branching point ^{204}Tl.

Thanks to a careful preparation, which included a gamma ray imaging inspection of the sample and modifications of the convetional C_6D_6 capture setup at n_TOF, the measurement could be performed, producing valuable experimental data. The positive outcome of the experimental ^{204}Tl(n, γ) campaign highlights, once more, the capabilities of the n_TOF facility for the realization of capture experiments on extremely radioactive, low mass samples. This could be achieved thanks to both the high instant flux of its neutron spallation source, and to the low intrinsic background of EAR1, which provides a excellent signal-to-background ratio.

Although the high neutron energy resolution achievable in EAR1 is important in general for any experiment, it was particularly crucial for a measurement involving a multi-nuclide sample, like the one employed in this work. In the measured capture yield, resonances from different isotopes appeared very close in neutron energy, or even partially overlapped. The high energy resolution enabled, in most cases, a clear separation and identification of capture resonances.

Finally, the measurement was also possible thanks to the use of C_6D_6 detectors. These detectors have very fast response, and low gamma ray efficiency. Both qualities were especially desirable in the context of a very high gamma ray background due to the sample activity. In addition, the C_6D_6 detectors at n_TOF are optimized for a very low neutron sensitivity, something particularly useful in measurements of nuclides with high scattering to capture ratios, like ^{203}Tl and ^{204}Tl. Despite this, the detector setup had to be modified with the addition of lead shields to reduce the signal background due to the very high activity. However, thanks to the flexibility of the Pulse Height Weighting Technique, the total energy detection

method could still be applied while keeping the associated systematic errors under control.

The ^{203}Tl capture experiment was originally planned as an ancillary measurement of the ^{204}Tl campaign. However, the experimental data obtained turned out to be of interest by itself. Particularly important was the resonance data under 3 keV, which contains the strongest resonances of ^{203}Tl. In this sense, the results reported here are the first detailed R-matrix analysis of these resonances in a high neutron energy resolution experiment. This has led to an improvement of the stellar cross section of ^{203}Tl in the thermal energy range between 1 keV and 10 keV. This is the relevant regime for ^{13}C pocket nucleosynthesis. In particular, it was observed a consistent trend of lower resonance kernels between 8 keV and 12 keV, compared to the previous experiment at ORNL. This led to a 12% decrease in the MACS at 10 keV, and to a different decreasing slope in the range between 5 keV and 10 keV. Thus, it is a matter for future nucleosynthesis studies to work out the possible impact on the s-process termination zone considering these new results.

In view of the results, a new measurement with more material and higher statistics could potentially improve the experimental data at higher thermal neutron energies ($\gtrsim$ 25 keV). Related to this, the measurement of ^{205}Tl(n, γ) performed at n_TOF in 2018 [45] could provide new insights. The measurement was carried out with a natural thallium sample, which contains 29.5% of ^{203}Tl. Since the sample was considerably larger, it contained almost 5 times the amount of ^{203}Tl present in the sample of this work.

In this way, the present measurement complements opportunely the ^{205}Tl(n, γ) of 2018. At low energies, the new ^{203}Tl data will be very useful to discriminate between low amplitude ^{205}Tl resonances and strong ^{203}Tl levels. On the other hand, due to the much better statistics, it is expected that the 2018 experiment will provide statistically more accurate ^{203}Tl resonance data in the range between 25 keV and 35 keV, with the possibility of detecting resonances up to 50 keV.

Concerning the ^{204}Tl(n, γ) measurement, a self-normalization based on resonances kernels was developed. This method enabled the first R-matrix resonance analysis of several ^{204}Tl levels in the range from 100 eV to 5 keV. Given the limitations in target material and statistics, the self-normalization method introduces an acceptable systematic uncertainty of 7%. It is believed that this new resonance data could lead to new and improved calculations of the ^{204}Tl(n, γ) cross section over a broader energy range.

The MACS results obtained in this work at low thermal energies have been extrapolated to higher energies, employing the current nuclear data evaluations. The result points towards a possible important increase in the MACS of ^{204}Tl, which would lead to a lower production of ^{204}Pb by current stellar models. Because the ^{204}Tl branching is very sensitive to temperature and neutron density conditions, the new MACS in contribution with thermally pulsating AGB models can be used to obtain new insights into the physical conditions of these red giant stars.

Appendix A

Description of the data sorting routine

Three were the scripts employed to produce the experimental capture yield. The activity of the ^{204}Tl enriched sample made it very convenient to separate the data sorting process and the posterior yield calculation. The data sorting of the full ^{204}Tl(n, γ) runs could last about three hours in a desktop PC. To reduce this time, the files were pre-processed to apply a low cut in amplitude, at about 400 keV. This eliminated 85% of the data to analyse in the sorting, and reduced the computing time to approximately 8 minutes.

1. A first script sorts, signal by signal, the PSA processed data, and performs the following tasks:

   i) It applies the calibrations to each detector, and applies the selection cuts in energy deposition.

   ii) It applies further cuts in time-of-flight, in γ-flash time, in proton intensity –namely to separate parasitic and dedicated pulses–, and in neutron intensity, if required.

   iii) Finally, it performs the time-of-flight to energy conversion, and applies the weights of the WF.

   iv) When the previous tasks done, the required histograms for the analysis are filled. These are: a) time-of-flight and neutron energy histograms, both weighted and unweighted; b) deposited energy histograms, and c) average counting rate histograms for monitoring purposes.

When the sorting of all signals is done, the histograms are saved in a ROOT file.

The total number of protons, neutrons and proton bunches are stored in a specific ROOT histogram. The list of runs to analyse, and the detector calibrations parameters are provided in separate input files, which are easy to modify without editing the script. This made it quicker to incorporate modifications over the course of the measurement, in order to facilitate the online analysis.

2. A second script unifies the output of the different samples of the experimental campaign. It normalizes the histograms, and in the case of the ^{204}Tl(n, γ) data, performs the subtraction of the activity background. The output of this script is a ROOT file containing the counting rate vs. neutron energy histograms of the particular experimental campaign.

3. A third script performs the subtraction of the beam-induced backgrounds, and carries out the calculation of the yield. This is done for each detector separately, in order to apply all the corresponding correction factors. Finally, the individual yields are summed and averaged to produce the final capture yield.

Appendix B

List of ^{203}Tl(n,γ) resonances employed in this work

Table B.1: *List of the capture resonances of ^{203}Tl employed in this work, up to 32 keV. Resonances without associated uncertainty are levels found by Macklin and Winters at ORNL. Their parameters have been adjusted and a 10% uncertainty has been employed in the MACS calculations.*

E_{res} (eV)	J	l	Γ_γ (meV)	Γ_n (meV)	$\Gamma_\gamma\Gamma_n/\Gamma$ (meV)
37.99(0.04)	1	1	117(83)	0.0185(0.0038)	0.014(0.003)
235.7(0.01)	1	0	634(7)	3814(10)	407.8(3.7)
539.21(0.05)	2	1	145(70)	2(0)	2.8(0.2)
841.72(0.03)	1	0	557(34)	373(27)	167.5(8.3)
857.7(0.01)	1	0	30(31)	2(0)	1.1(0.3)
995.6(0.06)	0	1	11(3)	31(8)	2.08(0.44)
1137.3(0.6)	0	0	634(19)	45962(1660)	156.3(4.6)
1274.78(0.05)	1	0	831(84)	643(66)	272(20)
1327.87(0.04)	1	0	406(100)	185(39)	95(16)
1432.5(0.2)	0	0	623(24)	6730(328)	143(5)
1917.3(0.3)	1	1	434(283)	15(2)	11.1(1.6)
2001.8(0.2)	0	1	160(91)	78(18)	13.1(3.2)
2789.4(0.2)	1	0	506(25)	3456(221)	331(14)
3551	0	1	229	17	4

Table B.1: *continued.*

E_{res} (eV)	J	l	Γ_γ (meV)	Γ_n (meV)	$\Gamma_\gamma\Gamma_n/\Gamma$ (meV)
3585.7(0.3)	1	1	1269(563)	94(10)	65.7(6.7)
3730.8(1.8)	0	0	739(76)	22720(3759)	179(18)
3905	0	1	218	14	3
4233.8	0	1	735	47	11
4398.2(5.2)	0	0	885(115)	62894(6865)	218(28)
4659.7(0.8)	1	0	767(45)	12398(1019)	542(30)
4785.7(0.2)	1	0	218(207)	33(12)	21.6(7.5)
5322.7(0.5)	0	1	292(73)	802(279)	54(11)
5394.7(0.6)	1	0	638(49)	7465(748)	441(31)
5540.9(0.1)	1	0	149(145)	28(12)	17.6(7)
5656	2	1	270	9	11
5686	2	1	270	11	13
5767	2	1	270	10	12
5807.9(0.55)	1	0	441(56)	1727(244)	263(28)
6206.4	1	1	157	13	9
6249.8	1	1	231	25	17
6331.2(1)	1	0	441(49)	5970(724)	308(32)
6606(14)	0	0	583(187)	48286(7692)	144(46)
6735.6(2)	1	0	278(244)	122(56)	64(26)
7413.4(0.7)	2	1	2287(978)	279(36)	311(38)
7564	1	1	293	29	20
7910.8(1.5)	1	0	312(284)	108(48)	60(24)
8151	1	1	187	16	11
8512.8(0.9)	1	0	322(52)	2041(590)	208(30)
8770	1	1	202	19	13
9179.5(1.4)	0	1	492(127)	1857(569)	97(21)
9350.6(2.4)	1	0	415(68)	5947(1284)	291(45)
9738(2.4)	2	1	177(0)	24(0)	26(0)
9939.7(0.4)	1	0	386(350)	186(93)	94(42)
10162.4(1.2)	1	1	565(126)	1650(1062)	316(74)
10550.4	1	1	359	78	48

Table B.1: *continued.*

E_{res} (eV)	J	l	Γ_γ (meV)	Γ_n (meV)	$\Gamma_\gamma\Gamma_n/\Gamma$ (meV)
10740.2	2	1	560	63	70
10884	1	1	287	40	26
10971.2(5.6)	0	0	893(300)	12814(3068)	209(66)
11180	2	1	182	25	28
11230	1	1	239	27	18
11290	2	1	207	41	42
11540	2	1	219	49	50
11770	1	1	375	95	57
12098.1(3)	1	1	967(639)	322(149)	181(70)
12339	2	1	269	71	70
12370.6(5.7)	1	0	345(135)	18639(2650)	254(97)
12606.7(4.1)	0	0	437(336)	24791(19023)	107(81)
12870(10)	0	0	513(407)	67923(56057)	127(100)
13016	1	1	407	61	40
13250	1	1	401	53	35
13500	1	1	405	80	50
14060	2	1	241	69	67
14161.7(0.8)	2	1	236(155)	261(191)	155(76)
14499.6(1.5)	2	1	324(315)	58(42)	61(39)
14752.2(0.2)	1	0	360(334)	113(56)	64(28)
14841.6(1.3)	1	1	689(274)	1006(329)	307(83)
15103.6(3.3)	1	0	712(131)	6777(5170)	483(88)
15221.6(2.3)	2	1	258(253)	73(54)	71(44)
15490	2	1	270	56	58
15584.8	2	1	240	188	132
15610	2	1	270	55	57
15670	2	1	242	55	56
15880	2	1	270	58	59
16080	2	1	270	29	33
16272(11)	1	0	652(185)	33770(17578)	479(134)
16360	2	1	270	147	119

Table B.1: *continued.*

E_{res} (eV)	J	l	Γ_γ (meV)	Γ_n (meV)	$\Gamma_\gamma\Gamma_n/\Gamma$ (meV)
16460	2	1	270	54	56
17337.5	1	0	400	44000	297
17651.2	2	1	270	66	66
17963(7)	1	0	420(175)	10911(5463)	303(122)
18448(1)	1	0	473(322)	596(491)	198(104)
18598.5(3.5)	1	0	581(358)	966(851)	272(138)
18730.2	2	1	350	53	58
18833.1	1	1	350	171	86
19170(14)	1	0	857(181)	21139(3821)	618(126)
19250	0	0	1000	64000	246
19300	2	1	270	66	66
19668(7)	1	0	520(241)	1581(1601)	294(126)
19900	2	1	600	170	166
20213.7	0	0	860	10000	198
20771(10)	1	0	607(162)	28389(14610)	446(116)
21087(5)	1	0	526(218)	4254(3578)	351(133)
21797(7)	1	0	597(216)	3946(3517)	389(130)
21978(7)	1	0	186(103)	3012(2891)	131(69)
22447(7)	1	0	943(483)	1952(1860)	477(221)
22630	2	1	270	55	57
22773(5)	1	0	165(0)	5285(0)	120(0)
23190	1	0	600	61	42
23290	0	0	600	80000	149
23662	1	0	300	13333	220
23790	2	1	270	50	53
23960.9	1	0	560	32000	413
24793(19)	1	0	466(190)	14265(12299)	338(134)
24820	0	0	690	60000	171
25723(9)	0	0	2350(923)	21065(15372)	528(191)
26020(8)	1	0	489(236)	3369(3257)	320(141)
26444(6)	1	0	951(314)	4439(4518)	588(192)

Table B.1: *continued.*

E_{res} (eV)	J	l	Γ_γ (meV)	Γ_n (meV)	$\Gamma_\gamma\Gamma_n/\Gamma$ (meV)
26670	1	0	623	11333	443
27470	1	0	560	100	64
27550	1	0	700	744	270
27700	1	0	560	560	210
28040	2	1	270	86	82
28180	0	0	1350	70000	331
28290	1	0	560	85	55
28629	1	0	516	11333	370
29219(7)	1	0	1255(687)	1829(1380)	558(250)
29366	0	0	526	50000	130
29728	1	0	467	48000	347
30452(6)	1	0	747(228)	6242(5823)	501(145)
31313(11)	1	0	321(194)	8516(8782)	232(135)
31763(6)	1	0	1391(613)	4588(3749)	800(311)
32310(3)	1	0	1852(647)	7258(5382)	1107(350)
32809(10)	1	0	790(308)	18167(16390)	568(214)

Bibliography

[1] P. W. Merrill, Astrophys. J. **116**, 21 (1952).

[2] E. M. Burbidge, G. R. Burbidge, W. A. Fowler, and F. Hoyle, Rev. Mod. Phys. **29**, 547 (1957).

[3] A. G. W. Cameron, *Stellar evolution, nuclear astrophysics, and nucleogenesis*, edited by D. M. Kahl (Dover Publications, 2013, originally published as a technical report by Atomic Energy of Canada, Ltd., 1957).

[4] F. Käppeler, R. Gallino, S. Bisterzo, and W. Aoki, Rev. Mod. Phys. **83**, 157 (2011).

[5] M. R. Drout et al., Science **358**, 1570 (2017).

[6] D. Watson et al., Nature **574**, 497 (2019).

[7] M. Arnould, S. Goriely, and K. Takahashi, Physics Reports **450**, 97 (2007).

[8] M. Arnould and S. Goriely, Physics Reports **384**, 1 (2003).

[9] C. Iliadis, *Nuclear physics of stars; 2nd ed.* (John Wiley & Sons, 2015).

[10] P. A. Seeger, W. A. Fowler, and D. D. Clayton, Astrophys. J. Suppl. Ser. **11**, 121 (1965).

[11] D. Clayton and R. Ward, Astrophys. J. **193**, 397 (1974).

[12] F Käppeler, R Gallino, M Busso, G Picchio, and C. Raiteri, Astrophys. J. **354**, 630 (1990).

[13] F. Käppeler, H. Beer, and K. Wisshak, Rep. Prog. Phys. **52**, 945 (1989).

[14] M. Pignatari, R. Gallino, M. Heil, M. Wiescher, F. Käppeler, F. Herwig, and S. Bisterzo, Astrophys. J. **710**, 1557 (2010).

[15] F. Voss, K. Wisshak, K. Guber, F. Käppeler, and G. Reffo, Phys. Rev. C **50**, 2582 (1994).

[16] K. Wisshak, F. Voss, C. Theis, F. Käppeler, K. Guber, L. Kazakov, N. Kornilov, and G. Reffo, Phys. Rev. C **54**, 1451 (1996).

[17] K. Wisshak, F. Voss, F. Käppeler, L. Kazakov, and G. Reffo, Phys. Rev. C **57**, 391 (1998).

[18] F. Käppeler, Prog. Part. Nucl. Phys. **43**, 419 (1999).

[19] K. Takahashi and K. Yokoi, At. Data Nucl. Data Tables **36**, 375 (1987).

[20] S. Degl'Innocenti, P. G. Prada Moroni, M. Marconi, and A. Ruoppo, Astrophys. Space Sci. **316**, 25 (2008).

[21] A. Chieffi, M. Limongi, and O. Straniero, Astrophys. J. **502**, 737 (1998).

[22] B. Paxton, L. Bildsten, A. Dotter, F. Herwig, P. Lesaffre, and F. Timmes, Astrophys. J. Suppl. Ser. **192**, 3 (2010).

[23] S. Cristallo, O. Straniero, R. Gallino, L. Piersanti, I. Domínguez, and M. T. Lederer, Astrophys. J. **696**, 797 (2009).

[24] M. Pignatari et al., Astrophys. J. Suppl. Ser. **225**, 24 (2016).

[25] R. Gallino, C. Arlandini, M. Busso, M. Lugaro, C. Travaglio, O. Straniero, A. Chieffi, and M. Limongi, Astrophys. J. **497**, 388 (1998).

[26] F. Herwig, Annual Review of Astronomy and Astrophysics **43**, 435 (2005).

[27] O. Straniero, R. Gallino, and S. Cristallo, Nucl. Phys. A **777**, Special Isseu on Nuclear Astrophysics, 311 (2006).

[28] S. Bisterzo, R. Gallino, F. Käppeler, M. Wiescher, G. Imbriani, O. Straniero, S. Cristallo, J. Görres, and R. J. deBoer, Mon. Not. R. Astron. Soc. **449**, 506 (2015).

[29] C. Domingo-Pardo et al., Phys. Rev. C **74**, 055802 (2006).

[30] C. Domingo-Pardo et al., Phys. Rev. C **76**, 045805 (2007).

[31] C. Domingo-Pardo et al., Phys. Rev. C **74**, 025807 (2006).

[32] K Lodders, H Palme, and H.-P. Gail, in *Solar system* (Springer, 2009), pp. 712–770.

[33] C. Domingo-Pardo et al., Phys. Rev. C **75**, 015806 (2007).

[34] C. Guerrero, C. Domingo-Pardo, D. Schumann, S. Heinitz, C. Lederer, J. Praena, M. Sabate, and J. M. Quesada, *Neutron capture at the s-process branching points* ^{171}Tm *and* ^{204}Tl, tech. rep. CERN-INTC-2014-003. INTC-P-404 (CERN, Geneva, 2014).

[35] K. Yokoi, K. Takahashi, and M. Arnould, Astron. Astrophys. **145**, 339 (1985).

[36] G. J. Wasserburg, M. Busso, R. Gallino, and C. M. Raiteri, Astrophys. J. **424**, 412 (1994).

[37] N. Mowlavi, S. Goriely, and M. Arnould, Astron. Astrophys. **330**, 206 (1998).

[38] B. Côté, M. Lugaro, R. Reifarth, M. Pignatari, B. Világos, A. Yagüe, and B. K. Gibson, Astrophys. J. **878**, 156 (2019).

[39] I. Dillmann, M. Heil, F. Käppeler, R. Plag, T. Rauscher, and F. Thielemann, AIP Conference Proceedings **819**, 123 (2006).

[40] J. B. Blake and D. N. Schramm, Astrophys. J. **197**, 615 (1975).

[41] S. G. Nielsen, M. Rehkämper, and A. N. Halliday, Geochim. Cosmochim. Acta **70**, 2643 (2006).

[42] R. Baker, M. Schönbächler, M. Rehkämper, H. Williams, and A. Halliday, Earth Planet. Sci. Lett. **291**, 39 (2010).

[43] C. Palk, R. Andreasen, M. Rehkämper, A. Stunt, K. Kreissig, B. Coles, M. Schönbächler, and C. Smith, Meteorit. Planet. Sci. **53**, 167 (2018).

[44] M. Lugaro, U. Ott, and Á. Kereszturi, Prog. Part. Nucl. Phys. **102**, 1 (2018).

[45] A. Casanovas et al., "Neutron capture measurement at the n_TOF facility of the ^{204}Tl and ^{205}Tl s-process branching points", Proceedings of the NPAIX (2020, Accepted for publication).

[46] Y. A. Litvinov, *Proposal E121: Measurement of the bound-state beta decay of bare ^{205}Tl ions*, tech. rep. (GSI, 2017).

[47] N. Bohr, Nature **137**, 344 (1936).

[48] A. M. Lane and R. G. Thomas, Rev. Mod. Phys. **30**, 257 (1958).

[49] F. Gunsing, *Introduction to neutron-induced reactions and the R-matrix formalism*, Joint ICTP-IAEA School on "Nuclear Data Measurements for Science and Applications" (2015).

[50] S. Chiba, H. Koura, T. Hayakawa, T. Maruyama, T. Kawano, and T. Kajino, Phys. Rev. C **77**, 015809 (2008).

[51] T. Rauscher, R. Bieber, H. Oberhummer, K.-L. Kratz, J. Dobaczewski, P. Möller, and M. M. Sharma, Phys. Rev. C **57**, 2031 (1998).

[52] E. P. Wigner and L. Eisenbud, Phys. Rev. **72**, 29 (1947).

[53] J. M. Blatt and L. C. Biedenharn, Rev. Mod. Phys. **24**, 258 (1952).

[54] F. Frohner, *Evaluation and Analysis of Nuclear Resonance Data* (Nuclear Energy Agency of the OECD (NEA), 2000).

[55] G. Breit and E. Wigner, Phys. Rev. **49**, 519 (1936).

[56] C. W. Reich and M. S. Moore, Phys. Rev. **111**, 929 (1958).

[57] N. M. Larson, *Updated User's Guide for Sammy: Multilevel R-Matrix Fits to Neutron Data Using Bayes' Equations*, tech. rep. (Oak Ridge National Laboratory, Oct. 2008).

[58] P. Schillebeeckx, *From experimental observables to model parameters in the resonance regionli*, 3rd n_TOF Winter School (2018).

[59] M. Moxon, T. Ware, and C. Dean, *REFIT-2009: A Least-square Fitting Program For Resonance Analysis Of Neutron Transmission, Capture, Fission And Scattering Data Users' Guide For REFIT-2009-10*, tech. rep. (UKNSF(2010)P243, April 2010).

[60] C. Guerrero et al., Nucl. Instrum. Methods Phys. Res., Sect. A **608**, 424 (2009).

[61] C. Massimi et al., Phys. Rev. C **81**, 044616 (2010).

[62] C. Domingo-Pardo, Nucl. Instrum. Methods Phys. Res., Sect. A **825**, 78 (2016).

[63] V. Babiano, J. Balibrea, L. Caballero, D. Calvo, I. Ladarescu, J. Lerendegui, S. M. Prats, and C. Domingo-Pardo, Nucl. Instrum. Methods Phys. Res., Sect. A **953**, 163228 (2020).

[64] P. Žugec et al., Nucl. Instrum. Methods Phys. Res., Sect. A **760**, 57 (2014).

[65] M. Moxon and E. Rae, Nucl. Instrum. Methods **24**, 445 (1963).

[66] R. L. Macklin and J. H. Gibbons, Phys. Rev. **159**, 1007 (1967).

[67] U Abbondanno et al., Nucl. Instrum. Methods Phys. Res., Sect. A **521**, 454 (2004).

[68] A. Borella, G. Aerts, F. Gunsing, M. Moxon, P. Schillebeeckx, and R. Wynants, Nucl. Instrum. Methods Phys. Res., Sect. A **577**, 626 (2007).

[69] C. Domingo-Pardo, "New radiative neutron capture measurement of ^{207}Pb and ^{209}Bi", PhD thesis (CSIC - Universitat de València, 2004).

[70] W. H. Press, S. A. Teukolsky, W. T. Vetterling, and B. P. Flannery, *Numerical recipes 3rd edition: the art of scientific computing*, 3rd ed. (Cambridge University Press, USA, 2007).

[71] F. Gunsing et al., Eur. Phys. J. Plus **131**, 371 (2016).

[72] N. Colonna et al., Eur. Phys. J. A **56**, 48 (2020).

[73] M. Barbagallo et al., Phys. Rev. Lett. **117**, 152701 (2016).

[74] L. Damone et al., Phys. Rev. Lett. **121**, 042701 (2018).

[75] M. Sabaté-Gilarte, J. Praena, I. Porras, J. M. Quesada, and P. Mastinu, Reports of Practical Oncology & Radiotherapy **21**, 7th Young BNCT meeting, 113 (2016).

[76] A. Mengoni, *NEAR station physics*, n_TOF Collaboration meeting (Prague, October 2019).

[77] M. Barbagallo et al., Eur. Phys. J. A **49**, 156 (2013).

[78] *International Evaluation of Neutron Cross-Section Standards*, Non-serial Publications (IAEA, Vienna, 2007).

[79] S. Marrone et al., Nucl. Instrum. Methods Phys. Res., Sect. A **517**, 389 (2004).

[80] S. A. Andriamonje et al., J. Korean Phys. Soc. **59**, 1597 (2011).

[81] Y. Giomataris, P. Rebourgeard, J. Robert, and G. Charpak, Nucl. Instrum. Methods Phys. Res., Sect. A **376**, 29 (1996).

[82] C. Guerrero et al., J. Korean Phys. Soc. **59**, 1624 (2011).

[83] D. B. Gayther, Metrologia **27**, 221 (1990).

[84] C. Paradela et al., Phys. Rev. C **82**, 034601 (2010).

[85] D. Tarrío et al., Phys. Rev. C **83**, 044620 (2011).

[86] A Ferrari, P. R. Sala, A Fassò, and J. Ranft, *FLUKA: A multi-particle transport code (program version 2005)*, CERN Yellow Reports: Monographs (CERN, Geneva, 2005).

[87] E. D.B. Pelowitz, *MCNPX Users Manual Version 2.7.0*, tech. rep. (LA-CP-11-00438, 2011).

[88] J. Allison et al., IEEE T. Nucl. Sci. **53**, 270 (2006).

[89] J. Allison et al., Nucl. Instrum. Methods Phys. Res., Sect. A **835**, 186 (2016).

[90] S. Lo Meo et al., Eur. Phys. J. A **51**, 160 (2015).

[91] S. Andriamonje et al., J. Korean Phys. Soc. **59**, 1601 (2011).

[92] C. Guerrero et al., Eur. Phys. J. A **49**, 27 (2013).

[93] R. Plag, M. Heil, F. Käppeler, P. Pavlopoulos, R. Reifarth, and K. Wisshak, Nucl. Instrum. Methods Phys. Res., Sect. A **496**, 425 (2003).

[94] O. Klein and Y. Nishina, Z. Phys. **52**, 853 (1929).

[95] U. Abbondanno et al., Nucl. Instrum. Methods Phys. Res., Sect. A **538**, 692 (2005).

[96] A. Masi et al., in 16th Int. Conf. on Accelerator and Large Experimental Control Systems (ICALEPCS'17), Barcelona, Spain, 8-13 October 2017 (JACOW, Geneva, Switzerland, 2018), pp. 1900–1905.

[97] E. Cano, S. Murray, D. F. Kruse, V. Kotlyar, and D. Côme, J. Phys.: Conf. Ser. **664**, 042007. 8 p (2015).

[98] P. Žugec et al., Nucl. Instrum. Methods Phys. Res., Sect. A **812**, 134 (2016).

[99] P Žugec, *User's guide through Pulse Shape Analysis routines*, Internal Report (n_TOF Collaboration).

[100] R. Brun and F. Rademakers, Nucl. Instrum. Methods Phys. Res., Sect. A **389**, New Computing Techniques in Physics Research V, 81 (1997).

[101] M. Wang, G. Audi, A. H. Wapstra, F. G. Kondev, M. MacCormick, X. Xu, and B. Pfeiffer, Chin. Phys. C **36**, 1603 (2012).

[102] J. Lerendegui-Marco, "Radiative neutron capture on ^{242}Pu: addressing the target accuracies for innovative nuclear systems.", PhD thesis (Universidad de Sevilla, 2019).

[103] J. Lerendegui-Marco et al., Phys. Rev. C **97**, 024605 (2018).

[104] N. Akchurin and H. Kim, Nucl. Instrum. Methods Phys. Res., Sect. A **574**, 121 (2007).

[105] S. S. Stevens and J. W. Longworth, IEEE T. Nucl. Sci. **19**, 356 (1972).

[106] F. Gunsing et al., Phys. Rev. C **85**, 064601 (2012).

[107] G. F. Knoll, *Radiation detection and measurement; 4th ed.* (Wiley, New York, NY, 2010).

[108] J. Tain and D. Cano-Ott, Nucl. Instrum. Methods Phys. Res., Sect. A **571**, 719 (2007).

[109] *Evaluated Nuclear Structure Data File*, National Nuclear Data Center (NNDC), Brookhaven National Laboratory.

[110] W. Dilg, W. Schantl, H. Vonach, and M. Uhl, Nucl. Phys. A **217**, 269 (1973).

[111] A. Gilbert and A. G. W. Cameron, Canadian Journal of Physics **43**, 1446 (1965).

[112] J. Kopecky and M. Uhl, Phys. Rev. C **41**, 1941 (1990).

[113] J. Voignier, S. Joly, and G. Grenier, Nucl. Sci. Eng. **93**, 43 (1986).

[114] H. D. Choi et al., *Database of prompt gamma rays from slow neutron capture for elemental analysis*, tech. rep. IAEA-STI/PUB/1263 (IAEA, 2007).

[115] R. Capote et al., Nucl. Data Sheets **110**, Special Issue on Nuclear Reaction Data, 3107 (2009).

[116] S. F. Mughabghab, *Atlas of neutron resonances; 5th ed.* (Elsevier Science & Technology, 2006).

[117] V. I. Plyaskin and R. A. Kosilov, *Level density parameters for the back-shifted fermi gas model in the mass range $24 \leq A \leq 250$*, tech. rep. (INDC(CCP)–424, IAEA, 2000), pp. 27–44.

[118] H. I. Kim, M. J. Yi, and Y.-O. Lee, J. Nucl. Sci. Technol. **44**, 1117 (2007).

[119] J. Kopecky, *Handbook for calculations of nuclear reaction data reference input parameter library*, edited by IAEA, TECDOC Series 1034 (IAEA, Vienna, 1998) Chap. 6, p. 123.

[120] *Joint Evaluated Fission and Fusion (JEFF) Nuclear Data Library 3.3*, Nuclear Energy Agency (NEA).

[121] D. Brown et al., Nuclear Data Sheets **148**, Special Issue on Nuclear Reaction Data, 1 (2018).

[122] R. L. Macklin and R. R. Winters, Astrophys. J. **208**, 812 (1976).

[123] R. L. Macklin and R. R. Winters, Nucl. Sci. Eng. **78**, 110 (1981).

[124] H. I. Liou, J. Rainwater, G. Hacken, and U. N. Singh, Phys. Rev. C **12**, 102 (1975).

[125] V. Konks and F. Shapiro, J. Exp. Theor. Phys. **20**, 531 (1965).

[126] P. R. Oliva, D. Prosperi, and R. Alberini, Il Nuovo Cimento A (1965-1970) **19**, 294 (1974).

[127] P Schillebeeckx et al., J. Instrum. **7**, C03009 (2012).

[128] P. Schillebeeckx et al., Nucl. Instrum. Methods Phys. Res., Sect. A **613**, 378 (2010).

[129] J. Sublet, A. Koning, D. Rochman, M. Fleming, and M. Gilbert, in Advances in nuclear nonproliferation technology and policy conference (2015).

[130] T Watanabe, G. E. Stokes, and R. P. Schuman, pp 893-6 of Neutron Cross Sections and Technology. Goldman, D. T. (ed.). Washington, D. C., National Bureau of Standards, 1968. (1969).

[131] Z. Bao, H. Beer, F. Käppeler, F. Voss, K. Wisshak, and T. Rauscher, At. Data Nucl. Data Tables **76**, 70 (2000).